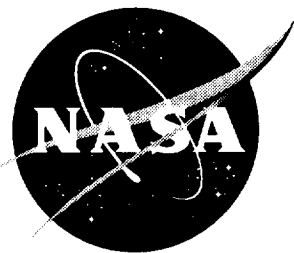


NASA/CR-1999-209002



Advanced Turbofan Duct Liner Concepts

*Gerald W. Bielak and John W. Premo
Boeing Commercial Airplane Group, Seattle, Washington*

*Alan S. Hersh
Hersh Acoustical Engineering, Inc., Westlake Village, California*

National Aeronautics and
Space Administration

Langley Research Center
Hampton, Virginia 23681-2199

Prepared for Langley Research Center
under Contract NAS1-20090

February 1999

The use of trademarks or names of manufacturers in the report is for accurate reporting and does not constitute an official endorsement, either expressed or implied, of such products or manufacturers by the National Aeronautics and Space Administration.

Available from:

NASA Center for AeroSpace Information (CASI)
7121 Standard Drive
Hanover, MD 21076-1320
(301) 621-0390

National Technical Information Service (NTIS)
5285 Port Royal Road
Springfield, VA 22161-2171
(703) 605-6000

Table Of Contents

	Page
LIST OF FIGURES	v
LIST OF TABLES	viii
1.0 Summary	1
2.0 Introduction	5
2.1 Technical Approach	5
2.2 Report Organization	6
3.0 Passive Acoustic Liners	8
3.1 Acoustic Liner Characteristics	8
3.2 Summary Of Preliminary NASA/FAA Contract Investigating Broadband Liner Concepts	8
3.3 Passive Liner Tests.	10
3.3.1 Grazing Flow Impedance Measurement Technique	11
3.3.2 Grazing Flow Impedance Measurements For Passive Element Liners	12
3.3.3 Bulk Absorber Materials Study	13
3.3.4 Linear Liners	15
3.3.4.1 Slot Linear Liners	16
3.3.4.2 Micro-perforate Linear Liners	16
4.0 Adaptive Liners	19
4.1 Introduction	19
4.2 Bias Flow Adaptive Liner Designs	19
4.3 High Temperature Adaptive Liner Design	20
5.0 ADP Model Fan Acoustic Liner Design	21
5.1 Aft Liner Depth Constraints	21
5.2 Target ADP 22” Fan Rig Hardwall Fan Noise Spectra	22
5.2.1 ADP Demo Hardwalled Aft Fan Spectra	23
5.2.2 22” ADP Fan Rig Hardwalled Spectra	23
5.3 Liner Design Points for the Aft Fan	24

5.4 Source Noise Modal Energy Assumptions	24
5.5 Optimum Liner Impedances for the Aft Fan	25
5.6 Design Methodologies for the Aft Duct	26
5.6.1 Optimize Lining Parameters to Match Admittance	26
5.6.2 Optimize PNLT Attenuations (both sides the same)	28
5.6.3 Optimize PNLT Attenuations (allow two sides to be different)	28
5.6.4 Calculate the Cross-Performance	28
5.7 Predicted Liner Attenuations for the AFT Fan	28
5.8 Conclusions	29
6.0 Evaluation of Broadband Liners for a Mid-Sized Twin Engine Airplane	31
6.1 Program Overview	31
6.1.1 Airplane/Engine Definition	31
6.1.1.1 Airplane Definition	31
6.1.1.2 Engine Definition	32
6.1.1.3 Nacelle Definition–Inlet	32
6.1.1.4 Nacelle Definition–Aft Duct	32
6.1.2 Target Spectra	32
6.1.2.1 Inlet Noise	32
6.1.2.2 AftFan Noise	33
6.1.3 Types of Nacelle Noise Suppression Technologies	33
6.1.4 Linings Evaluated in the Study	34
6.2 Inlet Trade Studies	34
6.2.1 Technologies Evaluated	35
6.2.2 Liner Depth Constraints	35
6.2.3 Source Assumptions	35
6.2.4 Optimum Liner Impedances	35
6.2.5 Evaluation Process	36
6.2.5.1 Optimize Lining Parameters to Match Admittance	36

6.2.5.2	Run Rdiff Code to Determine Lining Attenuations	36
6.2.5.3	Add Attenuations to Hardwall Data	37
6.2.5.4	Extrapolate Dats to FAR 36 Condition	37
6.2.6	Trade Study Results	37
6.2.6.1	Impedance Trade Study	37
6.2.6.2	Lining Area and Configuration Trade Study	39
6.2.7	Conclusions	40
6.3	Aft Duct Trade Studies	41
6.3.1	Technologies Evaluated	42
6.3.2	Liner Depth Constraints	43
6.3.3	Source Modal Energy Assumptions	43
6.3.4	Optimum Liner Impedances	43
6.3.5	Evaluation Process	44
6.3.5.1	Optimize Lining Parameters to Match Admittance	44
6.3.5.2	Optimize PNLT Attenuations Using the YMATCH starting points	45
6.3.5.3	Choose Best Lining Based on PNLT Attenuations	45
6.3.5.4	Calculate the Off-Design Perfomance	46
6.3.6	Trade Study Results	46
6.3.6.1	Approach Design Point Impedance Study	46
6.3.6.2	Cutback Design Point Impedance Study	46
6.3.6.3	Off-Design Point Study	47

6.3.7 Conclusions	47
7.0 References	49
Appendices	111
A1. “Theory And Design Of Helmholtz Resonators Constructed With Slot Perforates” Allen Hersh and Bruce Walker	
A2. “Theory And Design Of Helmholtz Resonators To Suppress Aircraft Engine Noise” Allen Hersh and Bruce Walker	
A3. “Theory And Design Of Helmholtz Resonators Constructed With Micro–Diameter Perforates” Allen Hersh, Joseph W. Celano and Bruce Walker	
A4. Impedance Models.	

List of Figures

Fig. No.	Fig. Title	Page
1.	Single Layer Acoustic Liners	50
2.	Double & Triple Layer Acoustic Liners	51
3.	Parallel Element Acoustic Liners	52
4.	Double Layer Parallel Element Acoustic Liner	53
5.	Typical Wide Chord Fan Spectrum Shape	54
6.	Fan Duct OAPWL Attenuations	55
7.	Inlet OAPWL Attenuations	56
8.	Inlet Impedance and Attenuation Spectra	57
9.	Fan Duct Impedance and Attenuation Spectra	58
10.	Schematic of NASA Langley Standard Grazing Flow Impedance Sample	59
11.	Passive Liner Test Designs	60
12.	Schematic Of Wichita Grazing Flow Impedance Measurement System	61
13.	Comparison Of NASA And Boeing Wichita Grazing Flow Resistance Test Data	62
14.	Comparison Of NASA And Boeing Wichita Grazing Flow Reactance Test Data	63
15.	Measured And Predicted Impedance Of The Double Layer Perforate Liner; $M=0.0, 0.33, \text{ and } 0.50$	64
16.	Measured And Predicted Impedances Compared To Target Impedance, $M=0.33$	65
17.	Measured vs. Predicted Surface Impedance – Fiberglass Bulk Absorber	66
18.	Measured Surface and Characteristic Impedance	67
19.	Measured vs. Predicted Characteristic Impedance	68
20.	Measured vs. Predicted Attenuation Constant	69
21.	Measured vs. Predicted Phase Speed Ratio	70
22.	Effect Of Orifice Number, Grazing Flow Speed and SPL on Resonator Tuned Resistance	71
23.	Effect Of Orifice Number and Grazing Flow Speed on Resonator Face–Sheet Mass Reactance: $SPL=135 \text{ dB}$	72
24.	Comparison Of Effect Of Grazing Flow AND SPL Changes On Acoustic Resistance Of Currently Used Perforates With Micro–Perforate	73
25.	Comparison Of Acoustic Mass Reactance For Currently Used Perforates With Micro–Perforate	74

26.	Adaptive Liner Test Designs	75
27.	Bias Flow Impedance Changes For Test Liner	76
28.	Comparison Of Predicted Impedance Spectra For The Bias Flow Test Liner With The Original and Updated Bias Flow Impedance Models.	77
29	High Temperature Liner Impedance and Attenuation	78
30	Cartoon of Lining Segments	79
31	Comparison of the Design ADP Hardwalled Data Predictions	80
32	Hardwall Target Spectra Based On ADP Demo Data	81
33	Comparison of Hardwalled 22” ADP Data	82
34	Hardwall Target Spectra Based On ADP Model Fan Data	83
35	Representation of the Fan Duct with the MELO Program	84
36	Optimum Lining Impedance for the ADP Fan Duct	85
37	Preliminary Ideal Impedance Calculations for the ADP Fan Duct	86
38	Ideal Impedance Calculations for the ADP Fan Duct	87
39	Comparison of Boundary Layer Effect on Optimum Impedances	88
40	Block Diagram of the Design Process	89
41	MELO Predicted Lining Attenuations vs the Optimum Attenuations	90
42	Predicted Lining Impedance vs the Optimum Impedance (1 layer)	91
43	Predicted Lining Impedance vs the Optimum Impedance (2 layer)	92
44	Conventional and Scarf Inlets	93
45.	MELO Representation of the Fan Duct Nacelle	94
46	Inlet Spectra for the Approach, Cutback and Sideline Conditions	95
47	Aft Duct Spectra for the Approach, Cutback and Sideline Conditions	96
48	Examples of Linings Considered in the Trade Study	97
49	Block Diagram of the Evaluation Process for the Inlet	98
50	Results of the Impedance Study for the Inlet Component	99
51	Impedance of the Inlet Liners (at the approach condition)	100
52	Ray Acoustic Argument for Low Inlet Attenuations	101
53	Impedance of the Inlet Liners (at the cutback condition)	102
54	Comparison of Lining Area Technologies	103
55	Conventional and Scarf Inlet Nacelles	104
56	Inlet Lining Area and Configuration Study	105
57	MELO Predicted Ideal Impedances	106
58	Block Diagram of the Evaluation Process for the Aft Duct	107

59	Comparison of Aftfan PNLT Attenuations at Approach	108
60	Comparison of Aftfan PNLT Attenuations at Cutback	109
61	Comparison of Aftfan PNLT Attenuations (summed approach and cutback condition)	110

List of Tables

Table No.	Table Title	Page
1.	Bulk Absorber Acoustic Materials Candidates Identified By Boeing Materials Technology	12
2.	Fluid Retention Properties Of Bulk Absorber Material Candidates	13
3.	Summary Of Micro-Diameter Resonator Geometry	16
4.	Preliminary 22" Fan Rig Lining Depth Constraints	20
5.	Definition of the ADP Demo Aft Liner	22
6.	Frequency Weightings Used for YMATCH by Band Number	26
7.	Single Layer/ Single Layer Final Designs	27
8.	Double Layer/ Double Layer Final Designs	27
9.	FAR 36 Operating Conditions for Trade Study Airplane	31
10.	YMATCH Frequency Weightings for the Inlet	35
11.	Results of the Impedance Study for the Inlet Component	36
12.	Results of the Lining Area and Configuration Study for the Inlet Component	39
13.	Frequency Weightings Used for the Narrow Chord Fan at Approach	43
14.	Frequency Weightings Used for the Narrow Chord Fan at Cutback	43
15.	Frequency Weightings Used for the Wide Chord Fan at Approach	43
16.	Frequency Weightings Used for the Wide Chord Fan at Cutback	44
17.	Results of the Impedance Study for the Aft Component at Approach	45
18.	Results of the Impedance Study for the Aft Component at Cutback	46

1. Summary

The Advanced Subsonic Technology (AST) Noise Reduction Program goal is to reduce aircraft noise by 10 EPNdB by the year 2000, relative to 1992 technology. Interim goals have been established which include a goal to validate concepts to improve nacelle duct treatment effectiveness by 25% relative to 1992 technology by the second quarter of fiscal year 1997. The Advanced Turbofan Duct Liner Concepts Task (Task 1 NAS-20090) work by Boeing was supporting this goal. The duration of this contract was February 1994 to September 1996.

The technical approach was to investigate methods for increasing the attenuation bandwidth of nacelle acoustic linings. The primary motivation for this approach is the character of the fan noise spectrum generated by modern wide chord fan engines. The wide chord fans have approximately 50% fewer blades and run at slightly reduced tip speeds compared to older narrow chord fans. As a result, the fan blade passing harmonic frequencies are significantly lower than for narrow chord fans. For example, blade passing frequency (BPF) at landing for the engines powering the Boeing 777 airplane is in the 630 to 800 Hz 1/3 octave band range. The broadband fan noise spectrum however is very similar for the narrow and wide chord fans with the peak Noy weighted levels in the 3 kHz to 4 kHz region. Therefore, for effective PNLT attenuation, approximately 3 octave bandwidth lining attenuation is required for wide chord fans in order to attenuate the peak NOY region of the spectrum and reduce the tone correction resulting from the BPF.

The basis for the technical approach was a Boeing study conducted in 1993-94 under NASA/FAA contract NAS1-19349, Task 6 investigating broadband acoustic liner concepts. As a result of this work, it was recommended that linear double layer, linear and perforate triple layer, parallel element, and bulk absorber liners be further investigated to improve nacelle attenuations. NASA Langley also suggested that "adaptive" liner concepts, which would allow "in-situ" acoustic impedance control, be considered. As a result, bias flow and high temperature liner concepts were added to the investigation. The following summarizes the specific studies conducted for Task1 NAS-20090:

1. **Passive Acoustic Liners.** This study investigated liner designs with increased degrees-of-freedom such as double layer, triple layer and parallel element liners; liners with linear resistance elements such as the currently used woven wire as well as new concepts such as slots and micro-perforates; and bulk absorber materials such as fiberglass, kevlar felts and ceramic foam. Subcontracts were given to Hersh Acoustical Engineering (HAE) to study the linear liner concepts of narrow slots and micro-perforates.

Analysis of the grazing flow impedance test data gathered to verify the impedance models used for the analytical study of the passive and adaptive liners was not complete at the time this contract concluded. However, passive liner concepts, which included triple layer and parallel element liners designed for fan duct application, were tested and preliminary data analysis was completed. This data indicated that the liners may be slightly better than predicted, but there was sufficient scatter in the data that its accuracy, particularly at grazing flow Mach numbers greater than 0.3, is questionable.

Boeing does not use woven wire resistance elements in the nacelles it

builds because of a number of concerns associated with manufacturing and in-service durability. However, the above studies showed important potential acoustic benefits from use of linear materials. The slot concept proposed by Hersh Acoustical Engineering showed good acoustic properties, but it was concluded that slots had strength and manufacturing efficiency difficulties which would result in very heavy liners. Therefore, their development was terminated in favor of micro-perforates. Initial acoustic testing with micro-perforates with hole sizes down to .004 in. laser drilled into .040 in. thick titanium plate showed acoustic characteristics very similar to currently used woven wire. As a result, further work with micro-perforate liners is planned for follow on work. Although a number of bulk absorber materials were found with good acoustic characteristics, none were considered usable in aircraft engines because fluid absorption testing showed a strong tendency to absorb hydrocarbons such as jet fuel and hydraulic fluid. Further bulk absorber investigations were therefore terminated.

2. **Adaptive Acoustic Liners.** Two concepts were chosen for investigation. The first was a bias flow concept which uses a steady bias flow (blowing or suction) through the liner to modify the acoustic properties of the liner. The second concept involved increasing the temperature of the liner to modify its acoustic properties. The design application investigated for bias flow was to design a non-linear liner for the high engine power condition (high local SPL) and use bias flow to maintain the desired acoustic resistance at low engine powers (low local SPL). Although grazing flow impedance tests were completed the data analysis has not been completed for the adaptive liner concepts.
3. **ADP Model Fan Acoustic Liner Design.** This was the first of two airplane nacelle design studies conducted. It was a joint study to design and build acoustic liners for testing on the NASA Lewis 22 inch Advanced Ducted Propeller (ADP) model scale fan. The airplane application was assumed to be a Boeing 747 derivative powered by ADP engines. The scale factor assumed was 5.91. Boeing had responsibility for design of the fan duct liners, PW had responsibility for designing the inlet liners, Rohr manufactured the liners and NASA Lewis performed the testing in their 9x15 acoustic wind tunnel. NASA Langley served as consultant and coordinator for the lining design work. There was a great deal of interaction among the participants during the design phase to insure that the best technology available was being applied. Preliminary analysis of the model scale ADP acoustic lining data indicates that the fan duct liners were behaving as predicted, but a detailed analysis with narrow band data is planned in the follow on work.
4. **Medium Sized Twin-Engine Airplane Liner Study.** The purpose of this design study was to apply the design concepts developed from the above work to engines representing 1992 technology powering a mid-sized, twin-engine, commercial airplane. The Boeing 767 airplane was used to represent this class of airplane. Both inlet and fan duct lining

studies were conducted. For the inlet, the effect of increasing the lining area by improvements in manufacturing and structural design, as well as increasing the inlet length, were examined in addition to lining acoustic impedance improvements. Also, the impact of a scarf inlet concept, which uses the inlet shape to direct noise upward above the airplane while reducing energy propagating to the ground, was examined.

The major conclusion from the above studies is that improvements in nacelle liner average impedance characteristics alone will not result in 25% increased nacelle noise attenuation improvements relative to 1992 technology. (The liner assumed for 1992 technology was a double layer, perforate liner using the Boeing buried septum technology.) Optimum uniform liners, i.e. imaginary liners with optimum impedance at each frequency, were predicted to result in improvements of approximately 10% for inlets and 15% for fan ducts at the airplane landing condition. Liners with increased degrees-of-freedom such as triple layer perforates were estimated to offer only 2% – 3% improvement for inlets and 6% – 10% improvement for fan ducts. Liners with linear resistance elements such as linear double and linear triple layer liners were estimated to offer 6% – 7% improvement for inlets and 7% – 10% for fan ducts.

The effects of varying liner impedance within the nacelle was not evaluated in detail in this study. A previous inlet study using an early version of the ray tracing code used here found only a small benefit for varying liner impedance in the inlet. For the fan duct, the duct wave propagation code used only applies to ducts with constant geometry, lining and flow conditions. An approximate calculation indicated that varying liner impedance axially in a constant geometry fan duct gives approximately the same attenuation bandwidth as calculated for the uniform impedance spectrum of parallel element liners.

One aspect of varying liner impedance which may be particularly beneficial for fan ducts is modal scattering. This could not be analytically evaluated with the code used in the present study however. For typical length fan ducts the duct propagation studies indicated that the attenuation was limited by the modest attenuation of low order modes. This suggests a concept where the initial fan duct lining is used to attenuate the higher order modes; which is then directly followed by a mode scattering device (such as an impedance discontinuity) used to scatter the energy in the remaining low order modes into high order modes that the following lining can more effectively attenuate. Inlet broadband noise is composed of a large number of cut-on modes, so scattering would not be expected to do anything more than re-mix the modal energy distribution.

The possibility of taking advantage of the 3-D geometry of fan ducts has also been suggested for improving fan duct attenuation. The rectangular/circular/annular duct code used for the present fan duct studies did not allow anything but idealized geometries. The fan duct scattering and 3D geometry concepts will be evaluated later with a new code being developed at Boeing under AST contract.

Additional nacelle advancements such as liner structural design improvements to allow reduction in panel area used for fasteners and strength reinforcement are presently being studied with internal funds at Boeing. Additionally, the effects of liners on the boundary layer in the inlet throat region are being studied which may allow lining forward of the throat. These nacelle design advancements are expected to add 20% to 40% more active acoustic lining area in current inlets which is predicted to result in a 40% – 80% attenuation improvement. Similar advancements are expected to allow 10% to 30% more acoustic lining in current fan ducts with 10% to 30% more attenuation expected. In addition, Boeing is currently developing a scarf inlet

concept which is expected to give an additional 40% to 80% attenuation improvement for an equivalent lining area.

2. Introduction

The Advanced Subsonic Technology Noise Reduction Program (AST) goal is to develop technology by the year 2000 to reduce aircraft noise by 10 EPNdB relative to 1992 technology. The technology development strategy is a coordinated effort among government, industry and academia addressing engine source understanding and reduction, nacelle aero-acoustics, engine/airframe integration and flight procedures. Interim goals have been established which includes a goal to validate concepts to improve nacelle duct treatment effectiveness by 25% relative to 1992 technology by the second quarter of fiscal year 1997 (FY '97).

The Advanced Turbofan Duct Liner Concepts Task (Task 1 NAS1-20090) reported here was assigned to pursue the above goals. The basis for the technical approach was a Boeing study conducted in 1993-94 under NASA/FAA contract NAS1-19349, Task 6 investigating broadband acoustic liner concepts. As a result of this work, it was recommended that linear double layer, linear and perforate triple layer, parallel element, and bulk absorber liners be further investigated to improve nacelle liners. NASA Langley also suggested that "adaptive" liner concepts which would allow "in-situ" acoustic impedance control also be considered. As a result, bias flow and heated core liner concepts were added to the investigation.

The purpose of this report is to communicate the work done under contract NAS1-20090, Task #1, "Advanced Turbofan Duct Liner Concepts." This report represents a fulfillment of deliverable items specified in the contract.

2.1 Technical Approach

Using Boeing design tools and experience with parallel element, double layer and triple layer liners, a complement of linings was designed for improved fan duct broadband attenuation. These design studies were guided by the results of a Boeing study conducted in 1993-94 under NASA/FAA contract NAS1-19349, Task 6 investigating broadband acoustic liner concepts. Panels using these designs were then manufactured for testing in Boeing's grazing flow impedance measurement facility. This facility propagates the fundamental mode over the acoustic liner with a flow Mach number up to $M=0.5$ and determines the effective liner impedance from the measurement of the complex acoustic pressure pattern over the length of the liner. The purpose of the testing was to verify the designed impedance spectrum of the liners with a grazing flow and a noise environment representative of an engine fan duct at typical landing and takeoff conditions.

The Boeing Materials Engineering group completed a survey of potential bulk absorber materials and together with Noise Engineering selected five materials for further investigation: Manville Fiberglass batting, Osaka Gas (ANA) Carbon fiber batting, Tex Tech Kevlar felt, Tex Tech Polyimide felt and Lockheed Ceramic fiber. Acoustic impedance testing, including measurement of the characteristic impedances and propagation constants, and fluid absorption tests were conducted on the five selected materials. While all five of the materials tested showed good acoustic characteristics, they all showed unacceptable hydrocarbon fluid wicking. As a result the bulk absorber investigation was essentially terminated. One supplier, Osaka Gas, said they would study ways to correct this problem on a very low priority level.

Under subcontract to Boeing, Hersh Acoustical Engineering (HAE), in conjunction with testing at NASA Langley, developed verification and modeling data demonstrating the nonlinearity and grazing flow independence of their slotted liner concept. However, Boeing structural design

personnel concluded that the concept posed serious structural and manufacturing difficulties for nacelle application. As a result, development of this concept did not continue beyond 1995. In 1996 HAE began an investigation of the impedance properties of micro-perforate sheets to develop acoustic data which could be used to evaluate their feasibility for linear liner systems. HAE developed both circular and slotted orifice semi-empirical acoustic impedance models using the data from these tasks as well as past HAE work.

Boeing participated with P&W, Rohr, NASA Langley and NASA Lewis to design acoustic liners for the 22 in. model scale ADP fan to be tested at NASA Lewis in 1996. Boeing had prime responsibility for the fan duct liner design and P&W had prime responsibility for the inlet and fan case liner designs. This division of responsibility was somewhat arbitrary. Initially it was envisioned that both Boeing and PW would be strongly involved in the design of all of the liners (even doing independent designs for the same part) but in the end there was only time for each company to review the others progress during the design period. The objective was to demonstrate advanced liner design and analysis concepts and show a 25% attenuation improvement relative to the baseline liner which was scaled from the Advanced Ducted Propeller (ADP) demonstrator engine test in 1992.

An analytical evaluation study was conducted applying the design concepts developed from the above work to engines representative of 1992 technology powering a medium twin commercial airplane. The objective of this study was to design liners which would be predicted to give at least 25% attenuation improvement relative to a 1992 technology engine nacelle. Both narrow chord and wide chord fan engine representations were evaluated. A major element of this study was to be the choice of mode energy distribution assumed for the tones. It was expected that the mode predictions and measurements made for the 22" ADP model would influence this choice. Unfortunately the modal data was not available in time to be used. Therefore, the standard Boeing assumption of nearly equal energy in each propagating mode was used. For the inlet, ray acoustics was used, which is equivalent to assuming a very large number of modes with equal energy. For the fan duct, a rectangular duct model was used with the mode energies being approximately equal except near cut-off where the assumed energies drop off significantly.

2.2 Report Organization

This report is organized in sections which describe the details of the work conducted for the above investigations. The report is a composite of mini-reports on all of the studies conducted over the term of the contract. The sections are somewhat chronological, but there is also a logical flow moving from investigation of lining design concepts to application of these concepts to a specific airplane noise reduction study. Section 3 describes the passive liner investigations including the grazing flow impedance tests, the bulk absorber materials investigations and the linear materials investigations. Reports from Hersh Acoustical Engineering on the slot liner development, the single orifice impedance modeling and the preliminary micro-perforate investigation are contained in Appendices 1, 2 and 3 respectively. A brief summary of the preliminary analytical passive liner studies conducted in 1993-94 under NASA/FAA contract is contained in this section for completeness since this work formed the basis for all of the follow on passive liner studies. Although the NASA/FAA contract studies were somewhat idealized in that specific airplane noise design and attenuation metrics were not used, we felt the results apply to the airplane design and the community noise evaluation metrics generally used (EPNdB).

Section 4 describes the adaptive liner work status at this point, but is not yet complete since the measured impedance data has not yet been analyzed.

Section 5 describes the details of the ADP fan duct liner and design process including the predicted attenuations for the ADP model scale fan test.

Finally, the analytical evaluation of the passive liners applied to the nacelles on a medium twin airplane powered by narrow chord and wide chord fan engines is contained in Section 6. This work used the design tools and experience developed from the above work and analytically evaluated the primary passive liner design concepts of single, double and triple layer perforate and linear liners considering the specific constraints, noise characteristics, aerodynamics and certification metrics of a medium sized, twin engine airplane. In addition, the acoustic benefits of new nacelle manufacturing concepts allowing more acoustic lining within the current nacelle envelope and a new inlet geometry (scarf inlet) were analytically evaluated for comparison.

Appendix 4 is a listing of the lumped element acoustic impedance models developed under this contract and coded into the Boeing impedance library. These models were used in the calculation of liner acoustic impedances.

3. Passive Acoustic Liners

3.1 Acoustic Liner Characteristics

The following discussion is intended to introduce the reader to the nomenclature of acoustic linings which is utilized in the later sections.

A typical single layer acoustic lining, shown in Figure 1, is composed of a face sheet and honeycomb core with an impervious backing sheet. Face sheets are usually composed of a perforated plate or woven wire/perforated plate sandwich. The honeycomb core is composed of cells which, when bonded to the face sheet, create cavities behind the face sheet. The attachment of an impervious backing sheet to the honeycomb core seals the honeycomb so that each cavity is isolated from its neighbors. This creates a single-layer resonator, whose impedance (Z) is characterized by a resistive (R) real part and reactive (X) imaginary part, $Z = R + i X$. The resistive impedance is only a function of the face sheet configuration. The reactive impedance is a function of the face sheet configuration and the cavity depth behind the face sheet. Characterizing the impedance in such a way as to isolate the effect of the cavity reactance, leads to

$$Z = Z_{face\ sheet} - i \cot(kd) . \quad (+ i\omega t \text{ convention})$$

The cavity reactance, $- i \cot(kd)$, strongly influences the frequency response characteristics of the liner. As frequencies increase above the first resonance ($X=0$, approximately where the attenuation is maximum), the reactance approaches positive infinity. At frequencies below the resonance frequency, the reactance approaches negative infinity. There are several methods to modify this behavior. One method is to create multiple layer liners as shown in Figure 2. Another method is to create a multi-segment parallel element liner, shown in Figure 3.

Figure 4 is a diagram of the two parallel element, double perforate layer liner to aid in understanding of the nomenclature.

3.2 Summary Of Preliminary NASA/FAA Contract Investigating Broadband Acoustic Liner Concepts

This section summarizes the results of a Boeing analytical study conducted in 1993–94 under NASA/FAA contract NAS1–19349, Task 6 investigating broadband acoustic liner concepts. The results of this work formed the basis for the passive liner work conducted under the present AST contract. The main objective of this study was to investigate acoustic linings which have increased bandwidth attenuation compared to conventional nacelle liners. Broad bandwidth liner attenuation was believed necessary for new turbofan engines which use wide chord fan blades. The number of fan blades for these engines is much fewer than in the past. These fans therefore generate much lower frequency blade passing tone noise (of the order of 800 Hertz at approach power). The broadband fan noise spectrum however, is very similar for the narrow and wide chord fans with the peak NOY weighted levels in the 3 kHz to 4 kHz region (see Figure 5). Therefore, for effective PNLT attenuation, approximately 3 octave bandwidth lining attenuation is required for wide chord fans in order to attenuate the peak NOY region of the spectrum and reduce the tone correction resulting from the BPF.

There are several techniques for achieving increased bandwidth attenuation with acoustic liners. This study concentrated on liners with distributions of parallel elements while examining other

designs for comparison. Although the impedance of the individual elements of the parallel element liner was allowed to vary, an effective uniform impedance was assumed to determine its effect on sound propagation. Therefore, all of the liner designs (except for the two segment series duct configuration) were studied as constant impedance liners.

Candidate lining concepts were evaluated using Boeing lining design optimization tools. Two different approaches were applied for the design and evaluation of the lining concepts. The first was a “plane wave” approach and the second a “mode” approach. Most of the attenuation trends concluded from the plane wave reflection design optimizations were also observed for the duct propagation design optimizations although not as strongly. The following are the primary conclusions for nacelle liner design for broadband attenuation from this study:

1. Maximum attenuation was attained with the triple layer and bulk absorber liners.
2. Triple layer liner attenuation was greater than double layer liner attenuation which was greater than single layer liner attenuation
3. The parallel element liners resulted in superior attenuation compared to the constant geometry liners.
4. The two segment series duct version of the parallel element double layer liner gave nearly identical attenuation as the parallel element liner for aft duct propagation.
5. Linear liner face sheets and septa did not show as large a benefit for the duct propagation analysis as seen for the plane wave analysis, but still generally resulted in attenuation improvements.

The above results are summarized in figures 6 and 7. Figure 6 is a plot of the estimated OAPWL attenuation of a given liner in an engine fan duct vs. the number of parameters which could be varied to optimize the liner design (DOF—degrees of freedom). For example a double layer perforate liner is shown to have 4 DOF since the face sheet and septum open areas and the top and lower depths were optimized. Figure 7 shows the same results for engine inlet liners. Impedance and attenuation spectra for perforate single, double and triple layer fan duct and inlet liners are shown in figures 8 and 9.

Comparison of the predicted maximum attenuation attainable from a uniform “ideal” liner impedance with the predicted attenuation of the current production perforate double layer liner concept indicates that the potential for improvement with uniform impedance is approximately 30% (overall power level (OAPWL) dB improvement) for the inlet and 60% for the fan duct. The best liner designs developed in the above study are predicted to attain approximately 25% improvement (both inlet and fan duct) relative to that attainable with the current perforate double layer liner concept, using the broadband OAPWL noise metric for comparison.

The bulk absorber liners are predicted to give the most attenuation of all of the liners studied followed closely by the triple layer liner. The application of bulk absorbers for turbofan engine nacelle application has not been pursued in the past because of structural and maintainability concerns. Several new bulk absorber materials have become available which were recommended for examination. These materials included polyimide foam, ceramic felt and metal matrix foam. It was recommended that the examination include acoustic characterization and consideration of the structural, weight and other mechanical issues associated with their use.

“Linear” acoustic materials clearly showed predicted acoustic advantages with the plane wave evaluation but the duct propagation analysis showed less and somewhat inconsistent benefits. At the design engine power condition a “linear” liner gives greater attenuation bandwidth compared to a perforate liner because of the lower mass reactance of the linear liner. Consideration of the acoustic performance of “linear” vs. perforate liners at higher engine power conditions (off design), where the liner is exposed to higher grazing flow Mach numbers and higher sound levels, showed higher OAPWL attenuation for the linear liner compared to the perforate liner, for both fan duct and inlet models. “Linear” materials such as woven wire over aluminum, woven wire over composite, laser drilled thermoplastic, laser drilled graphite epoxy composite and pre-preg polyimide were recommended for study. Again, consideration of the structural, weight and other mechanical issues associated with “linear” materials as well as the acoustic characteristics (impedance) was recommended.

The effects of varying liner impedance within the nacelle or varying nacelle geometry were not evaluated in detail in this study. However, an approximate calculation indicated that varying liner impedance in a constant geometry fan duct gives approximately the same attenuation bandwidth as calculated for the uniform impedance spectrum of parallel element liners. One aspect of varying liner impedance, which may be particularly beneficial for fan ducts, is modal scattering. Scattering could not be analytically evaluated with the code used in the present study however. For typical length fan ducts, the duct propagation studies indicated that the attenuation was limited by the modest attenuation of low order modes. A concept is therefore suggested whereby the initial fan duct lining is used to attenuate the higher order modes and is followed by a mode scattering device (such as an impedance discontinuity) to scatter the energy in the remaining low order modes into high order modes so that the following lining can more effectively attenuate the remaining noise.

The results from the study of the application of advanced liners to a medium twin airplane discussed in section 6 showed approximately 1/4 of the improvements relative to 1992 perforate double layer liner technology found in the FAA study. The primary reasons for this discrepancy are the differences in the source noise spectral characteristics assumed and the evaluation metric used. For the NASA/FAA study the assumed source spectrum was a 1/3 octave spectrum with constant SPL from 500 Hz to 4000 Hz. The evaluation metric was overall power level (OAPWL). For the medium twin study, the evaluation metric was fan component peak flyover PNLT, where the source spectrum had maximum NOY weighting in the frequency range of 2 to 5 kHz. The maximum attainable attenuation in this frequency range is significantly lower than in the lower frequencies because of the beaming effect of higher frequency modes. Also, attenuation bandwidth was not as important for the airplane study as it was for the 500 Hz to 4 kHz power level attenuation study. This was even the case for the wide chord fan which had a relatively low frequency BPF at approach (630 Hz band), with a resulting 2.2 dB tone correction. Attenuation of noise in the BPF frequency region in this case had only a small contribution to PNLT attenuation since the tone correction did not change very much. In reality the masking effect of other noise sources such as airframe noise would probably cause the tone correction to be reduced as the inlet radiated fan noise is reduced in the BPF region. This effect however was not accounted for in the airplane study.

3.3 Passive Liner Tests

The above analytical studies made use of Boeing semi-empirical models for predicting the acoustic impedance of the elements of a liner and a transmission line analogy analysis tool for

calculating the impedance of the arrangement of the elements to form a liner design. In order to verify the calculated impedances, measurements were made at the Boeing Wichita facility. The objectives of these measurements were:

1. Measure the “standard sample” from NASA Langley for comparison of measurement processes.
2. Measure no flow impedance (Z) in a normal incidence impedance tube.
3. Measure no flow and with flow Z in Wichita grazing flow Z duct for comparison to predictions and targets. (Grazing flow effects and parallel element assumption investigated).
4. Measure Hersh slot resistance elements sample in grazing flow to compare with data taken at NASA Langley and to expand Mach number range if possible.

The liners chosen for testing were (See Figure 11):

1. NASA Langley standard sample.
2. Perforate double layer (for reference –1992 technology).
3. 5 element parallel element linear double layer.
4. 2 element parallel element double / triple layer – perforate.
5. Triple layer– perforate.
6. Hersh slotted face sheet single layer liner.

Figure 10 is a schematic of the NASA Langley “standard sample.” This sample was borrowed from NASA to develop confidence in the accuracy of the Langley and Wichita grazing flow impedance measurement facilities. The Boeing liner designs tested are shown schematically in Figure 11. These designs were optimized for fan duct broadband acoustic attenuation application. However, the designs are thicker (3 in. to 4 in.) than those allowed in today's fan ducts. Even today's largest engines limit the fan duct liner thickness to approximately 2 in. Liner thickness is not as severely limited for the engine inlet application where 3 to 4 inch deep liners are feasible.

3.3.1 Grazing Flow Impedance Measurement Technique

The technique used at the Boeing Wichita facility to measure liner impedance in the presence of grazing flow is called the “waveguide” technique. The waveguide method involves measuring sound attenuation properties in an acoustically lined flow duct. One wall of the duct contains the acoustic liner being evaluated. A wall mounted traversing microphone on the opposite hard wall is used to measure the attenuation and phase variation down the duct. These data are used in conjunction with the convected wave equation for establishing the acoustic liner impedance. Figure 12 is a schematic of the measurement system. The test section used for the measurements had a 2 x 2 in. cross section and was 16 inches in length. The resulting frequency range for the system is 1000 to 6000 Hz and the Mach number range is up to $M=0.5$. Sound levels over the lining can be as high as 150 dB OASPL. Data analysis consists of using an optimization technique to find the liner impedance which will give the “best” match of the analytically calculated pressure and phase to the measured data. The analytical calculation allows for segmentation of the duct to account for reflection effects at impedance discontinuities and impedance variation with non-linear liners, but assumes plug flow.

3.3.2 Grazing Flow Impedance Measurements For Passive Element Liners

Boeing borrowed the NASA Langley “standard” grazing flow test sample and tested it in the Wichita facility. The NASA “standard” sample is a porous ceramic 3.25 in. thick. The pores are nearly cylindrical with a diameter of approximately .025 in. extending the entire thickness of the material. The surface open area is approximately 60%. NASA has shown that the standard liner impedance is linear and minimally affected by grazing flow. The liner is of such depth that the frequency range from 0.5 kHz to 3.0 kHz encompasses two resonance frequencies and one anti-resonance, so that the measurement procedure gets exercised across a significant range of resistance and reactance. Langley data are generally consistent for both downstream and upstream propagation except where an anti-resonance has a pronounced effect on the measurement uncertainty.

The Boeing measured resistances and reactances for the NASA Langley standard sample are compared with NASA data (Ref. 1) in Figures 13 and 14 respectfully. The agreement with the NASA data is reasonably good for $M=0.0$ and 0.3 , but the Boeing resistances for $M=0.5$ are lower than the Langley results. Even for $M=0.0$ and 0.3 , the Boeing data deviates significantly from the NASA data near 2 kHz. Given the expectation that the standard sample should show little grazing flow dependence, the Boeing data appears inconsistent at this frequency. NASA shows the largest deviation of their upstream vs. downstream propagation data near 2 kHz as well. In Ref.12 they describe a procedure for estimating measurement accuracy and find that near anti-resonance the measurement accuracy is poor for the wave guide impedance measurement procedure.

Figure 15 compares Boeing measured and predicted impedance results for the double layer liner shown in Figure 11, at grazing flow Mach numbers of 0, 0.33 and 0.50. While the agreement is fairly good at $M=0$, it is seen that it gets poorer as Mach number increases. Generally, it was found that the $M=0.5$ results seemed highly suspect. Note that the $M=0.5$ measured resistances are lower than those at $M=0.33$. The measured data also showed lower reactances than the predictions at $M=0.33$ and 0.5 . At the 5 kHz predicted anti-resonance, the measured data agrees poorly with the predictions. This even happens for the $M=0.0$ case. Figure 16 compares predicted and measured impedances with the design target impedance spectra at $M=0.33$ for all four liners tested (Figure 11). It is interesting to note that all of the liners showed measured impedances which better matched the target impedance spectra (fan duct propagation target) than was predicted for $500 \text{ Hz} \leq \text{frequency} \leq 3150 \text{ Hz}$. It was estimated that the measured impedance spectrum for the double layer liner would result in 2 – 5 dB better attenuation for the fan duct geometry assumed for Figure 6 than with the predicted impedance spectrum. Much of this benefit is probably due to the lower than predicted reactance in the 1–4 kHz region. Unfortunately, the measured resistance data at grazing flow Mach number of .5 is sufficiently suspect to cause one to question the validity of the $M=.3$ results as well. Therefore, the Boeing impedance models were not modified to reflect the reactance effect of grazing flow observed in this data. In addition this data was not available prior to beginning the mid-sized twin lining design study discussed in section 6. A new AST initiative, led by NASA Langley, is planned to define the lining impedance changes caused by grazing flow. Measurements will be made by NASA Langley, GE, Boeing and BF Goodrich (Rohr) with different perforate geometries, both in order to define the relative merits of the different measurement techniques, as well as to define the parametric dependencies.

The following conclusions were drawn from the grazing flow impedance test results:

1. Predicted and measured impedance agreed fairly well at zero grazing flow but agreement was poor with grazing flow.
2. The accuracy of the grazing flow impedance measurement needs to be quantified.
3. The triple layer and triple/double layer liners showed similar impedance characteristics.
4. The measured data showed better agreement with the target impedance spectrum than was predicted.

3.3.3 Bulk Absorber Materials Study

The following is the list of bulk absorber material candidates identified as having potential for nacelle application developed by Boeing noise and materials engineering personnel:

Table 1: Bulk Absorber Acoustic Material Candidates Identified by Boeing Material Technology

MATERIAL TYPE	SUPPLIER	COMMENTS
Carbon fiber batting	Osaka Gas (ANA Trading Corp.)	Very low density, 0.3 pcf. Osaka seems to understand the problem. Aggressive marketing from ANA.
Kevlar, Nomex Polyimide etc. (Needle felting)	Tex Tech Industries	Wide range of materials. Require water repellent. Suggested Zonyl
Ceramic batting	Carborundum Hi Temp Insulation Cotronics Corp. Zircor Products Orcon Corp.	Must have water repellent
Pyroloft AA—fiberglass batt Pyropel – polyimide felt	A.L. International L.P.	
Polyurethane foam	General Plastics	Requires sealing foam or hydrophobic coating
Polyimide foam	Imi-Tech	Requires sealing foam or hydrophobic coating
Ceramic tiles (aluminum oxide and silicon dioxide)	Lockheed	In development stage. Approx 4 pcf
Polyurethane and polyester foams	Illbruck	Requires sealing foam or hydrophobic coating
Copper and nickel foam metals	Hogen Industries	High cost
Aluminum and ceramic open cell foams	ERG, Inc. Astro Met, Inc	High cost (\$100 per cubic inch)
Silicon rubber based systems	CHR Div. of Furon Co.	Heavy
Fiberglass	Manville	Fluid absorption and sonic fatigue concerns

From this list the following materials were chosen for normal incidence impedance tube and fluid retention testing:

Manville Fiberglass batt, Osaka Gas (ANA) Carbon fiber batt, Tex Tech Kevlar felt, Tex Tech Polyimide felt and Lockheed Ceramic fiber.

The fluid retention testing consisted of “ground–air–ground” simulation of a complete mission including takeoff, cruise and landing as well as fluid wicking testing. The ground–air–ground simulation consisted of 100 simulated flight cycles of temperature, pressure and humidity. The fluid wicking testing measured the weight gain after samples of the material floated on the surface of water, jet fuel and hydraulic fluid for 24 hours. The results were as follows:

Table 2: Fluid Retention Properties of Bulk Absorber Material Candidates

MATERIAL	% WEIGHT GAIN			
	GROUND AIR GROUND	WICKING		
		WATER	JET FUEL	HY- DRAULIC FLUID
Fiberglass 1, .6 lb/ft ³	9.34	11	3620	7810
Fiberglass 2, .4 lb/ft ³	7.03	-2	4310	6460
Fiberglass 2, 1.5 lb/ft ³	2.49	4	3540	4870
ANA Carbon .44 lb/ft ³	1.09	2	6550	9290
ANA Carbon 1.33 lb/ft ³	1.13	82	3950	5430
Lockheed #13-031	0.27	1630	1020	1460
Lockheed #11-107	-0.15	1370	1050	1380
Kevlar Style 4681	0.99	1910	1180	2510
P84 Polyimide Style 4682	1.15	1760	9940	1580

Normal incidence impedance tube measurements before and after the ground–air ground cycling did not show any significant changes for any of the materials.

Normal incidence surface impedance and characteristic impedance measurements were made with a nominal material thickness of 3 in. for a frequency range of 200 to 6000 Hz. for the above materials. The characteristic impedance calculation followed the equations in Ref. 2 and Ref. 3 requiring measurements of surface impedance using two backing cavity depths. This is a new procedure at Boeing, but was easily implemented since our surface impedance measurement process automatically measures data either with zero depth backing cavity or 1/4 wavelength backing cavity depth (one tone frequency at a time).

The measured impedances were compared with the Delaney and Bazley (Ref.4) and the Voronina (Ref.5) impedance models. Figure 17 shows comparisons of the measured surface impedance with predictions using the above procedures for fiberglass with a nominal density of 0.44 lb/ft³. The Delaney and Bazley (D&B) prediction model requires input of bulk absorber resistivity and lining depth. For this prediction, the resistivity was calculated from an estimate of the fiber diameter and bulk density using the equation (Ref. 6):

$$R = (1.273 \cdot 10^{-3}) \rho^{1.53} / d_f^2 \quad (\text{cgs units})$$

(A nominal measured value of 18 cgs R/cm was also used for the D&B prediction of the 0.44 lb/ft³ material).

The Voronina (V) model requires input of material density, fiber diameter, fiber length and material thickness. Through experimentation it was found that the V model predictions were not very sensitive to the fiber length parameter, so a nominal value of 4 cm was used for all predictions. Both prediction procedures gave similar results for higher frequencies but the Voronina procedure appeared superior below 1000 Hz., particularly at higher densities.

The next set of figures compare measurements of characteristic impedance and propagation constant with predictions for the 0.44 lb/ft³ density fiberglass. Figure 18 shows measurements of both the surface impedance (8.5 cm thick material) and the characteristic impedance. The high frequency surface impedance data matches the characteristic impedance data as expected because of the large material thickness. Figure 19 shows measured and predicted characteristic impedance. Figure 20 shows the measured vs. predicted attenuation constant in dB/cm and Figure 21 shows the propagation speed to air propagation speed ratio vs. frequency. There were cases for which the agreement between the V model predicted trends and measurements were not as good as those shown in figures 18 – 21 and the reasons for these discrepancies have not been thoroughly pursued. The equation used to calculate the propagation constant from measured data is probably subject to large error when the characteristic impedance and measurement surface impedance are nearly equal. This suggests that thinner material samples may give better results for propagation constant at higher frequencies. Also, material fit within the impedance tube and methods for holding the material in place were found to be important elements in obtaining good data.

The above described acoustic and fluid retention testing led to the conclusion that all of the materials showed good acoustic attenuation properties for nacelle application, but the fluid absorption affinity is a major problem. The fiberglass and carbon fiber materials showed good results for water wicking and perhaps a fiber coating could be found to reduce hydrocarbon wicking. The manufacturer of the carbon fiber material, Osaka Gas, has been asked to investigate methods to reduce hydrocarbon wicking.

Osaka Gas has been responsive to helping develop nacelle application capability for their material to date. They recently experimented with methods for inserting the carbon fiber material into honeycomb core and returned samples to Boeing which are planned to be used for normal incidence impedance testing, with a full panel impedance meter now under development.

3.3.4 Linear Liners

Linear liners refer to liners with resistance elements whose resistance shows a small dependence on the SPL level of the sound incident on them. Fiber metal mesh and woven wire, usually overlaid on perforate plate for face sheets and without perforated plate for septa, are commonly used examples of linear materials. These materials usually have the additional properties of being insensitive to grazing flow variations and having mass reactances significantly lower than for perforates. The smaller mass reactance results in increased attenuation bandwidth. The

insensitivity to SPL and Mach number variations makes it possible to maintain liner impedance closer to desired values over the length of the liner while the sound levels are changing due to attenuation and the Mach numbers are changing due to duct cross sectional area changes. Also, increases in engine power setting result in SPL and Mach number increases. For the fan duct, uniform lining optimum impedances do not change with engine power setting, giving linear liners an advantage. For the inlet, the small increase in resistance which occurs with woven wire linear materials when SPL changes very nearly matches the increase in uniform lining optimum resistance as engine power is increased. While the woven wire and felted metal materials offer very good acoustic characteristics, problems with in-service maintainability has resulted in a strong resistance to their use. Non-Boeing manufactured nacelles and engine treatment sections have commonly utilized these materials in a single layer liner application but it is becoming increasingly common to see their use discontinued as repair becomes necessary. For these reasons, effort is being made to find alternative linear materials which can meet the multi-discipline requirements of noise, structures, maintenance, etc.

3.3.4.1 Slot Linear Liners

Under an AST subcontract to Boeing, Hersh Acoustical Engineering (HAE) developed an impedance data base for slotted perforates incorporating both normal incidence and grazing flow impedance data measured at NASA Langley. While there were some difficulties with the data, HAE concluded that the data was consistent with their in-house testing, showing good linearity and low sensitivity to grazing flow. Hersh also manufactured two test liners for grazing flow testing at the Boeing Wichita grazing flow test facility. Testing has been completed with the 0.002 in. width slot liner for the frequency range 1 to 6 kHz, SPL range of approximately 130 to 150 dB and grazing flow Mach number range of 0 to 0.50. Unfortunately there appears to be problems with the data. The 0.004 in. slot width liner was damaged in shipment and was not tested.

HAE consulted with Boeing nacelle structural design and manufacturing personnel with the objective of defining a method of manufacturing slotted perforates which meets nacelle structural and manufacturing requirements. HAE proposed a concept which, after preliminary study, was judged to only be suitable for non-load carrying designs and would be significantly heavier than current liners.

HAE has developed preliminary computer impedance models for both slotted and circular perforates under the AST contract. The circular perforate impedance models are for single orifices with thickness to hole diameter ratios of the order of 1. HAE reports on the orifice and slot impedance measurement and impedance modeling are contained as Appendices A1 and A2.

3.3.4.2 Micro-perforate Linear Liners

It is well known that as the airflow passages of the resistance element of the acoustic liner get smaller, the material gets more linear due to the increased importance of viscous losses compared to inertial losses. For this reason, it was decided to obtain data to quantify the relationship of small perforate geometry to acoustic impedance. Most of the data available was for perforates with hole diameters in the range of 0.050 in. whereas hole sizes of the order of .001 in. were believed to be necessary for linearity similar to woven wire materials. HAE therefore was given a subcontract to investigate the impedance properties of micro-perforate materials. The objectives of this work were:

1. Measure the acoustic impedance properties of micro-diameter perforates with and without grazing flow.
2. Develop a semi-empirical model for predicting the acoustic impedance of micro-diameter perforates.
3. Compare the acoustic properties of micro-diameter perforates with currently used perforates such as punched aluminum, woven wire and laser drilled thermoplastic.
4. Determine the advantages and disadvantages of using micro-diameter perforates for nacelle acoustic lining applications in place of current perforates.

HAE constructed resonators with face sheet orifice hole diameters ranging from .079 in. down to approximately .004 in. for acoustic impedance testing in the HAE wind tunnel. A brief description of the HAE Subsonic Wind Tunnel facility is contained in Appendix A2. Table 3 lists the geometry of the laser drilled micro-diameter resonators for which impedance data was measured by HAE. The schematic below defines the parameters listed in the table.

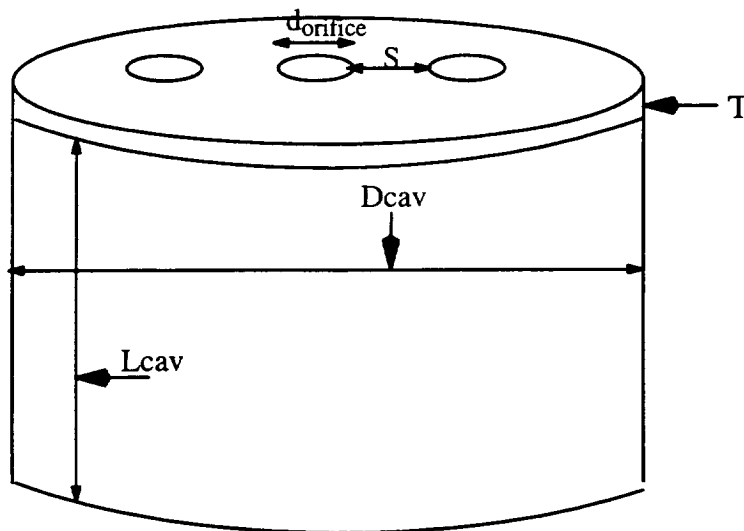


Table 3: Summary Of Micro-Diameter Resonator Geometry

N, # of holes	d_{orifice} (inches)	S (inches)	S/d_{orifice}	Open area ratio	D_{cav} (inches)	L_{cav} (inches)	T (inches)	T/d_{orifice}
1	0.079			0.0343	0.3906	4.0	0.040	0.506
4	0.0380	0.06	1.58	0.0379	0.3906	4.0	0.040	1.053
	0.0385	0.08	2.08	0.0389	0.3906	4.0	0.040	1.039
	0.0373	0.10	2.68	0.0364	0.3906	4.0	0.040	1.072

16	0.0210	0.03	1.43	0.0461	0.3906	4.0	0.040	1.905
	0.0213	0.04	1.88	0.0476	0.3906	4.0	0.040	1.878
	0.0213	0.05	2.34	0.0478	0.3906	4.0	0.040	1.878
100	0.0063	0.012	1.91	0.0258	0.3906	4.0	0.040	6.349
	0.0061	0.013	2.64	0.0240	0.3906	4.0	0.040	6.557
	0.0063	0.020	3.18	0.0259	0.3906	4.0	0.040	6.349
400	0.0035	0.008	2.32	0.0314	0.3906	4.0	0.040	11.429
	0.0031	0.010	3.21	0.0255	0.3906	4.0	0.040	12.903

Normalized acoustic resistance data for the resonators is shown in Figure 22 showing the dependence on sound pressure and grazing flow velocity. It is clearly seen that, as the orifice diameter decreases, the resonators become less sensitive to both of these parameters. Figure 23 shows the effect of grazing flow on the normalized acoustic mass reactance of the orifice system. At a grazing flow velocity of 77 m/s ($M=0.23$), the smallest orifice tested (approx. 0.004 in.) only reduces the mass reactance by a small amount. Unfortunately, the frequency limit of the HAE facility does not permit data to be taken above 1 kHz where the mass reactance for perforates can get very large. Reactance data is only shown for one SPL level since reactance did not vary strongly with SPL.

HAE has constructed a preliminary, semi-empirical impedance model for large T/d_{orifice} perforates based on the data collected in this effort. This work is contained in Appendix A3. Close examination of the tested orifice shapes under a microscope revealed that the hole shapes were somewhat irregular. HAE is therefore planning to make new samples using machine drilled perforates in thick face-sheets to provide the same range of T/d_{orifice} tested above. A data base will be generated including the effects of T/d_{orifice} , S/d_{orifice} , SPL, frequency, grazing flow velocity and boundary layer thickness.

Figure 24 compares the above measured resistance data from the $d_{\text{orifice}}=.0035$ in. sample with estimates of the resistance properties of currently used liner resistance materials. These include punched perforates with d_{orifice} and T approximately equal to .040 in., Boeing laser drilled septum material and woven wire overlaid over perforate plate. These materials were all chosen so as to have a normalized resistance of approximately $2\rho c$ at SPL=135dB and grazing flow velocity of 70 m/s (the grazing flow velocity is 0 for the laser drilled septum). It is seen that the micro-diameter material behaved very similarly to the woven wire material showing much smaller dependence on SPL and grazing flow compared to the laser drilled septum and punched perforate used by Boeing today. A similar comparison is shown in Figure 25 for the mass reactance. Although data was measured for only a very limited frequency range, it appears that the micro-diameter material has less mass reactance than the punched perforate, but it is not as good as the woven wire material. The attenuation consequence of this will require higher frequency data but it probably would result in a lower attenuation bandwidth than that possible with the woven wire material.

4. Adaptive Acoustic Liners

4.1 Introduction

Two “adaptive” acoustic liner concepts were chosen for investigation. The first is a concept, discussed by P. Dean in 1976 (Ref. 7), uses a steady bias flow through the liner resistive elements to control the acoustic resistance. The second concept uses heating to increase the liner temperature which reduces the acoustic resistance by changing the local density. Both concepts are expected to change the acoustic reactance of the liners as well. The approach used to study the application of these concepts for nacelle acoustic liners was to study their effect on acoustic impedance with the Boeing lumped element liner impedance computer program (YMOD). This program uses a transmission line electrical analogy with lumped elements representing the elements of an acoustic liner. Existing semi-empirical models for perforated sheet and cavities with temperature dependence were used for the temperature variation calculations. The bias flow calculations were done using the Hersh orifice impedance model in Ref. 8 and Ref. 9 with the modifications suggested by Dean in Ref. 7. Using these element impedance models, liner impedance studies were conducted to define liners to be tested in the Boeing grazing flow impedance testing facility.

4.2 Bias Flow Adaptive Liner Design

Figure 26 shows the designs of the two adaptive liners manufactured for grazing flow impedance testing. The design objective for the bias flow liner was to have a double layer lining with a nonlinear perforate face sheet and septum which would have good impedance properties for a fan duct application when the local sound levels are high (as for takeoff), and use bias flow to maintain good fan duct impedance properties when the local sound levels are low (as for landing). Figure 27 shows the predicted behavior of the grazing flow test bias flow liner design as bias flow is increased at the landing condition local sound level condition (OASPL at lining approximately 130 dB, grazing flow $M=0.3$). At the time of this writing the test liner has been fabricated and tested in the Wichita grazing flow impedance measurement facility but the data has not been analyzed. The maximum mean Mach number attainable for this test data was 0.004.

Two significant effects of a bias flow mean Mach number of 0.002 are predicted for the test liner as shown in Figure 28. They are the removal of the strong anti-resonance around 2 kHz. and the increased resistance in the higher frequencies. Unfortunately, an error has been recently found in the perforate impedance model constructed from the above Refs. 8 and 9. The error involved using the bias flow velocity to modify the orifice unsteady velocity as well as including an additive resistance term proportional to the bias flow Mach number as recommended by Dean. When this error was corrected the anti-resonance at 2 kHz. does not disappear with bias flow. This prediction implies that the bias flow liner design chosen for testing will not fulfill the design objective.

Ingard and Ising (Ref. 10) recommend a resistance bias flow Mach number dependence similar to Dean for low SPLs but appear to conclude that bias flow will not strongly affect orifice resistance at high SPL. If this is the case the concept may not be applicable to aero-engine nacelles since the SPL's even at landing within the nacelle are of the order of 140 dB. It is hoped that the test data will give some insight into the SPL dependence.

4.3 High Temperature Adaptive Liner Design

The high temperature liner design objective was to design a double layer lining with nonlinear perforate face sheet and septum which would have good fan duct impedance properties when the local sound levels were low and use heating to maintain good fan duct impedance properties when the local sound levels are high. Figure 29 shows the predicted behavior of the high temperature liner at takeoff for an assumed fan duct lining application. Note that this liner design is the same as the double layer liner tested in the passive liner program described above (Figure 11).

This liner was designed for a fan duct application at the airplane landing condition. At takeoff engine power, the liner is predicted to have a relatively high resistance due to a combination of the high grazing flow speed and duct OASPL. The strongest predicted effect of increased temperature within the lining appears to be a decreased resistance. In the non-linear region Ingard (Ref. 10) shows that the resistance of an orifice goes as Qv_{orifice} . Therefore, the reduction in density associated with an increased temperature should reduce the resistance. This analysis assumes that the liner temperature jumps discontinuously from the duct temperature. In reality this is not the case. In fact the grazing flow will act to cool the liner face sheet relative to the internal elements resulting in a relatively strong temperature gradient. Test data was measured in the Boeing Wichita grazing flow impedance with lining core temperatures to approximately 250 °F. This data has not yet been fully analyzed yet.

5. ADP Model Fan Acoustic Liner Design

In 1994 Boeing had recently completed a trade study ascertaining the value of advanced lining concepts for a broad-band spectra under a NASA/FAA contract. At this time PW and NASA decided to design, build, and test linings for the 22" Advanced Ducted Propulsor (ADP) fan rig to be tested at NASA LeRC. It was decided to have Boeing join the lining design/build team to offer expertise in the development of advanced lining concepts drawing on the earlier NASA/FAA study. Also, Boeing was asked to help determine the suitability of the ADP for a product including defining thrust and airplane performance for noise evaluation.

It was thought that the ADP engine would benefit from advanced (broadband) linings because it is a wide-chord fan engine with reduced tip speeds. This moves the BPF and harmonics down in frequency while the higher rotor/stator spacing and higher stator to rotor numbers help reduce the tone levels. The broadband noise still persists at higher frequencies and creates a situation where a broadband lining is required to attenuate both the tones and the higher frequency broadband noise.

The 22" ADP fan rig aft fan lining design was a joint effort with Boeing, Pratt and Whitney (P&W), Rohr, NASA LeRC, and NASA LaRC participating. Boeing had primary responsibility for the aft fan lining design with P&W providing consultation, Rohr had manufacturing responsibility, NASA LeRC provided the induct and far-field acoustic data for the design, and NASA LaRC provided overall program guidance and scheduling. The objective of the design was to demonstrate at least a 25% lining attenuations improvement relative to the previously tested "baseline" single layer linear design built by DEI and tested in 1995.

This report covers the design of the aft duct (fan-duct) liner for the 22" ADP fan rig. Each step of the process that was used to develop the final designs is described.

5.1 Aft Liner Depth Constraints

Initial depth constraints were defined by Pratt and Whitney and are shown in Table 4. Figure 30 shows the location of each liner segment. The lining segments C–H are in the aft duct.

Table 4: Preliminary 22" Fan Rig Lining Depth Constraints

Liner Segment		Max. Depth (in)	
Tag	Name	Model	Full Scale
A	Inlet	0.70	4.14
B	Aft OD Fan Case	0.60	3.55
C	Aft OD Aft Nacelle	0.60	3.55
D	Aft OD Forward Nozzle	0.50	2.95
E	Aft OD Aft Nozzle	0.38(0.20)	2.26(1.18)
F	Aft ID Aft Cowl	0.38	2.26
G	Aft ID Mid Cowl	0.75	4.43
H	Aft ID Aft Cowl	0.38(0.20)	2.26(1.18)
(x.xx) depth at minimum point – liner requires taper			

The depth constraints for the aft duct basically fall into two categories: relatively thick constraints like Segments C, D, and G and thin constraints like Segments E, F, and H. Also, the thick lining depth constraints are generally opposite a thin lining depth constraint. This is important because it suggested the simplifying assumption of using lining with one depth on one side and another lining with a different depth on the other side of a rectangular duct model when using the Boeing rectangular duct propagation computer code for designing the model ADP fan duct linings.

After Rohr published the preliminary assembly drawings in early November 1996, it was noticed that the thin double layer liner design was too thick to fit into Sections E, F, and H at all places. In these sections the drawings showed the linings tapered in places by reducing the honeycomb core depth under the septum so that the lining would fit into the cavity.

Boeing decided to re-optimize the double layer lining design with a more severe lining depth constraint. This was done because we ultimately wanted to compare our predictions, based on the design impedance, to the measured data. The preliminary designs required enough liner area to be tapered that a significant proportion of the lining area would have a different impedance affected by the depth constraint and the the predictions would not be valid. Discussions between Rohr and Boeing led to an updated maximum lining depth constraint of 0.285 inches compared to the 0.380 inches used initially. This minimized the lining area that was tapered to approximately 10% and only affected the double layer lining design. The single layer optimum designs could fit within the reduced depth constraint. The new, thinner lining constraint lowered the double layer sum PNLT attenuation (defined in section 5.4) by 0.6 dB from the value we had calculated with the older constraint.

5.2 Target ADP 22" Fan Rig Hardwall Fan Aft Fan Noise Spectra

A liner design is dependent on duct and lining geometry, modal assumptions, and far-field hardwalled spectra. In the 22" Fan Rig aft liner design, two different sets of far-field hardwalled spectra were used. The first set of spectra used were generated from the full-scale ADP Demo Engine data and were used to generate a preliminary liner design. Meanwhile, some preliminary hardwalled spectral data was taken with the 22" ADP Fan Rig with the composite blades. This data set was used to generate new target hardwall spectra which were used later in the program to refine the liner designs.

The metric used in certifying airplanes to the FAR 36 flight conditions is Effective Perceived Noise Level (EPNL), which is a time weighted sum of the tone corrected Perceived Noise Level (PNLT) calculated at 0.5 sec intervals as the airplane flies by the measurement point. Aft fan noise levels are important for all three of the FAR 36 flight conditions of approach, cutback, and sideline. Therefore, it was decided to evaluate a given lining design at all three conditions.

Since the EPNL metric is essentially the integration of the PNLT metric over time, we decided to choose hardwall design spectra representative of the peak PNLT levels. Examination of the PNLT versus emission angle showed that the peak PNLT for aft fan noise occurs near a 120 degree emission angle for all three FAR conditions; however, the tones in these spectra changed dramatically from angle to angle. It was decided to average two angles near 120 degrees to average out the tone level changes. A description of how each of the two sets of hardwalled design spectra were obtained follow in the next two sections.

5.2.1 ADP Demo Hardwalled Aft Fan Spectra

The first set of hardwall design spectra were generated from full scale ADP Demo data measured in 1992. This data set was for different geometry and Mach number than the FAR 36 operating conditions defined for the chosen design airplane which was a Boeing stretch 747. The ADP Demo Engine had a 110" fan which was different than the 130" fan required for a stretch Boeing 747. Also, operating conditions (Mach similitude) did not directly correspond to the conditions needed for the stretch 747 engine, particularly for the approach condition. Pratt and Whitney corrected the data to proper operating conditions before sending it to Boeing.

The ADP Demo Engine was not tested in a "hardwalled" configuration. Boeing therefore predicted the fan duct liner attenuation for the ADP Demo Engine and added it back to the scaled and extrapolated noise levels. This process, although crude, produced the best data set available at the time.

The ADP Demo Engine's aft lining definition used for the attenuation predictions is given in Table 5.

Table 5: Definition of the ADP Demo Aft Liner

Resistance at V=105 cm/s, R105	60 cgs Rayls
Non-Linearity Factor, NLF	1.60
Lining Depth, D	5.08 cm or 2 in.
Length to Height, L/H (includes aft fan case lining)	2.3
Crossover Frequency, f_c	30,000 Hz.
BL Momentum Thickness, Θ	0.3 cm.

The L/H used for the fan duct included the lining in the interstage area. The attenuations added back to the treated spectra included the effect of the interstage lining. Later in the program, it was decided that the interstage would be handled separately from the aft fan lining. Therefore, the levels used to define the hardwall spectra for the ADP were slightly too high in that they added the attenuations in the interstage area. This difference, although small, was not accounted for.

Figure 31 shows that the far-field, Noy weighted SPLs vary from angle to angle; this is especially true of tones. It was therefore decided to average the 110 and 120 degree spectra to generate a lining design target hardwall spectrum that would not over or under emphasize tones. Figure 32 shows the hardwall design spectrum shapes obtained from the ADP Demo Engine data in this manner.

5.2.2 22" ADP Fan Rig Hardwalled Spectra

There was concern about the validity of the ADP Demo Engine data to predict the 22" ADP Fan Rig hardwall spectra. During a 1995 workshop held at NASA Langley, some preliminary 22" ADP Fan Rig hardwalled data was shown. It was decided during this workshop that the preliminary hardwall data from the 22" ADP Fan Rig would be used to redefine the design hardwalled spectra. Clearly a better definition of the hardwalled design spectra should improve the liner design.

Pratt and Whitney, working with NASA Lewis, produced the hardwall data at the FAR 36 flight conditions. Some interpolation was necessary to produce these data.

Figure 33 shows the approach, cutback, and sideline conditions, respectively, at the 110, 120, and 130 degree angles. Note that there are some large variations between the spectra particularly at BPF harmonics. Again the process of averaging the 110 and 120 degree angles was used to minimize these fluctuations to produce the hardwall design spectra shown in Figure 34.

5.3 Liner Design Points for the Aft Fan

The aft liner design points were chosen by considering the contribution of the aft fan noise component at each of the FAR 36 conditions (approach, cutback, and sideline). It is known that the cutback condition is aft fan noise dominated. Typically, aft duct liners are designed for cutback condition at Boeing.

The sideline condition, typically dominated by jet noise for lower BPR engines, is dominated by aft fan noise for the ADP because the jet noise levels are very low due to the low jet velocities associated with the ADP engine configuration. Therefore, a lining design for an ADP engine should address the sideline condition.

The approach condition was more of a surprise. Upon examination of the approach condition for the ADP engine one notes that the contribution of aft radiated fan noise is nearly as significant as the inlet radiated fan noise. For these reasons, we chose a combination of the attenuations at the approach, cutback, and the sideline conditions for the design metric. More specifically, we chose:

$$J = \sum_i^{ap,cb,sl} PNLT \text{ Attenuation}_i$$

where J is the cost function which we want to maximize for the best design and is defined as the sum of the PNLT attenuations of the target spectra at the approach, cutback, and sideline conditions.

A better cost function could be developed that considered the masking of aft fan noise by other components, but was not used here. A good definition of the other full-scale engine components was not available for this design.

Typically in-duct SPLs need to be considered during a liner design for each operating condition. In-duct SPLs affect liner impedances by changing the particle velocity through the resistive layers. In this application, however, the impedance of the resistive layers used was only slightly sensitive to SPL. This is best shown by pointing out that the non-linearity factors (NLF) for the materials considered were between 1.2 and 1.4. The non-linearity factor is defined as the ratio of the resistance at 200 cm/s divided by the resistance at 20 cm/s. Values below 1.4 show the material to basically be linear. Perforate liners, on the other hand, have effective NLFs of 10-15.

5.4 Source Noise Modal Energy Assumptions

The modal energy assumption affects both the optimum lining design impedance and the maximum lining attenuation. For this lining design, a modal energy distribution believed to be appropriate for random broad-band noise was used. This assumption is nearly an equal energy modal assumption where the propagating energy of each cut-on mode is identical. The Boeing assumption and an equal energy assumption are the same except near cutoff. The Boeing assumption forces lower energies near cutoff whereas the equal energy assumption would force

extremely high SPLs for modes near cut-off because the energy transport rate down the duct is very small for modes near cut-off. The difference between the Boeing assumption and the equal energy assumption probably does not have a significant effect on the resulting lining design since the modes near cut-off attenuate rapidly down the duct even if the lining design is not optimum for these modes. The energy assumption used by Boeing is:

$$\int_S p^2 dS = \text{constant for each mode}$$

or the integral of the pressure squared over the cross sectional area is constant for each mode.

At the beginning of this program it was anticipated that measurements of the modal energy distributions for the model ADP aft fan noise would be available for use for the lining design. Unfortunately NASA Lewis had problems with the fan duct modal measurement process and were not able to develop this information. As a result, there is no experimental verification of the Boeing modal distribution assumption.

It is believed that the use of a broad-band energy assumption should work well for the ADP. The larger diameter and reduced tip speeds create a situation where the rotor stator interaction generated BPF is always cutoff and at a lower frequency than conventional engines. The rotor stator interaction will cut-on the 2 BPF; however, the 2 BPF still does not dominate the far-field spectrum as can be seen by the Noy weighted design spectra in Figure 34.

The Boeing lining design and attenuation prediction processes used in this exercise use an empirical procedure to radiate noise to the far-field. Although some work was done to create a process to radiate energy based on the work of Rice (Ref. 12), time constraints forced us to use the older, established radiation process. This lining design maximized the PNLT attenuation of the input spectra using the power attenuations at each frequency within an infinite duct. A process that radiates each mode to the far-field and evaluates the attenuation at each angle should perform better and allow the use of hardwalled data at each angle.

5.5 Optimum Liner Impedance for the Aft Fan

The optimum liner impedances were determined using Boeing's Multi-Element Lining Optimization (MELO) program. The MELO program is an infinite duct, modal attenuation code. Given a rectangular, circular, or an annular duct geometry, the program calculates the duct eigenvalues which are directly related to the attenuation per unit duct length of a given mode. Multiplication by the lining length and summing over all the cut-on modes results in the attenuation for a given frequency.

As an infinite duct program, MELO does not consider changes in impedance down the duct. MELO does have the ability to handle a mean flow velocity in the duct with a boundary layer profile. Built around the modal attenuation prediction capability is an optimizer capable of changing the lining impedance to maximize the resulting attenuation. In this manner, an optimum, axially uniform impedance versus frequency can be determined.

The representation of the ADP fan duct lining with MELO is shown in Figure 35. A two dimensional, rectangular duct is assumed with the height of the duct chosen as the average height of the fan duct in the lined region. The lining length input into the MELO program was obtained by measuring the total duct lining length. No credit was taken for lining outside the nozzle exit plane. Different linings were allowed on the two sides of the duct to model the two lining depth constraints for this design. From Figure 30 we see that for the most part a thick

lining depth constraint is across from a thin lining depth constraint. Although the depth constraints swap going down the duct (the thick and thin constraints switch sides) we modelled the geometry by leaving the geometry on each side the same down the duct. This may be a conservative assumption because no credit is taken for modal scattering at the impedance discontinuities.

The optimum uniform impedance versus frequency plot produced with MELO is shown in Figure 36. Only one curve is shown representing the approach, cutback, and sideline conditions. Unlike the shorter inlet, the optimum impedance of the fan duct changes very little with operating condition. Figure 37 shows the predicted optimum impedance at several fan speeds (duct Mach numbers) initially predicted in the program.

In determining the optimum, axially uniform impedance for this ADP lining design, the following assumptions were made:

1. Assumed a two dimensional rectangular duct with different linings on each side
2. Assumed a linear boundary layer profile with momentum thickness of 0.3 cm.
3. Assumed all possible cut-on modes with a modal energies as discussed in Section 3.5.2

The two dimensional rectangular duct was chosen instead of the annular duct because the eigenvalues could be calculated much faster and without having eigenvalue failures. The optimum impedance did not change appreciable by using a rectangular instead of an annular representation of the fan duct as can be seen in Figure 38. Notice that the rectangular and annular duct solutions for optimum impedance are almost identical. This probably because the optimum impedance is controlled mainly by the lowest order modes. Note that for frequencies greater than 3150 Hz that there are no solutions shown for the annular duct. This is due to eigenvalue failures of the MELO program.

The MELO program allows a boundary layer profile to be specified. The effect of the boundary layer on optimum impedance is primarily at the higher frequencies where it increases the reactance and resistance. Figure 39 shows a comparison of the predicted optimum impedance with and without a 0.3 cm thick boundary layer momentum thickness. The boundary layer velocity gradient will tend to bend waves toward the lining for wave propagation in the same direction as the flow, increasing the incidence angle. It is expected that this would increase the optimum reactance (toward zero) but decrease the optimum resistance. The reasons why the boundary layer drove the optimum resistance higher and the optimum reactance to positive values at high frequencies were not investigated.

5.6 Design Methodologies for the Aft Duct

The process used to determine the aft fan duct liner is graphically shown in Figure 40. A description of each block follows.

5.6.1 Optimize Lining Parameters to Match Admittance

The lining's admittance (1/impedance) is matched to ideal admittance calculated with MELO (see Section 5.6) using Boeing's YMATCH program. The YMATCH program uses the lining parameters and constraints, target admittance, and frequency weightings to solve a least squares optimization problem resulting in a lining which minimizes

$$\Sigma[\text{Weight}(f) (Y(f)_{\text{Target}} - Y(f)_{\text{Trial}})^2]$$

The lining parameters define the independent and dependent variables in the optimization problem. For the ADP lining study these variables were the depth of the cavities and the resistances of the resistive layers. Additionally, constraints can be set on the problem. One example of a constraint would be a maximum depth constraint so the output liner could fit in the cavity. The target admittance/impedance spectra used for this design was the optimum impedance defined by MELO .

The frequency weightings are multiplied by the square differences between the target admittance and the calculated admittance. In this way, one can highlight important frequency regions where the liner and target admittances should be close. The six sets of frequency weightings used in the 22” ADP fan rig lining design optimization are shown in Table 6.

Table 6: Frequency Weightings Used for YMATCH by Band Number

#	B27	B28	B29	B30	B31	B32	B33	B34	B35	B36	B37	B38
1	1	1	3	3	3	3	3	3	3	3	1	1
2	0	1	1	1	1	1	1	0	0	0	0	0
3	0	1	2	1	1	1	1	0	0	0	0	0
4	0	0	0	0	1	1	1	1	1	1	0	0
5	0	1	2	1	0	0	0	0	0	0	0	0
6	0	0	0	0	1	1	1	0	0	0	0	0

The weightings are shown as a function of one-third octave band number. Band 27 would represent a 500 Hz center frequency and Band 38 represents a 6300 Hz center frequency. Note Weighting #1 has coefficients over 12 one-third octave bands or 4 octaves. Resulting YMATCH designs with this weighting set produced liners with impedance spectra that matched the optimum impedance at bands B30 to B35, but could not match the target outside these frequencies. Examination of the outputs from YMATCH show that single layer linings can match the target impedance over one octave and double layer linings can match a target impedance over two octaves.

YMATCH exhibits some starting point dependence for the output lining. To assure the “best” solution is found, multiple starting points are used and the lining is chosen that “best” matches the admittance target. This is accomplished by a global option that exists within the YMATCH program.

The liners that are output from the YMATCH optimization are next evaluated using a noise metric. Specifically, the lining definitions and hardwall spectra are input into MELO. MELO then calculates the predicted PNLT attenuations that each lining would produce assuming that the lining is on each side of the duct using geometry of Figure 35. These data were used to evaluate which uniform linings perform best.

It should be mentioned that there is a “factor” applied to the calculated attenuations within MELO. This “factor” is an empirical correction of the MELO predicted attenuations to match full-scale measured lining attenuation data. The accepted “factors” used at Boeing are 1.0, 0.8, 0.6 for the approach, cutback, and sideline conditions respectfully. The factors were applied to all the MELO duct attenuation predictions made in this design study.

5.6.2 Optimize PNLT Attenuations (both sides the same)

The next step in the lining design process (the second bubble in Figure 40) was to use MELO to optimize the lining using PNLT attenuation as the cost function. The reason that the YMATCH process was done first is it provided a good starting point for this optimization problem.

Like the YMATCH process, sometimes local maxima instead of global maxima are found in the MELO optimization. Using YMATCH helped minimize, but not completely eliminate, this problem. A global optimization using many starting points was not done in MELO because it would take much too long. Just one optimization takes about 30 minutes. If we used 50 different starting points to make sure we obtained a global optimum, it would take 25 hours.

This process was run with both double and single layer linings, two lining depth constraints, three far-field hardwalled spectra, and three in-duct spectra. Twelve different optimum linings were defined in this process (two lining types times two depth constraints times the three operating conditions and their associated spectra).

5.6.3 Optimize PNLT Attenuations (allow two sides to be different)

In this part of the lining design process the lining was allowed to be different on each side. One side was given a thick total lining depth constraint and the other a thin depth constraint. The lining starting points were the best linings as determined the last step in the process (Optimize PNLT attenuations – both sides the same).

The output from this process was a lining definition for each of the FAR 36 flight conditions (approach, cutback, and sideline) for both single and double layer linings.

5.6.4 Calculate the Cross-Performance

The final step in determining the best lining was to determine the cross-performance. For each of the linings generated from the last step, the attenuations at the other two operating conditions was determined. Then the PNLT attenuations were summed for each lining over the three operating conditions. The best single and double layer linings were chosen as the linings that gave the highest sum PNLT attenuations.

5.7 Predicted Liner Attenuations for the Aft Fan

The final linings and sum PNLT attenuations at approach, cutback, and sideline are shown in Tables 7 and 8.

Table 7: Single Layer/ Single Layer Final Designs

Side	Rfs (cgs Rayls)	Dfs (full scale) (cm)	Σ Atten (PNLT)
1	70.6	2.11	13.5
2	68.0	4.64	

Table 8: Double Layer/ Double Layer Final Designs

Side	Rfs (cgs Rayls)	Dfs (full scale) (cm)	R sep (cgs Rayls)	Dsep (full scale) (cm)	Σ Atten (PNLT)
1	49.8	1.40	88.2	2.72	16.6
2	12.9	2.10	53.1	3.87	

NOTE:

Rfs – Resistance of face sheet in cgs Rayls at $V=105$ cm/s

Dfs – Core depth of upper cavity in cm at full scale (scale factor=5.91)

Rsep – Resistance of the septum in cgs Rayls at $V=105$ cm/s

Dsep – Core depth of upper cavity in cm at full scale

Σ Atten – Σ PNLT Attenuations at approach, cutback, and sideline

The one-third octave band attenuations versus frequency are shown in Figure 41 for the cutback conditions. Recall the cutback condition has a “factor” of 0.8 multiplied by the attenuations within MELO. There are four lines on the plot representing the optimum (at optimum impedance), the double layer, the single layer, and the baseline single layer lining attenuations. The baseline liner was a DEI built lining that was scaled from the ADP Demo Engine Test. Examination of the attenuation plot shows that the DEI liner is tuned near 1000 Hz and its attenuation falls off rapidly with increasing frequency. This lining looks like it was tuned to lower the 2BPF tones. Recalling Figure 33 we see that the frequencies above 2BPF have NOY values equal to or greater than the 2BPF band. Therefore, the lining should be tuned at higher frequencies to equally attenuate them while attenuating 2BPF.

The single layer design attenuation spectrum resulting from this study is centered around 1600 Hz and has a broader bandwidth than the Baseline design. Notice the baseline liner attenuation spectrum is much more peaked than the optimized single layer design. The broader bandwidth was accomplished by having different depth liners on each side of the duct as well as tuning the lining to a higher frequency. Figure 42 shows the impedances for the liners on each side. Side 1, the thinner, matched the optimum resistance and reactance in the 1600–2000 Hz range and side 2 matches the optimum reactance near 1000 Hz. Generally attenuation falls off rapidly as the resistance falls below the optimum and fairly slowly as the resistance goes above the optimum. The fall off of attenuation as the reactance deviates from the optimum value is more symmetrical with a slope between that for increasing and decreasing resistance. Of note is the small variation of the liner impedances with engine power condition because of the linearity of the face sheet.

The double layer design showed the best overall attenuation and has the broadest bandwidth as expected. MELO predicted at 3.3 dB attenuation improvement summed over the approach, cutback, and sideline conditions relative to the optimized single layer design. The impedance plots, shown in Figure 43, show how the two lining impedances of each side match the optimum impedance. Side 1, the thinner side, nearly matches the optimum reactance in the 1200–4000 Hz range. Side 2 matches the optimum resistance and reactance at 900 Hertz and is pretty close for resistance and reactance from 1000–2500 Hertz. This is consistent with the attenuation plot which showed the double layer liner performing well from 800–4000 Hertz. Again the linearity of the face sheets and septa result in small changes of the impedances with engine power condition.

5.8 Conclusions

The double layer design showed the best overall attenuation and had the broadest bandwidth as expected. A 3.3 dB attenuation improvement summed over the approach, cutback, and sideline conditions relative to the optimized single layer design was predicted. Using different designs on opposite walls within the duct improved the predicted attenuation bandwidth. This is consistent with the attenuation plots which showed the double layer liners performing well from 800–4000 Hz and the single layer liners performing well from 1000 Hz–2500 Hz.

Unlike the shorter inlet, the optimum impedance of the fan duct changes very little with operating condition. It is believed that the reason that there is such a small change is that the optimum impedance is primarily controlled by the lowest order modes due to the large length to height of the duct, L/H .

The effect of the boundary layer on optimum impedance is primarily at the higher frequencies where it reduces the reactance and increases the resistance slightly. One possible explanation of the high frequency behavior has been suggested. The boundary layer velocity gradient tends to bend waves toward the lining increasing the incidence angle and thus increasing the reactance (toward zero). However, this should reduce the optimum resistance which is opposite to the duct propagation code calculation. The reason for this behavior is not understood.

The use of a random broad-band energy assumption is believed appropriate for the ADP. The larger diameter and reduced tip speeds create a situation where the rotor stator interaction BPF is always cutoff and at a lower frequency than conventional engines. The rotor stator interaction will cut-on the 2BPF, however, the 2BPF still does not dominate the far-field spectrum as can be seen by the Noy weighted design spectra.

Examination of the outputs from the impedance design study with YMATCH show that single layer linings can match the target impedance over one octave and double layer linings can match a target impedance over two octaves.

The design process of using an impedance optimization to various frequency weightings followed by an attenuation evaluation to determine a preliminary design and using this preliminary design as a starting point for the attenuation optimization seemed to work well. At Boeing we have had problems with optimizers with liner design to an attenuation cost function. Common optimization problems with local minima and constraints are made more severe by the large number of parameters being optimized. The pre-optimization of the impedance to the target impedance seemed to improve the reliability of the final attenuation cost function optimization.

6. Evaluation of Broadband Liners for a Med-Sized Twin Engine Airplane

The objective of this task was to evaluate the passive duct lining concepts considered earlier (Sec. 3) and the design experience from the model fan duct ADP design (Sec. 5) by applying them to an airplane analysis. Section 3 discussed the evaluation of broad-band lining concepts (linings that have a favorable impedance over a larger frequency range) for a target SPL 1/3 octave spectrum that was flat over a large frequency range (500 Hz to 4 kHz). This design case was chosen because new generation wide-chord fan engines require attenuation over a wide frequency range. A more representative evaluation of the technologies evaluated in the earlier studies could be done by choosing a specific airplane and engine type. Also, the study was expanded to include technologies other than those limited to changing liner impedance, which included increased acoustic lining coverage within an existing nacelle envelope and the “scarf” inlet concept.

This section is organized into three major sub-sections. The first sub-section contains introductory material and includes a description of the details which define the study. The next sub-section covers the results for the trade studies conducted for inlet noise propagation and radiation. The final sub-section describes the trades that were carried out for fan duct noise propagation and radiation.

6.1 Program Overview

6.1.1 Airplane/Engine Definition

The airplane/engine configuration decision controls the engine noise signature and airplane operating conditions which in turn establishes the target noise spectra to be attenuated.

6.1.1.1 Airplane Definition

For this study a mid-sized, twin engine airplane was suggested by NASA LaRC. It was originally suggested that the mid-sized, twin engine airplane defined in a report by Kumasaka (see Ref. 13) would be used as the study airplane. However, the report did not specify all of the parameters needed to accomplish this trade study and additional assumptions about the study airplane were required. This was particularly true in two areas. The first was the desire to consider a wide-chord fan, mid-twin airplane which was not considered in Ref.13. The other was that the definition of the nacelle configuration for the baseline airplane was not specified in Ref.13. Lining coverage area and duct lengths needed to be established to do the study. These areas and lengths varied depending on which of the three engine nacelles currently on the 767 airplane was considered. A nacelle was defined that represented what Boeing was able to manufacture in 1992 and the baseline lining in the nacelle was the best lining that we could have designed in 1992.

The Boeing 767, being a mid-sized twin engine airplane, was used to generate most of the airplane performance data needed for the study. Table 9 shows the operating conditions for the FAR 36 certification flight conditions chosen.

Table 9: FAR 36 Operating Conditions for Trade Study Airplane

Condition	Altitude (ft.)	Sideline (ft.)	Thrust (lb.)	Mach
Approach	394	0	10,900	0.23
Cutback	1452	0	30,800	0.30
Sideline	1085	1476	44,600	0.30

6.1.1.2 Engine Definition

The thrust requirements for the mid-sized twin engine airplane, as defined in Table 9, require approximately a 90 in. diameter fan. Both wide chord and narrow chord fan engines were considered for this study. Current wide chord fan engines have approximately 20 fan blades while narrow chord fans have approximately 40 blades.

6.1.1.3 Nacelle Definition – Inlet

The nacelle inlet definition determines the location and amount of lining in the inlet. For the mid-sized, twin engine trade studies, the baseline nacelle was chosen to be made from aluminum. The panel splices for such a nacelle would be on the order of 2.7 in. wide, with three axial splices in the inlet.

The inlet baseline nacelle was defined not to have lining next to the fan face. Lining in this region can increase the inlet tone levels enough that hard-walling this region reduces the inlet noise. The effect is caused by the circumferentially non-uniform lining near the fan.

Also, the lining was defined to extend forward to the throat of the nacelle, but not past. This is generally the current requirement for lining in the forward section of the inlet. The length to radius ratio for this nacelle is approximately 0.6.

Figure 44 is a schematic of the nacelle used for the study. Note the inlet splices and the hardwalled area near the lining lip.

6.1.1.4 Nacelle Definition – Aft Duct

The nacelle is much easier to define for the aft duct because the uniform, infinite, rectangular-duct analysis program does not require an exact definition; since it is not capable of analyzing the effect of lining non-uniformities and 3 dimensional geometries like the inlet analysis program. All that is required is a lining length and a duct height to represent the annular fan duct. Figure 45 shows the representation of the fan duct.

6.1.2 Target Spectra

Target hardwall one-third octave SPL spectra were generated for the three FAR 36 certification conditions for both the narrow chord and wide chord engines. The target spectra are generic representations of the narrow and wide chord fan engines and do not represent any particular engine. Boeing technology is well established to predict the attenuations of linings in the inlet and the fan duct. However, in the interstage area, between the fan rotor and the stators, it is difficult to predict acoustic lining attenuations for the inlet or aft fan noise components. Therefore, hardwall target spectra were generated from test data with interstage lining present. No analysis was done to evaluate interstage lining improvements.

6.1.2.1 Inlet Noise

Figure 46 shows the Noy weighted SPLs for the FAR 36 extrapolated conditions for the inlet radiated fan noise source component for both the narrow and wide chord fan engines. These

data were used as the target spectra for the trade study. Note that the narrow and wide chord fans have similar broadband noise, but the narrow chord engine's tones are at higher frequencies than the wide chord engine's. To attenuate both the peak Noy frequencies and provide attenuation at the tone frequencies, which provide a tone correction penalty, requires an extremely broad-band liner for the wide chord engine.

Also, the peak Noy weighted noise occurs at higher frequencies for approach than the higher RPM cutback or sideline conditions. This counter-intuitive observation is primarily due to atmospheric absorption. The atmospheric absorption increases with frequency and the propagation distances for cutback and sideline are considerably longer than the approach distance (see Table 9). Therefore, the cutback and sideline noise levels roll-off at higher frequencies.

6.1.2.2 Aft Fan Noise

Figure 47 shows the Noy weighted SPLs for the aft radiated fan noise source component at the 120 degree emission angle. The data look similar to the inlet noise data discussed above and similar observations can be made.

6.1.3 Types of Nacelle Noise Suppression Technologies

Inlet and aft fan noise suppression technologies studied can roughly be grouped into three categories if changes to the engine hardware are not allowed. These are lining impedance, lining area, and configuration technologies.

In its simplest form, lining impedance noise attenuation technology attempts to build a lining which matches a uniform optimum impedance target over a wide frequency range. This was the approach taken for the present study. A previous analytical inlet lining optimization study conducted at Boeing, using an early version of the ray tracing code used for the present study, showed only a small benefit for varying optimum impedance within an inlet compared to a uniform optimum impedance. Since a ray tracing code does not include modal or scattering effects the possible benefits of scattering were not considered in these optimizations. The lining designs of the present study were primarily aimed at broadband noise, so it was felt that consideration of detailed modal effects were not necessary because of the large number of modes supported by the inlet.

The analysis code used for the fan duct lining study is a very simplified duct wave propagation code which only considers rectangular or circular/annular, axially uniformly treated, infinitely long ducts. Therefore, this code is not capable of analyzing the effect of varying duct geometry, varying impedance or modal scattering. Boeing has found that using the rectangular duct option to model fan ducts does a good job matching engine test data for approach engine power but over predicts engine test data by approximately 20% at cutback engine power and 40% at takeoff engine power. The rectangular duct assumption was used for the present fan duct lining study. The conclusions reached from this study are therefore limited to fan ducts for which the computer modeling assumptions used hold, i.e. broadband noise in relatively long ducts with slowly varying geometry and uniform impedance. While it is understood that this is a fairly limiting set of constraints it was felt that the study was still useful for studying large bandwidth liners; especially since lining attenuation predictions with this code have compared well with engine data in the past. These studies did indicate that there may be a benefit from modal scattering in a fan duct due to the difficulty of attenuating low order modes. This indicates that a fan duct lining configuration which first uses a section of lining to attenuate higher order modes,

is then followed by some method of scattering the low order mode energy into higher order modes (e.g. a reactive lining) and is then followed by an additional lining section to attenuate higher order modes could improve attenuation relative to a uniform lining. It is planned to study this concept when a new 3D code, being developed by Boeing under the AST contract, is available.

Uniform lining impedance technologies use broadband or adaptive liners to better match the liner impedance to the ideal impedance over more frequencies and/or operating conditions. Examples would be linear liners, triple layer liners, parallel element liners, or bias flow liners.

Lining area technologies can improve attenuations by the elimination of hardwall areas in the form of panel splices, areas near the fan or near the anti-ice bulkhead and replacing them with lining. While this technology development was not an explicit element of the AST program, the inlet noise trades show that this technology may be valuable.

Configuration technologies modify the nacelle, not the engine, to change the radiation directivity or propagation of the source noise from the engine. The scarf inlet and sonic inlet are two examples of this type of technology.

This study primarily considers uniform lining impedance changes made through the use of broadband linings. However, some lining area and configuration change results from an internally funded inlet studies are briefly discussed.

6.1.4 Linings Evaluated in the Study

Six different linings were considered in the lining impedance studies for the mid-sized, twin engine airplane. They were single, double, and triple layer perforate and linear liners (see Figure 48).

Single, double, or triple layer liners refer to the number of resistive layers in the lining. The single layer liner has a resistive facesheet with a backing cavity. The double layer liner adds a resistive septum and a backing cavity while the triple layer adds two septa and cavities in series.

The linear or perforate liner classifications refer to the type of resistive layer. Linear liners are often made of wire and are sometimes called wire liners in these studies. They resist flow through them predominantly by viscosity and tend to have resistances that vary only weakly with particle velocity. Perforate resistive layers, on the other hand, use non-linear jetting as the primary loss mechanism and are dependent on particle velocity.

6.2 Inlet Trade Studies

The inlet trade study was only performed at the approach condition. This condition requires the widest liner bandwidth because the target spectra are generally broader. Therefore, the study examined the condition where liner technology should make the largest difference. However, the trade of how different liners work at off-design conditions is clearly absent and deserves attention. Some “quick look” data suggests that some of the advanced liner concepts may work better at the off-design points and thus their value may be underestimated with respect to a single point design.

The inlet component trades are based on an inlet fan noise source component Effective Perceived Noise Level (EPNL) metric. The use of component EPNLs can be problematic because of other components masking certain frequencies in the complete noise signature. This is particularly a problem when calculating tone corrections that are applied to the Perceived

Noise Levels (PNL). It may be desirable to define other noise components so the value of a change could be evaluated in the overall delta EPNL of the airplane. In practice, however, this is difficult because the answer is dependent on the other source levels which are also changing in the context of the total AST program.

6.2.1 Technologies Evaluated

The primary focus and original reason for doing this study was to look at how much noise improvement would result from applying uniform liner impedance control technologies. Uniform impedance technology improvements refer to the use of advanced linings to better match the optimum impedance over a larger frequency range. As mentioned above, a previous study showed that varying impedance over the inlet lining did not provide appreciable benefit over a uniform optimum impedance.

Some trade studies were also performed to evaluate lining area changes for the inlet. In particular, lining area changes associated with the ability to minimize segment splices in linings to 0.5 inches were studied. Smaller splices also allowed lining to be added near the fan where lining had been removed to reduce BPF tone noise generated by scattering of cut-off modes. Finally, the effect of lining extended from the throat up to the anti-ice bulkhead of the inlet was considered.

Trades were also performed to determine the value of a scarf inlet. A triple layer lining was chosen and the value of a scarf with different lining coverage areas was determined.

6.2.2 Liner Depth Constraints

A two inch depth constraint was used for the inlet of the study airplane. This constraint may be a little conservative in that there may often be more room in the barrel part of the inlet. However, near the fan-face two inches is a reasonable limit because of blade containment issues. Also, most of the lower degree of freedom liners optimized to a thickness that was considerably thinner than the 2 inch constraint. The triple layer linear liners optimized to the 2 in. depth constraint and may have benefitted from additional depth.

6.2.3 Source Assumptions

The analysis code used for the inlet trade study was a Boeing ray tracing code called RDIFF. The source region used in RDIFF for this study was a source covering the outer half of the annulus formed between the fan containment ring and the centerbody at the station containing the fan. This is the red region shown in Figure 44. Past experience has shown that this source location area results in radiation predictions which match the measured data well.

RDIFF assumes that all the rays that go from the receiver to the source are uncorrelated or equivalently any two different points on the source region are uncorrelated. As a result of this source distribution, RDIFF predicts broad-band attenuations well, but does not do as well predicting tone attenuations. Tone attenuations would be dominated by a few propagating modes whereas the source distribution defined has many modes and is more like a broad-band source. Past experience shows that RDIFF typically under-predicts the tone attenuations.

6.2.4 Optimum Liner Impedances

The optimum or “target” uniform lining impedance used in this study was $Z = 2.0 - i 0.5$ when normalized by ρc . This target was based on experience from running the RDIFF program in previous studies.

6.2.5 Evaluation Process

The evaluation process used for this trade study is shown in Figure 49. There are basically four steps to the process which are described below.

6.2.5.1 Optimize Lining Parameters to Match Admittance

The lining's normalized impedance is "matched" to the normalized optimum impedance of $2.0 - i * 0.5$. This target impedance was chosen because it represented the current thinking at Boeing on the best inlet impedance. The YMATCH program uses the lining parameters and constraints, target impedance, and frequency weightings to solve a least squares admittance (1/impedance) optimization problem resulting in the best lining.

$$\text{Min } \Sigma[\text{Weight}(f) (Y(f)_{\text{Target}} - Y(f)_{\text{Trial}})^2]$$

The lining parameters define the independent and dependent variables in the optimization problem. For this study the independent variables were the total lining depth, depth of all but one of the cavities and parameters controlling the resistances of the resistive layers. The dependent parameter was the depth of the remaining cavity (if any) depending on the total depth constraint used. For the inlet trade study a constraint was set such that the maximum depth of the lining would be 2 inches.

The frequency weightings are multiplied by the square of the differences between the target admittance and the calculated admittance. In this way, one can highlight important frequency regions where the liner and target admittances should be close. The four sets of frequency weightings used for the inlet trade study are shown in Table 10.

Table 10: YMATCH Frequency Weightings for the Inlet

#	B27	B28	B29	B30	B31	B32	B33	B34	B35	B36	B37	B38
1	0	0	0	0	1	1	2	3	1	2	1	1
2	0	0	0	0	1	1	1	1	2	1	0	0
3	0	0	0	0	0	0	1	2	1	0	0	0
4	0	0	0	0	0	0	0	0	0	1	1	1

The weightings are shown as a function of one-third octave band number. Band 27 would represent a 500 Hz center frequency and Band 38 represents a 6300 Hz center frequency. Note Weighting #1 has coefficients over 12 one-third octave bands or 4 octaves. YMATCH results with this weighting set produced results that matched the one-third octave bands B30 to B35, but could not match the target outside these frequencies. Examination of the outputs from YMATCH show that single layer linings can match the target impedance over one octave and double layer linings can match a target impedance over two octaves.

YMATCH exhibits some starting point dependence for the output lining. To assure the "best" solution is found, multiple starting points are used and the lining is chosen that "best" matches the admittance target. This is accomplished by a global option that exists within the YMATCH program.

6.2.5.2 Run RDIFF Code to Determine Lining Attenuations

The next step in the design process was to predict the lining attenuations using the RDIFF program. RDIFF is a 3-D, ray tracing code developed at Boeing that allows the actual 3-D

nacelle geometry and lining definition to be used as inputs. The program works well when the ray acoustic assumptions are valid (i.e. duct diameter is much greater than the acoustic wavelength, broadband noise). These assumptions are generally met for the modern HBPR engines where the inlets are very large and the important Noy weighted frequencies are from broadband noise around 2–4 kHz.

The attenuations as a function of frequency and emission angle can then be calculated by determining the level change with and without the defined lining in the inlet nacelle.

6.2.5.3 Add Attenuations to the Hardwall Data

The predicted attenuations from RDIFF are added to the static, 150' polar hardwall data discussed in the section on the target spectra (Section 6.1.2.5). RDIFF determines attenuations in a reference frame fixed with the fan. Therefore, lining attenuations need to be applied at frequencies in this frame and not the Doppler shifted frequencies that would be measured at the FAR 36 flight conditions.

6.2.5.4 Extrapolate Data to FAR 36 Condition

The final step in the process to determine the FAR 36 noise levels is to extrapolate the static, 150' polar data to the flight. In this step, the correct atmospheric attenuations and Doppler shifts are applied to the data.

6.2.6 Trade Study Results

Two separate trade studies were carried out for the inlet. The first was a study to determine the benefit of broad-band linings for the mid-size, twin engine airplane. This was a lining design impedance study. The second study looked at the effect of changing the lining coverage areas and the effect of a scarf inlet on inlet noise. These are considered area and configuration technology changes.

6.2.6.1 Impedance Trade Study

Table 11 tabulates the results of the inlet lining impedance study for narrow and wide chord fan engines. The table gives the inlet fan component EPNL attenuations (calculated as the difference of the hardwalled inlet fan EPNL minus the treated inlet fan EPNL) and the percent improvement relative to the double layer perforate design. The double layer perforate design was chosen as the baseline because it was the Boeing standard in 1992.

Table 11: Results of the Impedance Study for the Inlet Component at the Approach Condition

Lining	Narrow Chord		Wide Chord	
	Atten (EPNdB)	improv (%)	Atten (EPNdB)	improv (%)
1 layer perforate	3.48	-12.7	2.89	-11.1
1 layer linear	3.86	-3.3	3.15	-3.1
2 layer perforate	3.99	Base	3.25	Base
2 layer linear	4.09	2.5	3.37	3.7
3 layer perforate	4.07	2.0	3.35	3.1
3 layer linear	4.21	5.5	3.48	7.1
Optimum	4.38	9.7	3.67	12.9

Figure 50 shows the results of Table 11 graphically. The independent axis has the number of degrees of freedom of the liner. A single layer lining had two parameters that could change (depth and resistance of the facesheet) and thus has two degrees of freedom. Likewise, the double and triple layer liners had 4 and 6 degrees of freedom respectively. The attenuation from an imaginary liner with “optimum” impedance at all frequencies is also shown on the plots at zero degrees of freedom. The dependent variable of the plots is the inlet component EPNL attenuation.

The plots show the EPNL attenuation for the narrow (upper plot) and wide (lower plot) chord fan engines. Notice that the linear or “wire” designs outperform the perforate designs. Also, the curves increase with the number of degrees of freedom, but are tending to flatten out as the attenuations approach the optimum lining value.

Figure 51 shows the predicted impedance of the different linings at the approach condition. Notice that all the linings do well at matching the target resistance of $R/\rho c = 2.0$. However, the linings tend to match the target reactance of $X/\rho c = -0.5$ better as the lining complexity increases (single to double to triple layer). This benefit was expected to improve the lining attenuations for the narrow and wide chord fan target spectra. At the approach power condition the linear liner attenuation benefit relative to a perforate liner was due primarily to a flatter reactance curve with frequency. This resulted in the linear liner having reactances closer to the optimum value of $-i(0.5)\rho c$ over a wider frequency range than the perforate. This flatter reactance results from the lower mass reactance associated with linear liner materials (woven wire for example). The lower mass reactance allows the linear liner to be deeper than the perforate. This increases the low frequency reactance while keeping the high frequency reactance lower than for the perforate liner.

Clearly large inlet component EPNL benefits were not achieved by lining improvements at the approach condition design point. Even the optimum impedance lining, which has the target impedance at every frequency, only gives about a 10% improvement in attenuation. The reason why this happens can best be explained with ray acoustics (see Figure 52). Rays leaving the source (the fan) hit hardwalled areas such as splices in the inlet or hardwalled areas near the lip and are reflected to the observer. Even though other rays hit “good” lining and thus are attenuated, the rays that strike the hardwalled areas make a “noise floor.” This is the reason that even an optimum impedance liner cannot achieve appreciable gains in attenuation at the design point.

It needs to be pointed out that the impedance of the higher bandwidth liners tends to be less dependent on engine power condition (see Figure 53). The triple layer perforate is much less affected by the change in engine power conditions than the single or double layer perforate. Also, note that the resistance and reactance are changed from their values at the approach condition (Figure 51) when compared to those for cutback condition in Figure 53. As the engine power condition increases, the in-duct sound level also increase causing an increase in the resistance. Additionally, the perforates are much more sensitive to in-duct sound level changes than the linear liners.

The independence of lining impedance to SPLs is extremely advantageous for two reasons. First, SPLs change as the noise travels down the duct. Although this study did not take this into account when performing the attenuation calculations it is believed that the linings that are the least affected should perform better because they will remain closer to the optimum impedance target over a larger area. Second, the performance of broadband liner concepts will be greatly

improved because they should be able to match the optimum impedances over a greater range of the engine operating conditions (assuming the optimum impedance spectrum does not change significantly with engine operating condition). No quantification was done of the off-design engine condition performance improvements in this study due to time constraints. However it is believed that inlet impedance technologies should consider the control of impedance over a range of operating conditions as opposed to a single condition.

6.2.6.2 Lining Area and Configuration Trade Study

Two lining area technologies and one configuration technology were evaluated in the lining area and configuration trade study. The first lining area technology was designated AMAX after a Boeing in-house program to reduce splice widths. For this study the AMAX technology was assumed to reduce all inlet splices to 0.5” from the original 2.7” splice width. Also, as defined in this study, AMAX would further allow lining to be put near the fan where it is currently being hardwalled to reduce tone noise caused by an interaction with the splices. Figure 54 shows a diagram of the conventional and area technology nacelles.

The other lining technology considered for this study was the extension of the acoustic treatment to the thermal anti-ice bulkhead. This technology was termed “bulkhead” (BH) lining for obvious reasons. Figure 54 also shows a picture of this type of nacelle.

The configuration technology considered for this study was the scarf inlet. The Boeing company is currently developing this concept to allow the technology to be put on an airplane product. A drawing of the scarf inlet compared to a conventional inlet is included as Figure 55. The scarf inlet changes the inlet nacelle to preferentially radiate upward and not to the important 50–60 degree angles below the airplane. The same AMAX and BH lining additions considered for the conventional inlet were evaluated for the scarf inlet.

The results of the study are shown in Table 12. The first column indicates that the nacelle is a conventional or scarf inlet and shows the percentage length increase if any. The next column shows what type of lining was put into the nacelle. Most the configurations were evaluated with a triple layer perforate because the study was to look at the effectiveness of area and configuration technologies and not at linings. The next three columns show whether the AMAX and BH lining technologies were on the nacelle, and the total lining area. Finally, the lining attenuations and percent improvement over a conventional nacelle with a double layer perforate are shown for both a narrow and wide chord fan target spectrum. Notice that relatively large attenuation improvements can be made with lining area and/or configuration technologies.

Table 12: Results of the Lining Area and Configuration Study for the Inlet Component

Nacelle	Lining	Lining Tech.		Area (ft ²)	Narrow Chord		Wide Chord	
		Amax	BH		Atten (EPNdB)	Improv (%)	Atten (EPNdB)	Improv (%)
Conv	HW	–	–	0	N/A		N/A	
Conv	2L perf	N	N	66.0	3.25	Base	2.69	Base
Conv	3L perf	N	N	66.0	3.30	1.5	2.71	0.7
Conv+10%	3L perf	N	N	74.1	3.93	21	3.25	21
Conv+20%	3L perf	N	N	83.5	4.31	33	3.55	32
Conv+40%	3L perf	N	N	101.1	4.79	47	3.90	45
Conv	3L perf	Y	N	83.5	4.56	40	3.92	46
Conv	3L perf	Y	Y	94.9	5.82	79	4.96	84
Scarf	HW	–	–	0.0	1.94	–40	2.53	–30
Scarf	3L perf	N	N	65.5	4.51	39	4.51	68
Scarf	3L perf	Y	N	82.9	5.72	76	5.72	112
Scarf	3L perf	Y	Y	94.3	7.13	119	7.13	165

The attenuation predictions shown in Table 12 are plotted in graphical form versus lining area in Figure 56.

These data show liner impedance improvements result in relatively small attenuation improvements and that larger attenuation improvements need to focus on lining area and configuration technologies.

6.2.7 Conclusions

The major conclusion from the above study is that improvements in inlet liner impedance characteristics alone will not result in 25% increased noise reduction relative to 1992 technology. The liner assumed for 1992 technology was double layer perforate liner using the Boeing buried septum technology. Optimum liners, non-physically realizable liners with optimum impedance at each frequency, were predicted to result in improvements of approximately 10% for inlets. A previous analytical inlet lining optimization study conducted at Boeing showed only a small benefit for varying optimum impedance within an inlet compared to a uniform optimum impedance. Hence, the above conclusion is assumed to apply to inlets with varying impedance as well. Liners with increased degrees-of-freedom, such as triple layer perforates were estimated to offer only 2% – 3% improvement for inlets. Liners with linear resistance elements such as linear double and linear triple layer liners were estimated to offer 6% – 7% improvement. A ray tracing code does not include modal or scattering effects the possible benefits of modal scattering were not considered in these optimizations. However, these effects are not believed to be important for broadband noise attenuation in an inlet because of the large number of modes propagating.

The benefit of linear resistive liner elements is probably underestimated by these results. At the approach power condition, the linear liner attenuation benefit relative to a perforate liner was

due primarily to a flatter reactance curve with frequency. This resulted in the linear liner having reactances closer to the optimum value of $-i(0.5)\rho c$ over a wider frequency range than the perforate. This flatter reactance results from the lower mass reactance associated with linear liner materials (woven wire for example). The lower mass reactance allows the linear liner to be deeper than the perforate. This increases the low frequency reactance while keeping the high frequency reactance lower than for the perforate liner. A Boeing internal study (scarf inlet design) which considered the FAR 36 cutback condition as well as the landing condition showed that the linear liner designed for landing also behaved much better at the cutback condition than was the case for the perforates. The increase in impedance due to increased grazing flow Mach number and internal SPL for the cutback condition relative to landing is significantly larger for perforates compared to current approximately linear liners. Although the cutback condition target impedance has a larger resistance than for landing the resulting increase for current perforates is much larger than desired. Current “linear” liner resistive elements such as woven wire are not truly linear and the resulting resistance increase is close to what is desired for the inlet lining.

Additional nacelle advances, such as liner structural design improvements to allow reduction in panel area used for fasteners or understanding of the effects of liners on boundary layer growth in the inlet throat region, may allow additional lining in inlet nacelles. This work is expected to gain an additional 40% – 80% in attenuation improvement relative to 1992 technology. In addition, the scarf inlet concept being developed uses the inlet shape to direct noise upward above the airplane while reducing energy propagating to the ground. This concept is expected to give an additional 40%–80% improvement.

The results from the study of the application of advanced liners to a medium twin airplane showed approximately 1/4 of the improvements relative to 1992 perforate double layer liner technology found in the NASA/FAA study conducted in 1993–94. The primary reasons for this discrepancy are the source noise characteristic assumed and the evaluation metric used. For the NASA/FAA study, the assumed source spectrum was a one-third octave spectrum with constant SPL from 500 Hz to 4000 Hz. The evaluation metric was overall power level (OAPWL). For the medium twin study, the evaluation metric was fan component EPNL and the source spectrum had maximum Noy weighting in the frequency range of 2 to 5 kHz. The maximum attainable attenuation in this frequency range is significantly lower than in the lower frequencies because of the beaming character of higher frequency modes. Also, attenuation bandwidth was not as important for the airplane study as it was for the 500 Hz to 4000 Hz power level attenuation study. This was even the case for the wide chord fan which had a relatively low frequency BPF at approach (630 Hz band) with a resulting 2.2 dB tone correction. Attenuation of noise in the BPF frequency region in this case had only a small contribution to PNLT attenuation for the twin study since the tone correction did not change very much. Only the fan noise component was considered for this study. In reality the masking effect of other noise sources such as airframe noise would probably cause the tone correction to be reduced as the inlet radiated fan noise is reduced in the BPF region. However, this effect was not accounted for in the airplane study.

6.3 Aft Duct Trade Studies

The following section covers the aft fan noise trade study. The aft fan study was performed assuming both the approach and cutback condition as the design condition. Also, the off–design performance was evaluated for each resulting lining design. This allowed some conclusions to be made about the value of broadband lining concepts at off–design conditions.

The liner attenuations were calculated using Boeing's Multi-Element Lining Optimization (MELO) program. The MELO program is a very simplified infinite duct wave propagation, modal attenuation code. Given a rectangular, circular, or an annular duct geometry and an impedance wall specification, the program calculates the duct eigenvalues which are directly related to the attenuation of a given mode per length. Multiplication by the lining length and summing over all the cut-on modes results in the attenuation for a given frequency. MELO does have the ability to handle 1-D flow in the duct and a boundary layer profile. As an infinite duct program, MELO does not consider changes in impedance down the duct. Therefore, this code is not capable of analyzing the effect of varying duct geometry, varying impedance and modal scattering. The studies described in Section 3 showed that the triple layer liner attenuation bandwidth is equivalent to what one would expect from varying impedance liners with broadband noise and a large number of modes.

Boeing has found that using the rectangular duct option to model fan ducts does a good job matching engine test data for approach engine power but over-predicts engine test data by approximately 20% at cutback engine power and 40% at takeoff engine power. The rectangular duct assumption was used for the present fan duct lining study. The conclusions reached from this study are therefore limited to fan ducts for which the computer modeling assumptions used hold, i.e. broadband noise in relatively long ducts with slowly varying geometry and impedance. While it is understood that this is a fairly limiting set of constraints, it was felt that the study was still useful for studying large bandwidth liners, especially since lining attenuation predictions with this code have compared well with engine data in the past. These studies did indicate that there may be a benefit from modal scattering in a fan duct due to the difficulty of attenuating low order modes. This indicates that a fan duct lining configuration which first uses lining to attenuate higher order modes, is then followed by some method of scattering the low order mode energy into higher order modes and is then followed by additional lining could improve attenuation relative to a uniform lining. It is planned to study this concept when a new 3D code being developed a Boeing under AST contract is available.

The aft fan component trades are based on the tone corrected perceived noise level (PNLT) at the 120 deg radiation angle. Past experience has shown that PNLT attenuation at maximum PNLT radiation angle is representative of the aft fan component EPNL attenuation. The MELO attenuation prediction program used in these studies predicts power level attenuations which past experience has shown apply reasonably well to the maximum PNLT radiation angle. These attenuations are applied to the target spectrum to determine the PNLT attenuations.

6.3.1 Technologies Evaluated

The primary objective was to determine how much noise improvement could be obtained by applying axially uniform impedance improvement technologies. No studies were done to evaluate varying impedance, modal scattering, lining area or configuration differences affecting the aft fan component because of the inherent limitations of the analysis code used. These studies are planned after a new 3D code presently being developed is complete (approximately 1999).

6.3.2 Liner Depth Constraints

The lining depth constraints for the aft duct are much more severe than the inlet depth constraints. For this study depth constraints of 1.0, 1.5, and 2.0 inches were considered. The

actual aft duct lining depth constraints would be somewhere near these numbers and would depend on where the lining was located.

6.3.3 Source Modal Energy Assumptions

The modal energy assumptions affect both the optimum lining design impedances and the maximum lining attenuations. For this lining design, a modal energy distribution believed to be appropriate to random broad-band noise was used within our design program. This assumption approximates an equal energy modal assumption which states that the propagating energy of each cut-on mode is identical. The Boeing assumption and an equal energy assumption are the same except near cutoff where the assumption forces lower energies near cutoff where the equal energy assumption would force extremely high SPLs because the energy transport rate down the duct is very small. The difference between the Boeing assumption and the equal energy assumption probably does not have a significant effect on the resulting lining design since the modes near cut-off attenuate rapidly down the duct even if the lining design is not optimum for these modes. The energy assumption used by Boeing is:

$$\int_S p^2 dS = \text{constant for each mode}$$

or the integral of the pressure squared over the cross sectional area is constant for each mode.

The use of a broadband energy assumption works well for fan ducts where the spectrum is broadband dominated. This is somewhat the case for the target spectra for the approach and cutback conditions which can be seen in Figure 47.

6.3.4 Optimum Liner Impedances

The optimum liner impedances were determined using Boeing's Multi-Element Lining Optimization (MELO) program. Built around the modal prediction capability is an optimizer capable of changing the lining impedance to maximize the resulting attenuation. In this manner, an optimum impedance versus frequency can be determined.

The representation of the fan duct lining with MELO is shown in Figure 45. A two dimensional, rectangular duct was modeled with the height of the duct chosen as the average height of the fan duct in the lined region for a mid-sized, twin engine airplane. The lining length used for the MELO program was obtained by estimating the average lining length.

The optimum impedance versus frequency plot produced with MELO for both approach and cutback is shown in Figure 57. Notice the optimum impedance of the fan duct changes very little for these two operating conditions.

In determining the optimum impedance for the mid-sized, twin engine fan duct, the following assumptions were made:

- 1 A two dimensional rectangular duct with the same lining on each side
- 2 A linear boundary layer profile with momentum thickness of 0.3 cm.
- 3 Cut-on modes with a modal assumptions as discussed in the Source Assumptions section.

6.3.5 Evaluation Process

The process used to determine the aft fan duct liner design is graphically shown in Figure 58. A description of each block follows.

6.3.5.1 Optimize Lining Parameters to Match Admittance

The lining's admittance (1/impedance) is matched to ideal admittance (1/ideal impedance) as calculated with the MELO program using Boeing's YMATCH program. This is basically the same procedure as described in Section 6.2.5.1 except the ideal impedance is different and different weightings are used in the least squares optimization problem.

Like the inlet problem, the lining parameters define the independent and dependent variables in the optimization problem. Three different depth constraints were used for the aft duct problem.

The frequency weightings used for the narrow and wide chord fan spectra at the approach and cutback conditions are shown in Tables 13, 14, 15, and 16. Different weightings were chosen for each target spectra because the target spectra were different.

Table 13: Frequency Weightings Used for the Narrow Chord Fan at Approach

#	B27	B28	B29	B30	B31	B32	B33	B34	B35	B36	B37	B38
1	0	0	0	0	1	1	1	3	2	2	1	1
2	0	0	0	0	0	1	1	1	1	1	1	0
3	0	0	0	0	0	0	1	2	1	0	0	0
4	0	0	0	1	2	1	0	0	0	0	0	0

Table 14: Frequency Weightings Used for the Narrow Chord Fan at Cutback

#	B27	B28	B29	B30	B31	B32	B33	B34	B35	B36	B37	B38
1	0	0	0	0	0	1	4	1	1	2	1	1
2	0	0	0	0	0	1	2	1	1	1	1	0
3	0	0	0	0	0	0	0	0	1	2	1	0
4	0	0	0	0	0	1	2	1	0	0	0	0

Table 15: Frequency Weightings Used for the Wide Chord Fan at Approach

#	B27	B28	B29	B30	B31	B32	B33	B34	B35	B36	B37	B38
1	0	2	0	0	1	1	1	2	2	1	0	0
2	0	0	0	0	1	1	1	1	1	1	0	0
3	0	0	0	0	0	0	1	1	1	0	0	0
4	0	2	1	1	0	0	1	1	1	0	0	0

Table 16: Frequency Weightings Used for the Wide Chord Fan at Cutback

#	B27	B28	B29	B30	B31	B32	B33	B34	B35	B36	B37	B38
1	0	0	0	3	1	1	1	1	1	1	0	0
2	0	0	0	1	1	1	1	1	1	0	0	0
3	0	0	0	0	0	0	1	1	1	0	0	0
4	0	0	1	3	1	0	0	0	0	0	0	0

The weightings are shown as a function of one-third octave band number. Band 27 would represent a 500 Hz center frequency and Band 38 represents a 6300 Hz center frequency. Note Weighting #1 for the narrow chord fan target spectra at approach has coefficients over 8 one-third octave bands or about 3 octaves. Examination of the outputs from YMATCH show that single layer linings can match the target impedance over one octave and double layer linings can match a target impedance over two octaves. When YMATCH was used to match a single or double layer lining over 3 octave bands it produced results that matched the center bands, but not the edges. This process produced four designs for each type of liner (perforate and linear single, double and triple layer), each depth constraint (1 in., 1.5 in. and 2 in.), each type of fan (narrow chord and wide chord) and each design point power condition (approach and cutback). The impedance spectra of these four designs were examined and one chosen (subjective evaluation) for the starting point of a duct attenuation optimization calculation.

6.3.5.2 Optimize PNLT Attenuations Using the YMATCH Starting Points

MELO was next used in the optimization mode to find lining designs for each type of liner (perforate and linear single, double and triple layer), each depth constraint (1 in., 1.5 in. and 2 in.), each type of fan (narrow chord and wide chord) and each design point power condition (approach and cutback). The YMATCH defined liner definitions were used as starting points. Specifically, the lining definitions and hardwall spectra are input into MELO. MELO then uses the optimizer to find a design which minimizes the attenuated spectrum PNLT by varying the specified geometry parameters, with defined constraints. These results were used to determine a set of attenuations to evaluate which liners performed best.

Since this process was run with perforate and linear single, double and triple layer linings, three lining depth constraints and two design points for both the narrow chord and wide chord fan engines, 72 optimizations were run.

It should be mentioned that there is a “factor” applied to the calculated attenuations within MELO. This “factor” is an empirical correction for the MELO predicted attenuations to match full-scale, ground test measured lining attenuation data. The accepted “factors” used at Boeing are 1.0, 0.8, and 0.6 for the approach, cutback, and sideline conditions respectively. The factors were applied to all the MELO duct attenuation predictions made in this design.

6.3.5.3 Choose Best Lining Based on PNLT Attenuations

The best lining for each set of target spectra and constraints was chosen from the set generated with MELO. This part of the process was nothing more than choosing the linings that gave the highest attenuations.

6.3.5.4 Calculate the Off-Design Performance

The final step in determining the best lining was to determine the cross-performance. For each of the linings generated from the last step, the attenuation at the other operating condition was determined.

6.3.6 Trade Study Results

Liner impedance design trade studies were completed for the fan duct to evaluate the benefit of broadband linings for the approach and cutback operating conditions for both narrow and wide chord fan target spectra. Additionally, some work was done to evaluate point design linings for approach and cutback at the off-design points.

6.3.6.1 Approach Design Point Impedance Study

Six different linings were evaluated for the approach impedance study. These were the single, double, and triple layer perforate and linear linings as discussed in the section on Linings Evaluated in this Study. The purpose of the study was to evaluate how much improvement broadband linings could offer for a point design.

Table 17 gives the results of the study. Note that although triple layer linings offer more component attenuation improvement compared to the inlet, the improvements are still relatively small. Note also that a optimum uniform lining (one that matches the ideal impedance at every frequency) cannot reach the 25% attenuation improvement AST program goal.

Table 17: Results of the Impedance Study for the Aft Component at Approach

Lining	Narrow Chord		Wide Chord	
	Atten (PNLTdB)	improv (%)	Atten (PNLTdB)	improv (%)
1 layer perforate	6.6	-20.5	5.3	-25.4
1 layer linear	7.9	-4.8	6.7	-5.6
2 layer perforate	8.3	Base	7.1	Base
2 layer linear	8.8	6.0	7.6	7.0
3 layer perforate	8.8	6.0	7.5	5.6
3 layer linear	8.9	7.2	7.7	8.5
Optimum	10.3	11.3	8.4	18.3

Figure 59 shows a graphical representation of the approach design point attenuation results. As expected, the linear liners outperformed the perforates and the higher number of degrees freedom liners outperformed the lower.

6.3.6.2 Cutback Design Point Impedance Study

Table 18 and Figure 60 show the cutback power design point results. Generally, the results are similar to the approach design condition with the exception that the “optimum” liner shows larger attenuation improvements than is seen for approach.

Table 18: Results of the Impedance Study for the Aft Component at Cutback

Lining	Narrow Chord		Wide Chord	
	Atten (PNLTdB)	Improv (%)	Atten (PNLTdB)	Improv (%)
1 layer perforate	6.5	-18.8	3.9	-29.1
1 layer linear	7.0	-12.5	4.2	-23.6
2 layer perforate	8.0	N/A	5.5	N/A
2 layer linear	8.1	1.3	5.8	5.5
3 layer perforate	8.1	1.3	6.0	9.1
3 layer linear	8.3	3.8	5.9	7.3
Optimum	10.2	27.5	9.1	65.5

6.3.6.3 Off-Design Impedance Study

The off-design performance of the point linings defined for approach and cutback were evaluated at the other operating condition. Figure 61 shows the sum of the approach and cutback attenuations for each lining. Note that the cutback designs tended to have slightly higher summed attenuations than the approach designs. This suggests that if a point design was going to be used for both conditions, that a cutback design should be chosen.

6.3.7 Conclusions

As for the inlet, the major conclusion from the above study is that improvements in nacelle liner average impedance characteristics alone will not result in 25% increased nacelle noise reduction relative to 1992 technology. The liner assumed for 1992 technology was a double layer perforate liner using the Boeing buried septum technology. Optimum uniform liners, non-physically realizable liners with optimum impedance at each frequency, were predicted to result in improvements of approximately 15% for the fan duct at the airplane landing condition. Liners with increased degrees-of-freedom, such as triple layer perforates, were estimated to offer 6% – 10% improvement for the fan duct. Liners with linear resistance elements, such as linear double and linear triple layer liners, were estimated to offer 7% – 10% benefit. Since previous studies have shown that the triple layer liner gives attenuation values similar to liners with slowly varying impedance for broadband noise and a large number of modes, the above conclusion are expected to apply to ducts with slowly varying impedance as well.

These studies did indicate that there may be a benefit from modal scattering in a fan duct due to the difficulty of attenuating low order modes. This indicates that a fan duct lining configuration which first uses a broadband lining to attenuate higher order modes, is then followed by some method of scattering the low order mode energy into higher order modes (such as a reactive liner segment) and is then followed by additional broadband lining could improve attenuation relative to a uniform lining. It is planned to study this concept and the effects of varying non-circular/annular geometry when a new 3D code being developed a Boeing under AST contract is available.

Consideration of the FAR 36 cutback condition showed that if both landing and cutback are given equal weight, the design optimized for cutback (design point) was superior to that designed for landing, for the narrow chord fan engine. If the approach condition is chosen as the

design point, the benefit of using a linear liner was significant (approximately 16% relative to the sum of landing and cutback attenuation for a double layer perforate liner).

For the wide chord fan the landing plus cutback attenuation was not appreciably different for the landing or cutback optimized liners. The benefit of triple layer or linear liners for this metric was similar to that seen for the design point PNLT attenuations (approximately 10%).

Additional nacelle advancements such as liner structural design improvements to allow reduction in panel area used for fasteners and strength reinforcement, are presently being studied at Boeing but the noise reduction from this technology for the fan duct was not explicitly evaluated as part of this study. Preliminary estimates show a potential for increasing the lining area by approximately 30%.

7.0 References

1. Parrott, T. L.; Watson, W. R.; and Jones, M. G.: NASA TP-2679, 1987.
2. Utsuno H. et al., "Transfer function method for measuring characteristic impedance and propagation constant of porous materials", *J. Acoust. Soc. Am.* 86(2), August 1989
3. Yaniv S. "Impedance tube measurement of propagation constant and characteristic impedance of porous acoustical material", *J. Acoust. Soc. Am.* 54(5) 1973
4. Delaney M. & Bazley E., *Appl. Acoust.* 3, 105 (1970)
5. Voronina N. N., "Influence of the structure of fibrous sound-absorbing materials on their acoustical properties", *Sov. Phys. Acoust.* 29(5), Sept.-Oct. 1983
6. Beranek, L., "Noise and Vibration Control", p 248, 1971 Edition
7. Dean P., "On the "In-Situ" Control of Acoustic Liner Attenuation", ASME Paper No. 76-GT-61, Gas Turbine Conference, New Orleans, La., 3-21-76
8. Hersh A. S. & Rogers T., "Fluid Mechanical Model Of The Acoustic Impedance Of Small Orifices", AIAA 75-495, March, 1975
9. Rogers T. & Hersh A. S., "The Effect Of Grazing Flow On The Steady State Resistance Of Square- Edged Orifices" AIAA 75-493, March, 1975
10. Ingard U. & Ising H., "Acoustic Nonlinearity of an Orifice", *JASA*, Vol.42, No. 1, 6-17, July 1967
11. NASA Contractor Report 198298, "Definition of 1992 Technology Aircraft Noise Levels and the Methodology for Assessing Airplane Noise Impact of Component Noise Reduction Concepts," H. A. Kumasaka, M. M. Martinez, and D. S. Weir, June 1996.
12. Rice E. J. & Saule A. V., "Far-Field Radiation Of Aft Turbofan Noise", NASA TM 81506, 1980
13. Kumasaka H. A. & Martinez M. M., "Definition of 1992 Technology Aircraft Noise Levels and the Methodology for Assessing Airplane Noise Impact of Component Noise Reduction Concepts", NASA CR 198298, June 1996

Bielak, G., Diamond, J., "Analytical Study Of Turbofan Engine Nacelle Acoustic Liners For Broadband Attenuation With Emphasis On Parallel Element Liners"
Submitted to NASA Langley May 1994

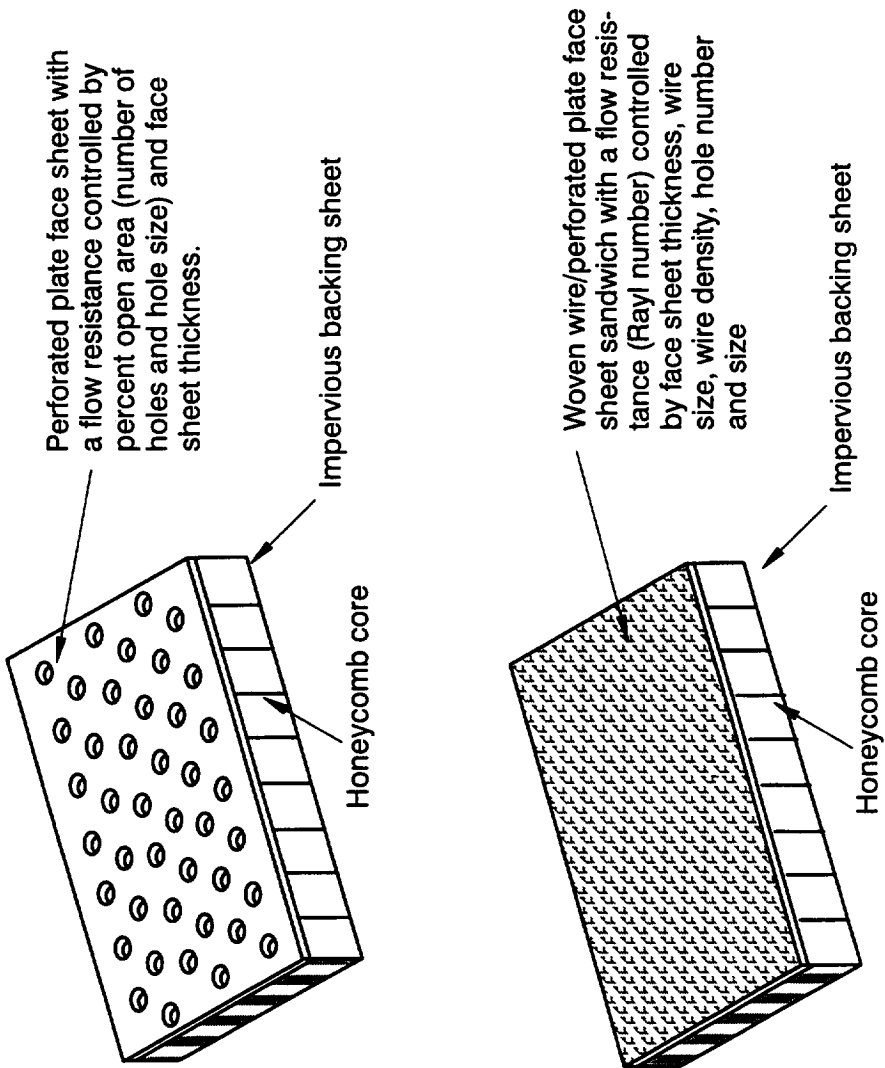


Figure 1: Single Layer Acoustic Liners

NOT TO SCALE

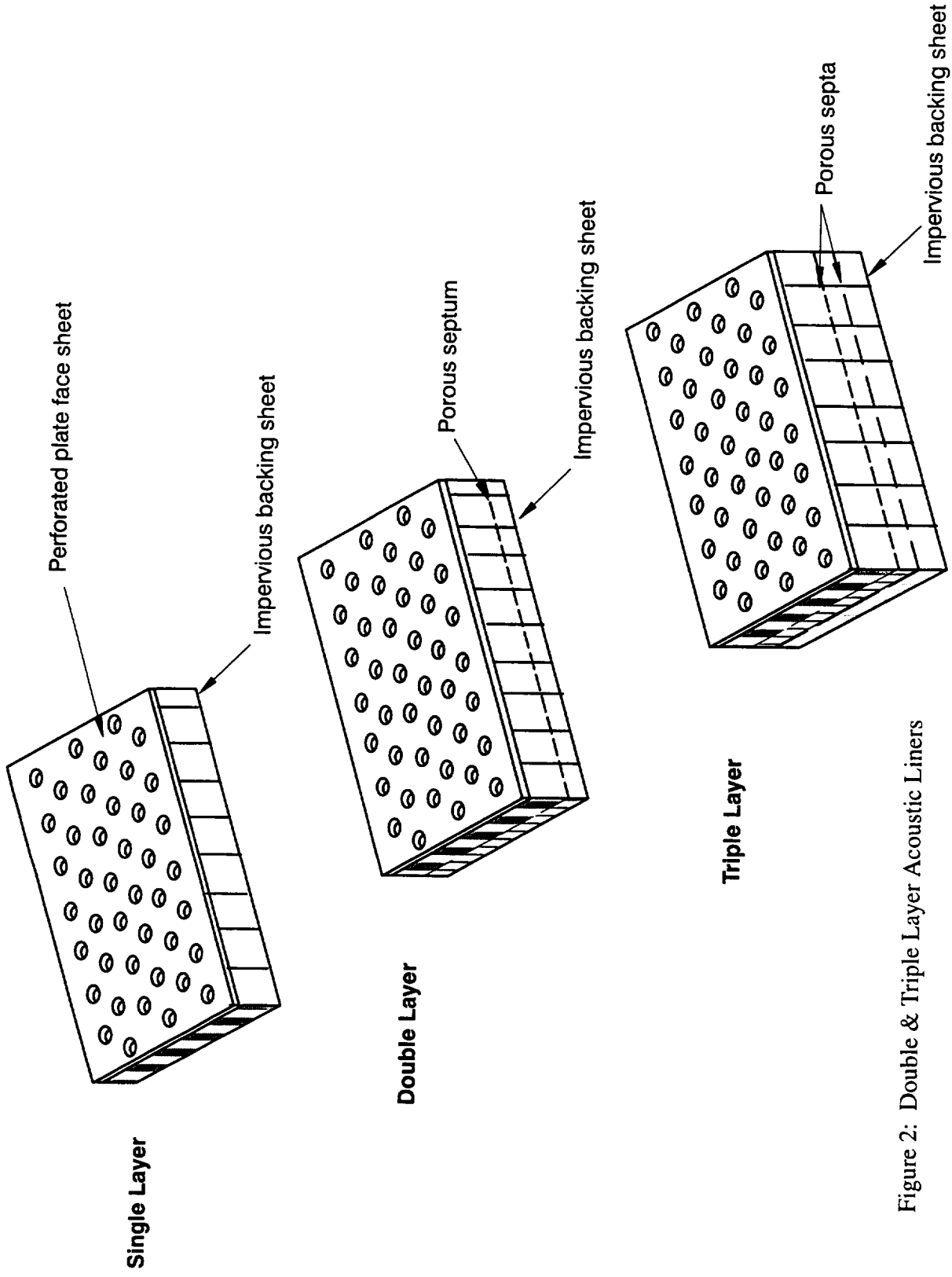


Figure 2: Double & Triple Layer Acoustic Liners

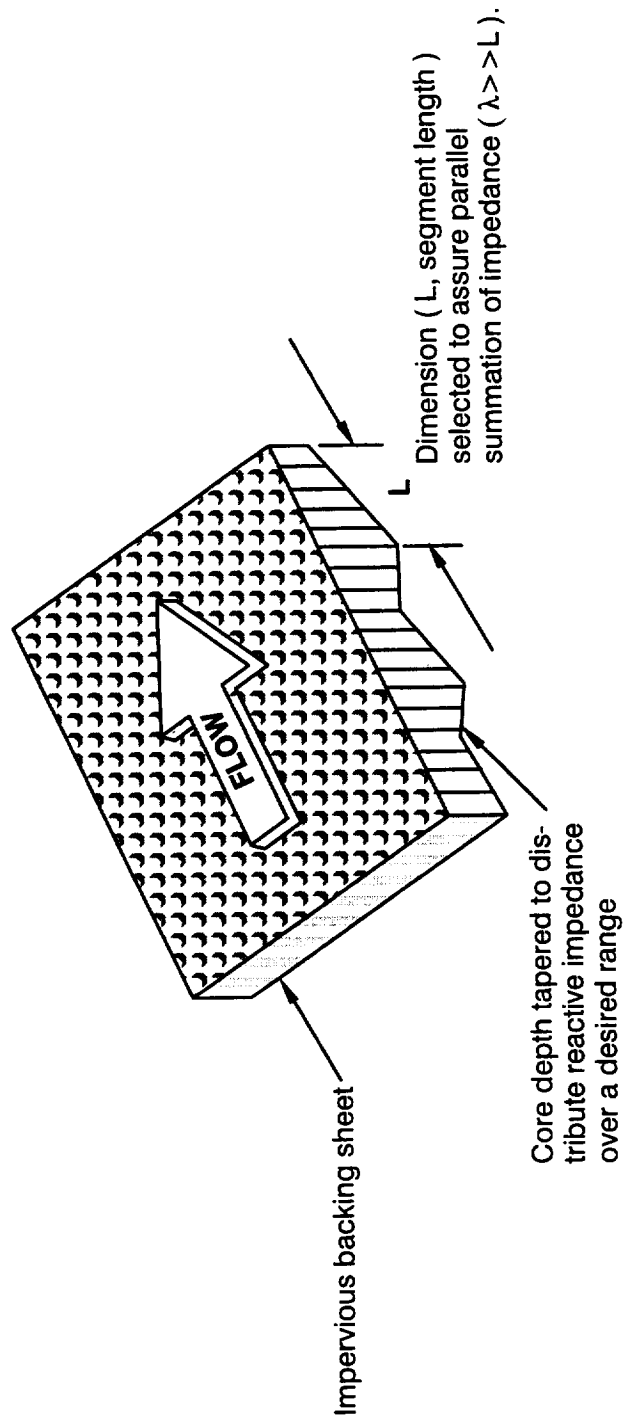


Figure 3: Parallel Element Acoustic Liner

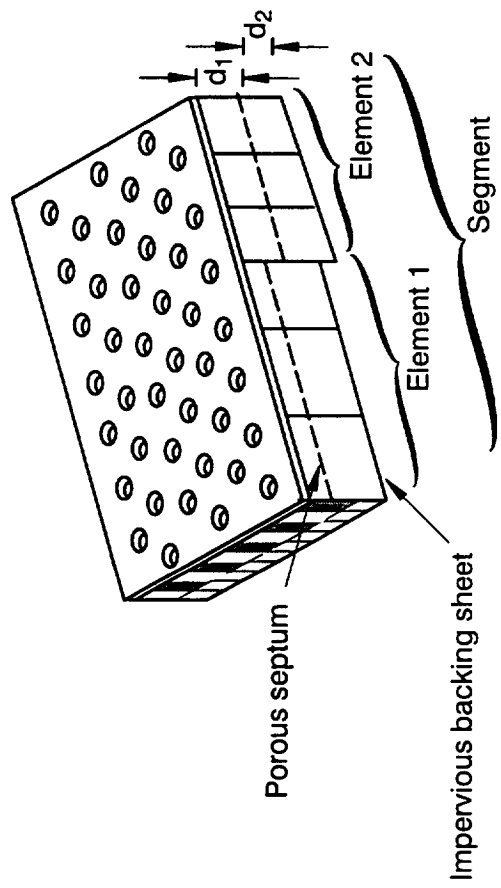


Figure 4: Double Layer Parallel Element Acoustic Liner

NOT TO SCALE

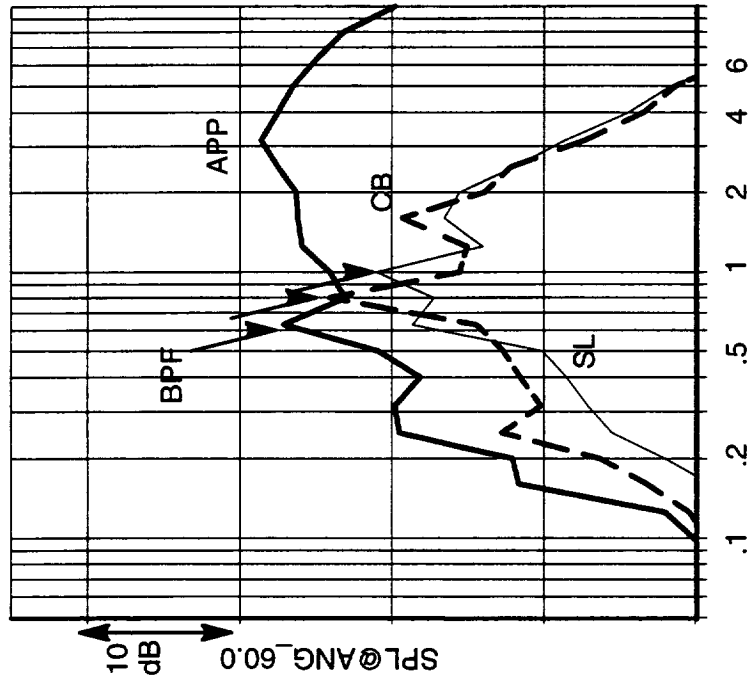
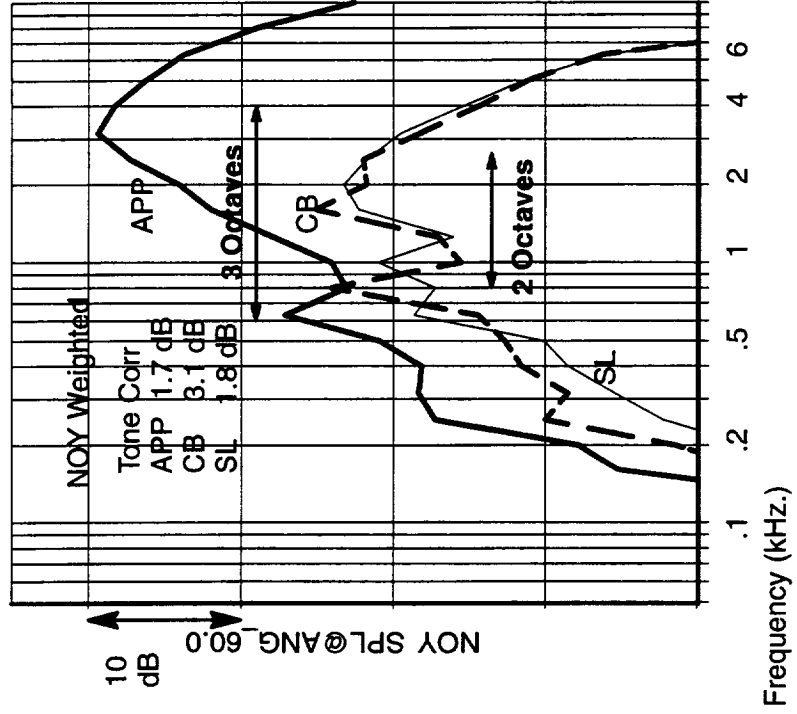


Figure 5: Typical Wide Chord Fan Spectrum Shapes At Peak PNLT Inlet Angle

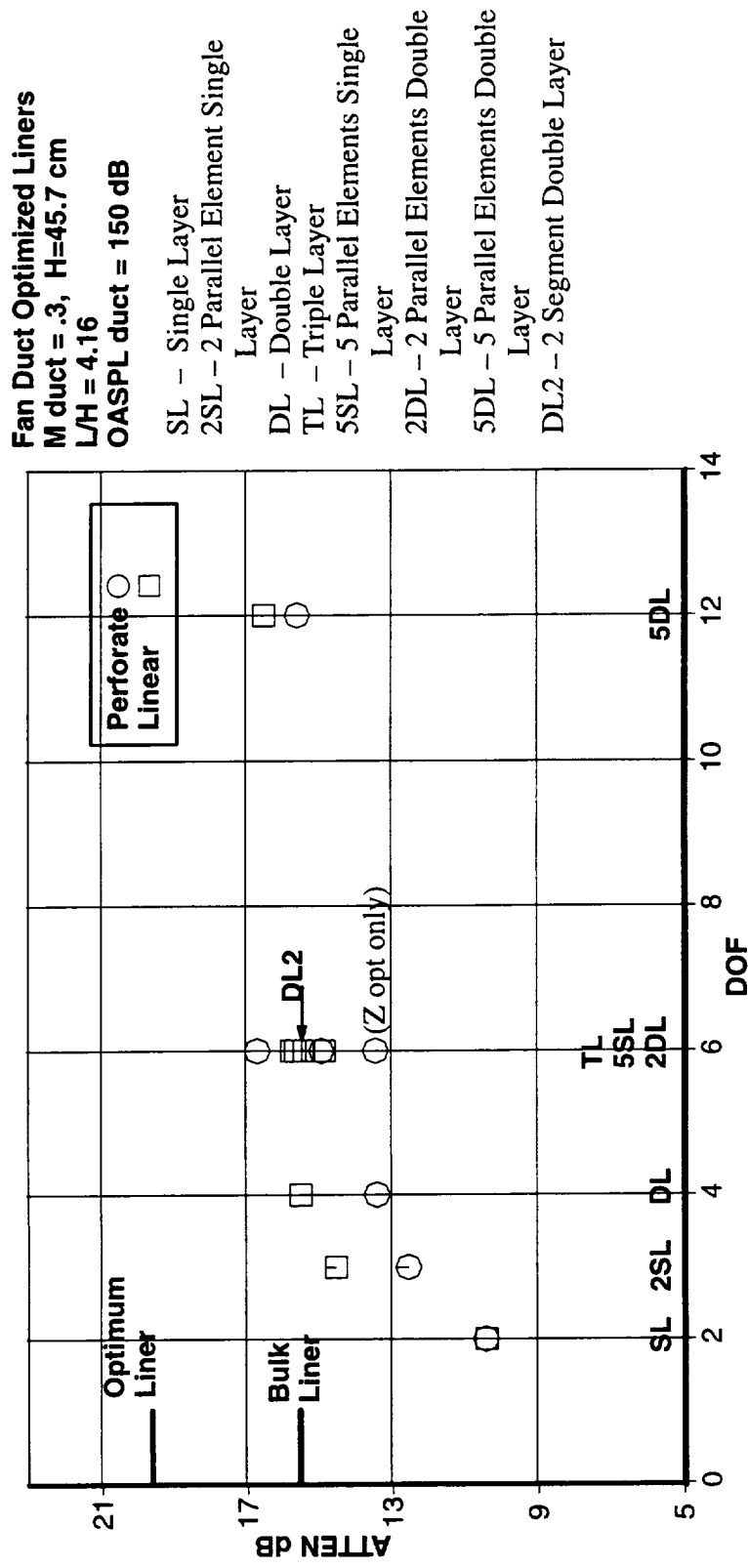


Figure 6: Fan Duct OAPWL Attenuations

Inlet Optimized Liners
 M duct = .3, R=130 cm
 L/R = .38
 OASPL duct = 150 dB

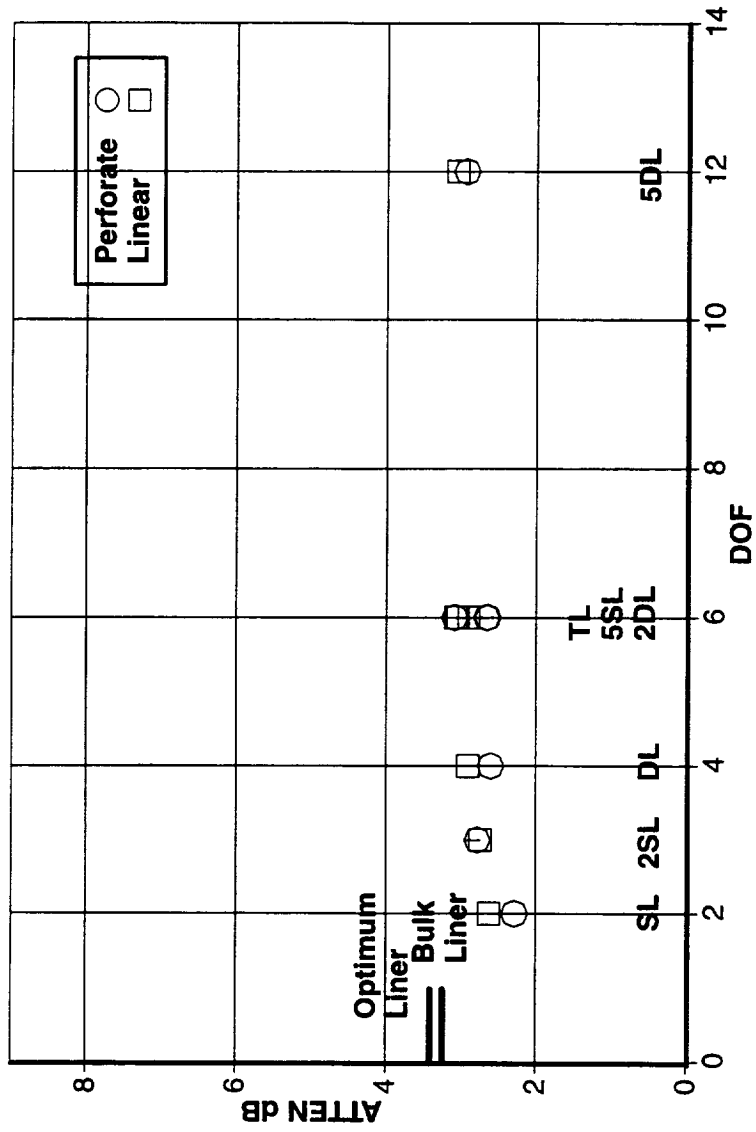


Figure 7: Inlet OAPWL Attenuations

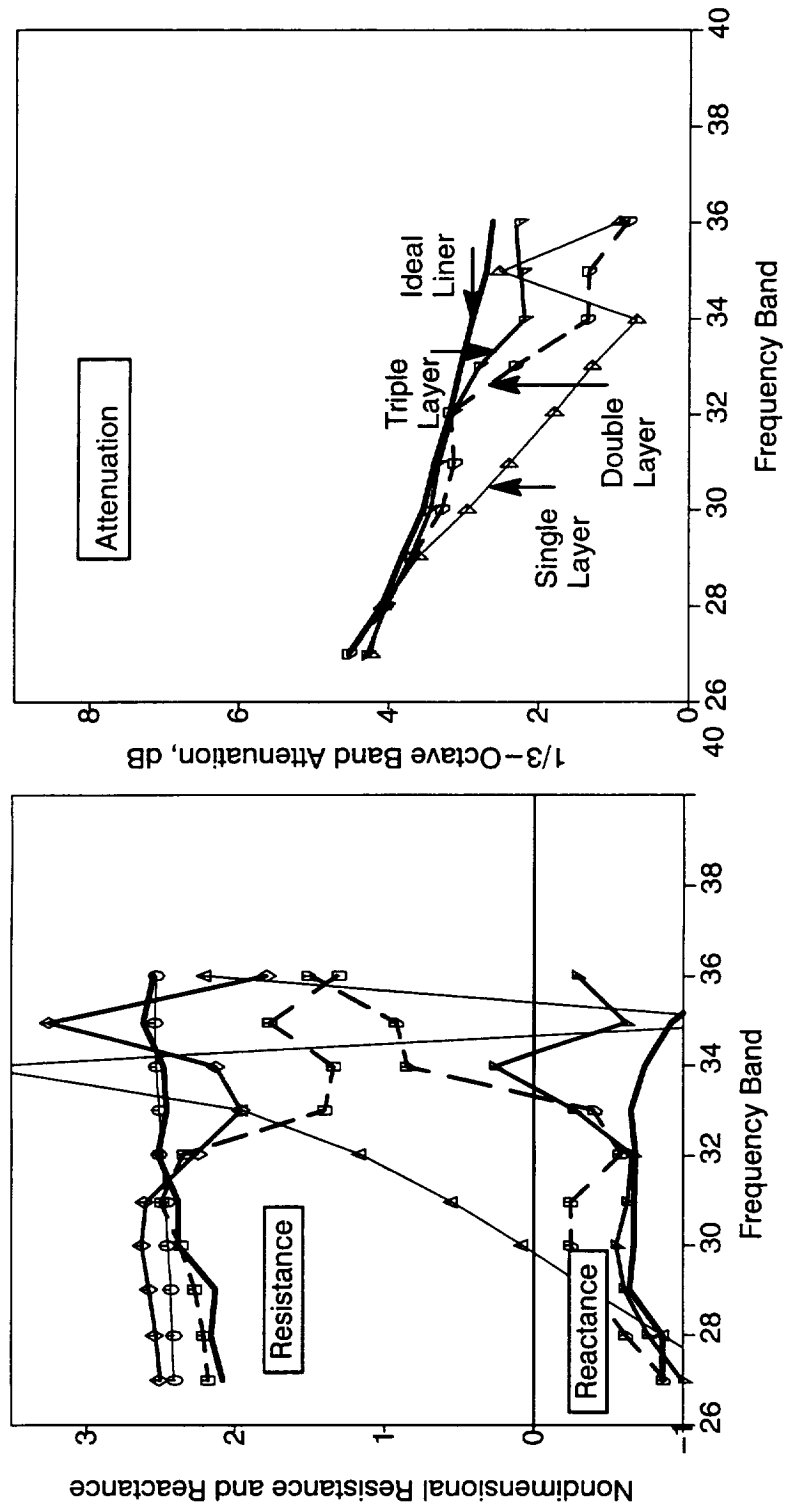


Figure 8: Inlet Impedance and Attenuation Spectra

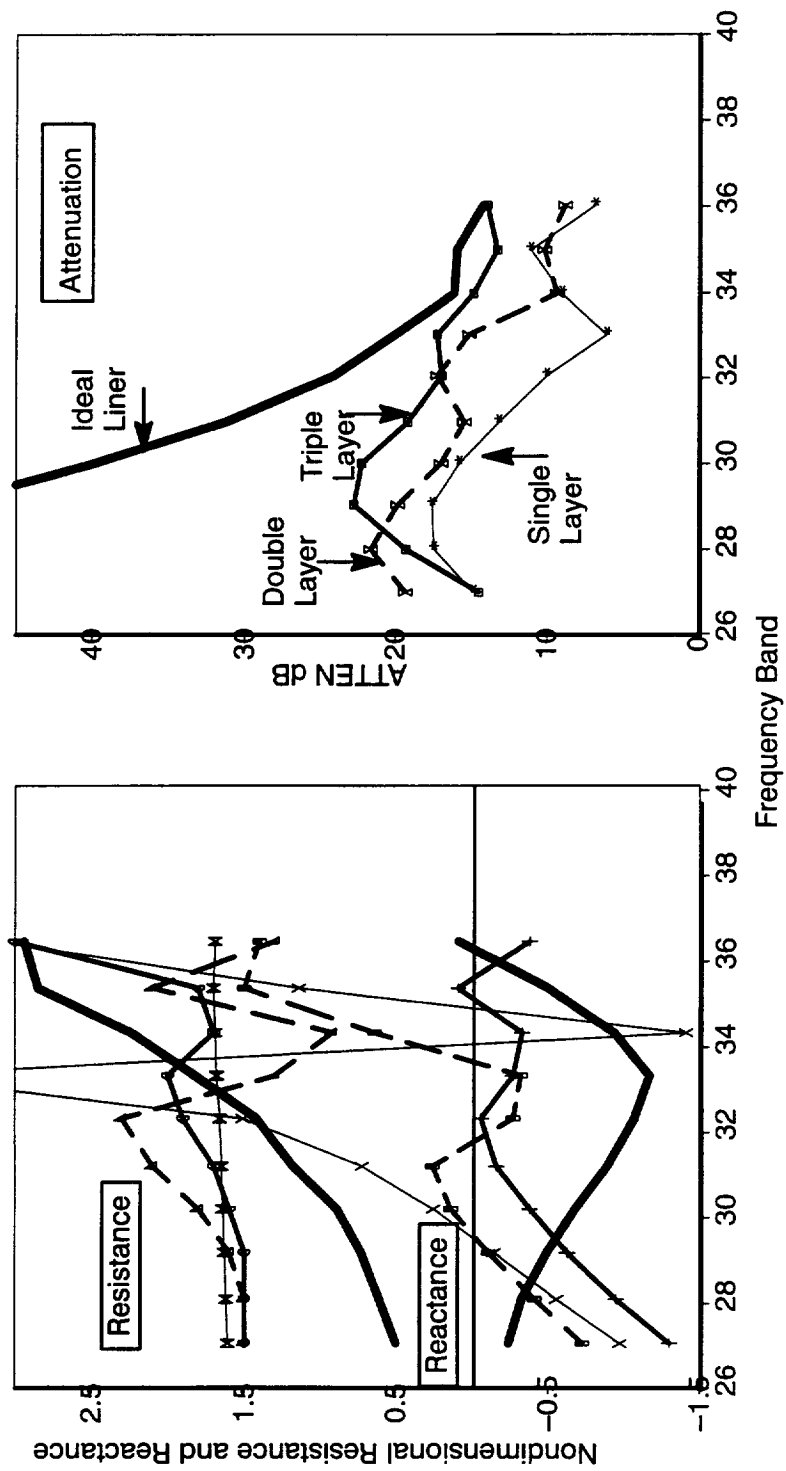


Figure 9: Fan Duct Impedance and Attenuation Spectra

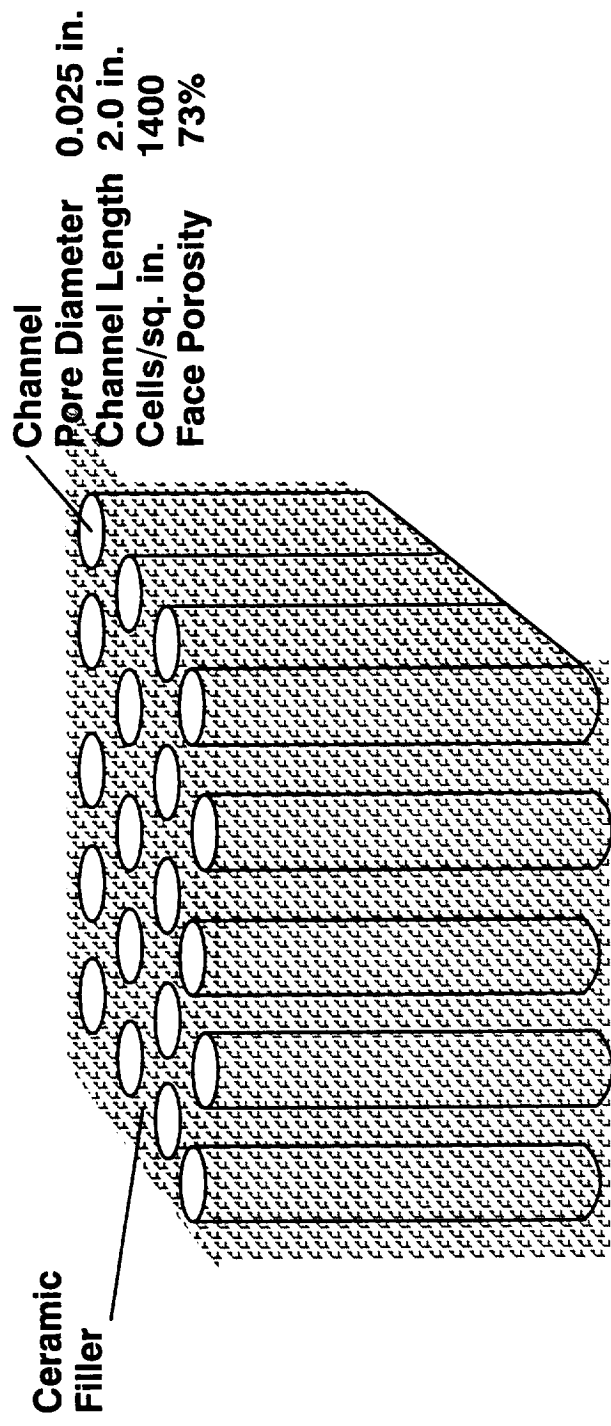


Figure 10: Schematic of NASA Langley Standard Grazing Flow Impedance Sample

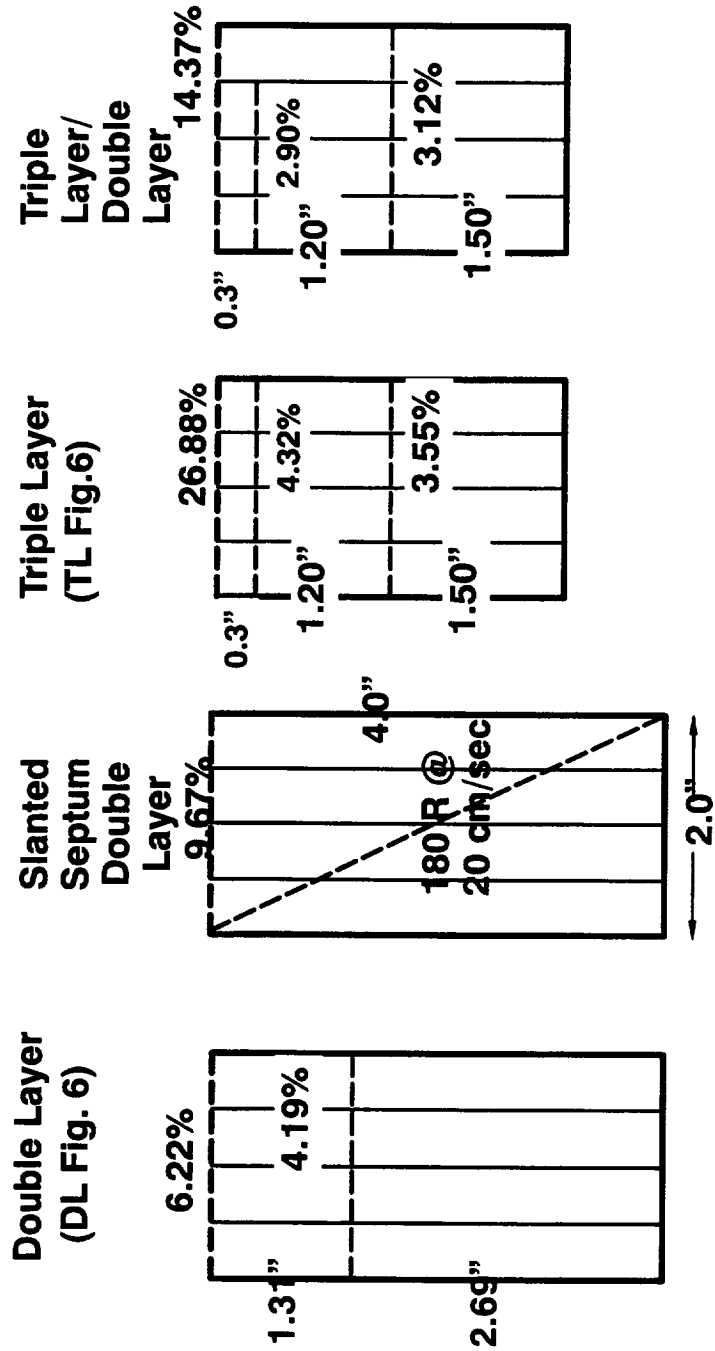


Figure 11: Passive Liner Test Designs

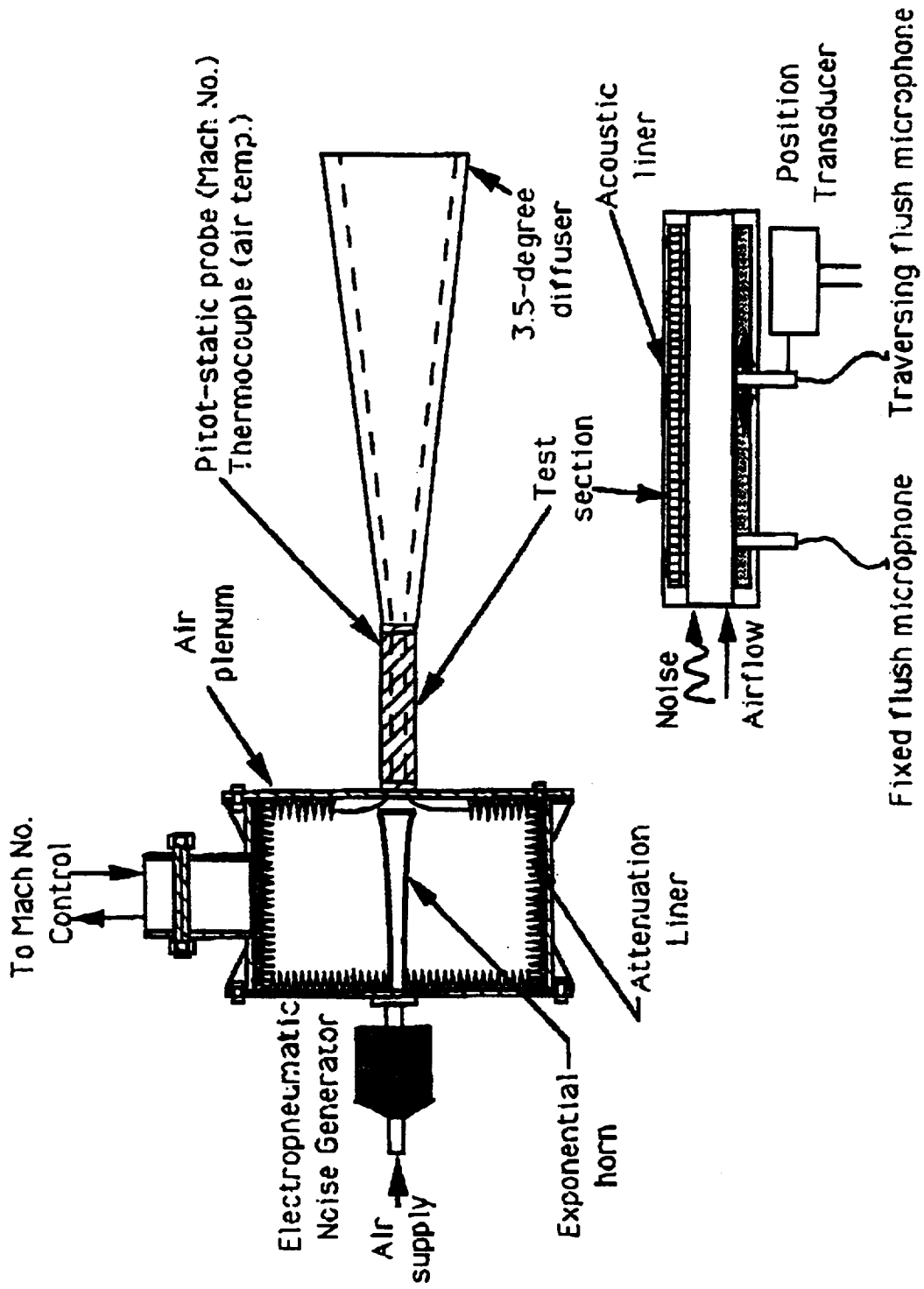
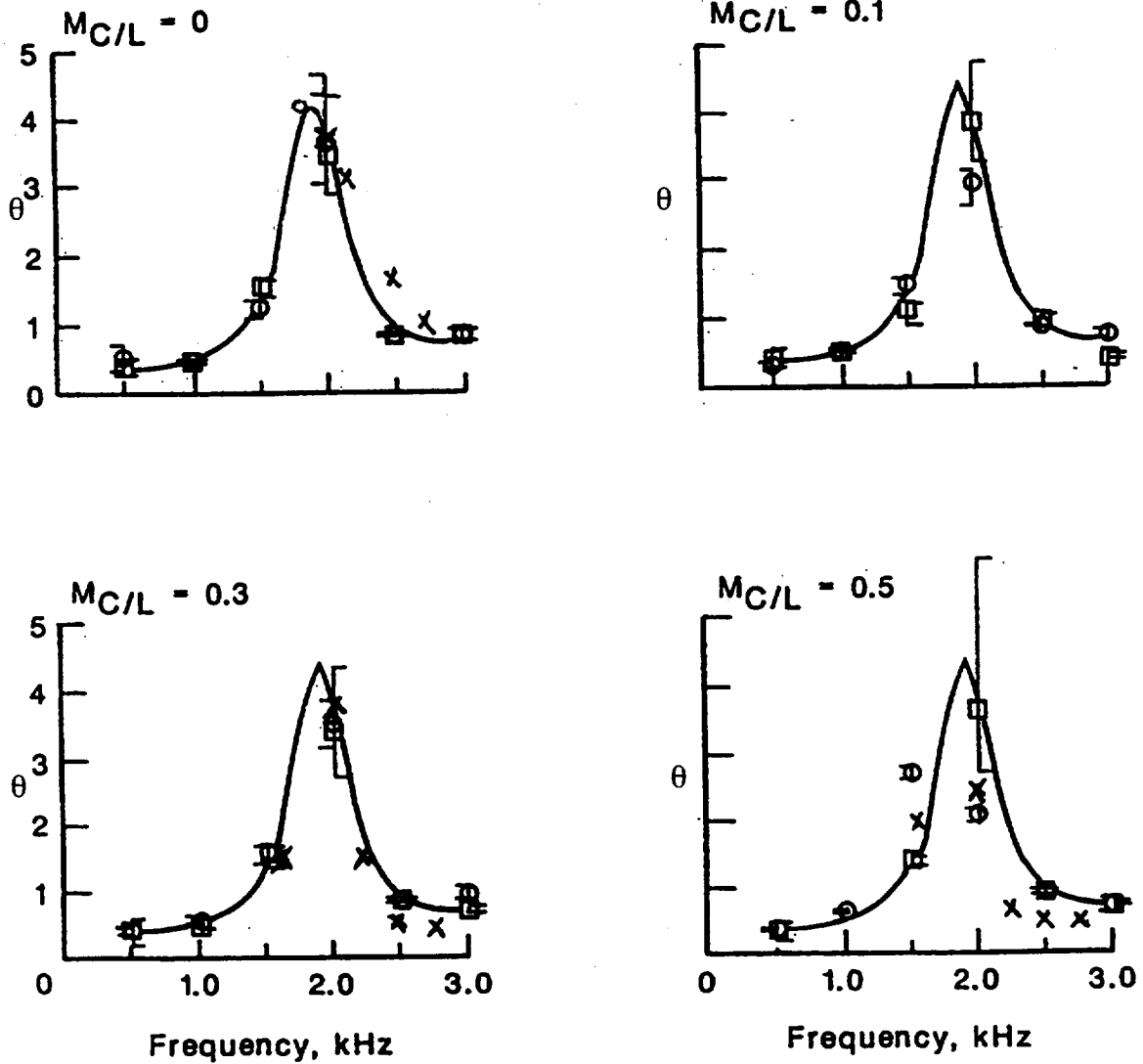
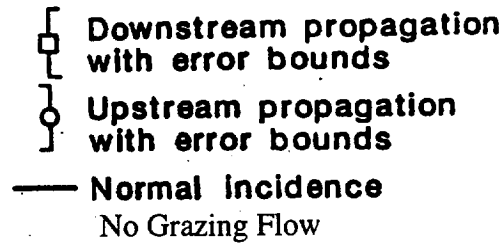


Figure 12: Schematic Of Wichita Grazing Flow Impedance Measurement System



(a) Normalized acoustic resistance, $\theta = R/\rho c$

Measured grazing-incidence impedance as inferred from two-dimensional shear-flow model.

Figure 13: Comparison Of NASA And Boeing Wichita Grazing Flow Resistance Test Data

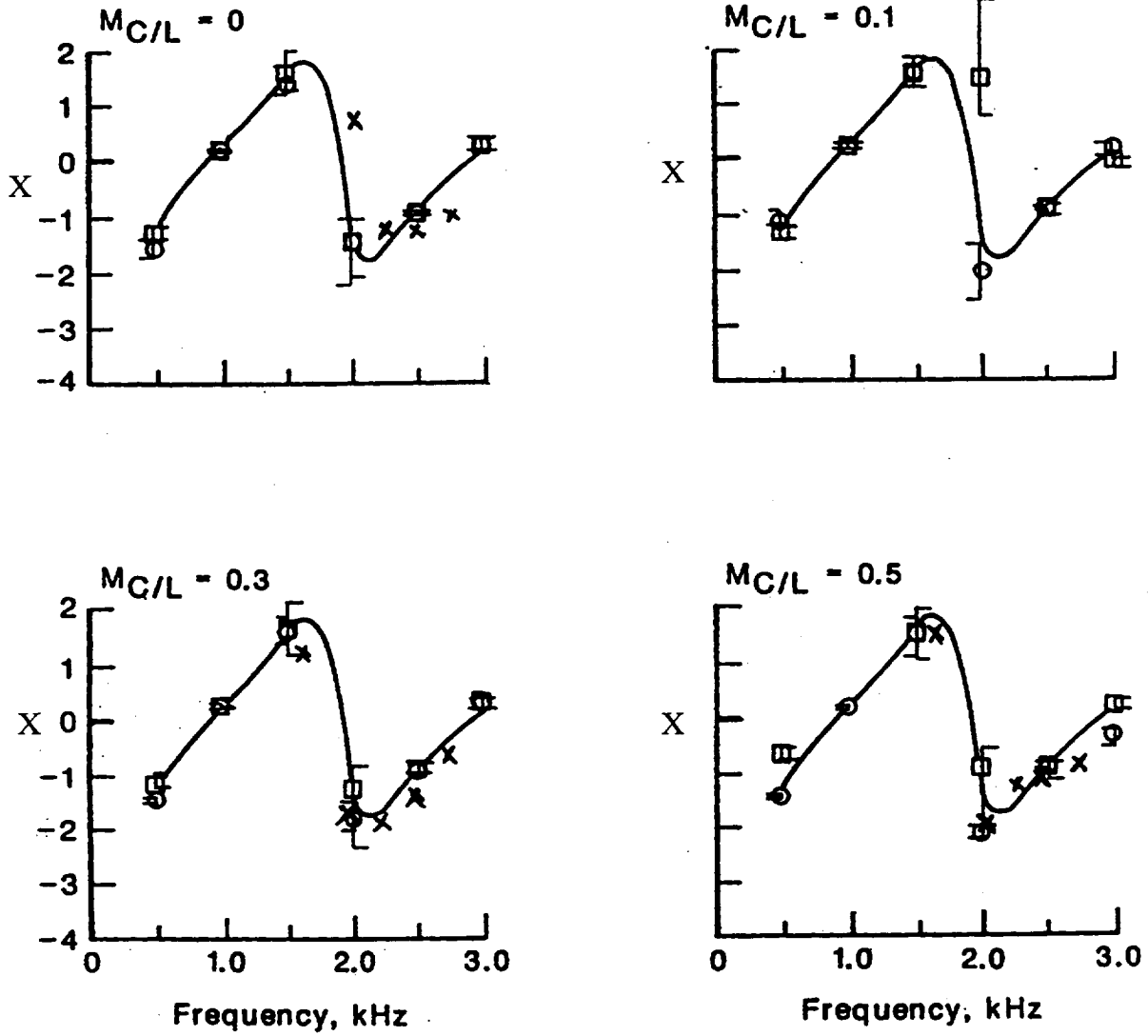
NASA Langley Data TP2679

X - Boeing Grazing Flow Impedance Data

□ Downstream propagation with error bounds

○ Upstream propagation with error bounds

— Normal Incidence



(b) Normalized acoustic reactance, $x = X/\rho c$

Figure 14: Comparison Of NASA And Boeing Wichita Grazing Flow Reactance Test Data

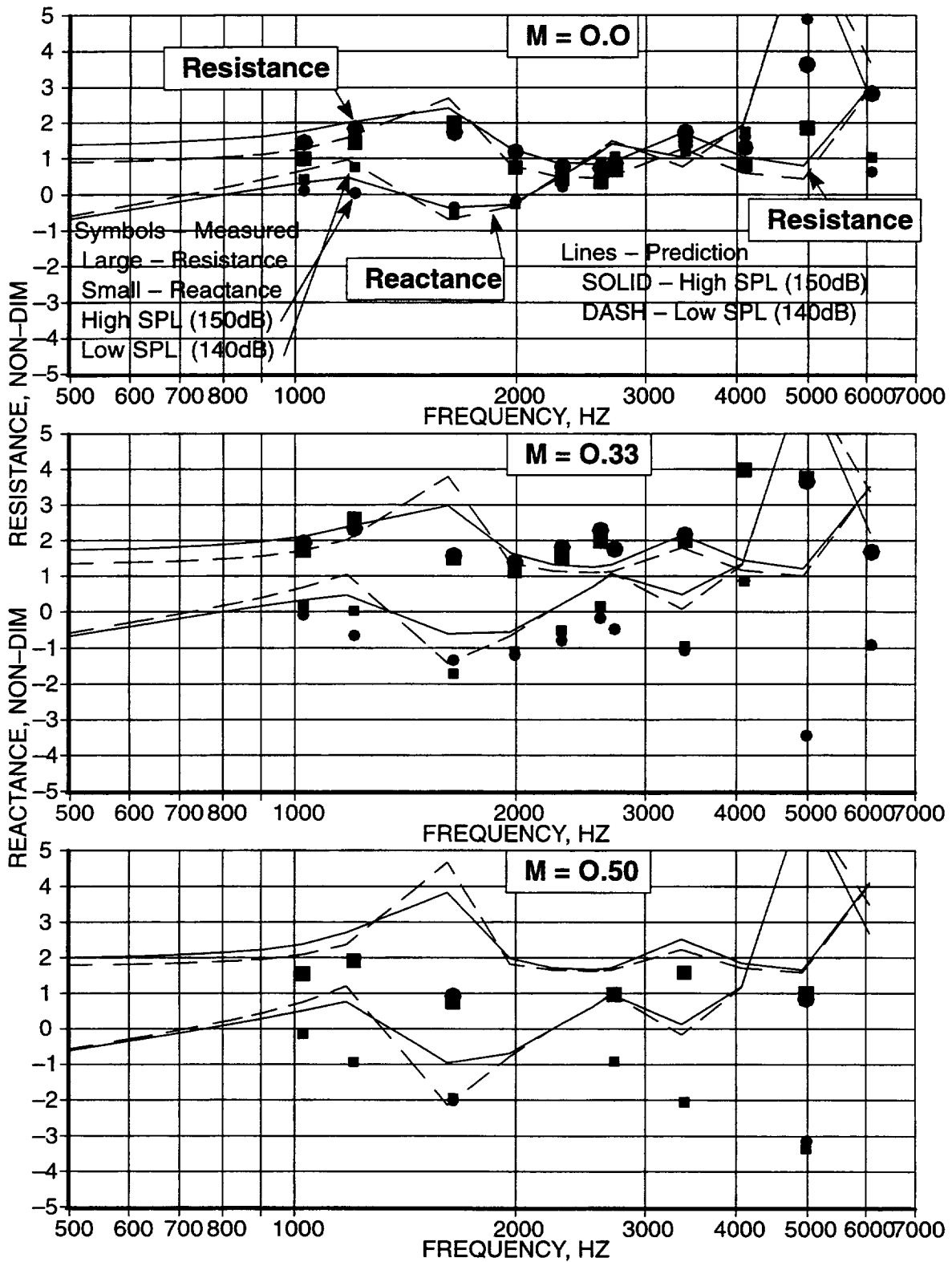


Figure 15: Measured And Predicted Impedance Of The Double Layer Liner Shown In Figure 11.

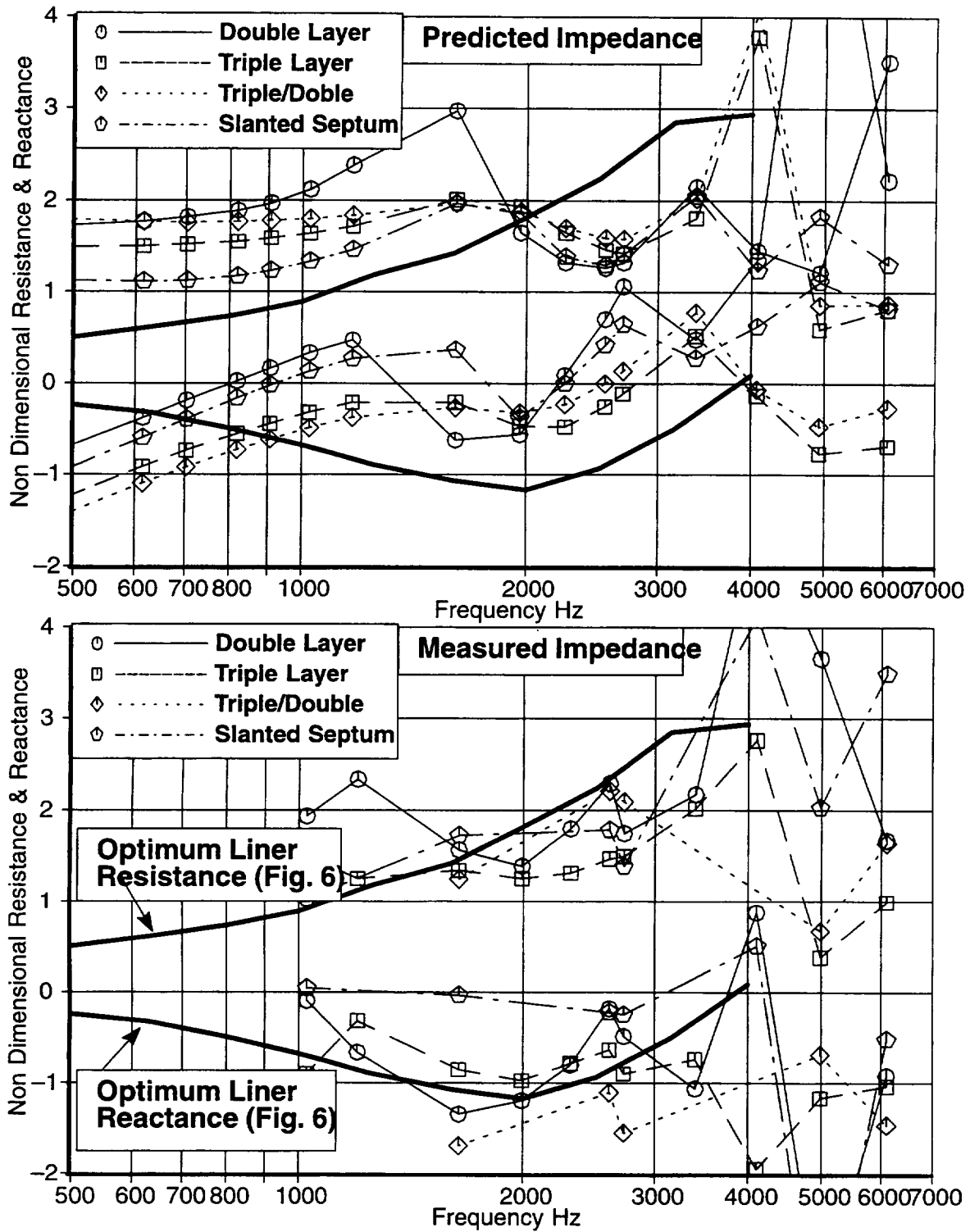


Figure 16: Measured And Predicted Impedances Of Liners Shown In Figure 11 Compared To Target Impedance ($M = 0.33$, Mom Thickness = .08 cm, OASPL = 150 dB)

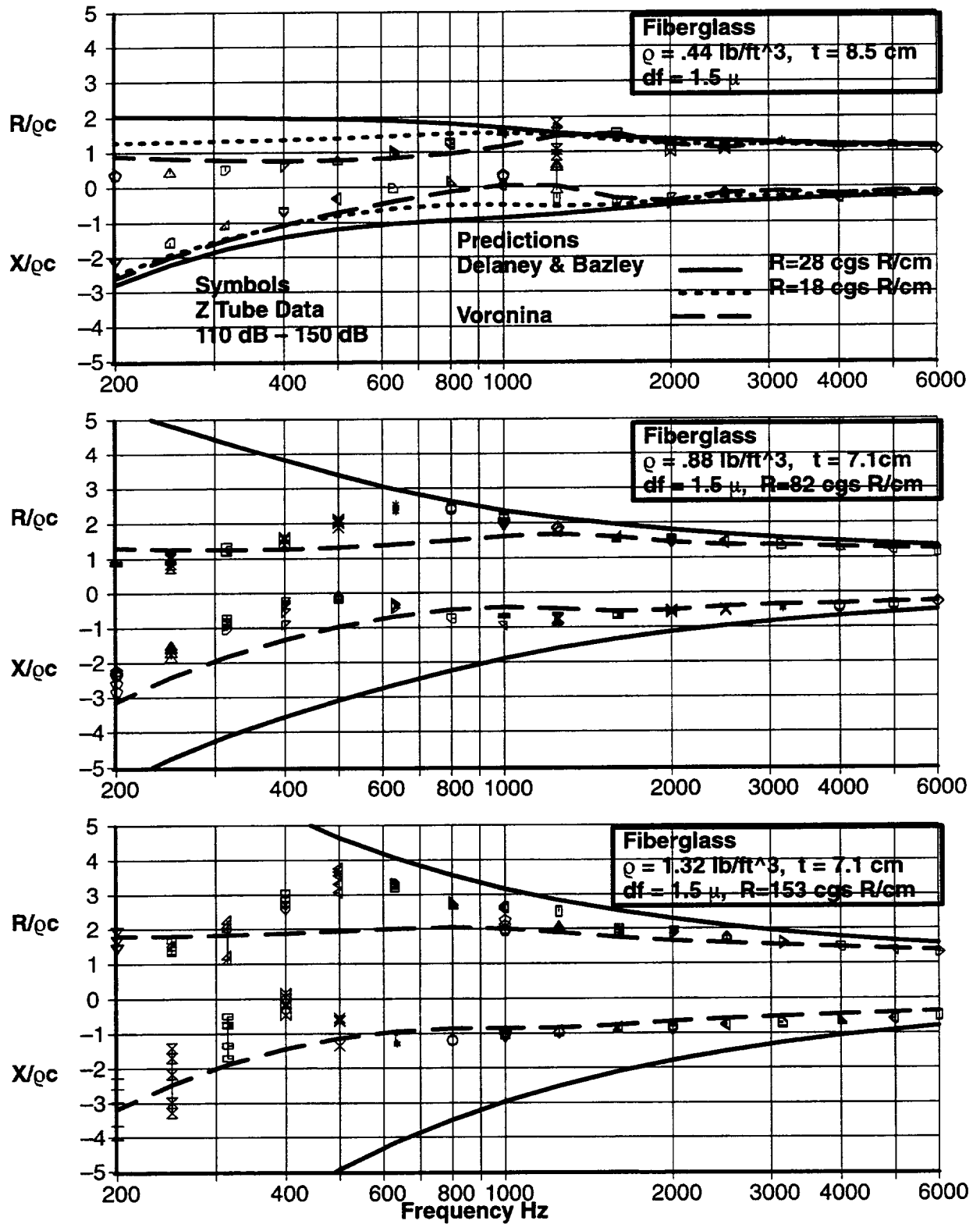


Figure 17: Measured vs. Predicted Surface Impedance – Fiberglass Bulk Absorber

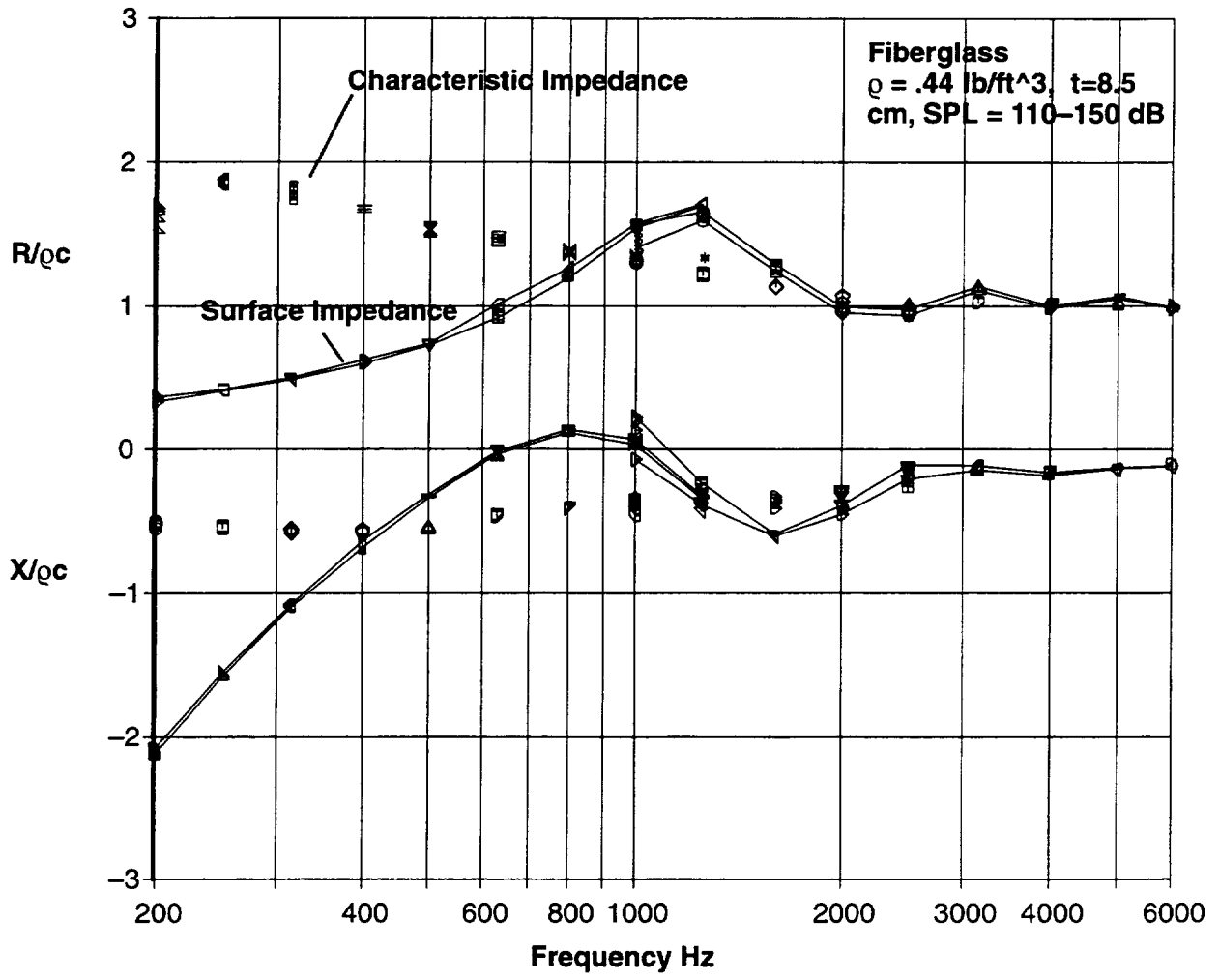


Figure 18: Measured Surface and Characteristic Impedance

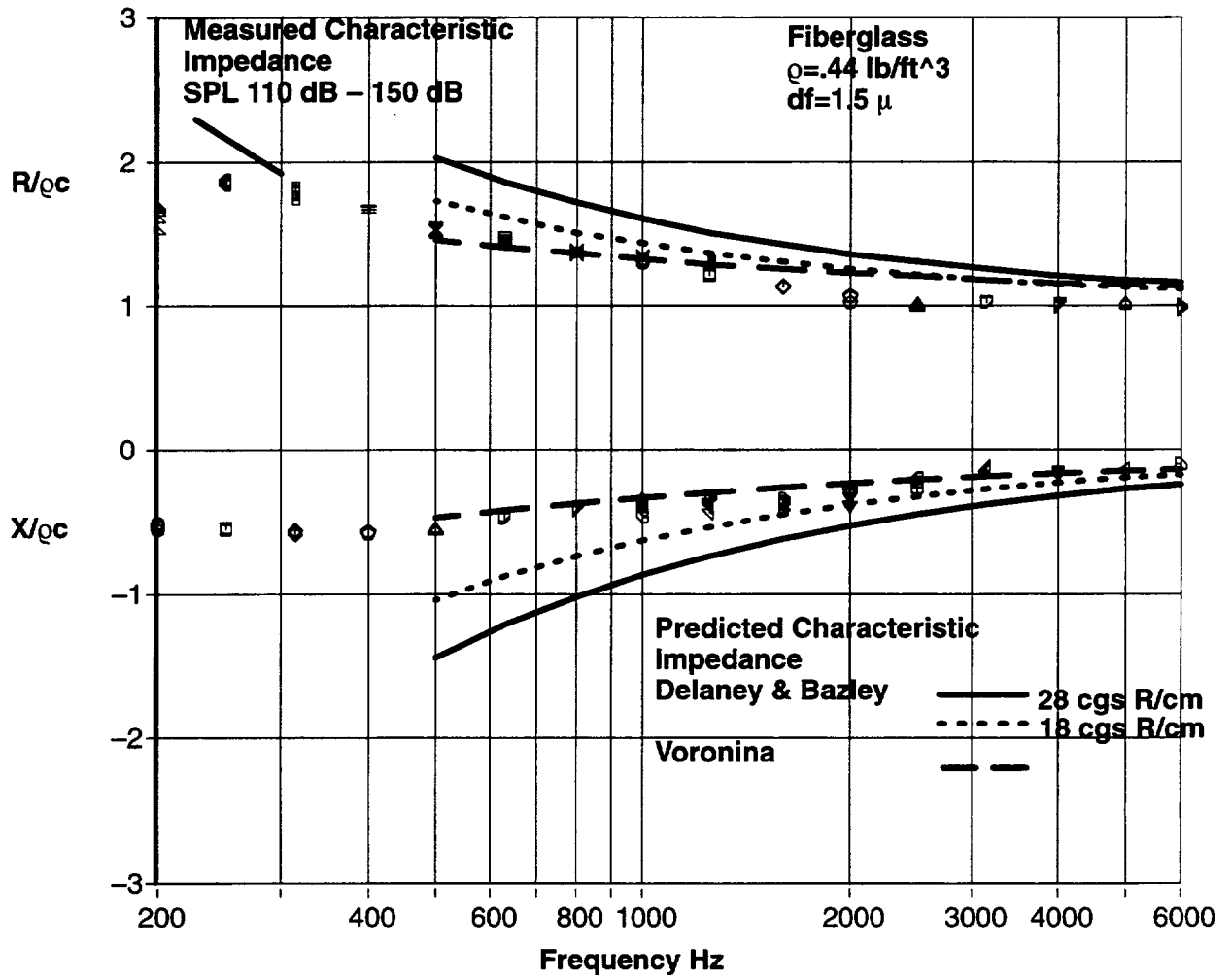


Figure 19: Measured vs. Predicted Characteristic Impedance

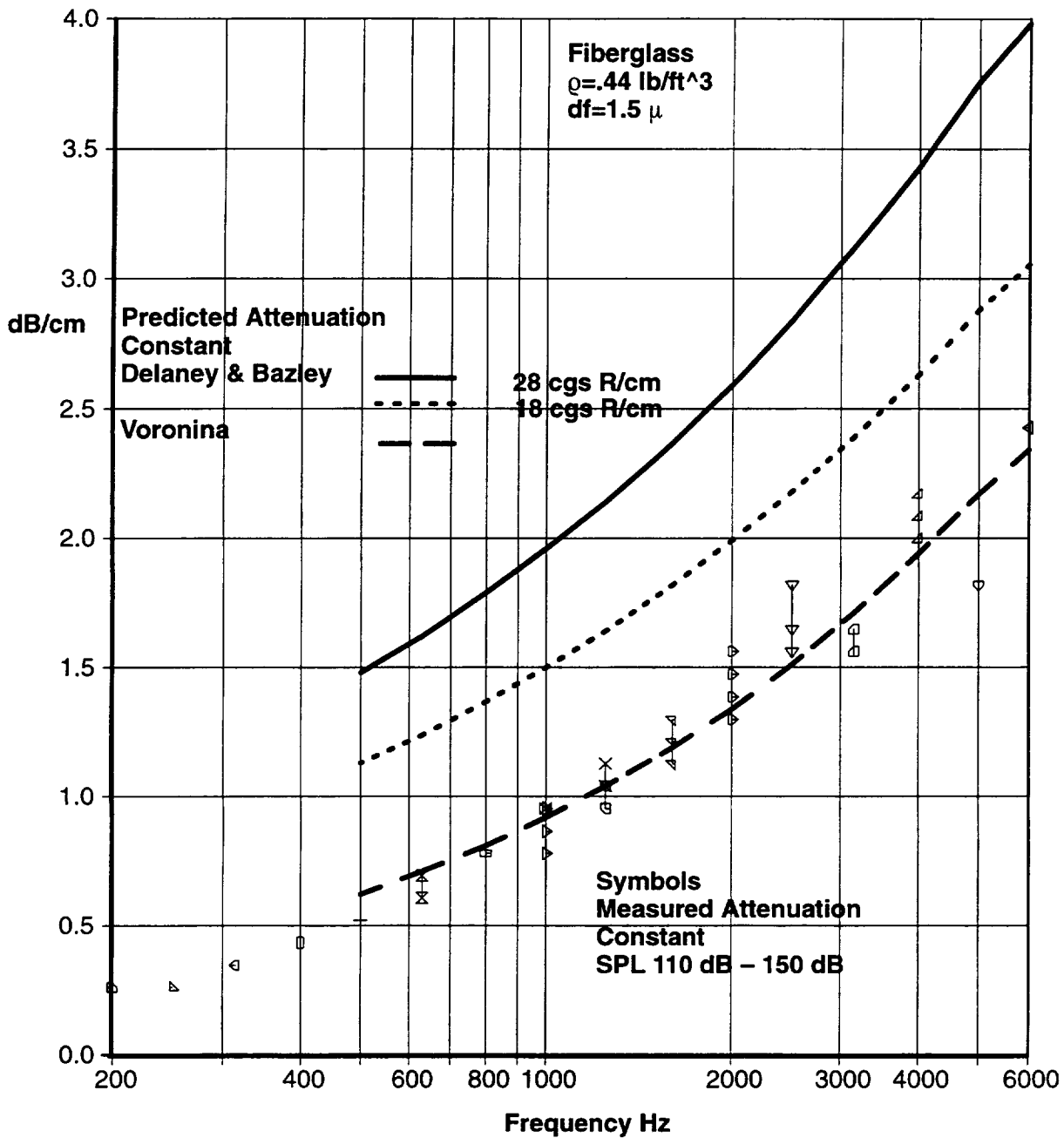


Figure 20: Measured vs. Predicted Attenuation Constant

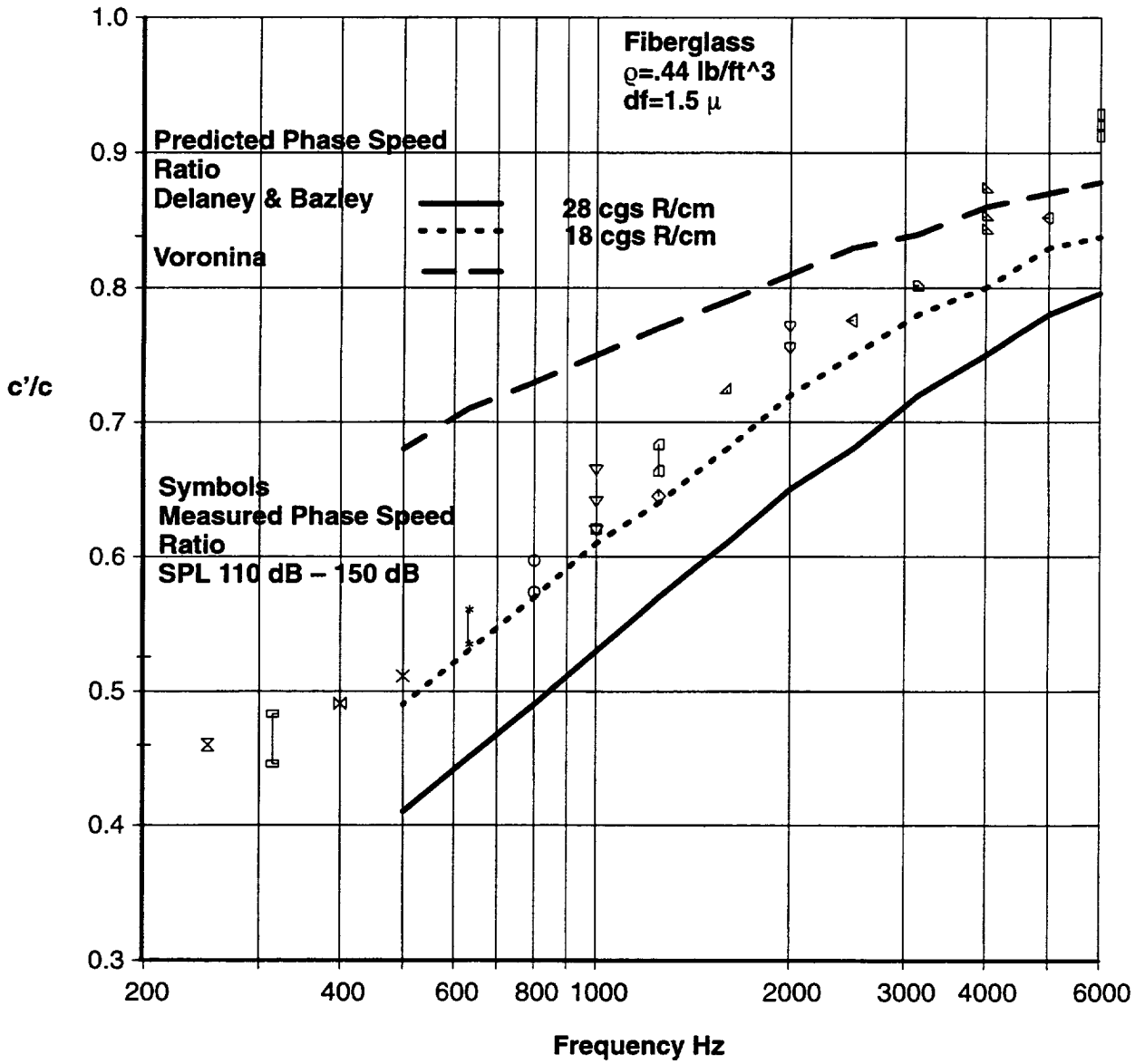
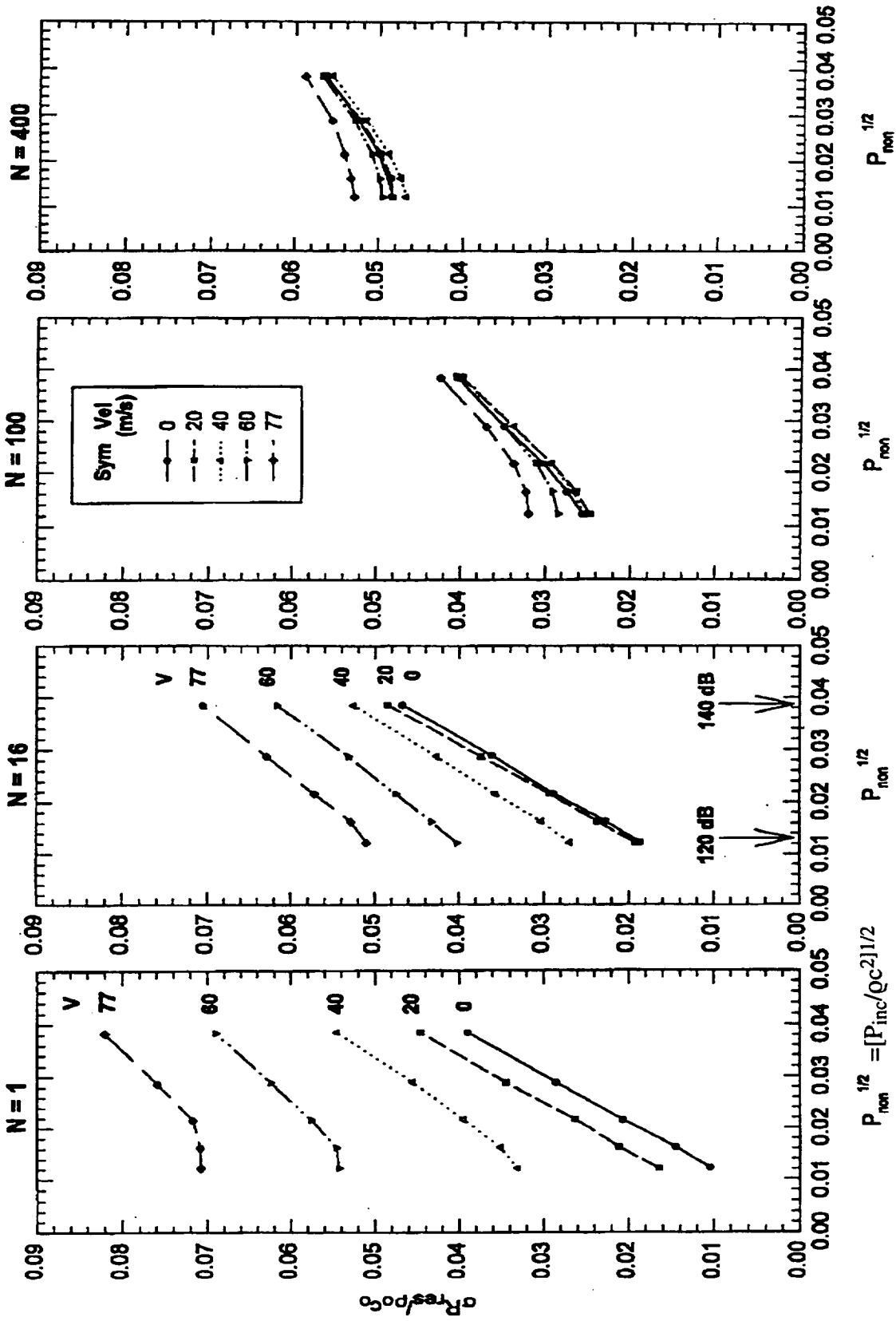


Figure 21: Measured vs. Predicted Phase Speed Ratio



$$P_{non}^{1/2} = [P_{inc}/(\rho c^2)]^{1/2}$$

Figure 22: Effect Of Orifice Number, Grazing Flow Speed and SPL on Resonator Tuned Resistance

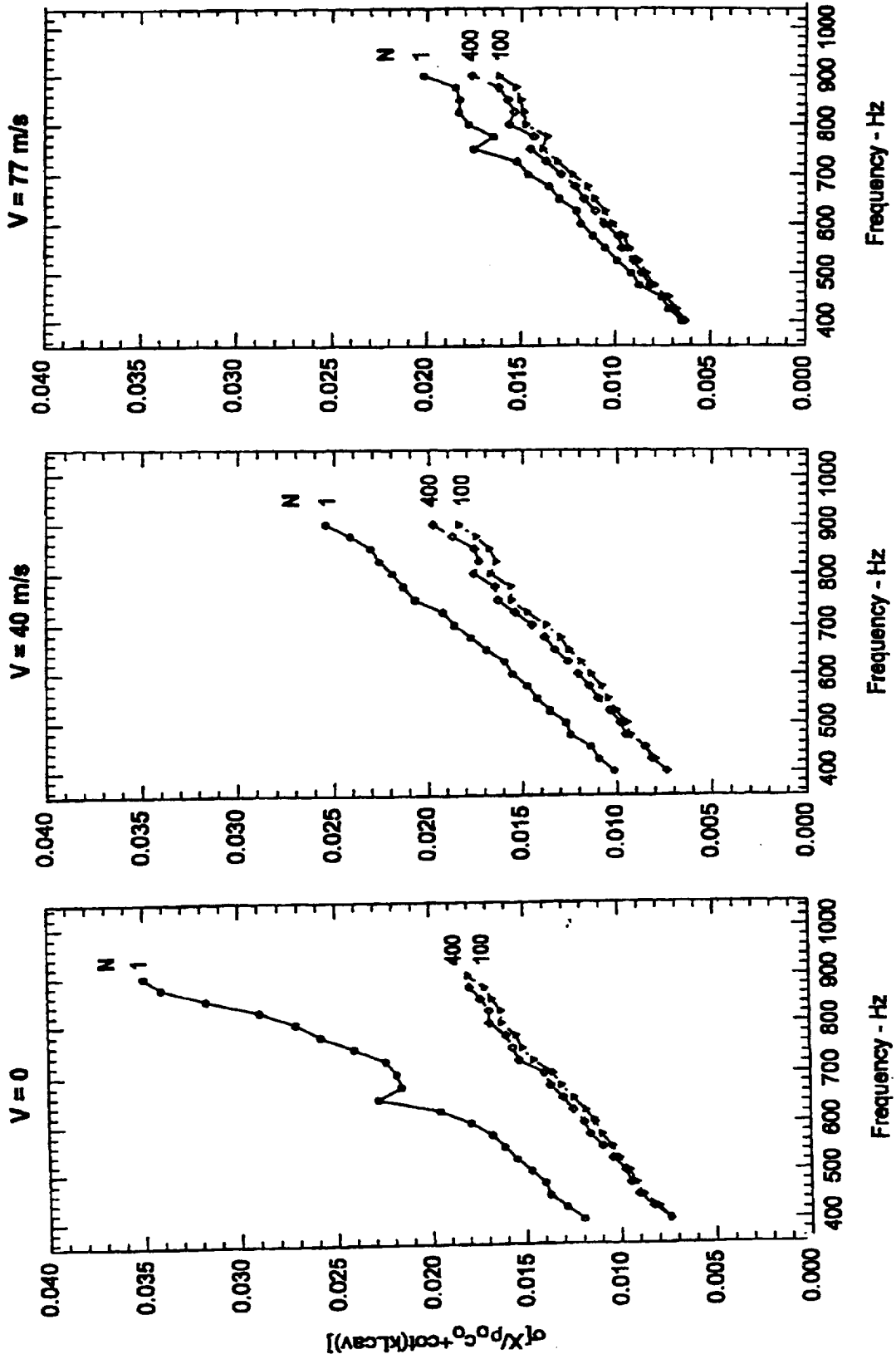


Figure 23: Effect Of Orifice Number and Grazing Flow Speed on Resonator Face-Sheet Mass Reactance: SPL = 135 dB

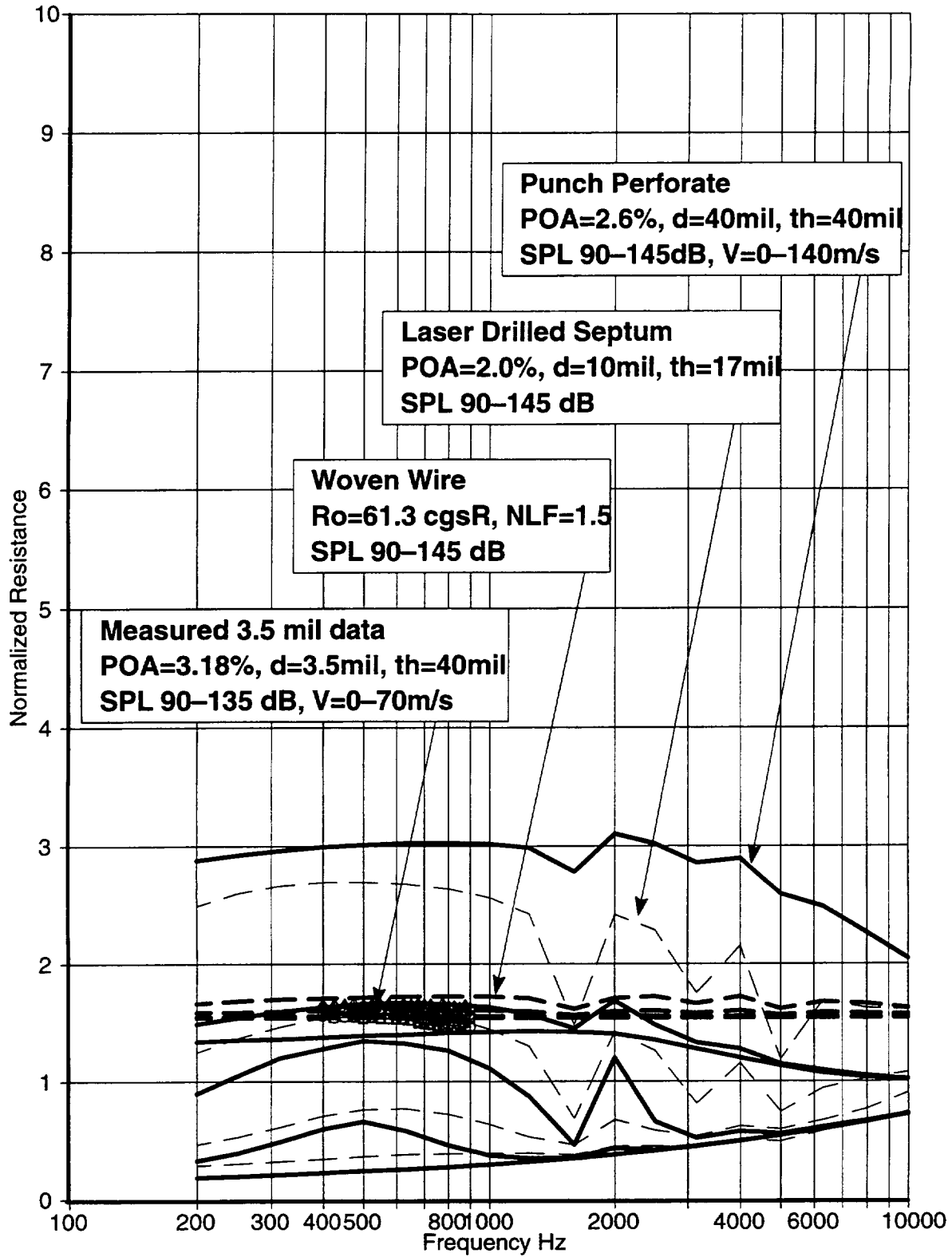


Figure 24: Comparison Of Effect Of Grazing Flow And SPL Changes On Acoustic Resistance Of Currently Used Perforates With Micro-Perforate

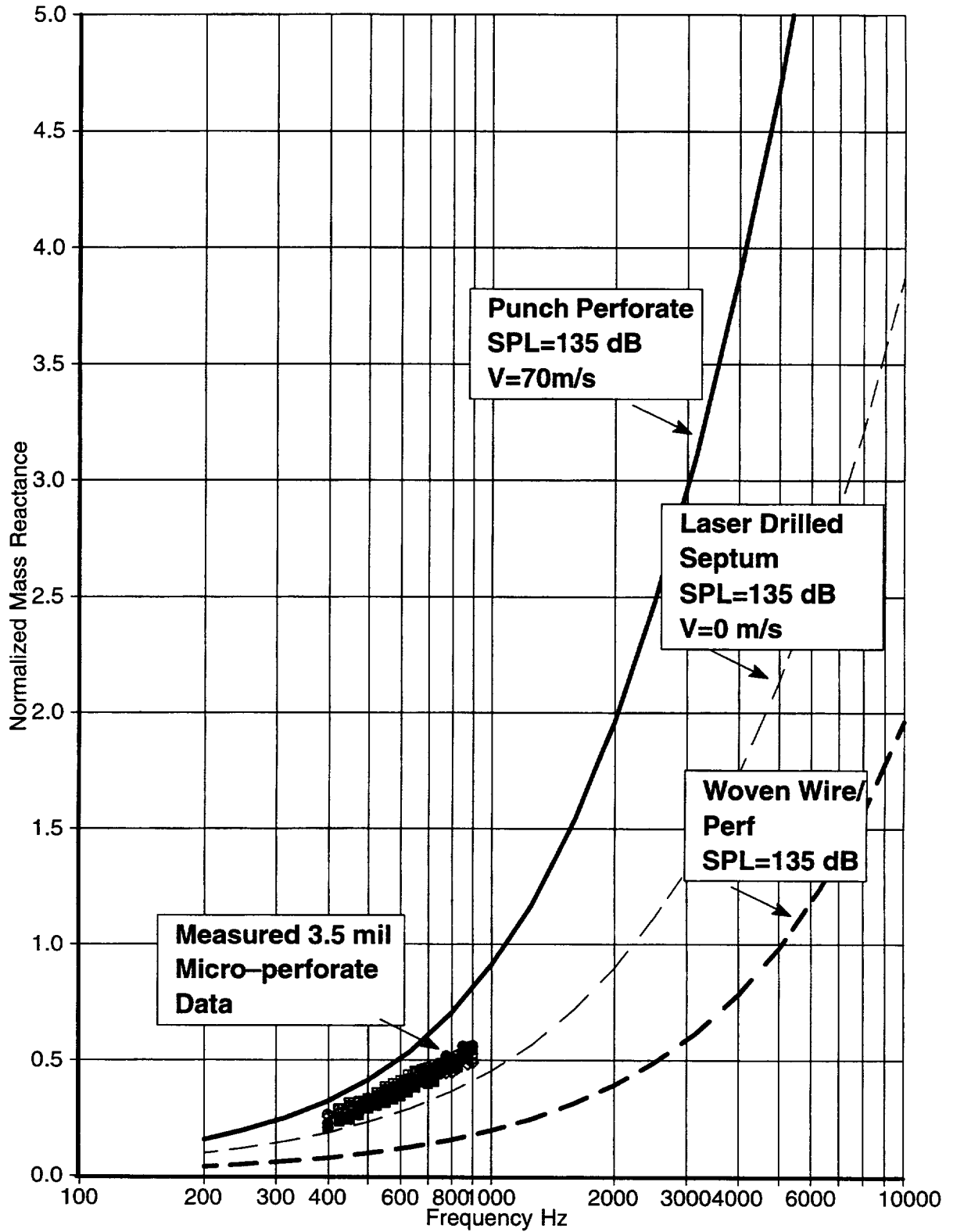
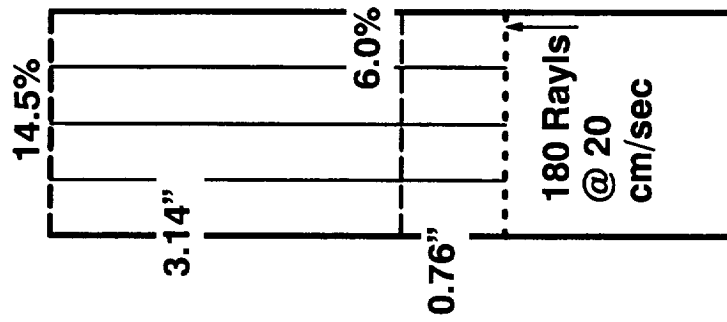


Figure 25: Comparison Of Acoustic Mass Reactance For Currently Used Perforates With Micro-Perforate

Bias Flow Liners



Elevated Core Temperature Double Layer

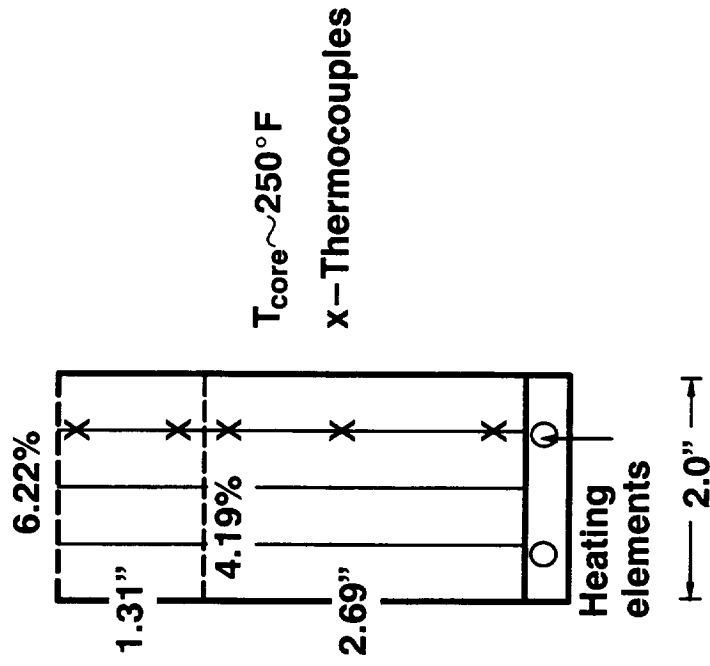


Figure 26: Adaptive Liner Test Designs

Predictions include the effect of the cavity behind the 180 Rayl septum

Approach Condition

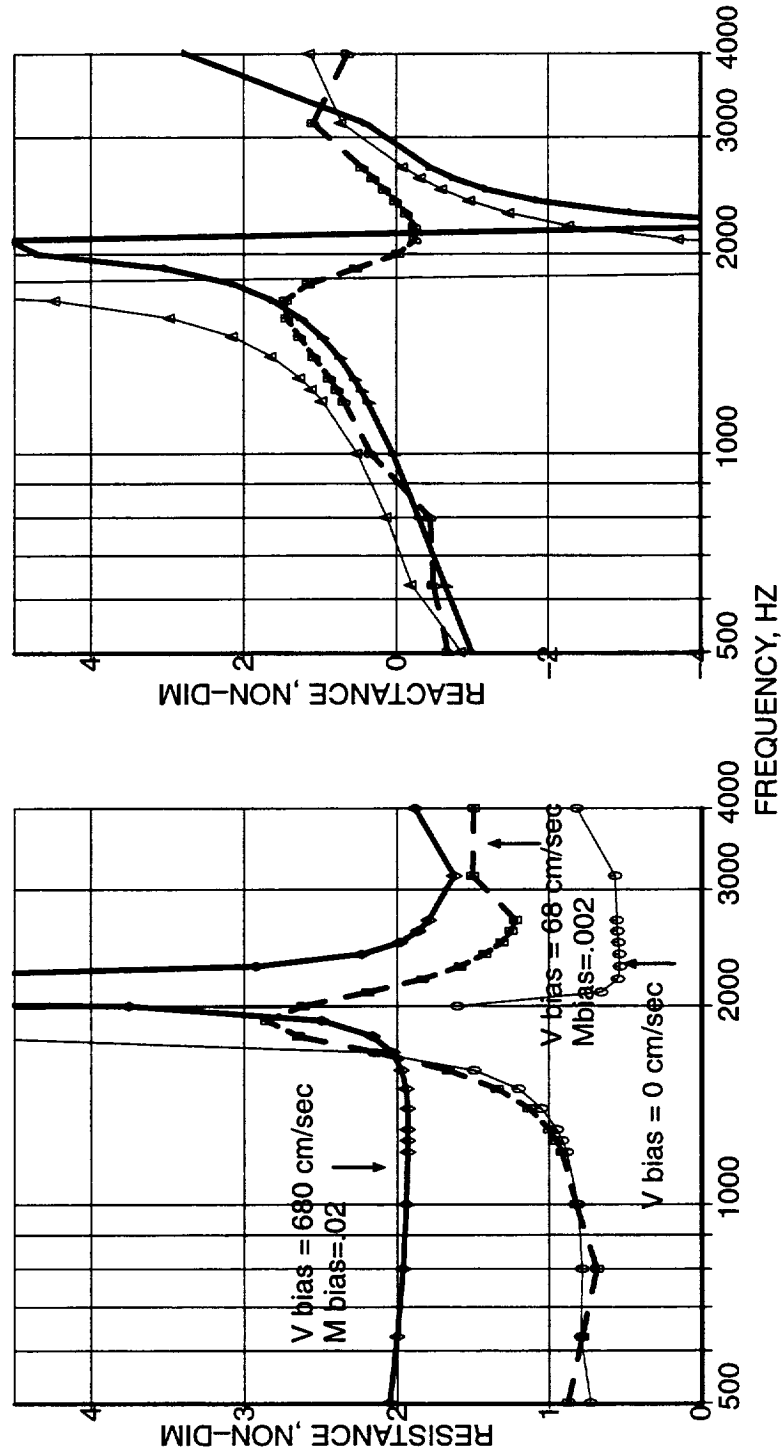


Figure 27: Predicted Bias Flow Impedance Changes For Test Liner

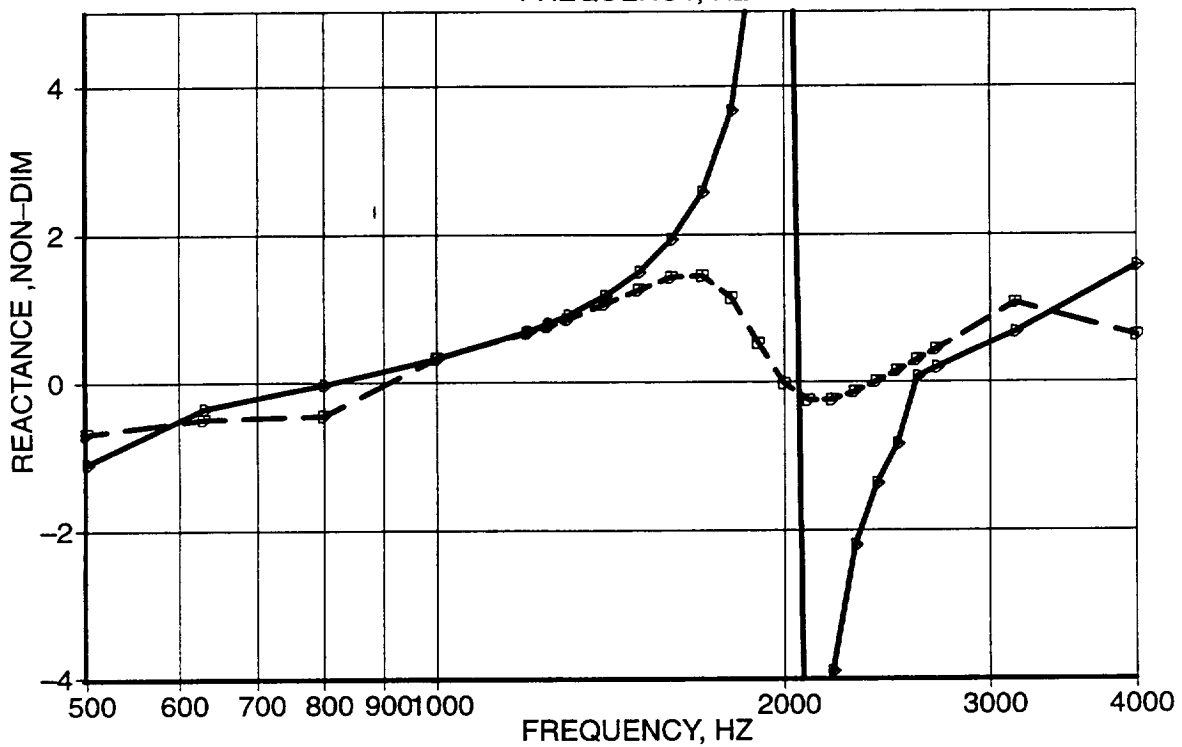
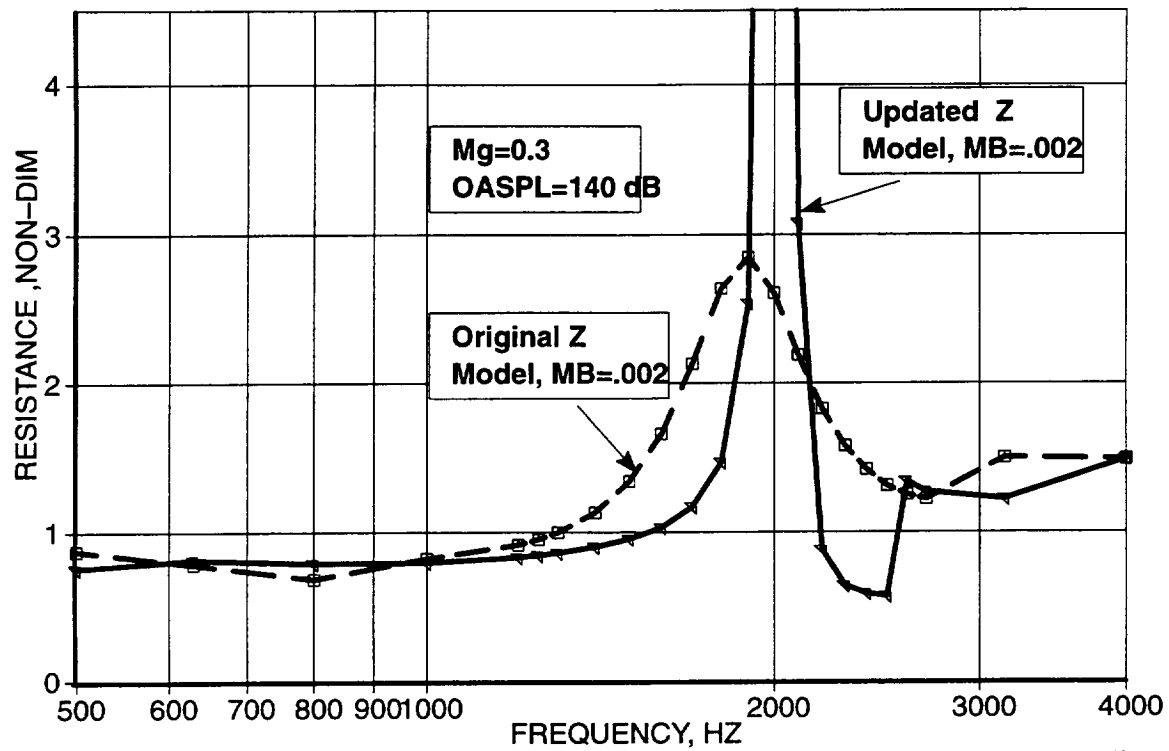


Figure 28: Comparison Of Predicted Impedance Spectra For The Bias Flow Test Liner With The Original And Updated Bias Flow Impedance Models.

Approach Optimized Liner At Takeoff Engine Condition

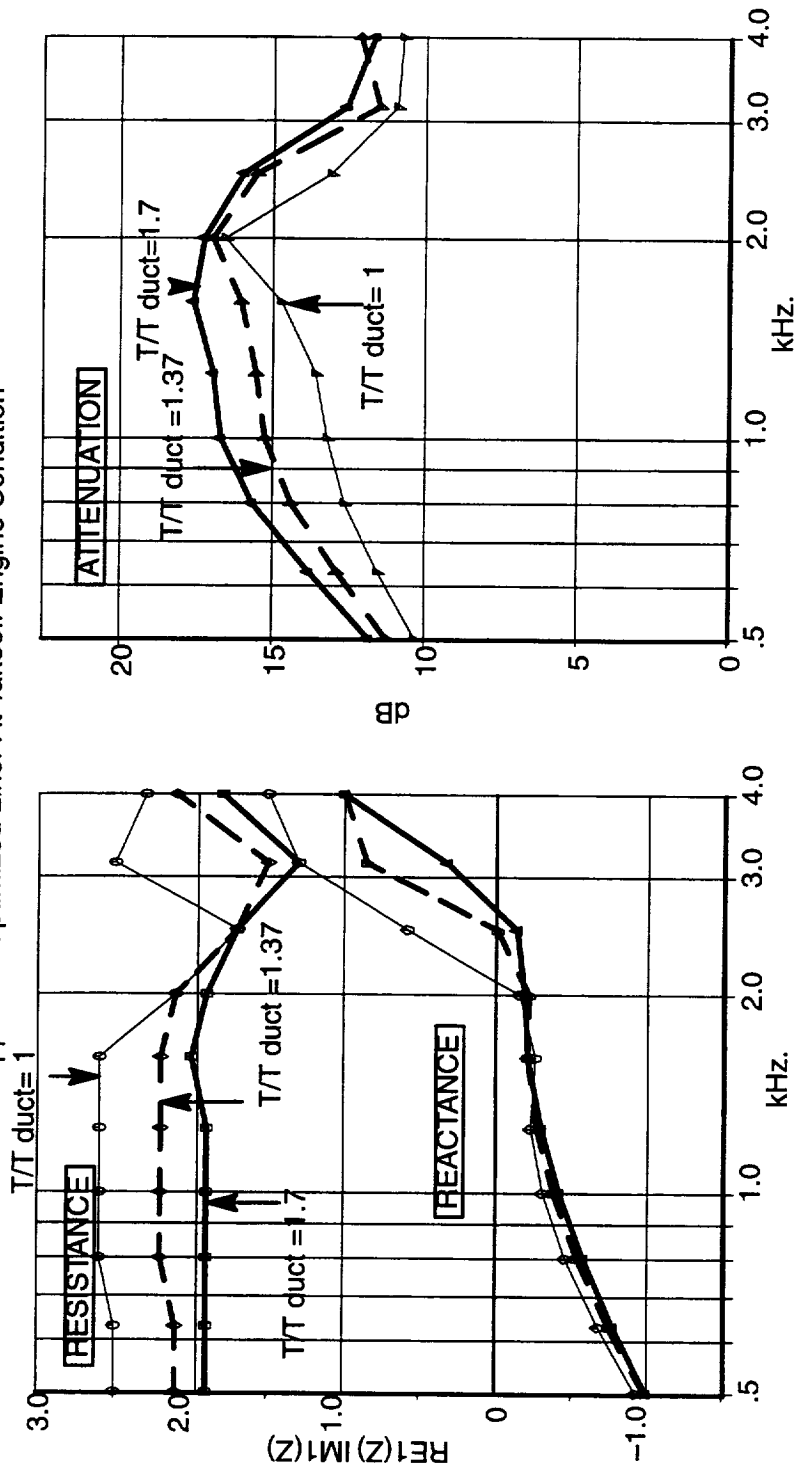


Figure 29: High Temperature Liner Predicted Impedance and Attenuation

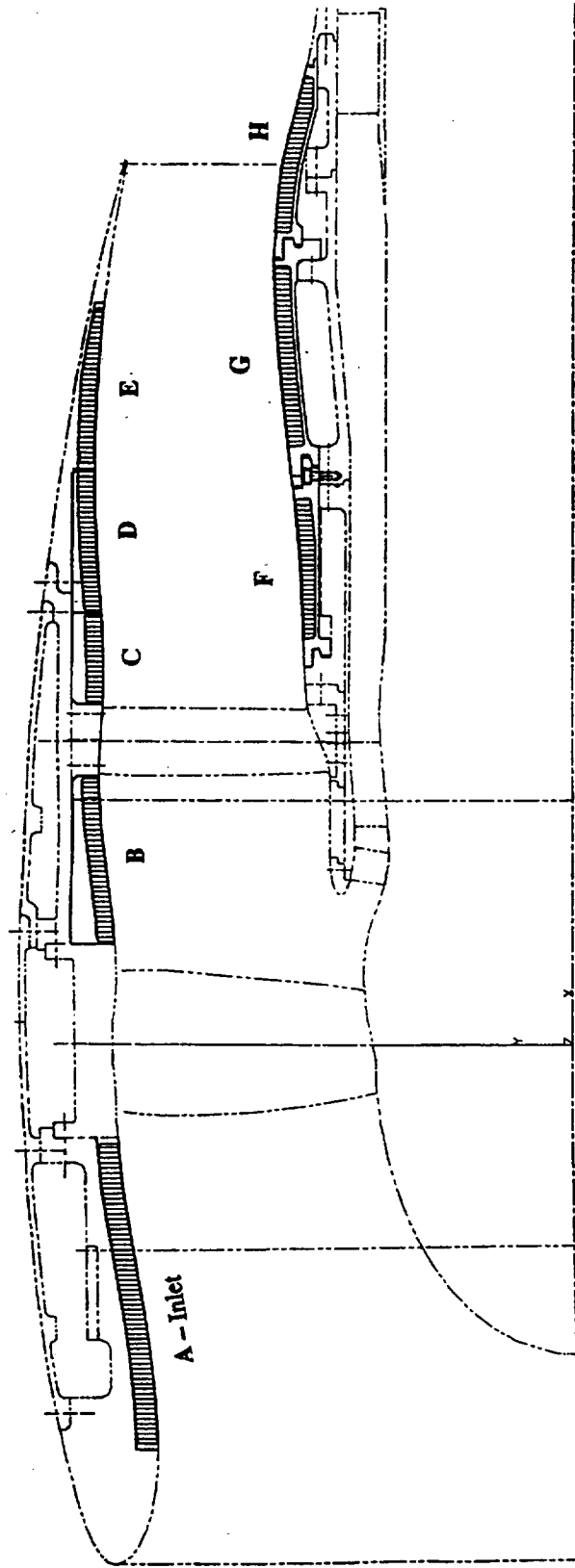


Figure 30: Cartoon of Lining Segments
Supplied by Pratt and Whitney

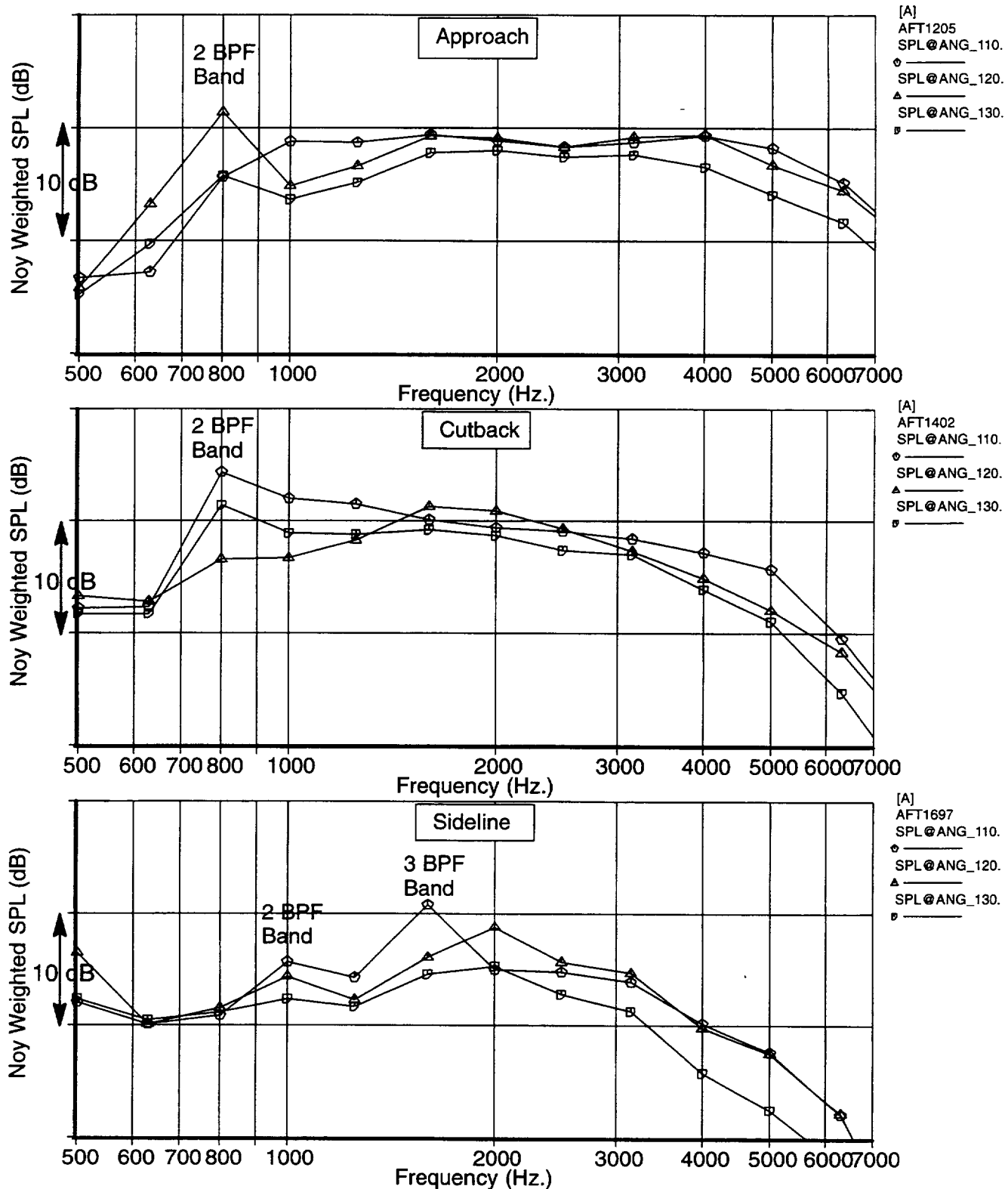


Figure 31: Comparison of the Design ADP Hardwalled Data Prediction SPL vs Frequency for 110, 120, and 130 Degrees (Approach, cutback, and sideline conditions)

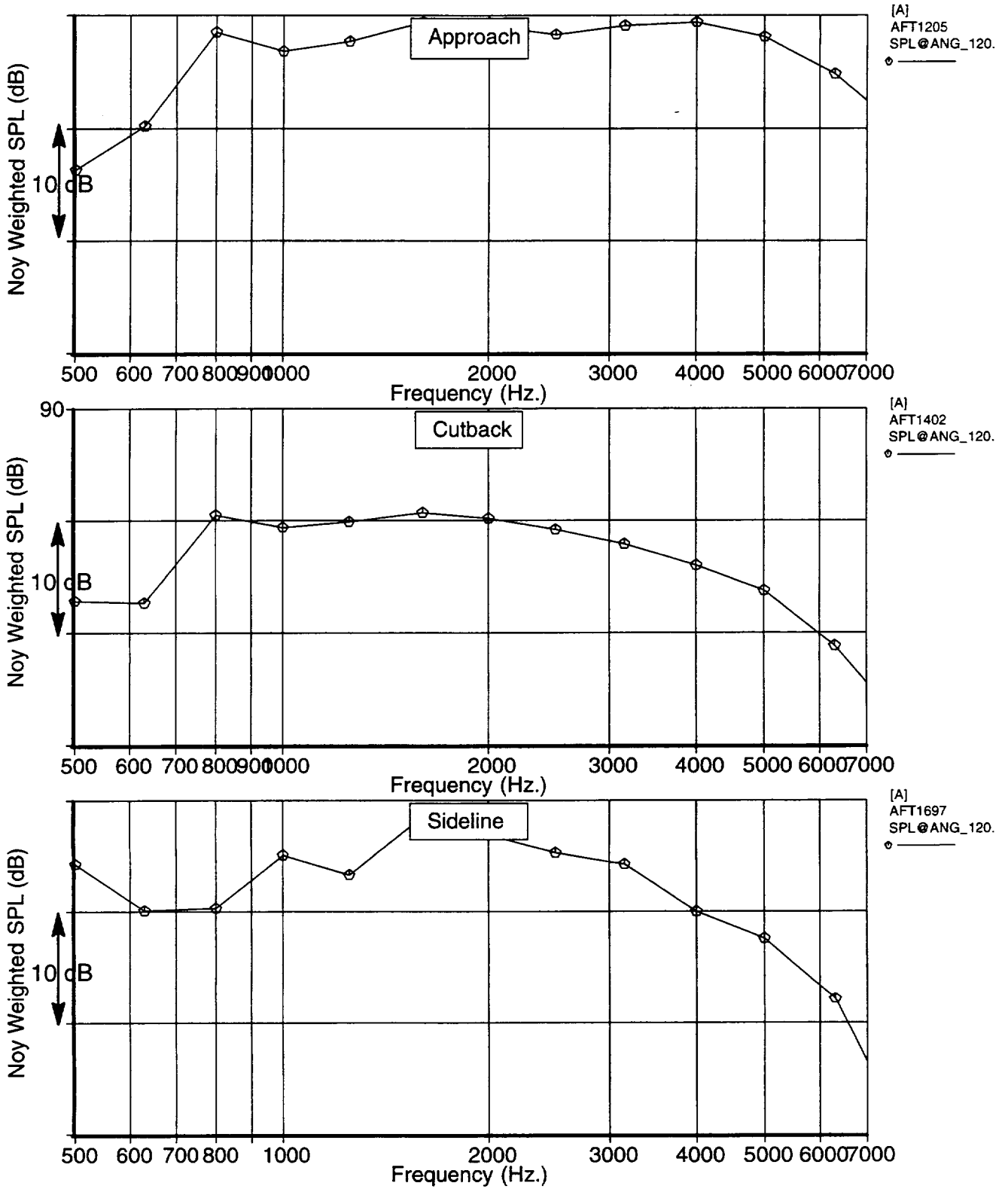


Figure 32: Hardwall Target Spectra Based On ADP Demo Data
 SPL vs Frequency for the average of 110 and 120 Degrees
 (Approach, cutback, and sideline conditions)

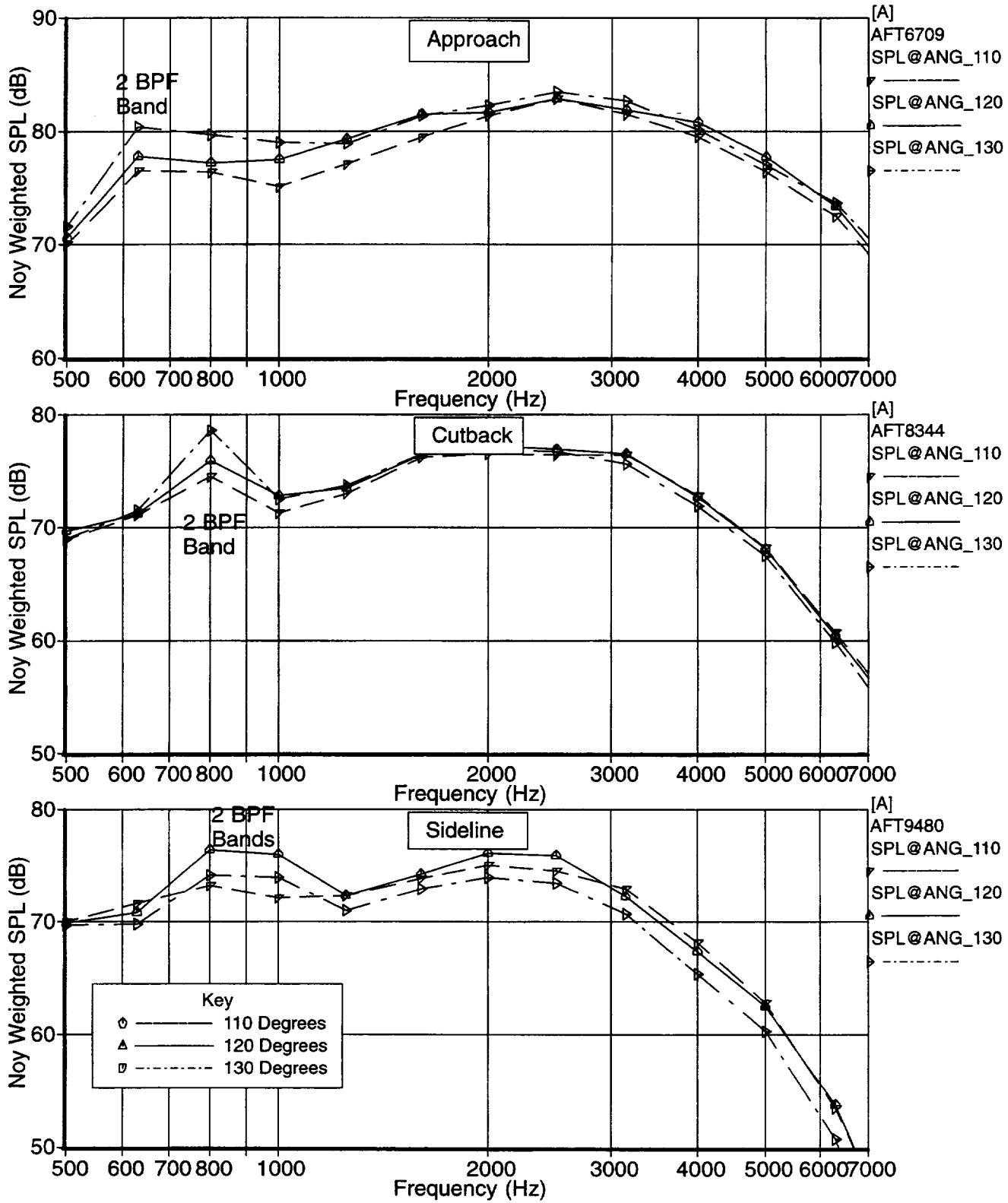


Figure 33: Comparison of Hardwalled 22" ADP Data SPL vs Frequency for 110, 120, and 130 Degrees (Approach, cutback, and sideline conditions)

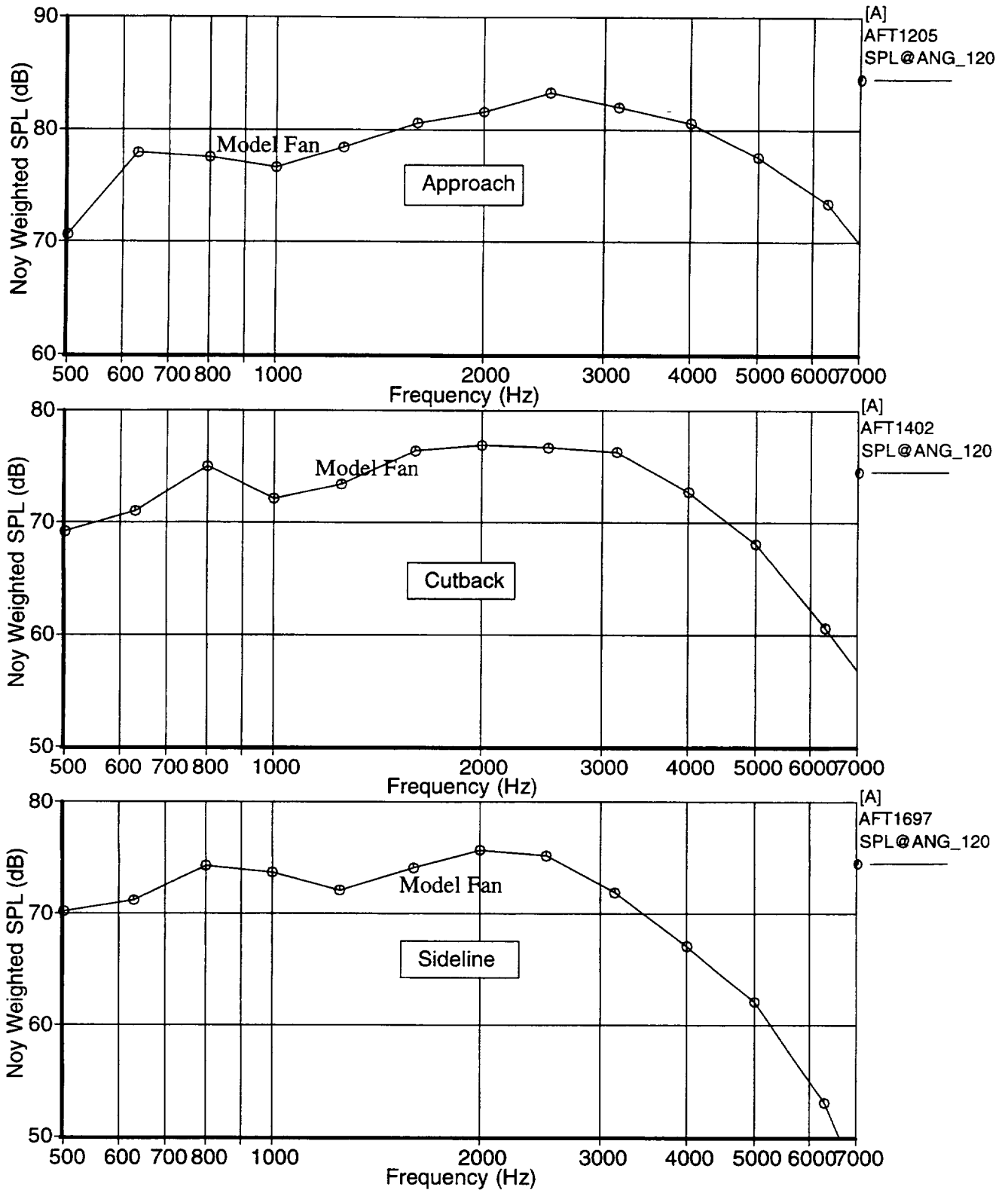


Figure 34: Hardwall Target Spectra Based On ADP Model Fan Data
 SPL vs Frequency for the average of 110 and 120 Degrees
 (Approach, cutback, and sideline conditions)

Fan Duct Model For Attenuation Calculations

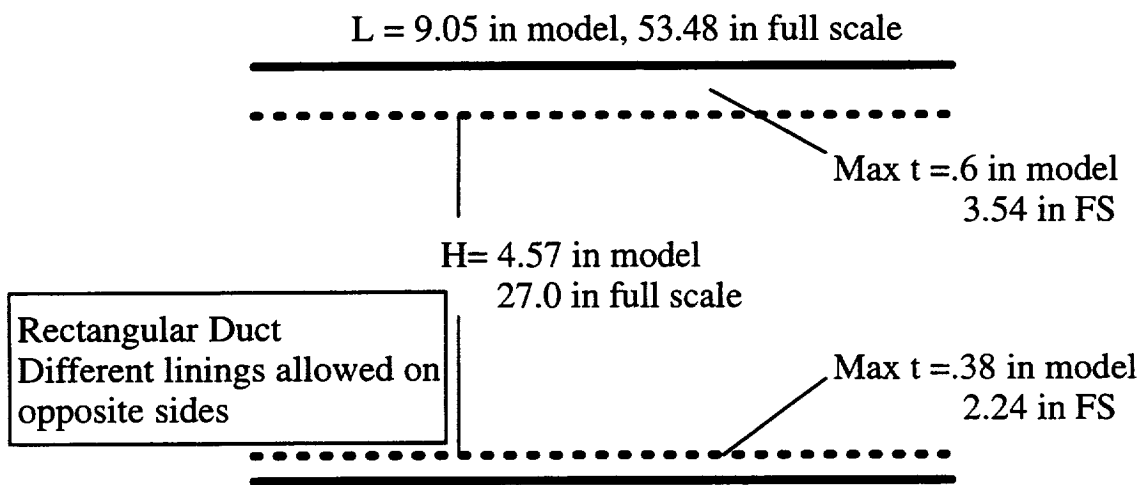


Figure 35: Representation of the Fan Duct with the MELO Program

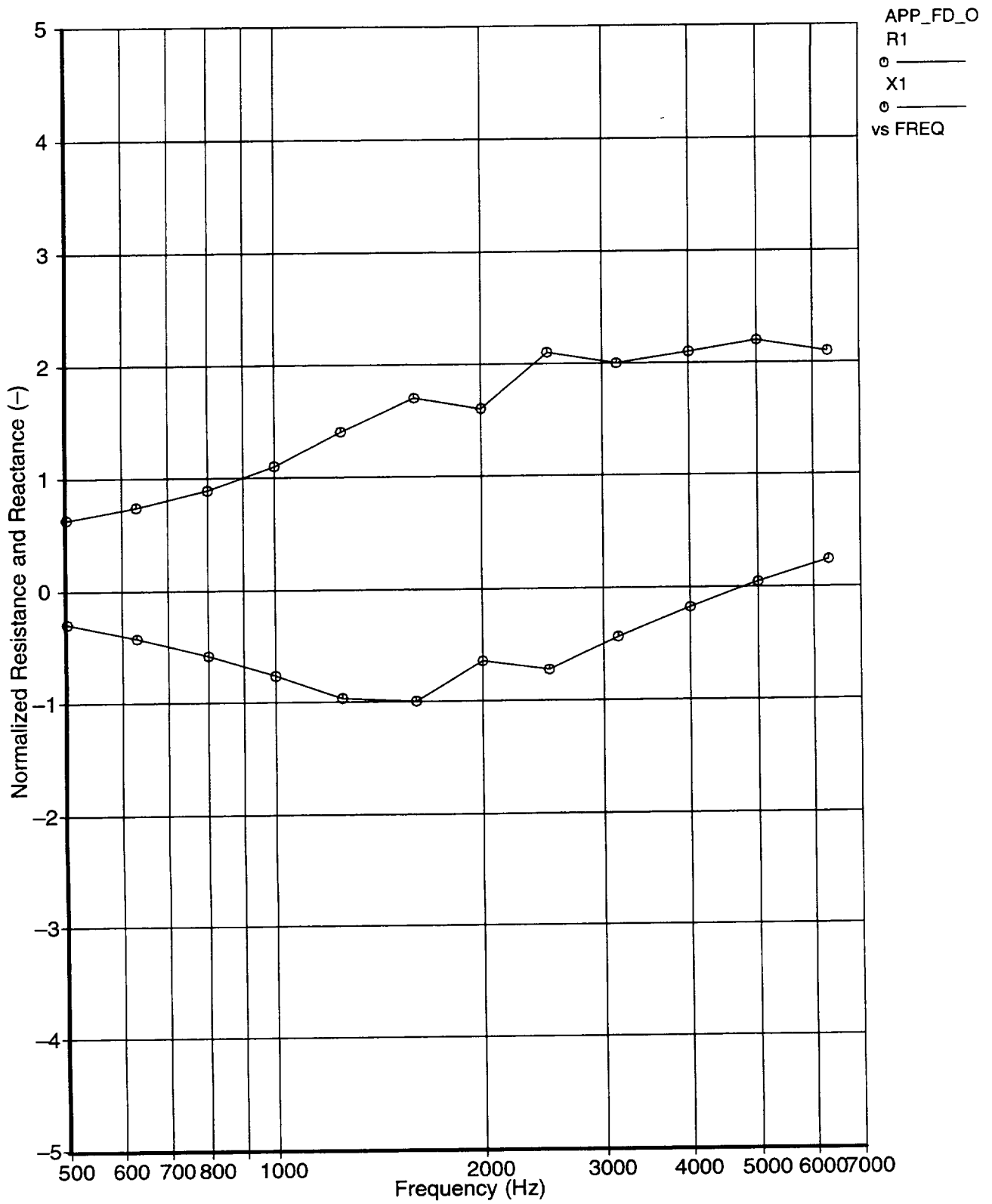


Figure 36: Optimum Lining Impedance for the ADP Fan Duct
 Predicted using Boeing's MELO Program
 (Boundary Layer Thickness = 0.3 cm)

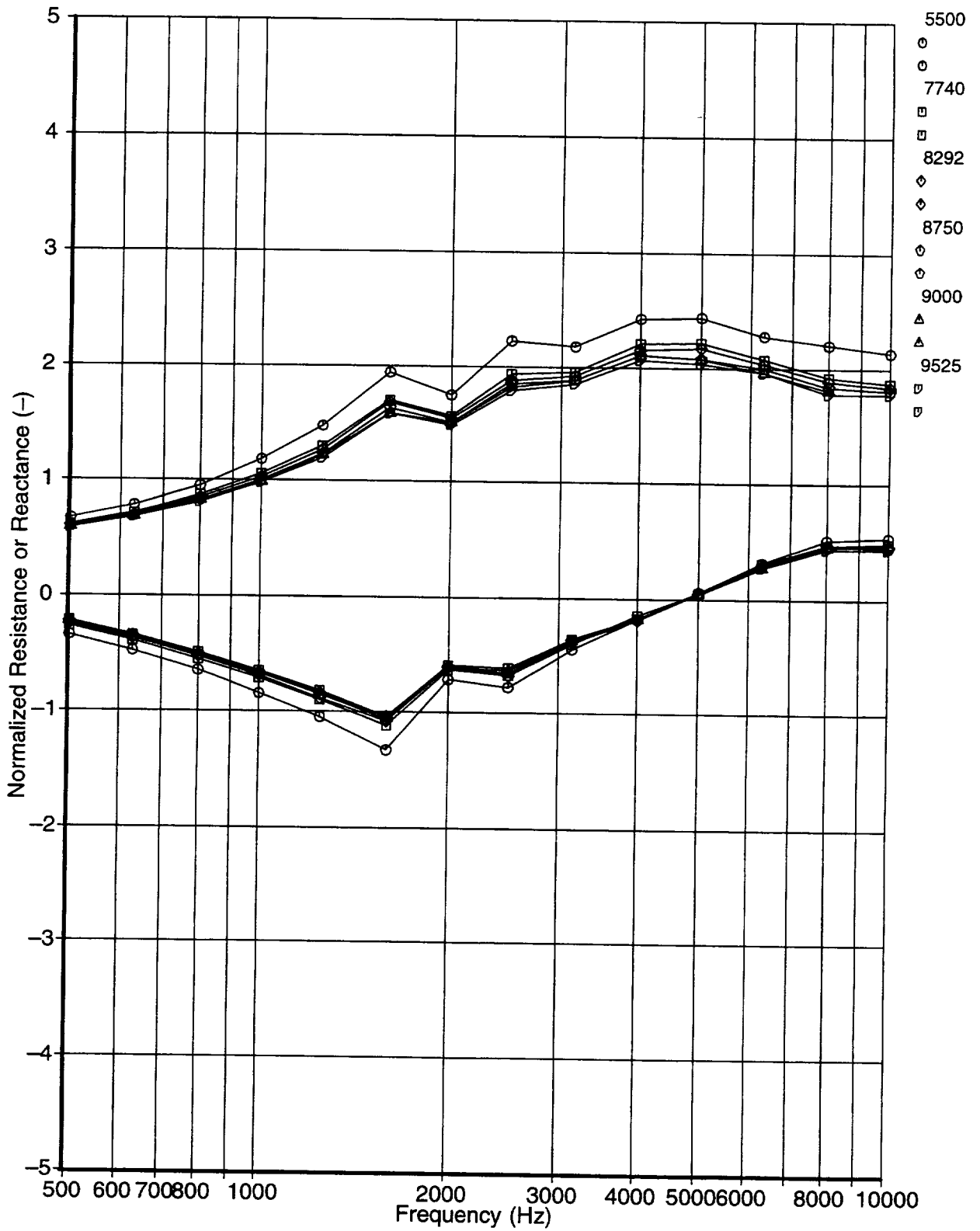


Figure 37: Preliminary Ideal Impedance Calculations for the ADP Fan Duct Based on Boeing Program MELO

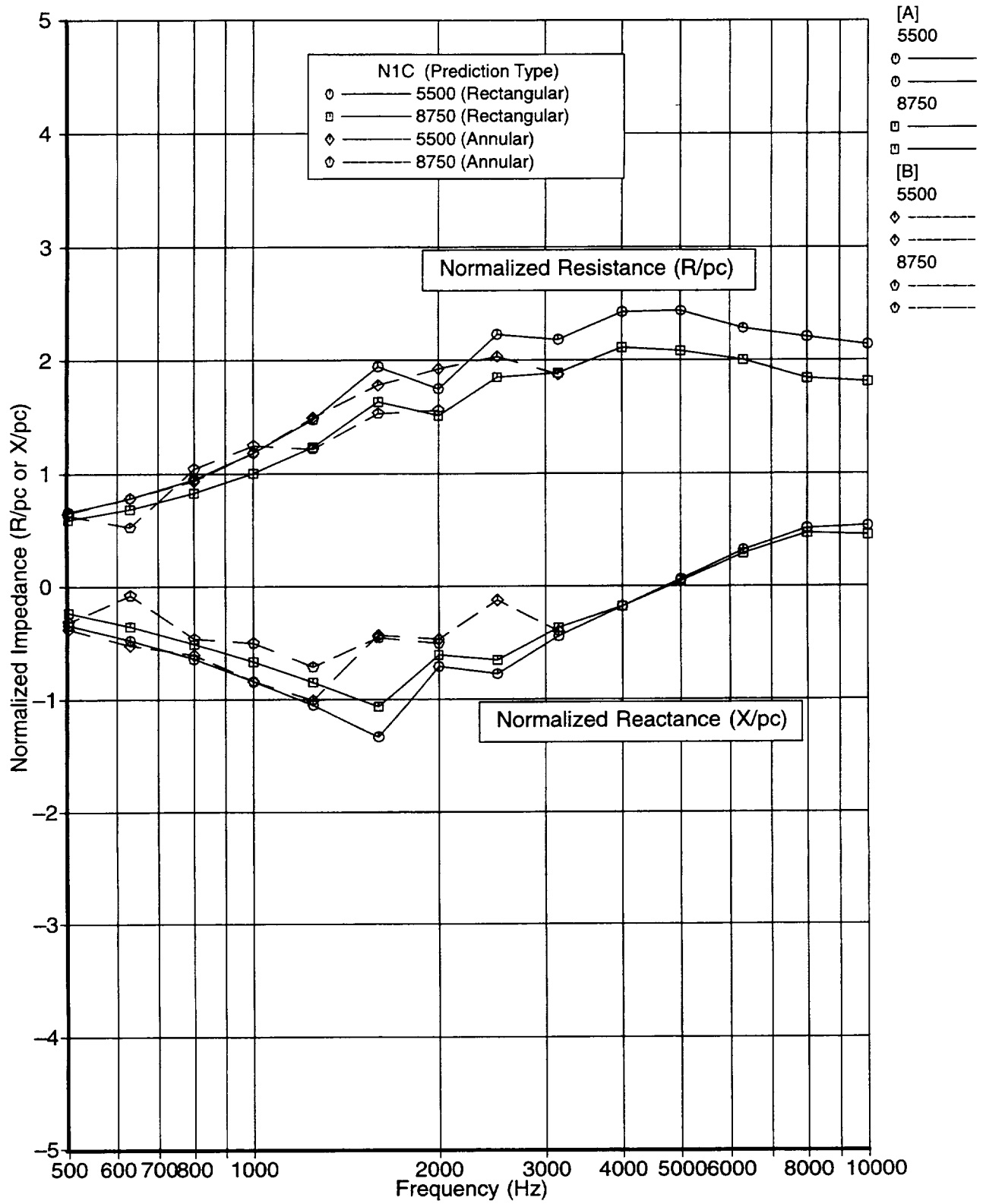


Figure 38: Ideal Impedance Calculations for the ADP Fan Duct Comparison of Annular and Rectangular Solutions from MELO

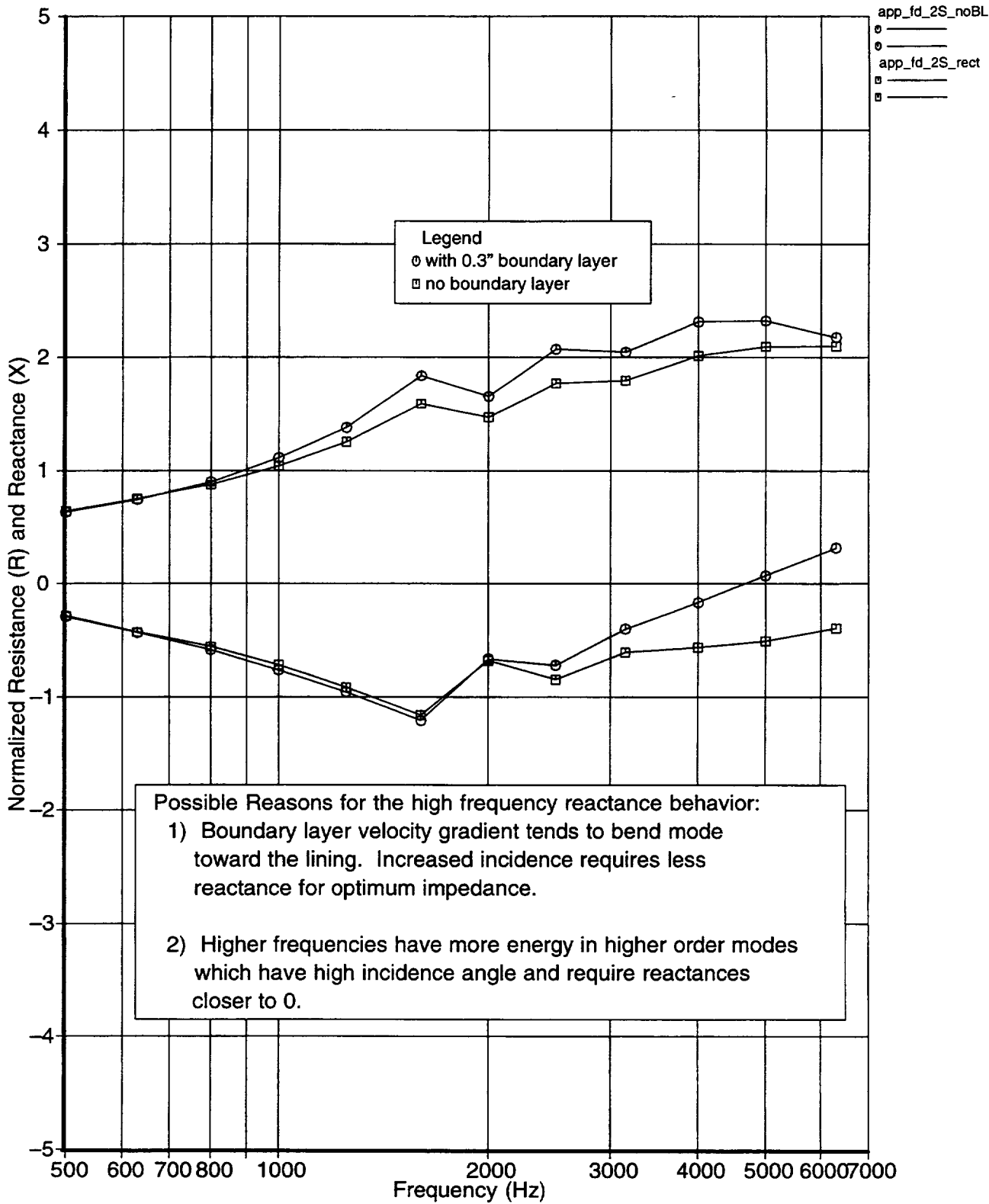


Figure 39: Comparison of Boundary Layer Effect on Optimum Impedances (2 sided w/BL and 2 sided w/out BL)

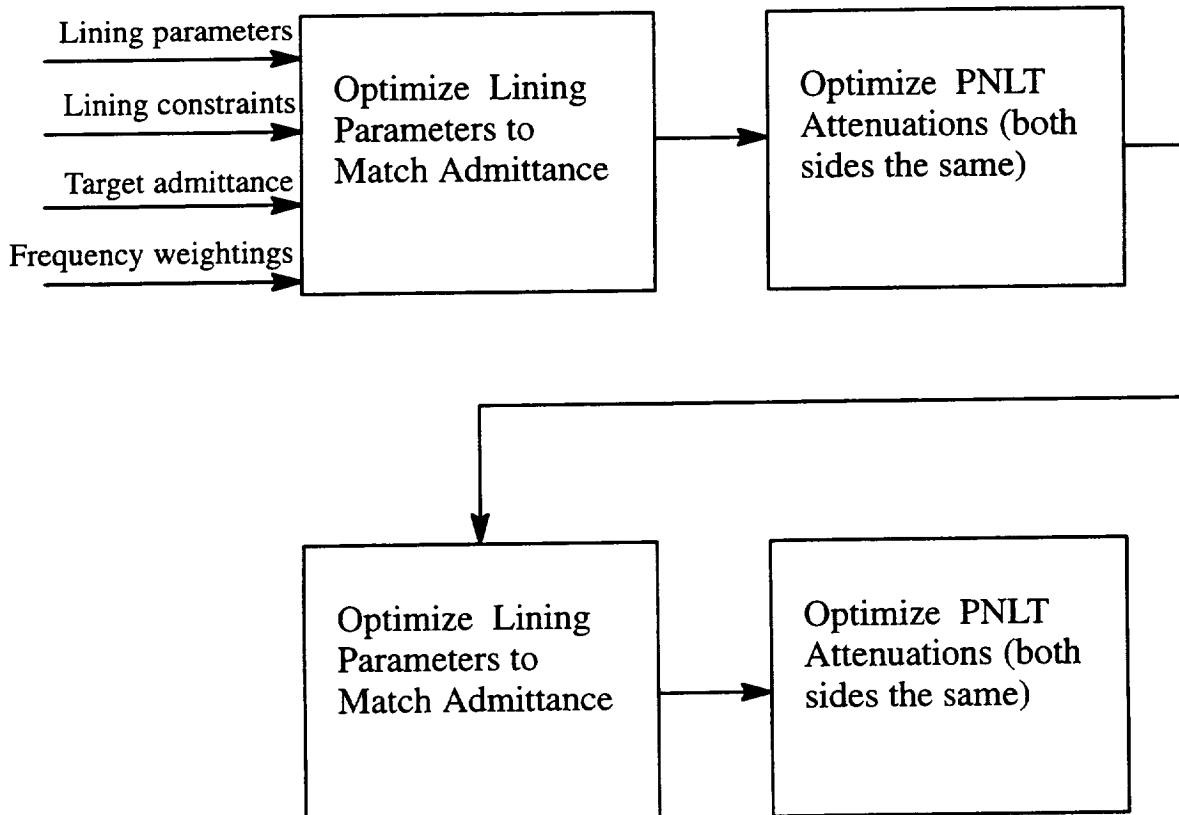


Figure 40: Block Diagram of the Design Process

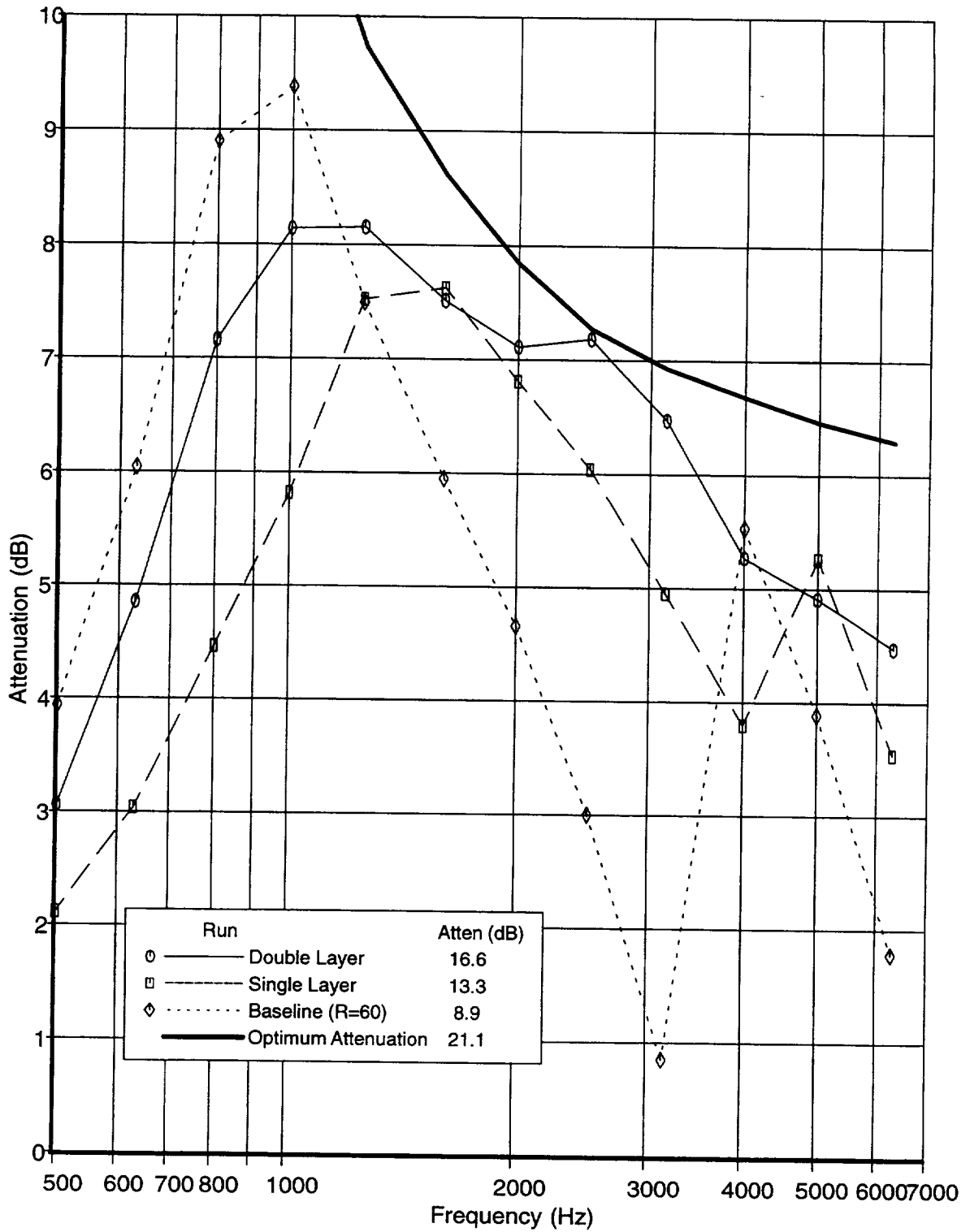


Figure 41: MELO Predicted Lining Attenuations vs the Optimum Attenuations Two-Sided Single and Double Layer Linings at Scaled Frequencies (at the cutback condition)

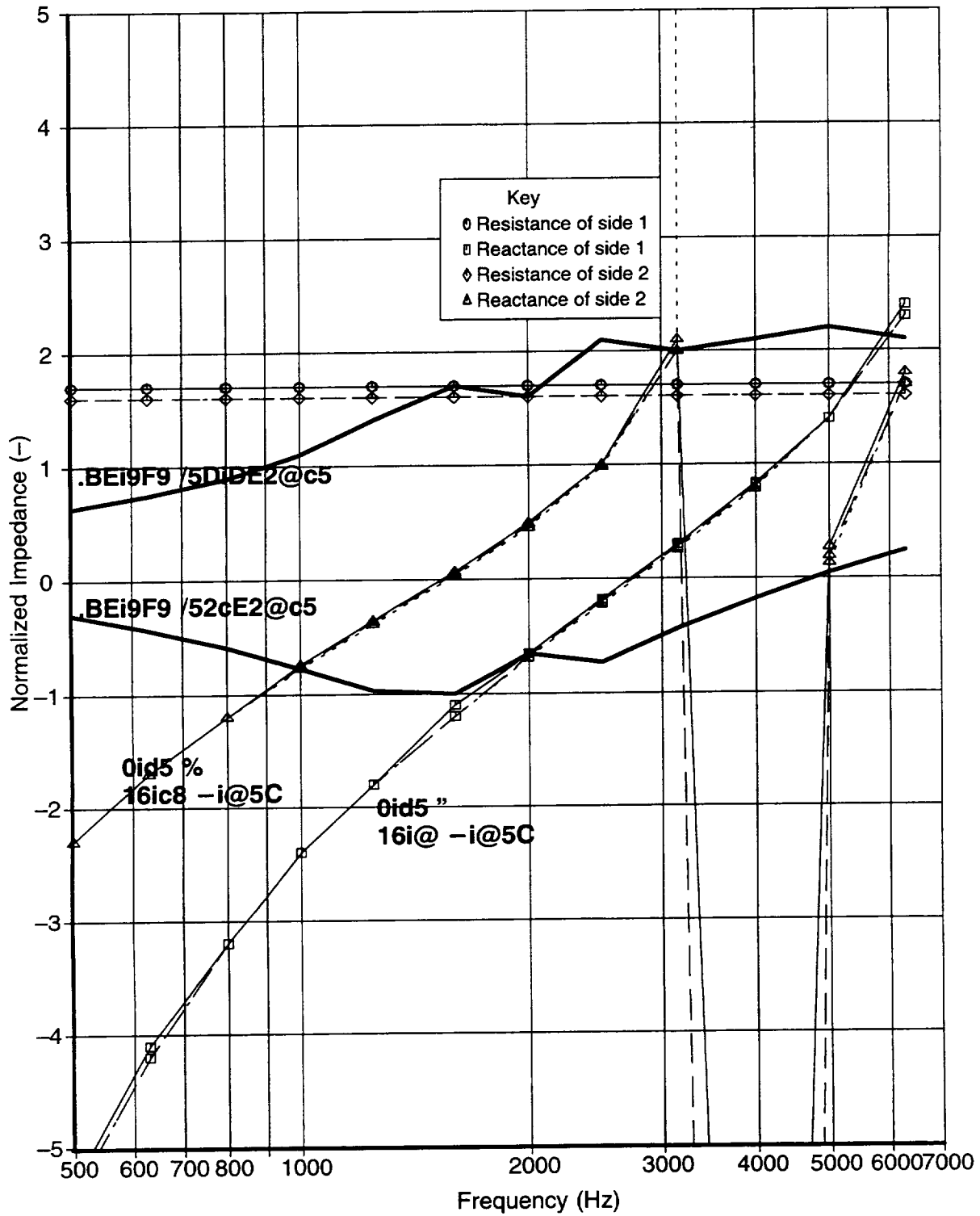


Figure 42: Predicted Lining Impedance vs the Optimum Impedance
 Two-Sided Single Layer Lining at Scaled Frequencies
 (approach, cutback, and sideline)

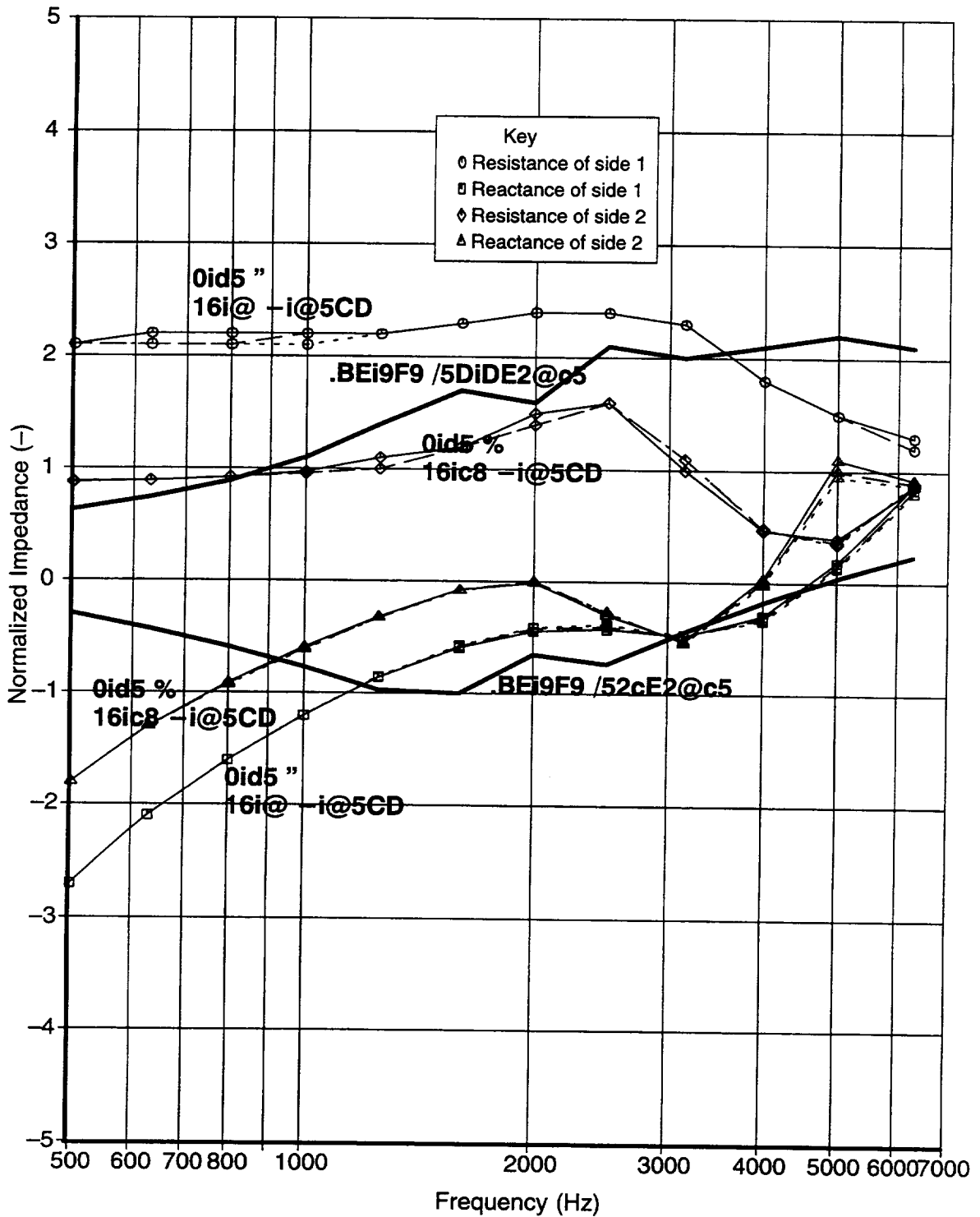


Figure 43: Predicted Lining Impedance vs the Optimum Impedance
 Two-Sided Double Layer Lining at Scaled Frequencies
 (approach, cutback, sideline)

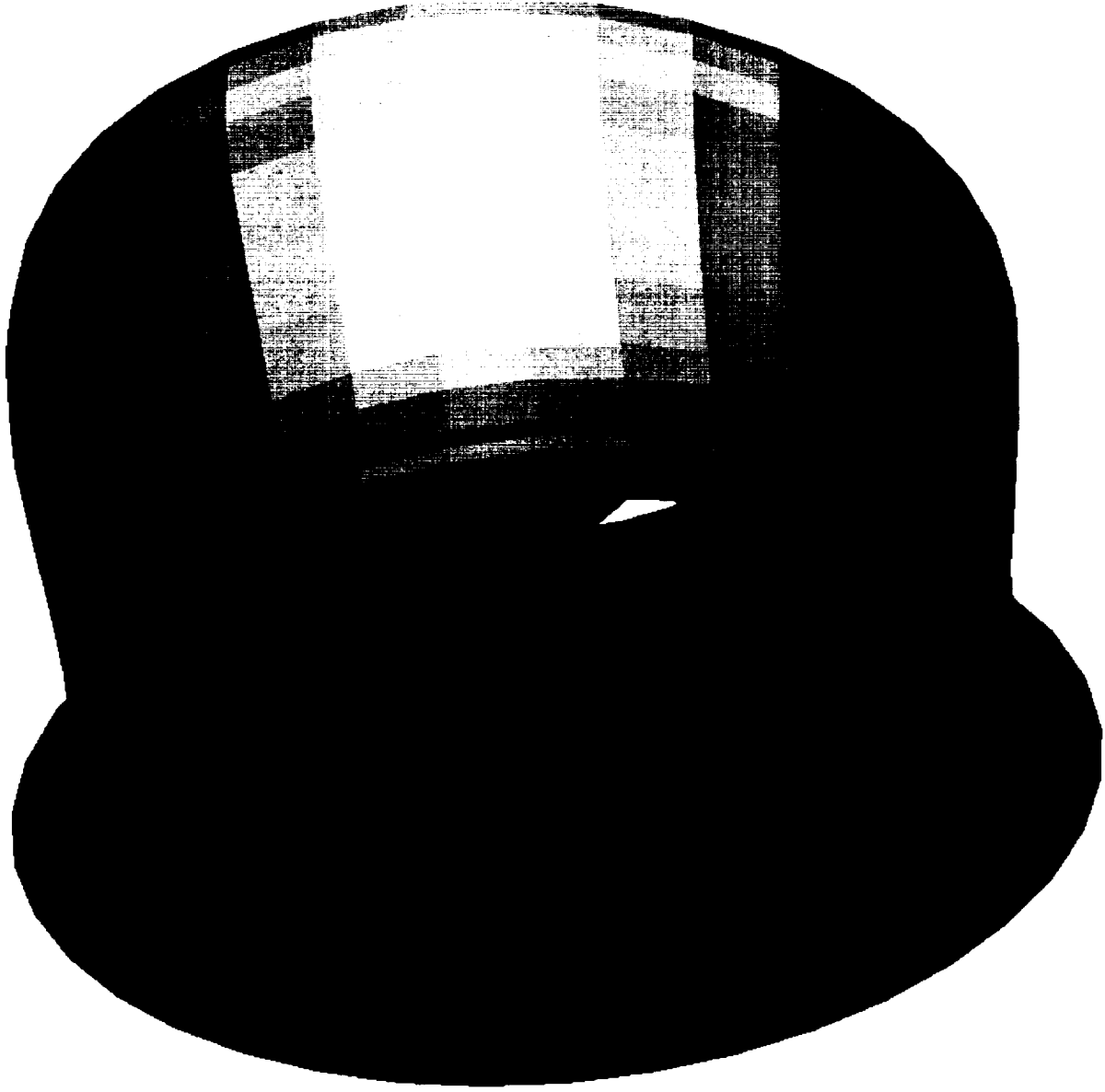


Figure 44: Conventional Inlet Used for the Inlet Trades

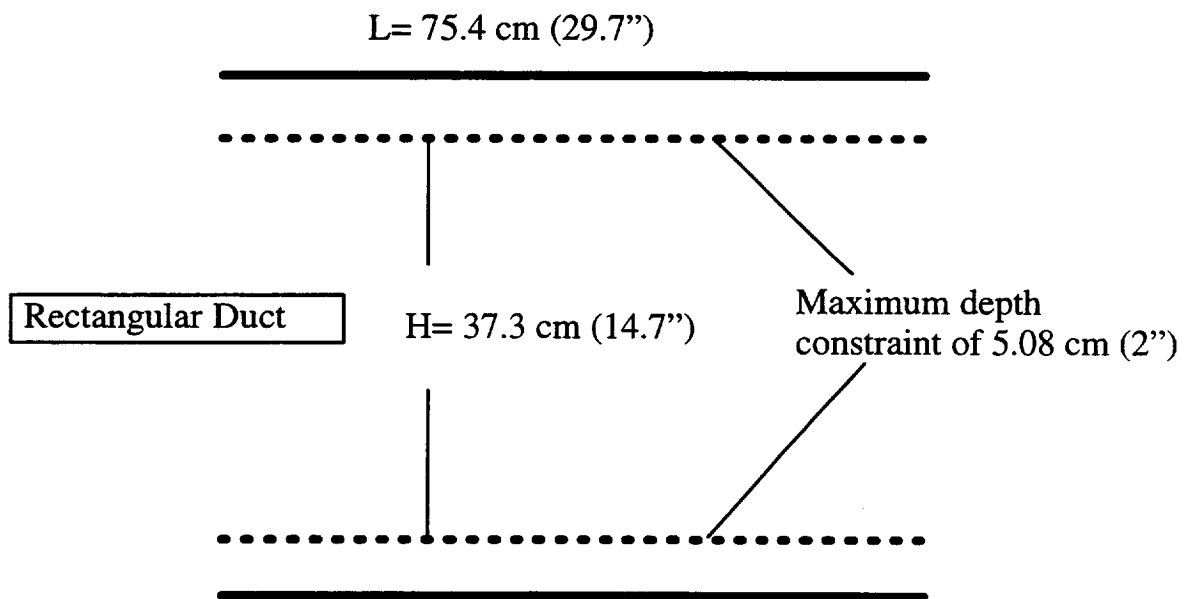
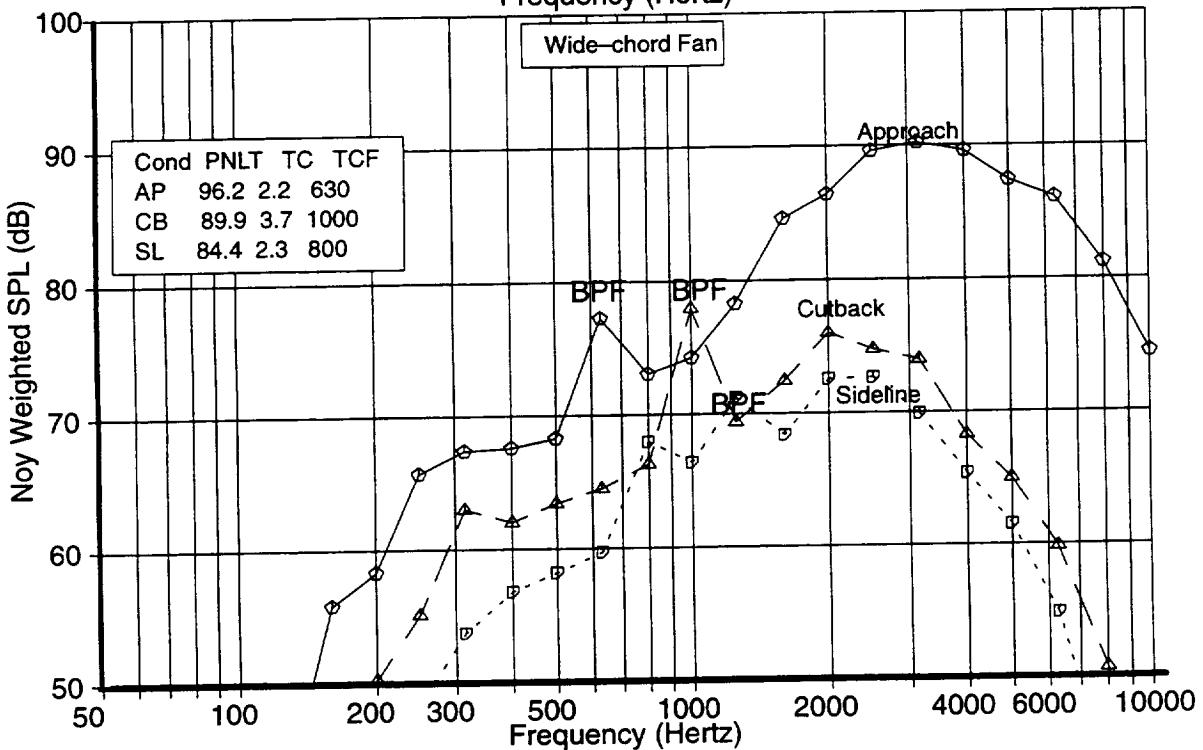
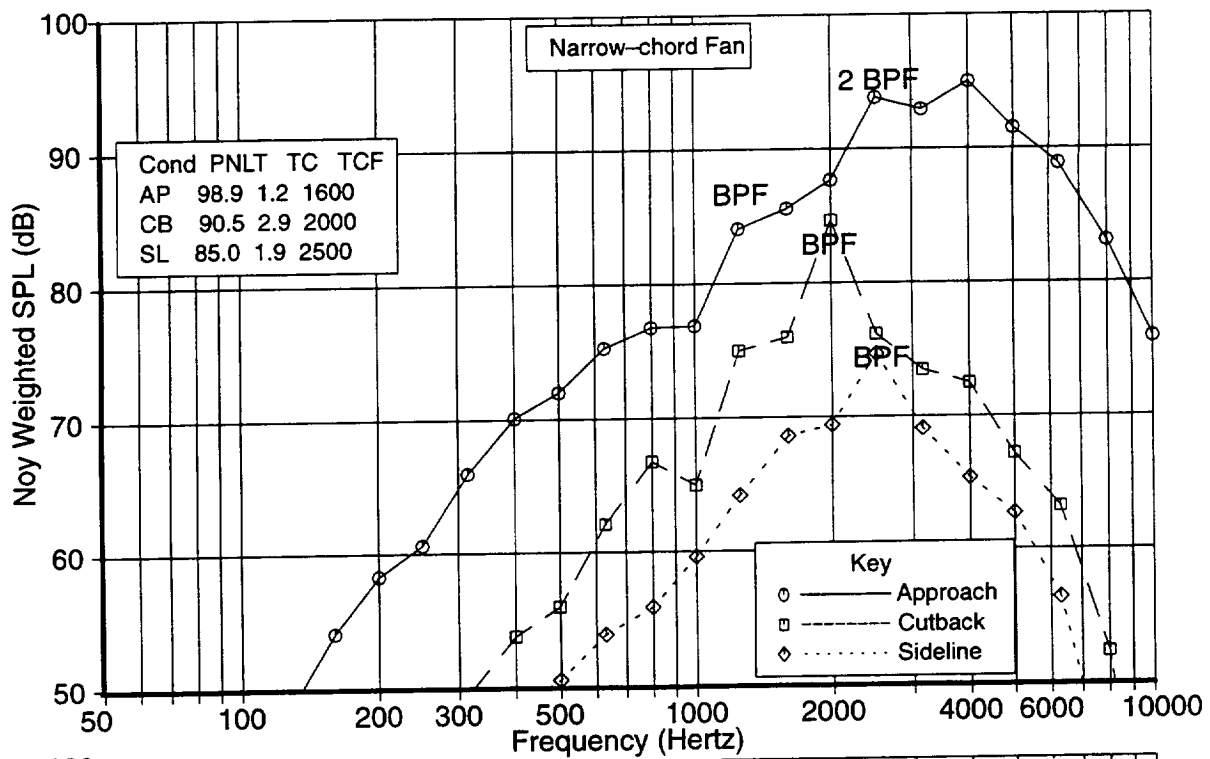


Figure 45: MELO Representation of the Fan Duct Nacelle



50

Figure 46: Inlet Spectra for the Approach, Cutback and Sideline Conditions (for the narrow and wide chord fan engines at 60 degrees)

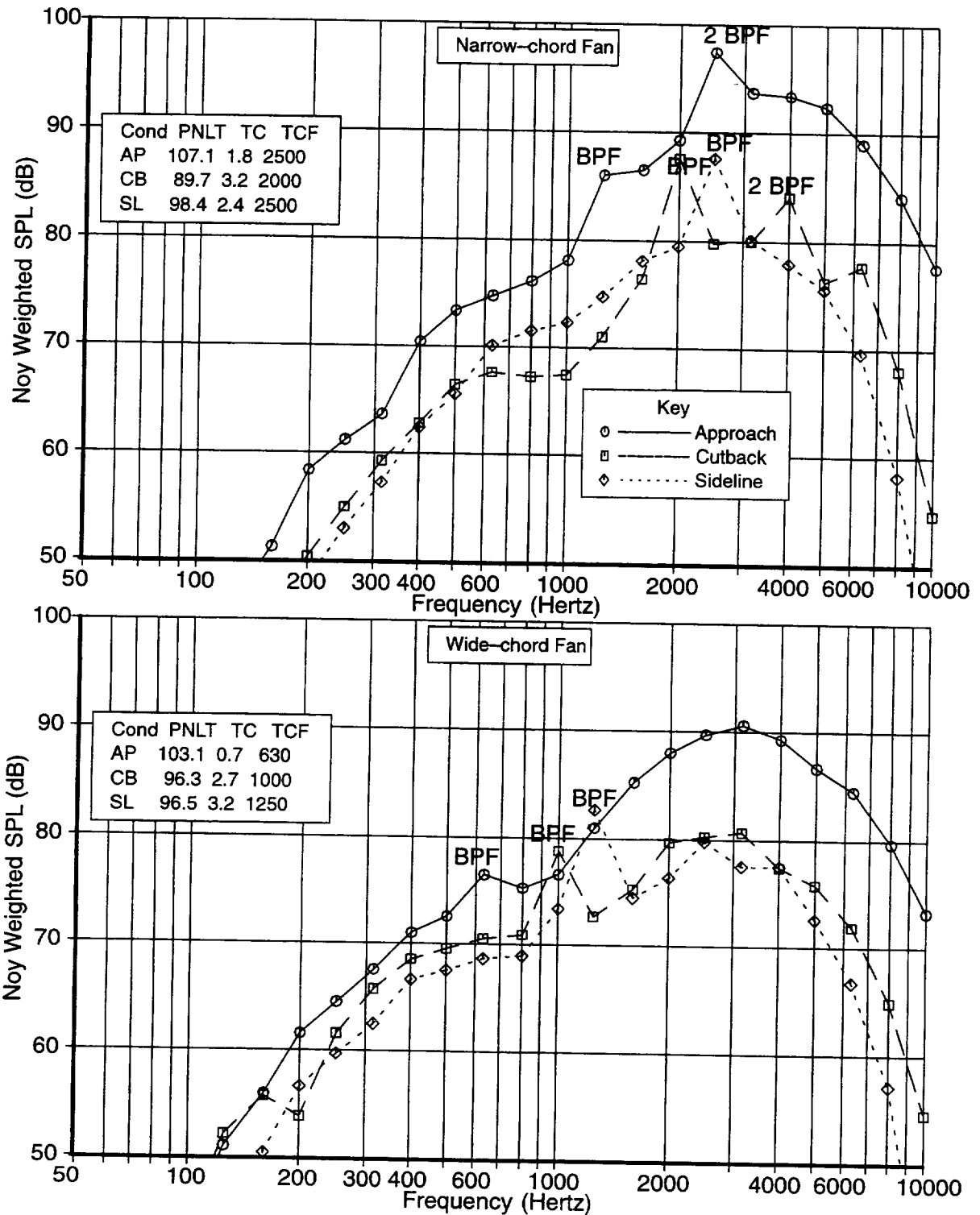
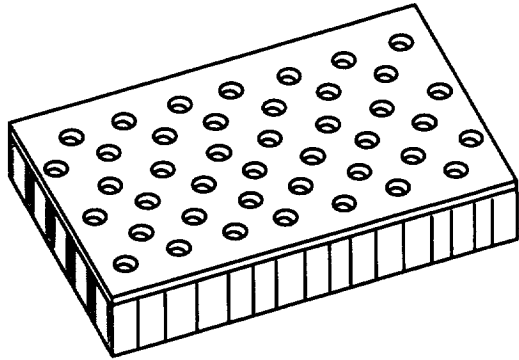
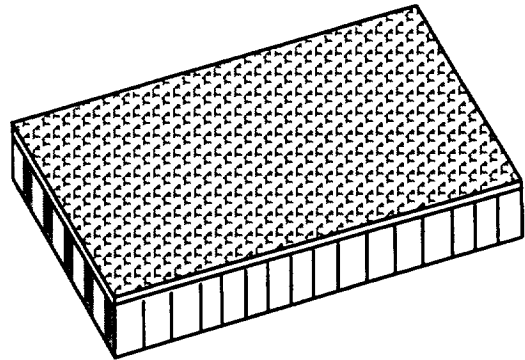


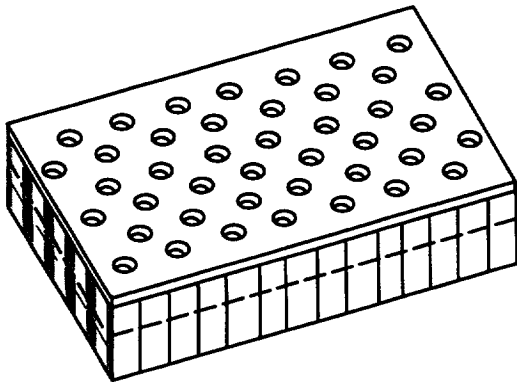
Figure 47: Aft Duct Spectra for the Approach, Cutback and Sideline Conditions (for the narrow and wide chord fan engines at 60 degrees)



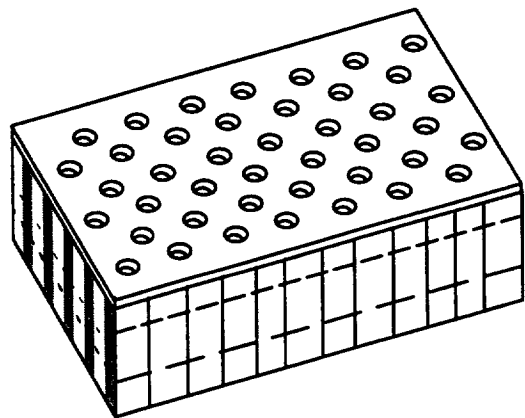
Perforate Single Layer



Linear Single Layer



**Perforate Double Layer
(one septum)**



**Perforate Triple Layer
(two septa)**

Figure 48: Examples of Linings Considered in the Trade Study

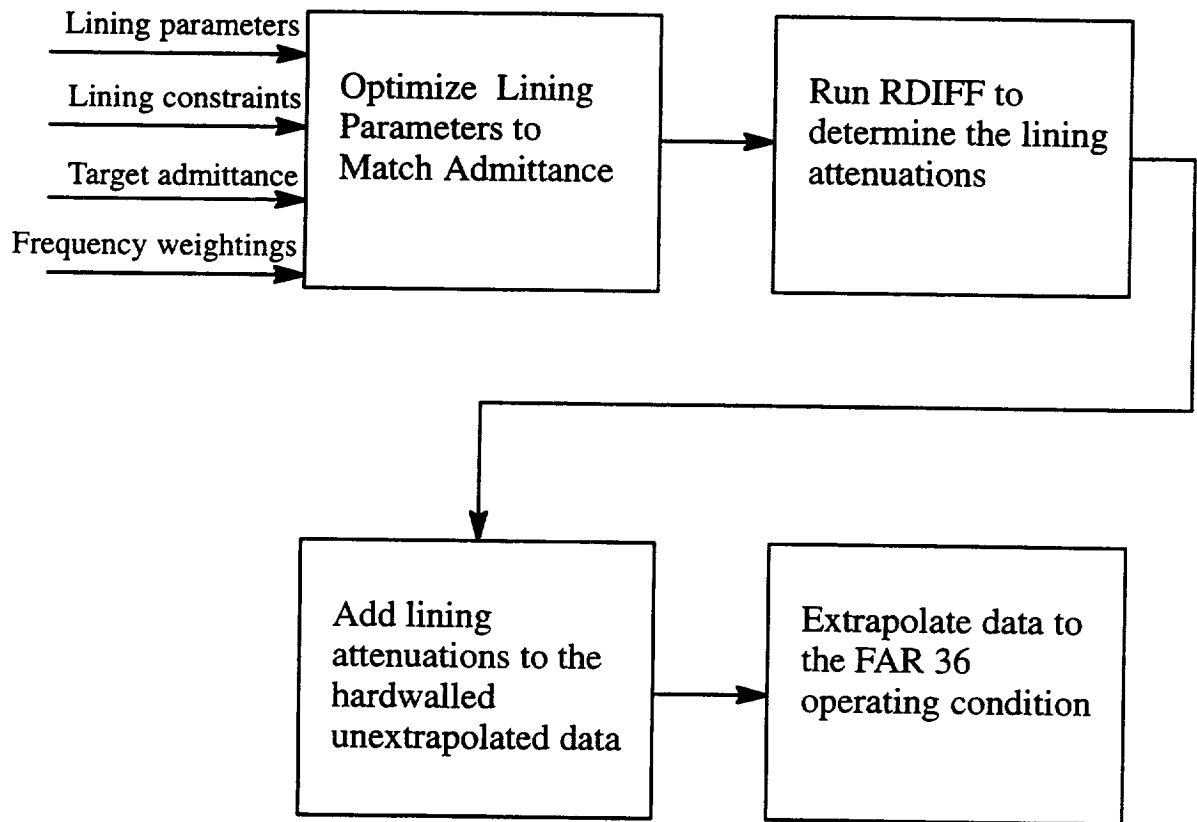


Figure 49: Block Diagram of the Evaluation Process for the Inlet

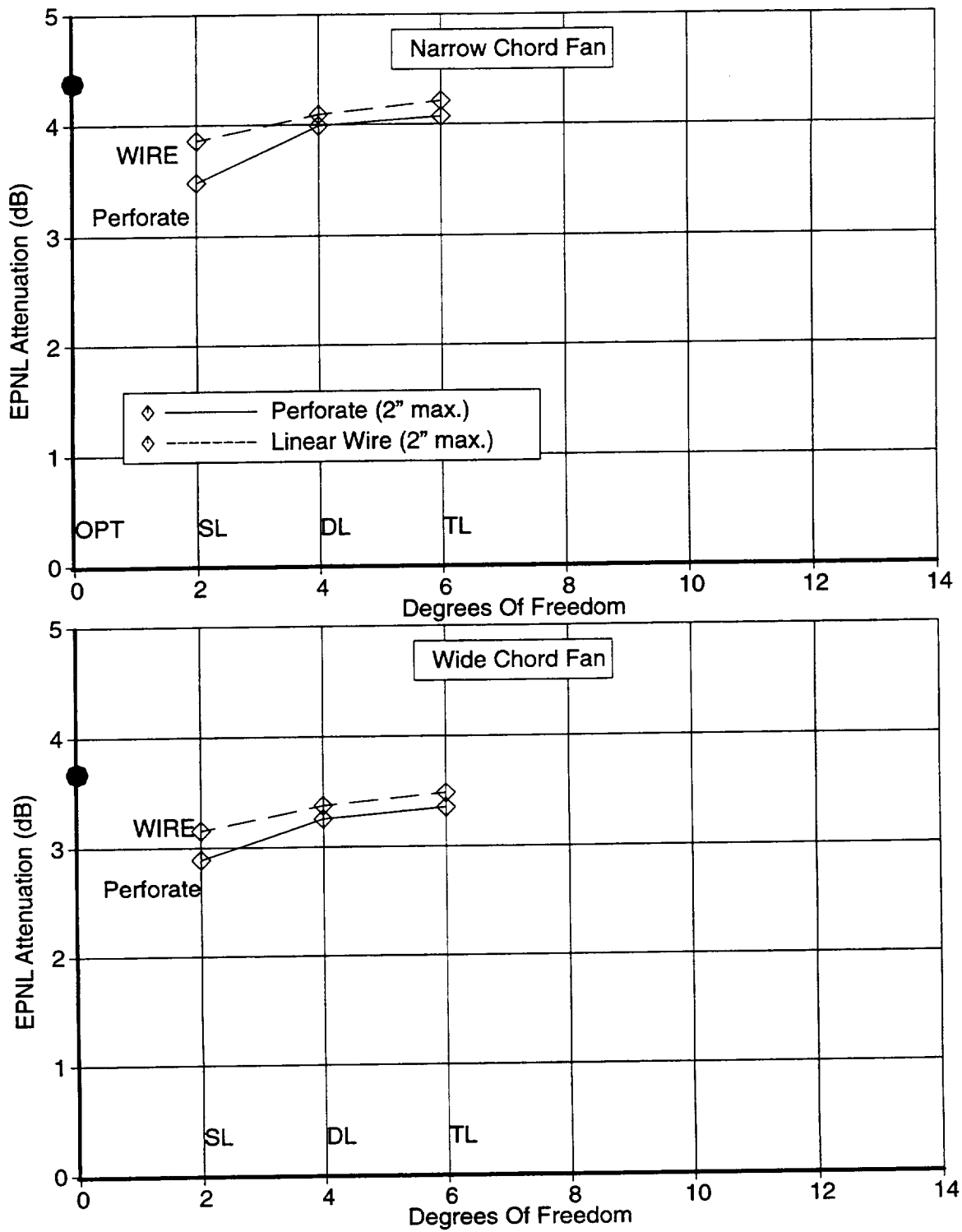


Figure 50: Results of the Impedance Study for the Inlet Component (at the approach condition)

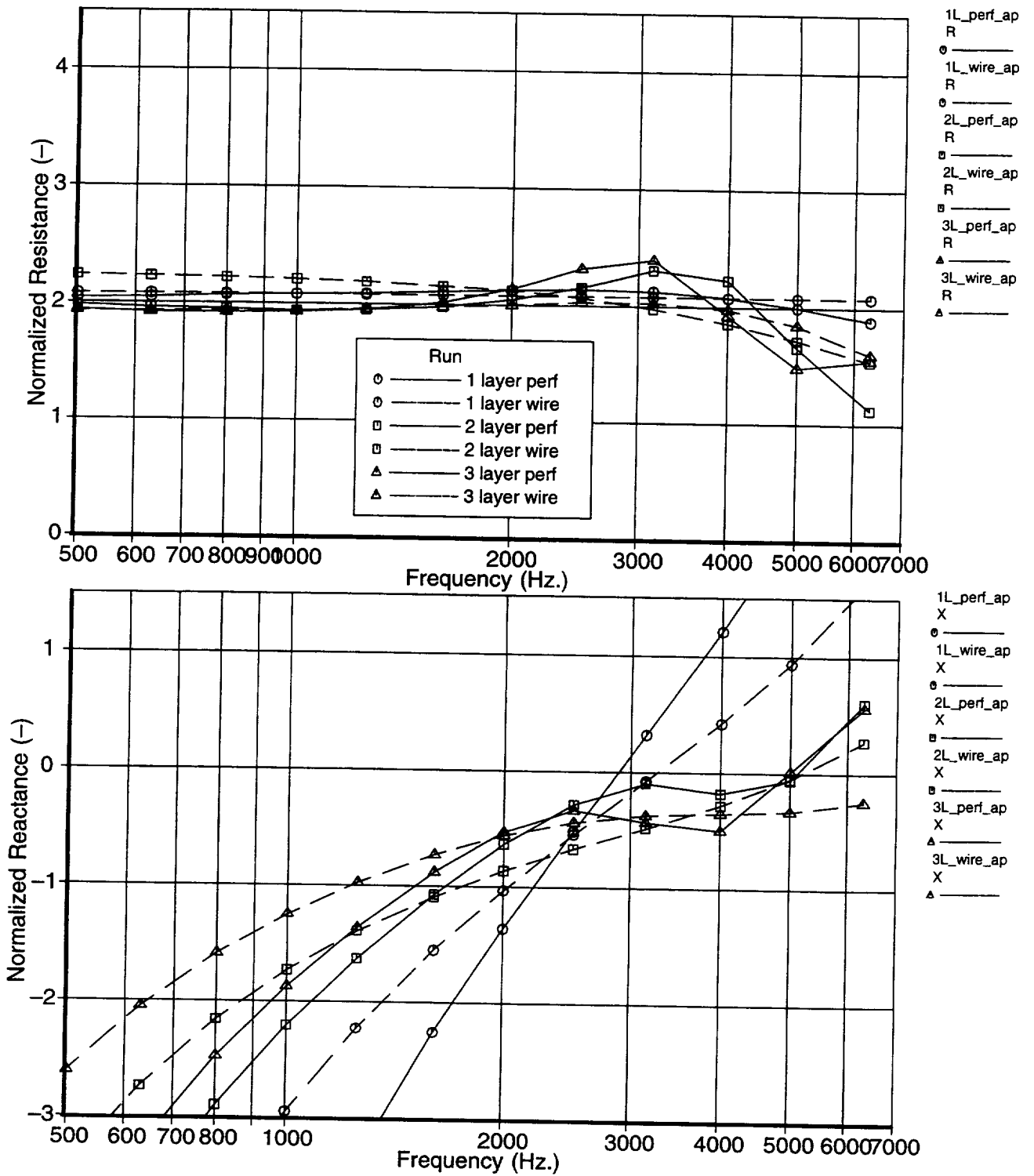
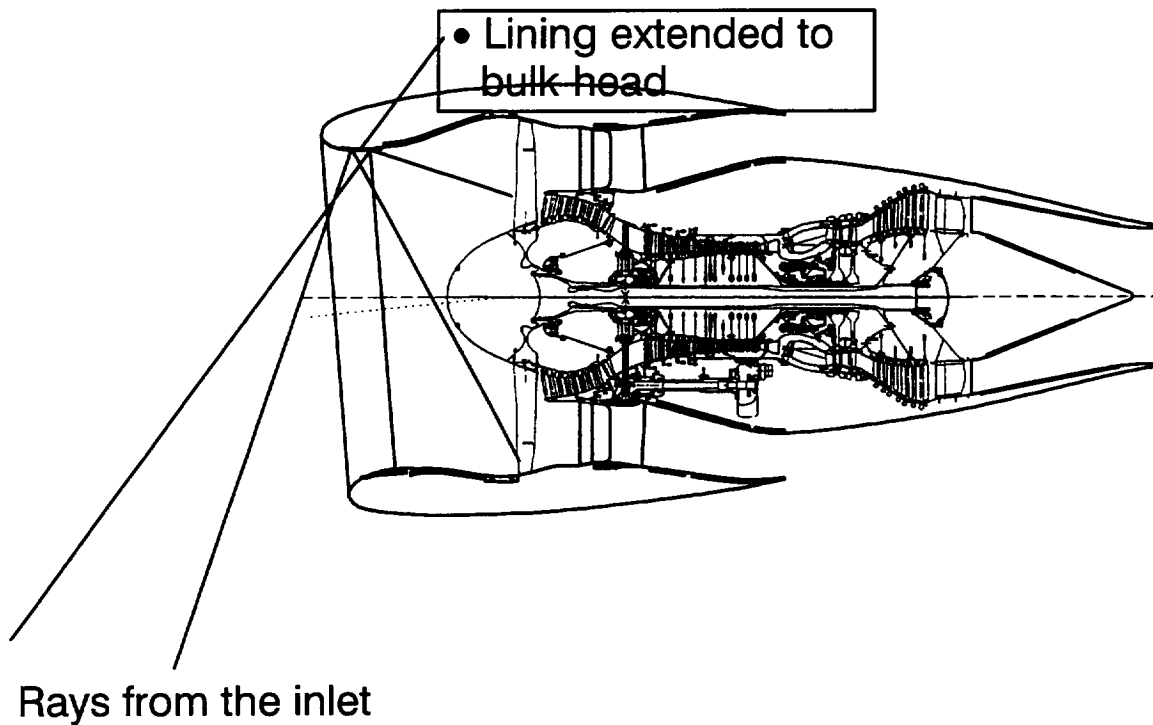


Figure 51: Impedance of the Inlet Liners
(at the approach condition)



Forward region in 1992 baseline sets floor on achievable lining improvement. The attenuations are controlled by the hardwalled areas not the lining panel attenuations. The options are:

- 1) Leave it and get 10–15% maximum improvement**
- 2) Extend treatment forward for 30–80% improvement**
- 3) Change the radiation directivity by scarfing the inlet**

Figure 52: Ray Acoustic Argument for Low Inlet Attenuations

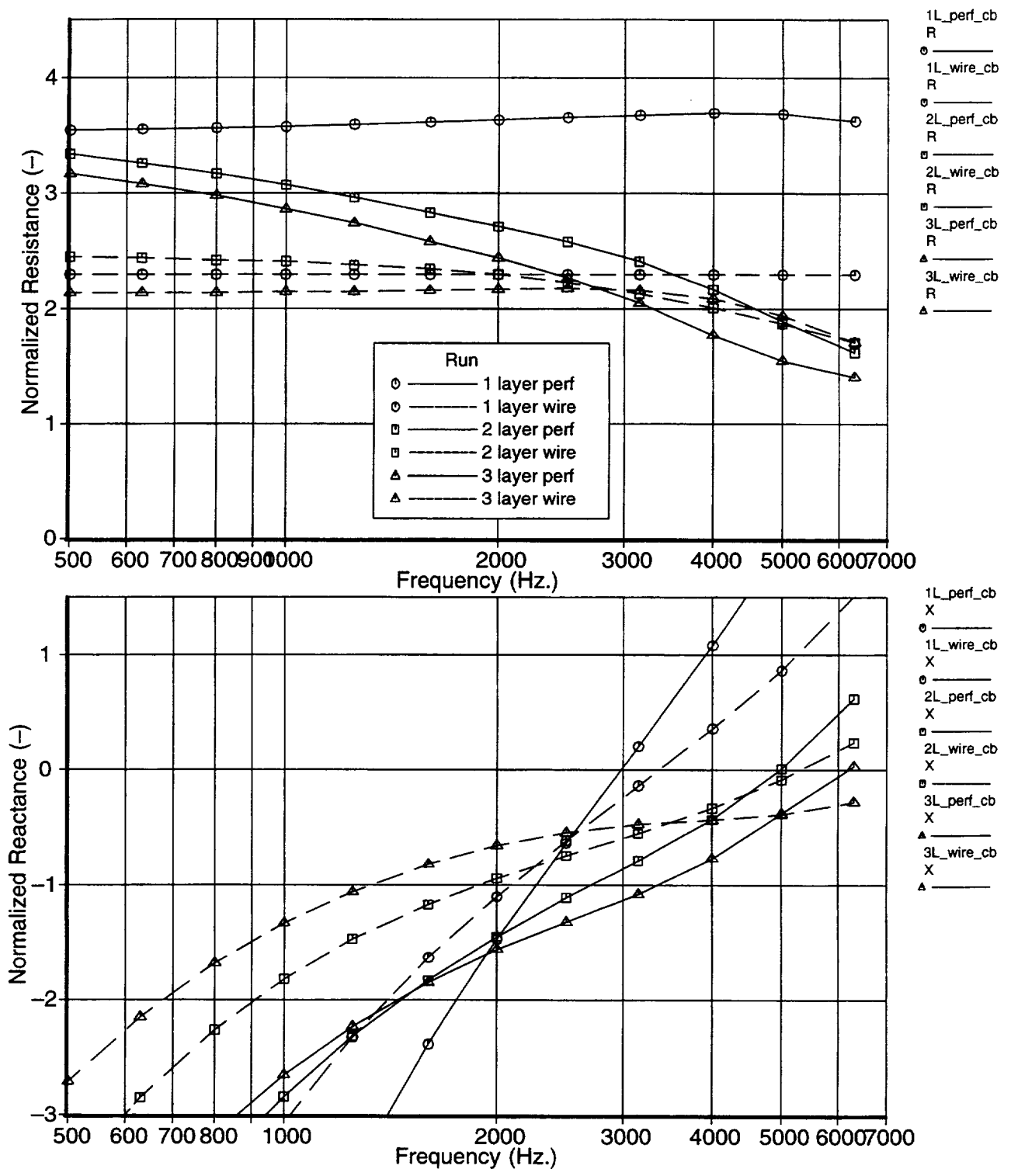
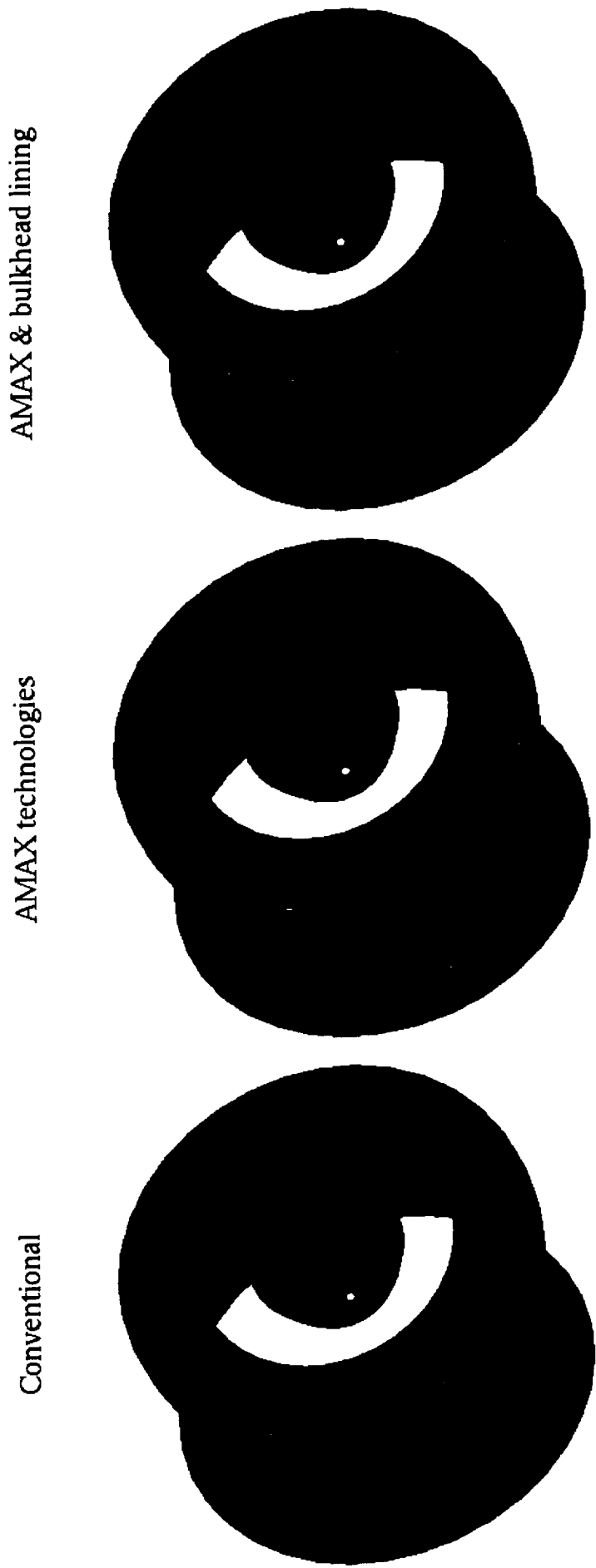
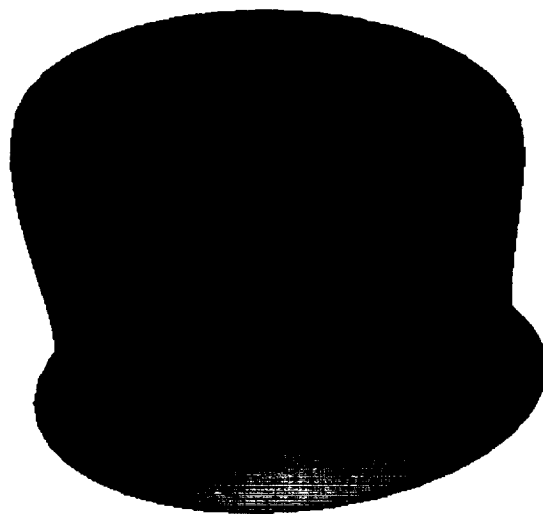


Figure 53: Impedance of the Inlet Liners
(at the cutback condition)

Figure 54: Comparison of Lining Area Technologies



Conventional



Scarf

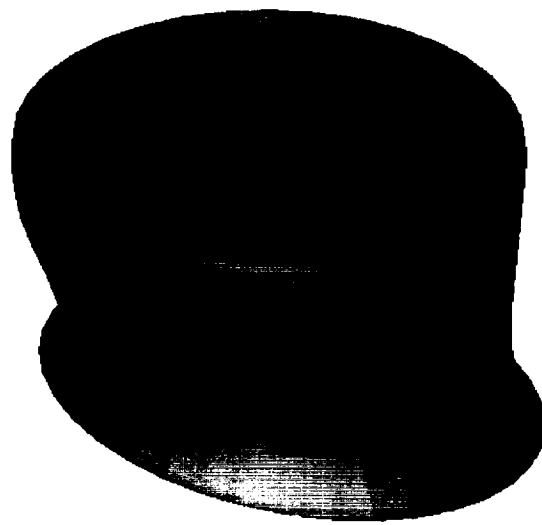


Figure 55: Conventional and Scarf Inlets

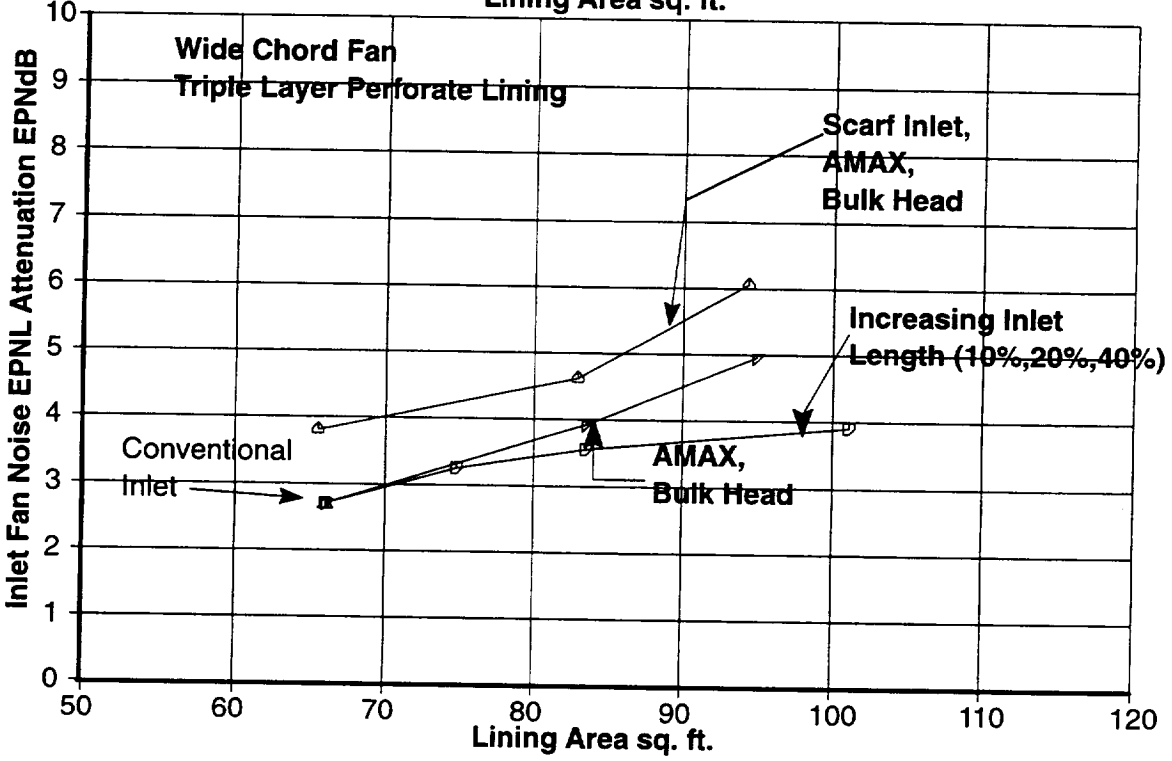
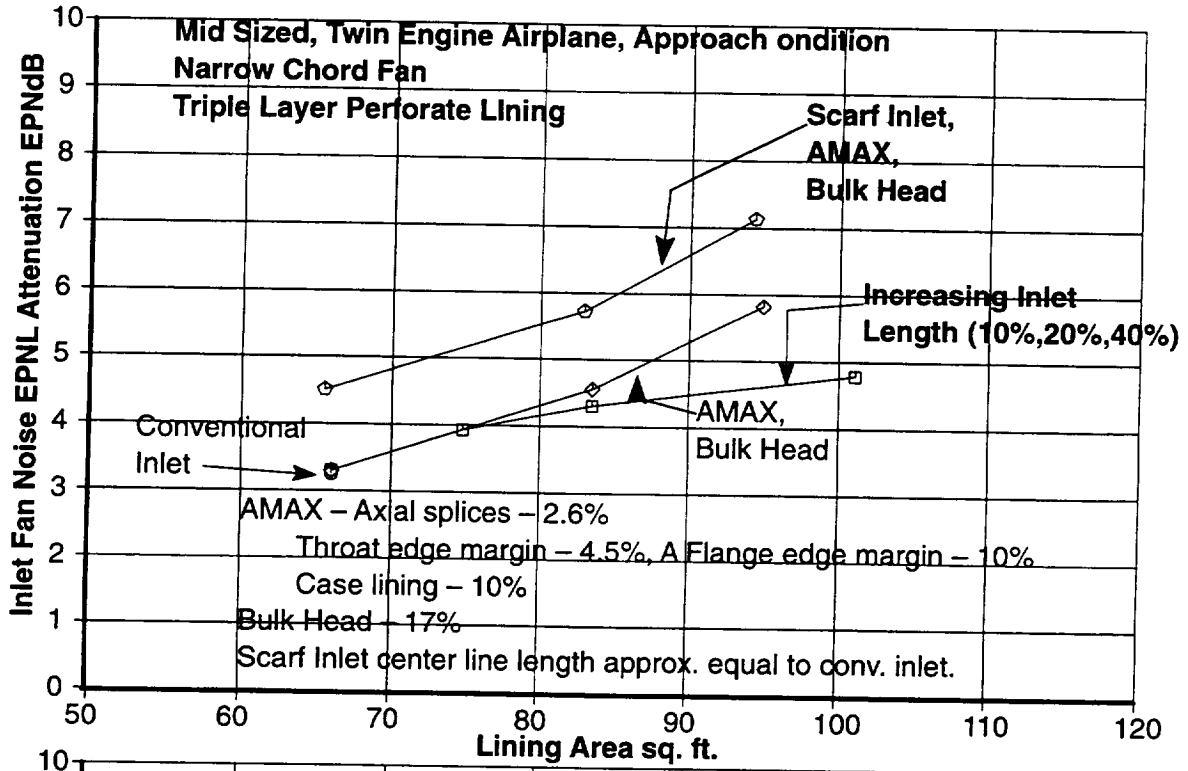


Figure 56: Inlet Lining Area and Configuration Study

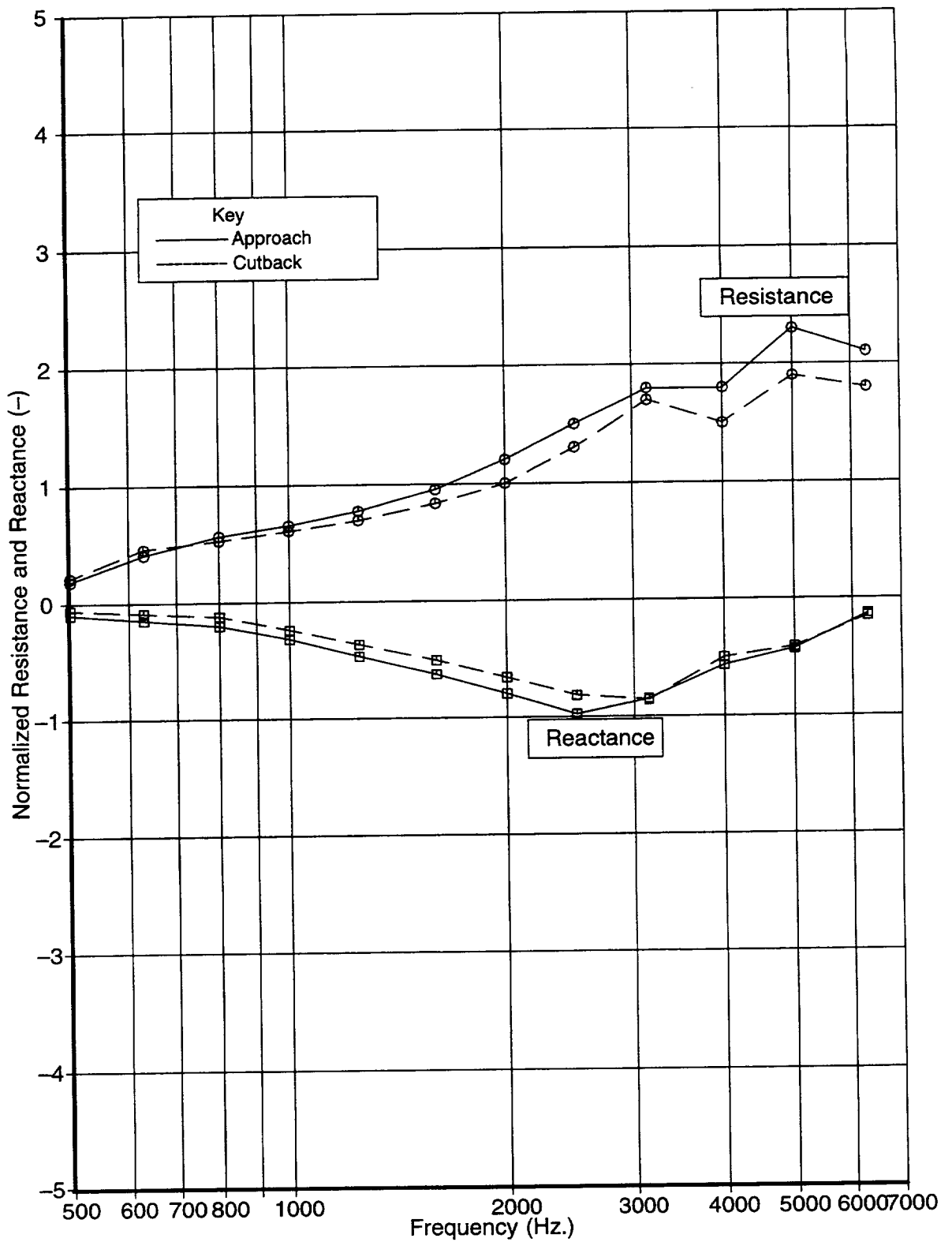


Figure 57: MELO Predicted Ideal Impedances
(for the approach and cutback conditions)

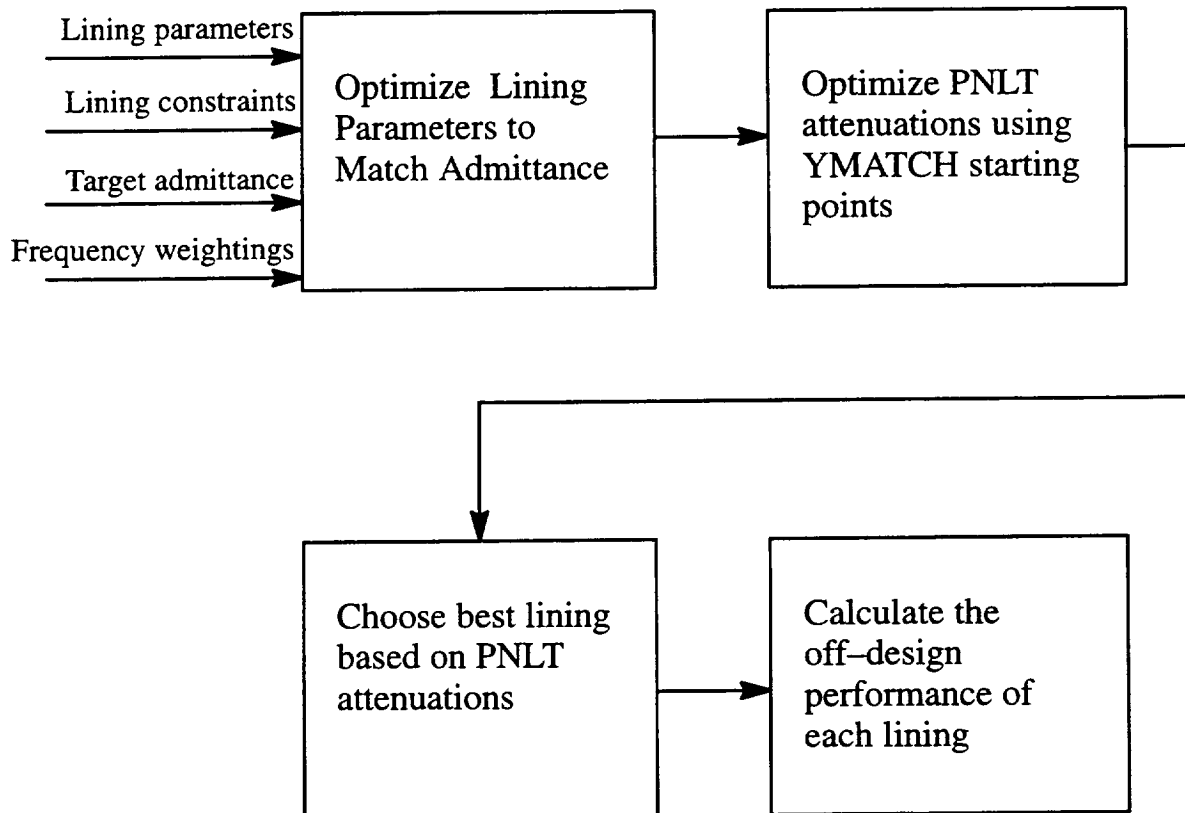


Figure 58: Block Diagram of the Evaluation Process for the Aft Duct

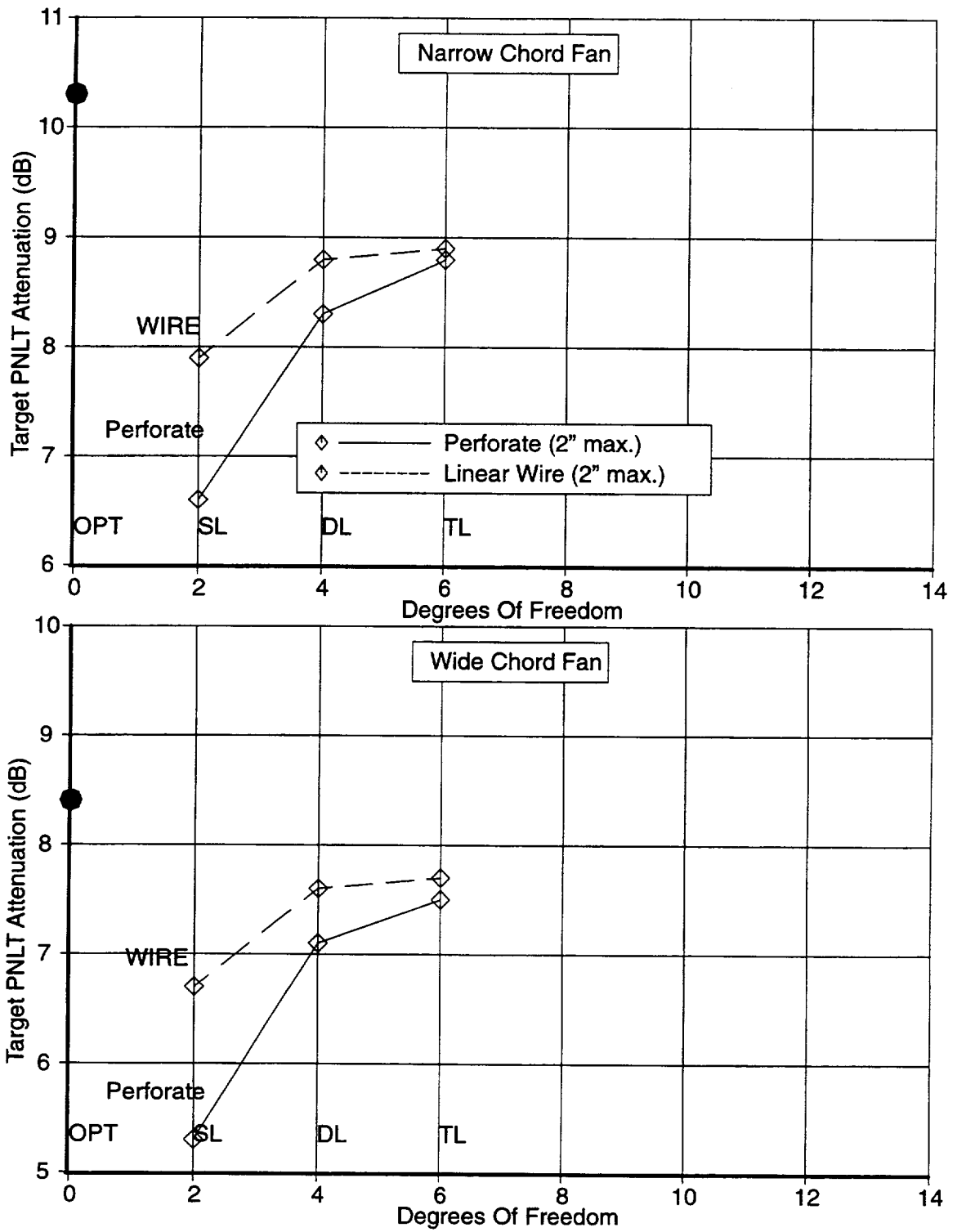


Figure 59: Comparison of Aftfan PNLT Attenuations at Approach

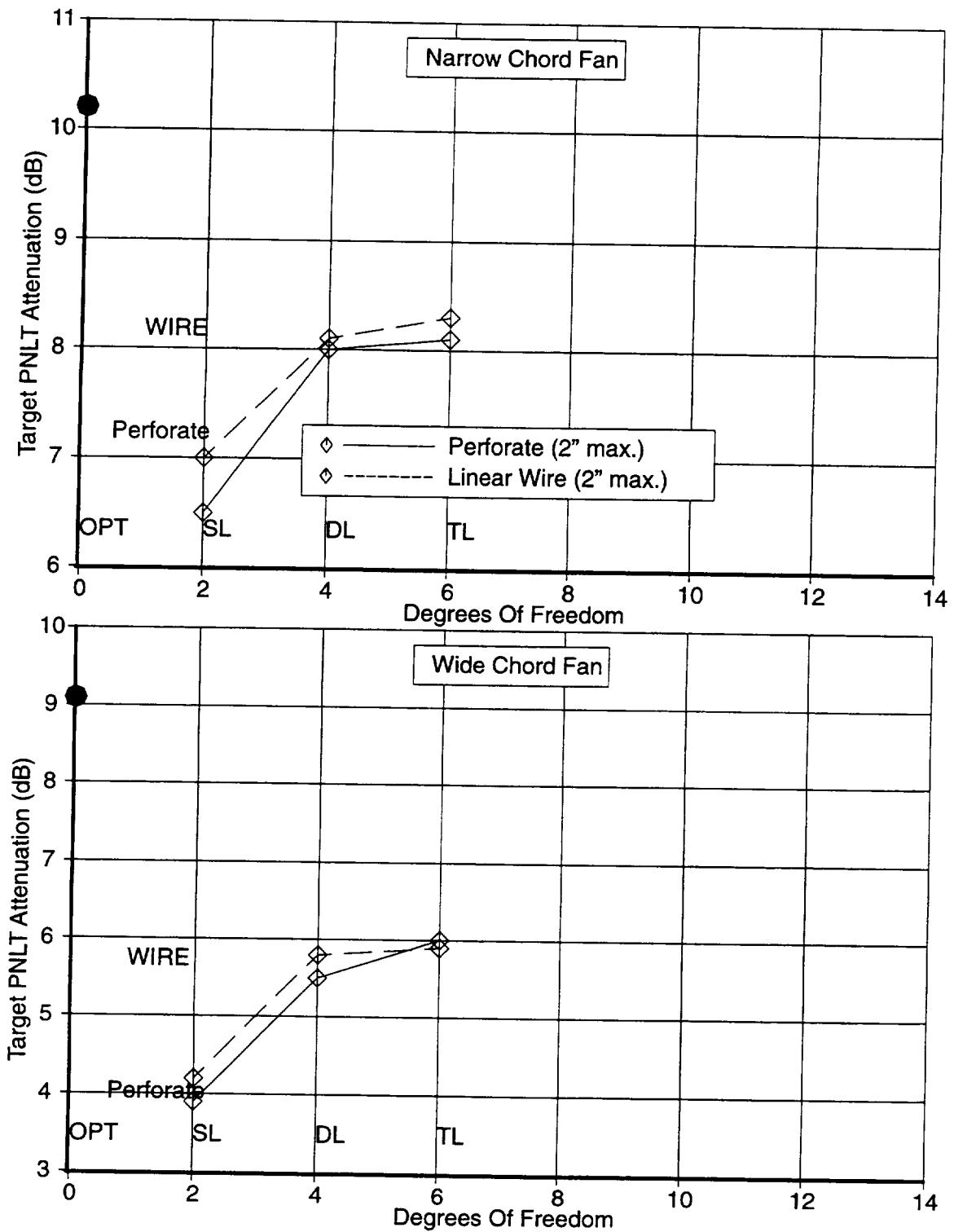


Figure 60: Comparison of Aftfan PNLT Attenuations at Cutback

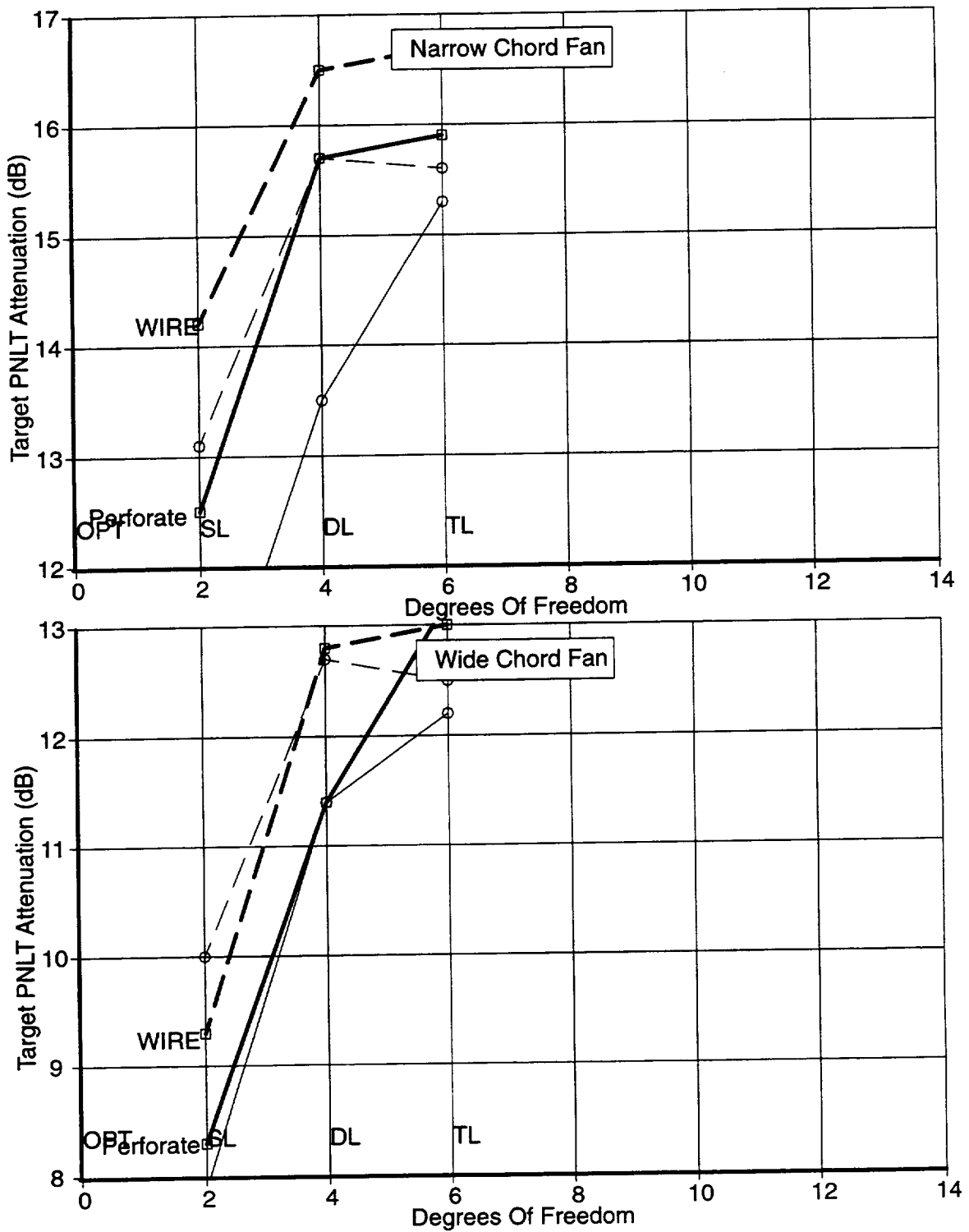


Figure 61: Comparison of Aftfan PNL Attenuations (summed approach and cutback conditions)

Appendicies:

A1. “Theory And Design Of Helmholtz Resonators Constructed With Slot Perforates”
Allen Hersh and Bruce Walker

A2. “Theory And Design Of Helmholtz Resonators To Suppress Aircraft Engine Noise”
Allen Hersh and Bruce Walker

A3. “Theory And Design Of Helmholtz Resonators Constructed With Micro–Diameter Perforates”
Allen Hersh, Joseph Celano and Bruce Walker

A4. Impedance Models.

The following are the references for the impedance models incorporated into the Boeing lumped element impedance model library as a result of work on this contract :

1. Small diameter cell (parallel cells) from empirical formulae in Tijdeman JSV Vol.39, No.1, 1975, p1–33.
2. Perforated plate face shet using a discharge coefficient formulation outlined in “Fluid Mechanical Model of the Acoustic Impedance of Small Orifaces ” , Hersh & Rogers, AIAA 75–495.
3. Bulk absorber model from empirical formulaae presented in Voronina, Soviet Phys. Acoust. 29(5) Sept. – Oct. 1983
4. Perforated Plate – Uses code from Appendix 2.

Hersh Acoustical Engineering, Inc.

***780 Lakefield Road, Unit G
Westlake Village, CA 91361
(805) 373-8533 Fax (805) 373-0733
e-mail: hae@iswest.com***

FINAL REPORT

BOEING PURCHASE CONTRACT # ZA0075

PRIME CONTRACT NAS1-20090

**THEORY AND DESIGN OF HELMHOLTZ RESONATORS CONSTRUCTED WITH
SLOT PERFORATES**

by:



Alan S. Hersh

and



Bruce E. Walker

March 7, 1997

Submitted to:

Mr. Jerry Bielak
Noise Research Unit, Noise Engineering
MS 67-ML
P. O. Box 3707
Boeing Commercial Airplane Group
Seattle, WA 98124-2207



I. INTRODUCTION

It is reasonable to assume that future commercial aircraft will have to comply with increasingly stringent environmental noise pollution regulations. This may require engine and engine nacelle manufacturers to improve the efficiency of current acoustic liner designs which often consist of fine wire-mesh screens bonded to honeycomb-backed circular orifices. It has been well documented that the acoustic resistance of these kinds of liners in flow duct applications are insensitive to the effects of grazing flow speed and sound pressure amplitude¹. However, the bonding of screens to honeycomb-backed circular orifices significantly increases production and maintenance costs and imposes additional weight relative to non-screen liners.

A novel and proprietary cavity-backed sound absorbing liner design concept has been developed, based on unique elongated orifice shapes that are insensitive to both grazing flow speed, grazing flow boundary-layer thickness and sound pressure amplitude. An impedance prediction model of the liner has been derived using fluid mechanical, lumped element concepts. The impedance model was calibrated and its accuracy verified experimentally in acoustic wind tunnel facilities.

The report is organized as follows. Following this introduction, the liner impedance model is derived in Section II. The results of the experimental program is described in Section III. The report closes in Section IV with an application of the impedance model to design linear or almost linear sound absorbing liners.

II. MODEL DERIVATION

A semi-empirical impedance prediction model is derived for the case of a cavity-backed, single orifice liner. Later, the model will be extended to multiple orifices backed by a common cavity. The derivation is based on applying conservation of unsteady mass and vertical momentum flux across the control volume shown in Figure 1. It is assumed that the cavity pressure P_{cav} can be accurately modeled using one-dimensional acoustics. Referring to Figure 1, V_{∞} represents the grazing flow incident to the resonator, $V_{\infty}S_{\infty}$ represents the grazing volume flow rate deflected into the elongated orifice by the local sound pressure field, $S_o = WL$ represents the control volume surface where W and L represent orifice width and length respectively, u_o represents the vertical acoustic velocity component within the orifice, H represents an orifice lumped element inertial length parameter, u_{vc} represents the sound particle velocity at the control volume "vena contracta", S_{vc} represents the cross-sectional area of the "vena contracta" and τ is the resonator face-sheet plate thickness,.

Conservation of Mass. Using the arguments proposed by Tempkin², when $H \ll \lambda$, the conservation of mass flux within the control volume may be written,

$$u_o S_o + V_{\infty} S_{\infty} = u_{vc} S_{vc} \quad (1)$$

Thus to first order, the pumping of volume flow into and out-of a resonator orifice is governed by unsteady, incompressible motion. This makes sense because acoustic changes can occur only over scale lengths on the order of an acoustic wavelength.

Conservation of Vertical Momentum. Again, following Tempkin, when $H \ll \lambda$, the conservation of momentum in the vertical direction may be written,

$$\rho_0 S_o H \frac{du_o}{dt} + \rho_0 (u_{vc}^2 S_{vc} - u_o^2 S_o) = P_{inc} S_o - P_{cav} S_o - \tau_w S_{w_o} \quad (2)$$

The various terms in Eq. (2) are explained below:

- The first term on the left-hand-side (LHS) represents the rate of increase of momentum stored in the control volume. Here ρ is the fluid density and H is an unknown lumped element inertial length parameter.
- The second term on the LHS represents a Bernoulli type of nonlinear momentum flux increase across the control surfaces S_o and S_{vc} .
- The first term on the right-hand-side (RHS) represents the incident acoustic driving force acting on the control surface S_o .
- The second term on the RHS represents the cavity restoring force acting upon the fluid pumped into the cavity interior volume. It can be estimated by solving the one-dimensional wave equation in the cavity resulting in the following expression,

$$P_{cav} = -i\rho_0 c_o \sigma \cot\left(\frac{\omega L_{cav}}{c_o}\right) u_o \quad (3)$$

where L_{cav} represents the cavity depth, c_o is the fluid speed of sound and σ is the perforate percent open area.

- The third term on the RHS represents the momentum loss from frictional wall shear stresses τ_w distributed over the face-plate thickness wetted area $S_w = 2L(\tau+W)$. The wall shear stress is defined as,

$$\tau_w \equiv \mu_o \left. \frac{\partial u}{\partial y} \right|_w \approx \frac{\mu_o u_o}{L_{ch}} \quad (4)$$

where L_{ch} is a characteristic length. The shear stresses are assumed to be generated from acoustic and steady-state (Poiseuille) shear stresses. The acoustic stresses are assumed to be proportional to the acoustic boundary-layer thickness $(\nu_o/\omega)^{1/2}$ and the steady-state stresses are assumed to be proportional to u_o/W . These assumptions result in derivation of the following model for the vertical shear stresses,

$$\tau_w S_w = 2\rho_o \tau (L+W) \left[K_{SS} \frac{\nu_o}{W} + K_{AC} \sqrt{\nu_o \omega} \right] u_o \quad (5)$$

The parameters K_{SS} and K_{AC} are unknown and must be determined from experimental data.

Substituting Eq. (1) into Eq. (2) and introducing an acoustic discharge coefficient C_D and a grazing flow coefficient C_{∞} defined as

$$C_D \equiv \frac{S_{vc}}{S_o} = \frac{u_o}{u_{vc}}; \quad C_\infty \equiv \frac{S_\infty}{S_o} \quad (6)$$

and combining Eqs. (1-6) yields after some algebra and retaining only acoustic terms,

$$H \frac{du_o}{dt} + \left[\left(\frac{1-C_D}{C_D} \right) u_o^2 + 2 \frac{C_\infty}{C_D} V_\infty u_o \right] + 2 \left(1 + \frac{W}{L} \right) \frac{\tau}{W} \left(K_{SS} \frac{v_o}{W} + K_{AC} \sqrt{v_o \omega} \right) u_o - i c_o \sigma \cot(kL_{cav}) u_o = \frac{P_{inc}}{\rho_o} \quad (7)$$

where $k = \omega/c_o$.

Equation (7) is nonlinear and should be solved numerically to achieve a dynamically steady-state solution followed by a FFT analysis to calculate the fundamental harmonic time-dependent velocity component. Although this procedure is numerically straight-forward, it complicates the liner design. The following simplified scheme is proposed. First, assume that the sound field is harmonic so that acoustic quantities are written as,

$$u_o = \hat{u}_o e^{i\omega t} \quad (8)$$

To simplify the notation, the symbol ($\hat{}$) is deleted in the remainder of this report and it is understood that only acoustic amplitudes are considered. Second, the quantity u_o^2 on the LHS of Eq. (7) is written as

$$u_o^2 \cong e^{i\omega t} u_o^2 \quad (9)$$

Equation (9) can be interpreted as retaining only the harmonic acoustic energy or equivalently the simplification results in the loss of higher harmonic acoustic energy. It is important to understand that nonlinear acoustic jetting effects are unaffected by this simplification. Since we are interested in using slot liners to achieve linear or near linear sound absorbing liners, this simplification is quite reasonable.

Substituting Eqs. (8 & 9) into Eq. (7) yields the following quadratic expression for u_o ,

$$u_o^2 + \frac{C_D}{(1-C_D)} \{ \alpha' + i\beta' \} u_o - \frac{C_D}{(1-C_D)} \frac{P_{inc}}{\rho_o} = 0 \quad (10)$$

where the parameters α' and β' are defined as

$$\alpha' \equiv 2 \left(1 + \frac{W}{L} \right) \left(\frac{\tau}{W} \right) \left[K_{SS} \left(\frac{v_o}{W} \right) + K_{AC} \sqrt{v_o \omega} \right] + 2 \frac{C_\infty}{C_D} V_\infty \quad (11a,b)$$

$$\beta' \equiv \omega H - c_o \sigma \cot(kL_{cav})$$

The solution to Eq. (10) is

$$u_o = \sqrt{\frac{C_D}{(1-C_D)} \frac{P_{inc}}{\rho_o} + \left[\frac{C_D}{2(1-C_D)} (\alpha' + i\beta') \right]^2} - \frac{C_D}{2(1-C_D)} (\alpha' + i\beta') \quad (12)$$

Since the acoustic velocity volume flow pumped into and out-of the resonator must be equal over an entire cycle, Eq. (12) is assumed to be also valid over an entire cycle. This is based upon the assumption that over long time periods relative to the incident sound period, the time-averaged volume inflow and out-flow must be equal over a cycle to insure that the mean cavity pressure is constant, independent of time.

The normalized impedance $Z/\rho_o c_o$ of a Helmholtz resonator is defined as

$$\frac{Z}{\rho_o c_o} \equiv \frac{P_{inc}}{\rho_o c_o u_{cav}} = \frac{P_{inc}}{\rho_o c_o \sigma u_o}; \quad u_{cav} = \sigma u_o \quad (13)$$

Substituting u_o from Eq. (12) into Eq. (13) results, after some algebra, in the following expression for impedance,

$$\frac{Z}{\rho_o c_o} = \frac{(\alpha + i\beta)}{2\sigma} + \frac{1}{\sigma} \sqrt{\frac{(1-C_D)}{C_D} \left(\frac{P_{inc}}{\rho_o c_o^2} \right) + \left(\frac{\alpha + i\beta}{2} \right)^2} \quad (14)$$

where the parameters α and β are now defined as

$$\alpha \equiv 2 \left(1 + \frac{W}{L} \right) \left(\frac{\tau}{W} \right) \left[K_{SS} \left(\frac{v_o}{WC_o} \right) + K_{AC} \sqrt{\frac{v_o \omega}{c_o^2}} \right] + 2 \frac{C_\infty}{C_D} \frac{V_\infty}{c_o} \quad (15a,b)$$

$$\beta \equiv \frac{\omega H}{c_o} - \sigma \cot(kL_{cav})$$

Equation (14) is defined in terms of the following unknown parameters: K_{SS} , K_{AC} , C_D , C_∞ and H . These parameters are assumed to be independent of time and hence frequency.

III. EXPERIMENTAL PROGRAM

An experimental program was undertaken to provide a data base in order to generate empirical curve-fits of the five parameters defined above. Table I defines the important parameters of nine perforate resonators, six of which were tested in the HAE Acoustic Wind Tunnel Facility and three in the NASA Langley Acoustic Wind Tunnel and Impedance Tube Facilities.

Table I. Summary of Perforate Resonator Properties

Slot ID	Slot Width (in)	τ (in)	W/τ	Slot Spacing (in)	L (in)	L_{cav} (in)	N	σ (%)	Test Location
4	0.00464	0.125	0.037	1.414	1.5	0.14	1	0.222	HAE
6	0.00696	0.125	0.056	1.414	1.5	0.33	1	0.332	HAE
8	0.00928	0.125	0.074	1.414	1.5	0.24	1	0.443	HAE
10	0.0116	0.125	0.093	1.414	1.5	0.36	1	0.554	HAE
E	0.0020	0.058	0.034	0.0156	1.25	3.14	80	6.37	HAE
D	0.0030	0.058	0.052	0.0179	1.25	4.5	70	8.36	HAE
C	0.0016	0.058	0.0276	0.0156	1.7	1.5	140	9.52	NASA LANGLEY
B	0.0020	0.058	0.0345	0.0173	1.7	1.5	100	8.50	NASA LANGLEY
A	0.0025	0.058	0.0431	0.0205	1.7	1.5	83	8.82	NASA LANGLEY

HAE Test Program

The perforates identified as 4, 6, 8 & 10 in Table I were constructed with single orifices ($N = 1$) and were used to provide initial design information. They were installed in the HAE Wind Tunnel and their tuned resistances measured as a function of SPL and grazing flow speed using the two microphone measurement scheme developed by Dean³. Figures 2 and 3 summarize test results. Referring to Table I and the upper-half of Figure 2, the tuned resistances of the resonators are plotted as a function of sound pressure amplitude. The lower-half of Figure 2 displays the resistance measurements normalized by their values at very low sound pressure amplitudes. Test results suggest that nonlinear effects become negligible when $W/\tau < 0.037$. Figure 3 display the effects of grazing flow on the tuned resistances of the resonators. Referring to the lower-half of Figure 3, test results suggest that the effects of grazing flow also become negligible when $W/\tau < 0.037$.

The high values of resistance of the single perforate resonators prompted the construction of multiple perforate resonators. In order to achieve resistances on the order of two-to-three " $\rho_0 c_0$ ", resonators A - E were constructed. A least-square-fit of the data was used to calculate the values of the parameters K_{SS} , K_{AC} , C_D , C_{∞} and H and the results of which are summarized below in Table II.

Table II. Least-Square Test Results of Parameters K_{SS} , K_{AC} , C_D , C_∞ and H

Perforate ID	K_{SS}	K_{AC}	C_D	C_∞	H/d_p
E	3.118	0.261	0.5	0.0012	0.7
D	2.564	2.571	0.5	NA	NA*
C	3.255	0.919	0.5	NA	0.7
B	3.442	0.666	0.5	NA	0.7
A	5.056	1.751	0.5	NA	0.7

Referring to Table II, the impedance of resonators A - D were not measured in a grazing flow test facility, only resonator E. Further, only the tuned resistance of resonator D was measured.

Figure 4 graphically display the parameters K_{ac} and K_{ss} as a function of perforate width to face-plate thickness (W/τ). The following empirical curve-fits of the data were derived,

$$K_{SS} = 8165 - 6.692 * 10^3 \left(\frac{W}{\tau}\right) + 1845 * 10^5 \left(\frac{W}{\tau}\right)^2 - 1636 * 10^6 \left(\frac{W}{\tau}\right)^3 \quad (14a)$$

$$K_{AC} = 5.27 - 295 \left(\frac{W}{\tau}\right) + 4734 \left(\frac{W}{\tau}\right)^2 \quad (14b)$$

Figures 5(a,b) summarize the effects of SPL and grazing flow on the impedance of the E resonator. Figures 5(a-c) show that the model equation predicts the resonator resistance and reactance reasonably accurately over the entire frequency, sound pressure amplitude and grazing flow speed range tested. Observe that the reactance data shown in Figure 5c showed no effect of grazing flow, thus the parameter H was assumed to be constant, independent of grazing flow (at least for $V_\infty < 77$ m/s). Figure 5c shows that the orientation of the perforate was insensitive to the direction of the mean flow for values of W/τ on the order of 0.035. This is of considerable importance in aircraft turbofan engine application because it eliminates the need to have an accurate description of the mean flow direction in order to design efficient sound absorbing perforate resonators. Finally, Figure 6 shows that the tuned resistance of the D resonator was also accurately predicted.

NASA Langley Tests

Because the HAE Wind Tunnel grazing flow maximum speed was 77 m/s ($M_\infty = 0.23$) and the corresponding frequency range was $400 < f < 800$ Hz, the three resonators identified as A, B and C in Table I were constructed and tested in the NASA LaRC Acoustic Wind Tunnel Facility to validate the design at grazing flow speeds as high as $M_\infty = 0.5$.

Figures 7(a-c) show the effect of grazing flow on the impedance of the A, B and C resonators as measured in the NASA LaRC Wind Tunnel. The results were compared to measurements of the

impedance of a 2-inch thick Ceramic Liner used by NASA LaRC as a reference linear liner. Test results show that the impedance of all three perforate resonators were about as insensitive to grazing flow as the Ceramic Liner demonstrating the linearity of the perforate resonators.

Figures 8(a-c) show the effect of broadband sound on the impedance of the A, B and C perforate resonators as measured in the NASA LaRC Impedance Tube facility. The resonators were exposed to broadband SPLs of 100 and 110 dB over the frequency range 200 - 3000 Hz. The measurements showed all three resonators were insensitive to SPL. It is important to point out that the derivation of the impedance model was based upon harmonically generated measurements obtained in the HAE Wind Tunnel Facility over the test frequency range 500 - 800 Hz. The accurate prediction of the *broadband* impedance measurements obtained in the NASA LaRC Impedance Tube Facility over the frequency range 200 - 3000 Hz further validates the model.

IV. CONCLUDING REMARKS

The design of sound absorbing liners for aircraft turbofan engines applications requires the liner weight, size and cost to be minimized and its absorption efficiency maximized. Because of the large number of parameters that characterize aircraft liners, this represents a formidable engineering effort. Aircraft liners are influenced by (1) mean flow speed, (2) mean flow speed boundary-layer thickness, (4) duct size, (4) sound amplitude, (5) sound frequency, (6) face-plate thickness, (7) cavity depth, (8) cavity cross-section area, (9) perforate width, (10) perforate length and (11) number of perforates. Three of these parameters can be eliminated with linear liners whose impedance are insensitive to the effects of grazing flow speed, grazing flow boundary-layer thickness and sound pressure amplitude.

The value of the impedance model is demonstrated below by using it to design linear or almost linear sound absorbing liners. The nonlinear factor (NLF) represents the industry standard for determining the linearity of a sound absorbing liner. NLF is defined as

$$NLF \equiv \frac{R_{DC} \left(200 \frac{cm}{sec} \right)}{R_{DC} \left(20 \frac{cm}{sec} \right)} \quad (15)$$

where R_{DC} represents the *steady-state* resistance of a liner defined as

$$R_{DC} \equiv \frac{\Delta P}{u} \quad (16)$$

Here ΔP represents the steady-state pressure drop across the liner and u , the spatial averaged fluid velocity approaching the liner. R_{DC} is usually measured in a flow duct.

To provide guidelines for the design of liners having $NLF < 1.5$, the perforate resonator impedance is assumed to be tuned so that the reactance vanishes and the resonator impedance

simplifies to

$$\frac{Z_{res}}{\rho c} = \frac{R_{res}}{\rho c} = \frac{P_{inc}}{\rho c u_{inc}} = \frac{\alpha}{2\sigma} + \frac{1}{\sigma} \sqrt{\frac{(1-C_D)}{C_D} \left(\frac{P_{inc}}{\rho c^2} \right) + \left(\frac{\alpha}{2} \right)^2} \quad (17)$$

Comparing Eq. (17) to (16), it is clear that the acoustic pressure and velocity P_{inc} and u_{inc} assume the role of the steady-state ΔP and u . With this understanding, the acoustic analogue of Eq. (15) is

$$NLF \equiv \frac{R_{res} \left(200 \frac{cm}{sec} \right)}{R_{res} \left(20 \frac{cm}{sec} \right)} \quad (18)$$

Assuming u_{inc} represents the root-mean-square (rms) acoustic particle velocity approaching a perforate resonator, the following relationship between resonator geometry and incident sound pressure amplitude P_{inc} follows from Eq. (17),

$$u_{inc} = \frac{P_{inc}}{R_{res}} \rightarrow \frac{P_{inc}}{\rho c} = u_{inc} \left[\frac{\alpha}{2\sigma c} + \frac{1}{\sigma} \sqrt{\frac{(1-C_D)}{C_D} \frac{P_{inc}}{\rho c^2} + \left(\frac{\alpha}{2c} \right)^2} \right] \quad (19)$$

Rearranging Eq. (19) to solve for the required incident sound pressure amplitude P_{inc} yields

$$P_{inc} = \frac{\rho u_{inc}^2}{\sigma^2} \left[\frac{\alpha \sigma}{u_{inc}} + \frac{1-C_D}{C_D} \right] \quad (20)$$

The final expression for the NLF follows by substituting Eq. (20) into Eq. (13) and substituting the resulting expression into Eq. (18) to yield, after some algebra,

$$NLF = \frac{\frac{\alpha \sigma}{2c} + \sqrt{\left(\frac{1-C_D}{C_D} \right) \left\{ \left(\frac{200}{c} \right)^2 \left[\frac{\alpha \sigma}{200} + \frac{1-C_D}{C_D} \right] \right\} + \left(\frac{\alpha \sigma}{2c} \right)^2}}{\frac{\alpha \sigma}{2c} + \sqrt{\left(\frac{1-C_D}{C_D} \right) \left\{ \left(\frac{20}{c} \right)^2 \left[\frac{\alpha \sigma}{20} + \frac{1-C_D}{C_D} \right] \right\} + \left(\frac{\alpha \sigma}{2c} \right)^2}} \quad (21)$$

The following sample calculation demonstrates the value of the model is designing liners having $NLF < 1.5$. Assume a liner has the following geometric and fluid properties: face-plate thickness $\tau = 0.04$ -inches, cavity depth $L_{cav} = 1.5$ -inches, cavity diameter $D_{cav} = 0.375$ -inches,

perforate length $L = 0.35$ -inches and perforate open area ratios $\sigma = 0.04, 0.08, 0.12$ and 0.16 , fluid density $\rho = 0.0012$ gm/cm³, fluid sound speed $c = 34,000$ cm/sec and fluid viscosity $\nu = 0.15$ cm²/sec.

Figure 10 shows the results of substituting these values into Eq. (21) as a function of the ratio of perforate width-to-face-sheet thickness, W/τ . In interpreting Figure 10, the following relationship between number of perforates N , perforate width W , perforate length L and cavity cross-section area $S_{cav} = \pi D_{cav}^2/4$ was used,

$$\sigma = \frac{NWL}{S_{cav}} \rightarrow N = \frac{\sigma S_{cav}}{WL} \quad (22)$$

Referring to Eq. (22), small values of W/τ for fixed values of σ and τ require large numbers of perforates. Conversely, large values of W/τ require small numbers of perforates. For values of $W/\tau > 0.1$, the number of perforates $N < 10$ which is less than the number of perforates used in the derivation of the perforate impedance model (see Table I). For this reason, the accuracy of Figure 10 is not known for values of $W/\tau > 0.1$.

References

1. Rice, E. J., "A Model for the Acoustic Impedance of Linear Suppressor Materials Bonded on Perforated Plate", AIAA Paper 81-1999.
2. Temkin, S. Elements of Acoustics, John Wiley & Sons, pg. 179, 1981.
3. Dean, P. D. , "An In-Situ Method of Wall Acoustic Impedance Measurement in Flow Ducts", JSV, Vol. 34, No. 1, p. 97, 1974.

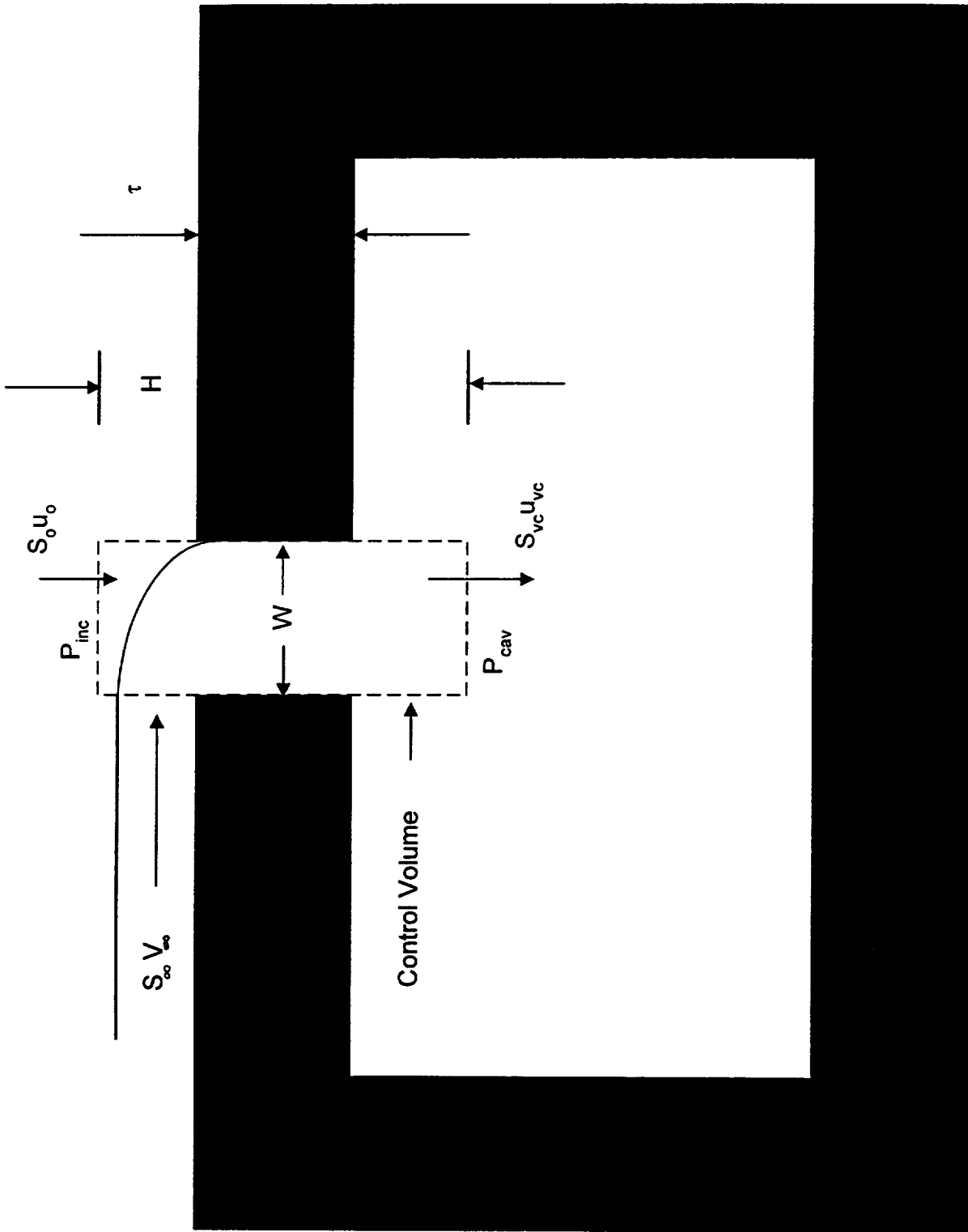


Figure 1. Control Volume Used in Model Derivation

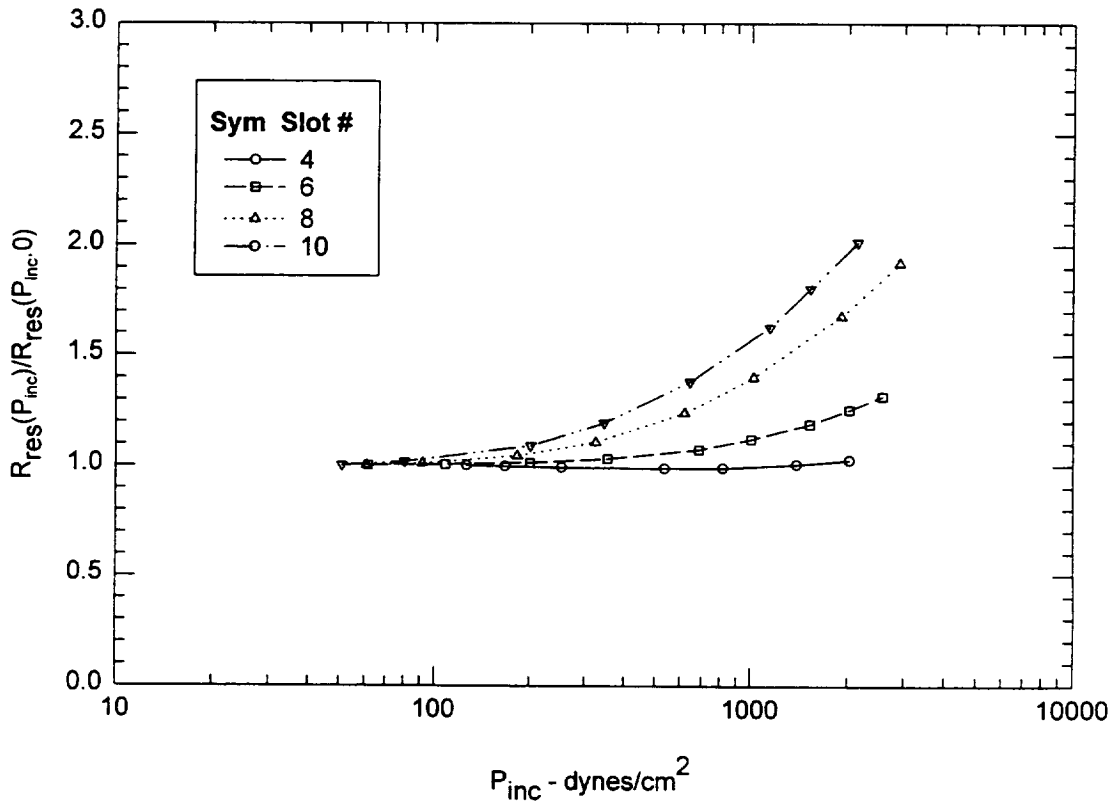
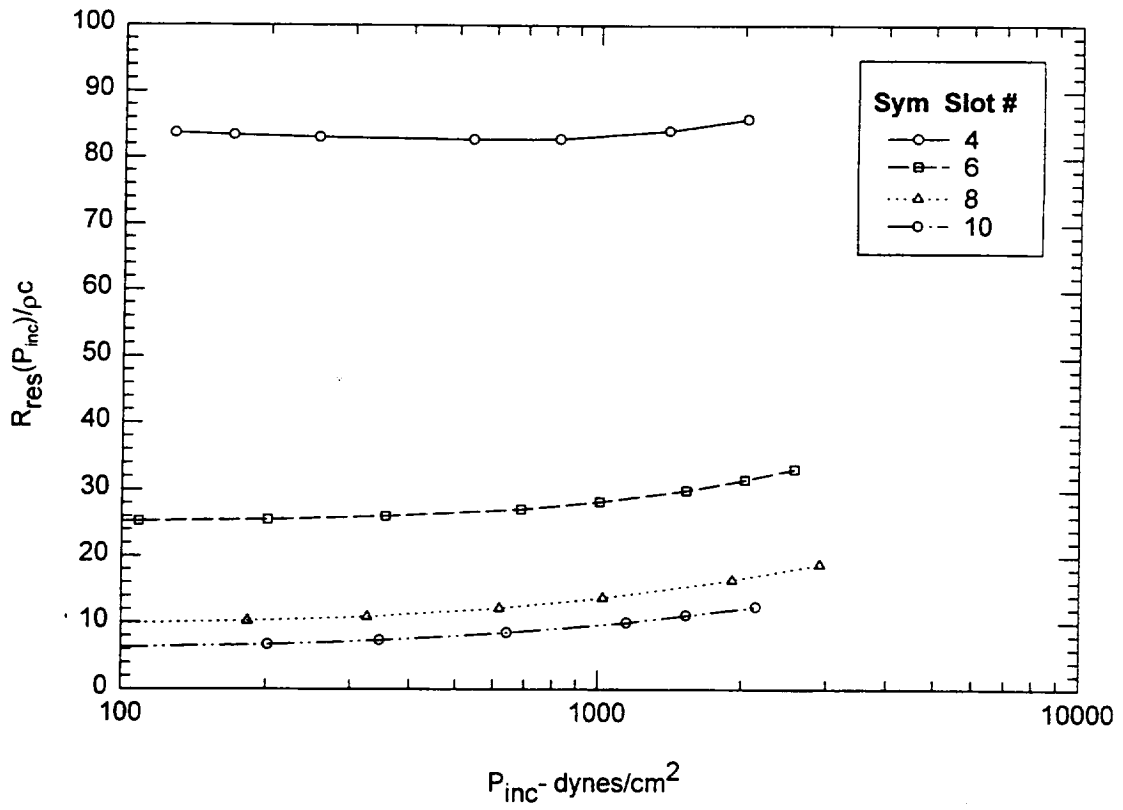


Figure 2. Effect of SPL on Tuned Resistances of Slot Resonators 4, 6, 8 & 10

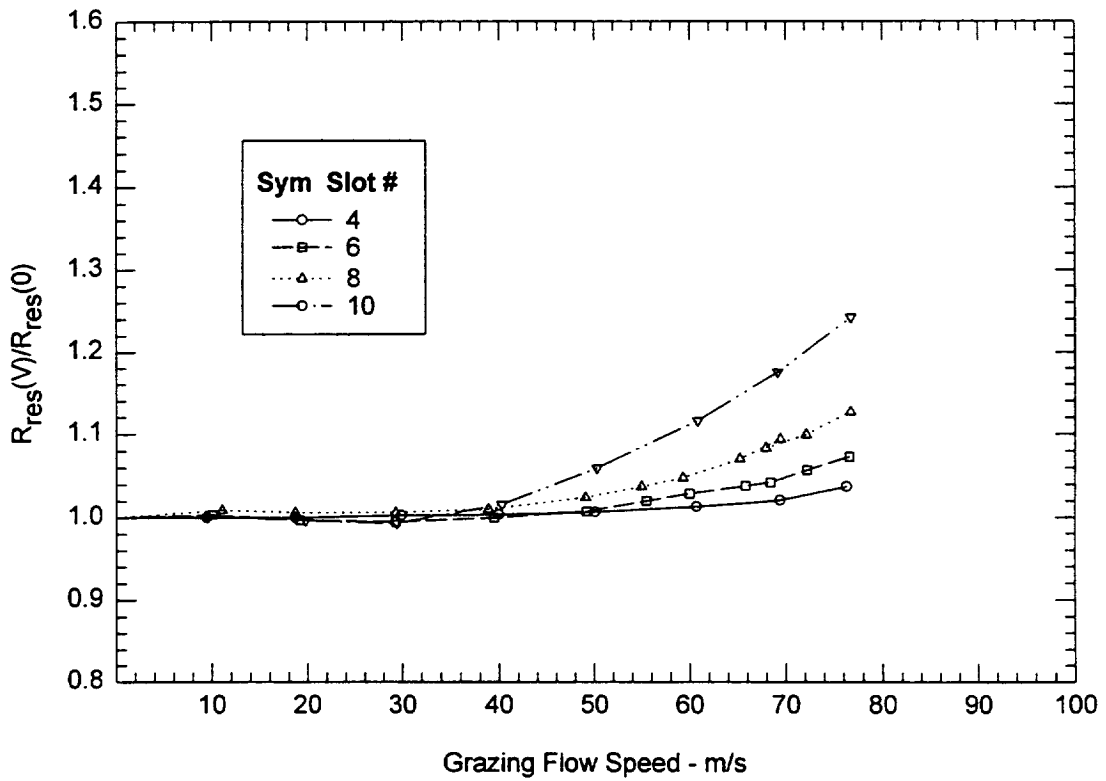
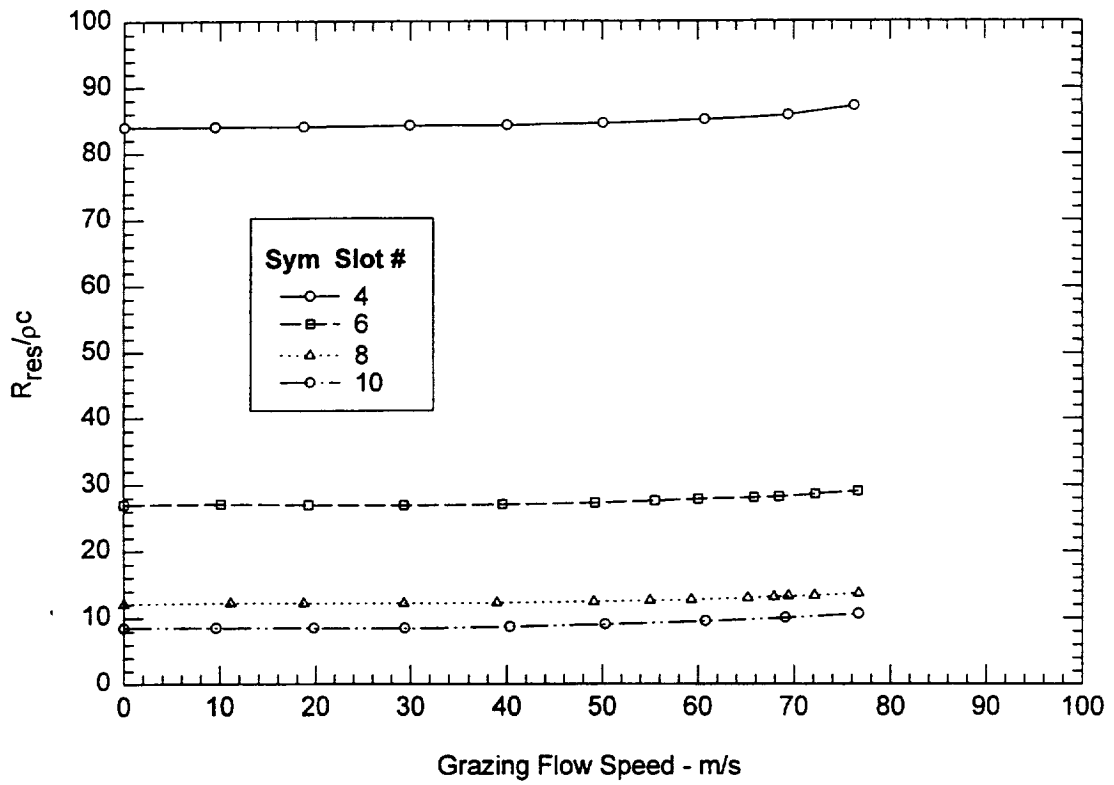


Figure 3. Effect of Grazing Flow on Tuned Resistances of Slot Resonators 4, 6, 8 & 10

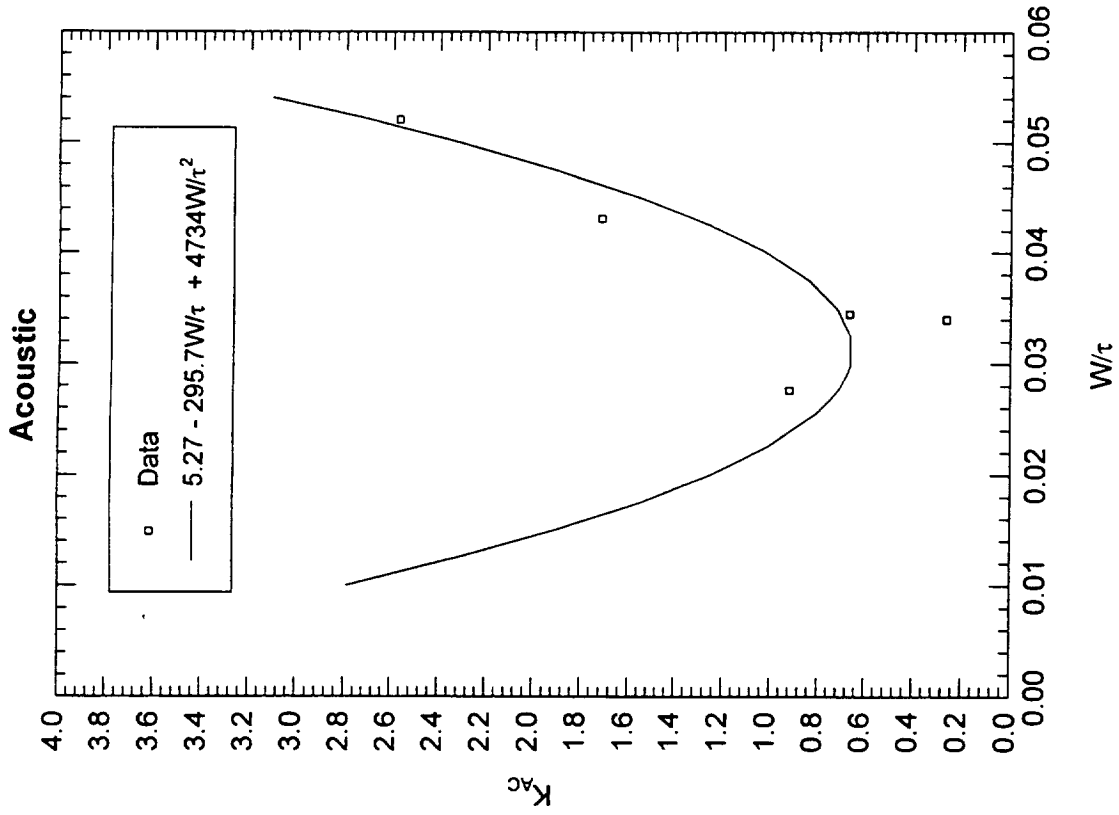
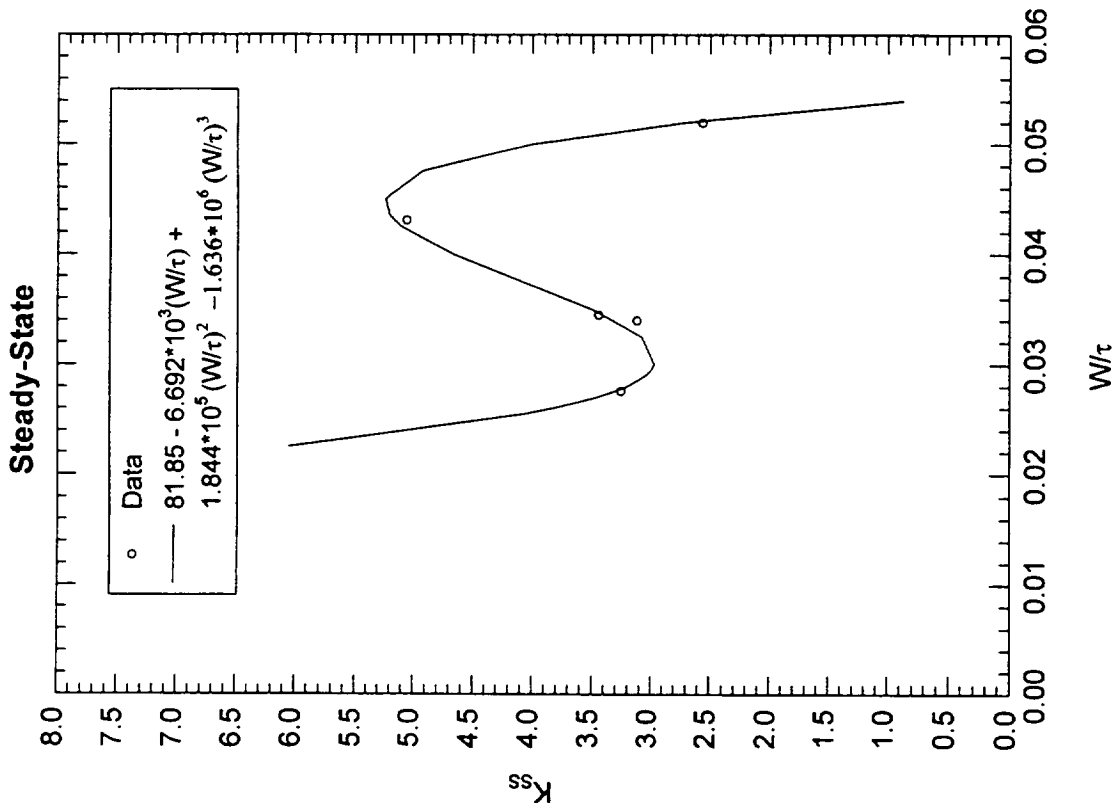


Figure 4. Effect of W/τ on Parameters K_{SS} and K_{AC} for Slots A, B, C, D & E

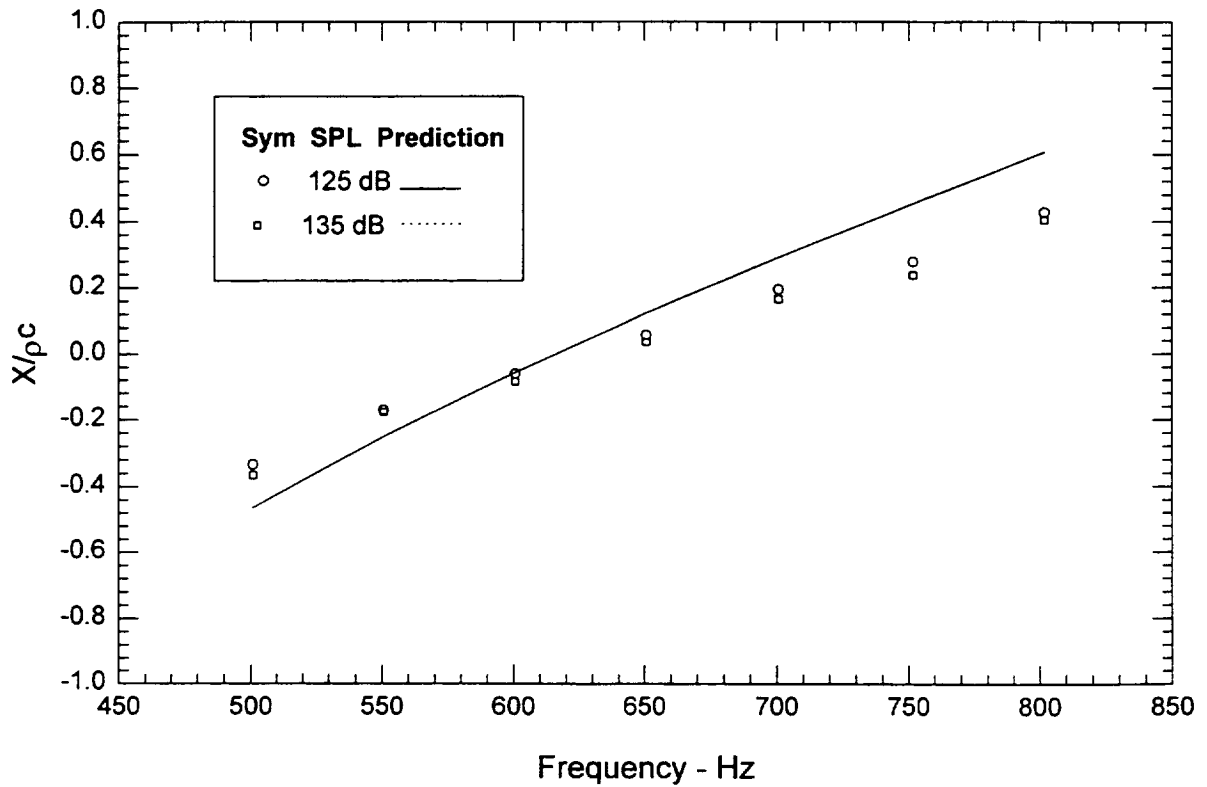
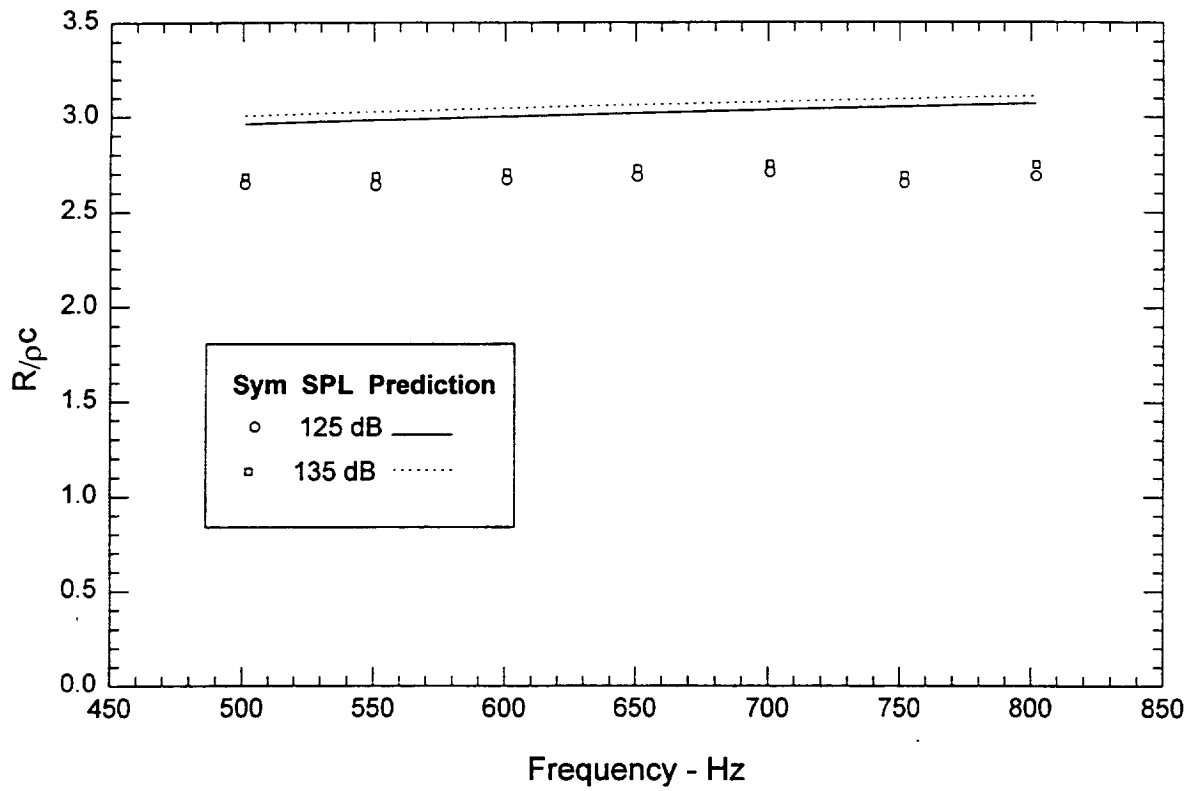


Figure 5a. Predicted vs Measured Impedance of Slot E Resonator: $V = 0$
A1-14

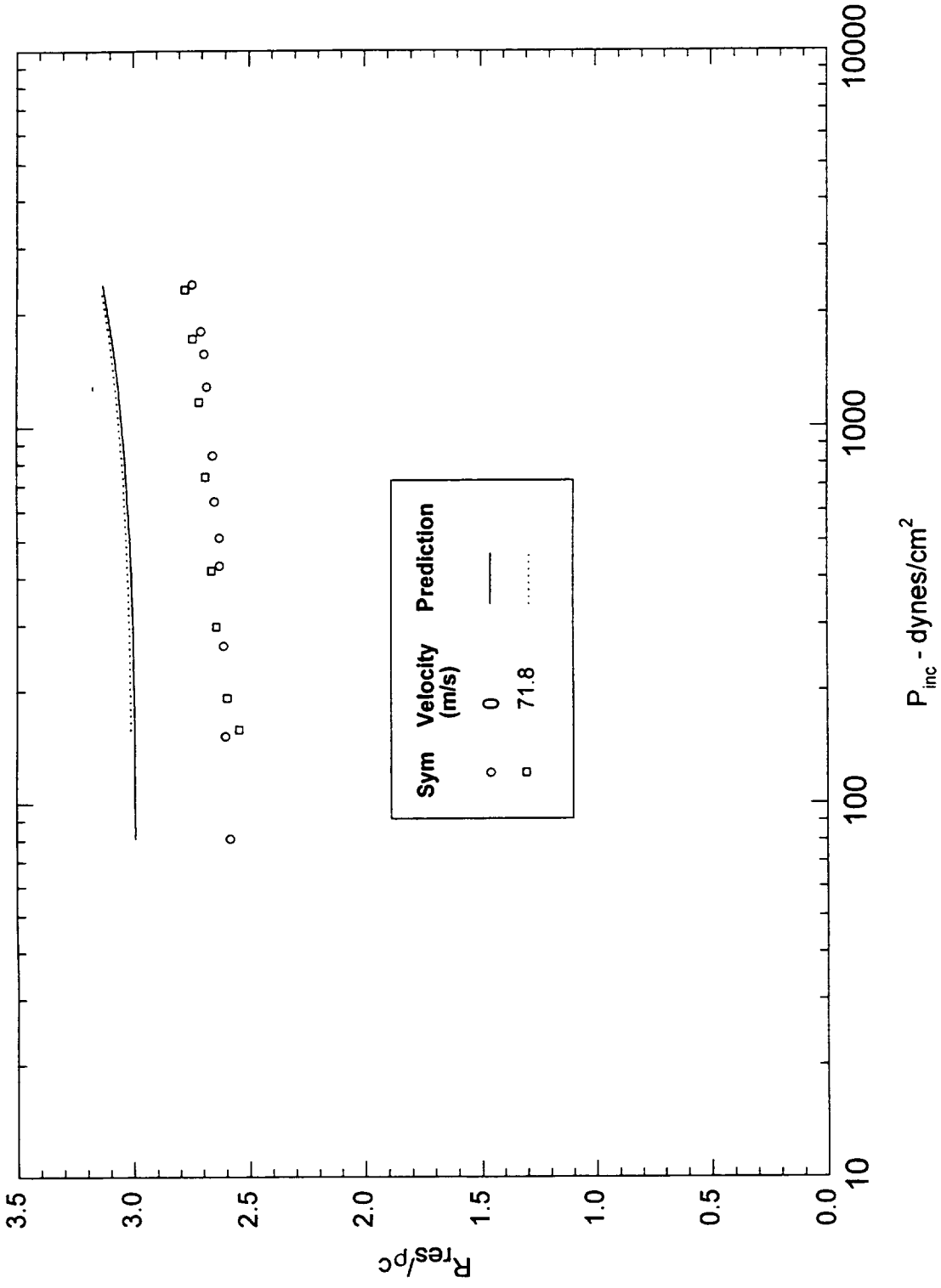


Figure 5b. Measured and Predicted Effect of SPL and Grazing Flow on Tuned Resistance of Slot E Resonator

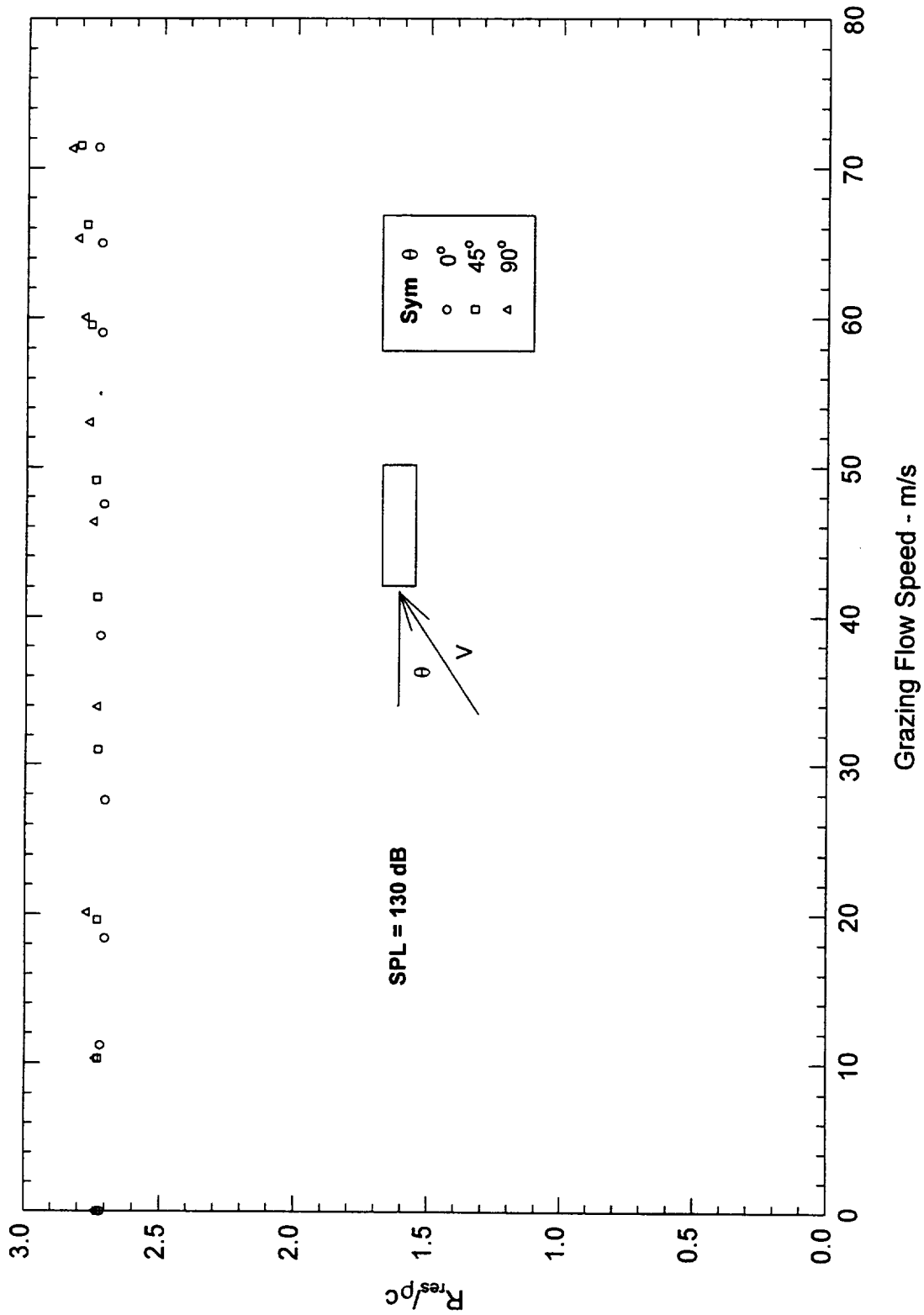


Figure 5c. Effect of Orifice Slot Orientation Relative to Grazing Flow on Tuned Resistance of Slot E Resonator

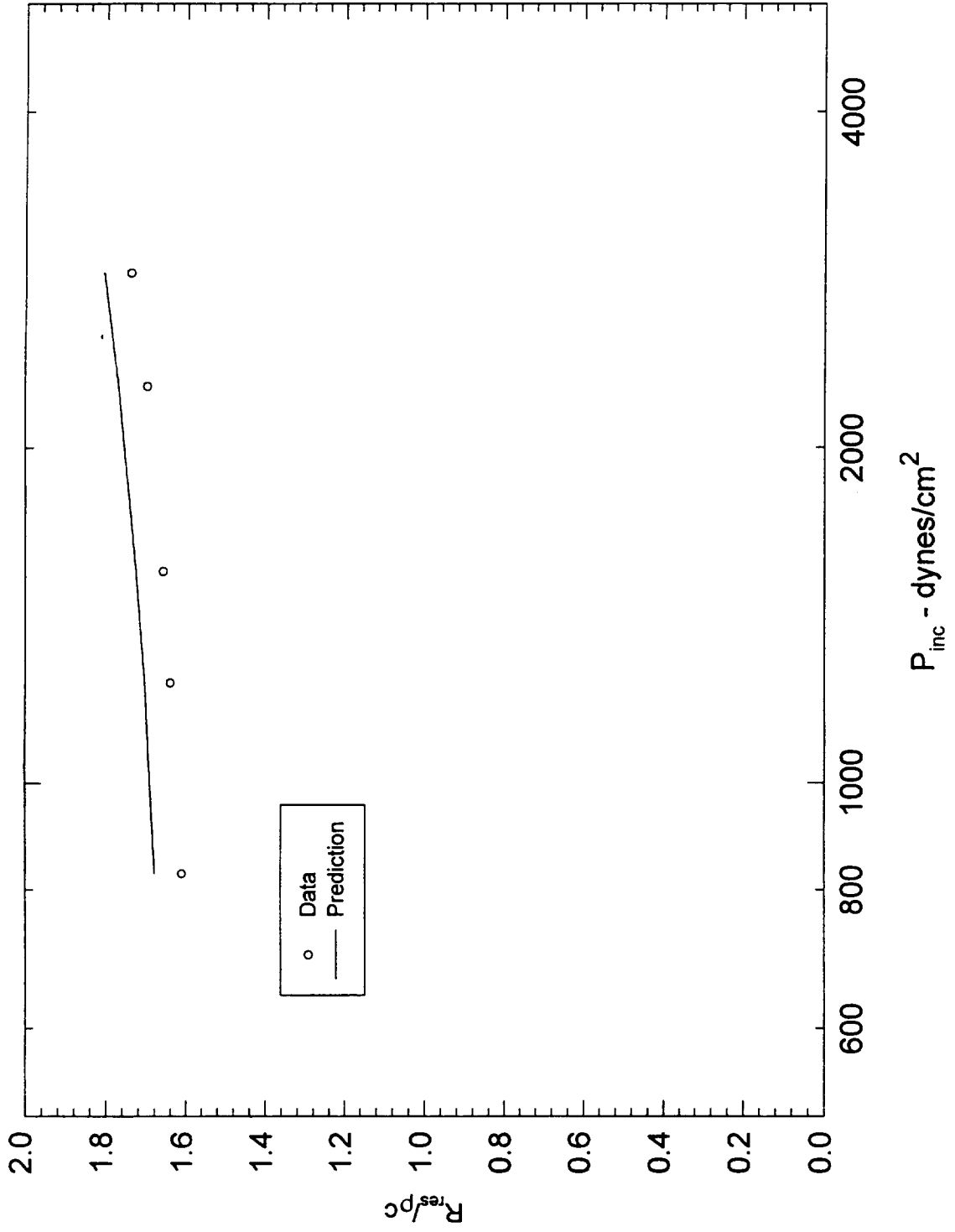


Figure 6. Predicted and Measured Tuned Resistance of Slot D Resonator

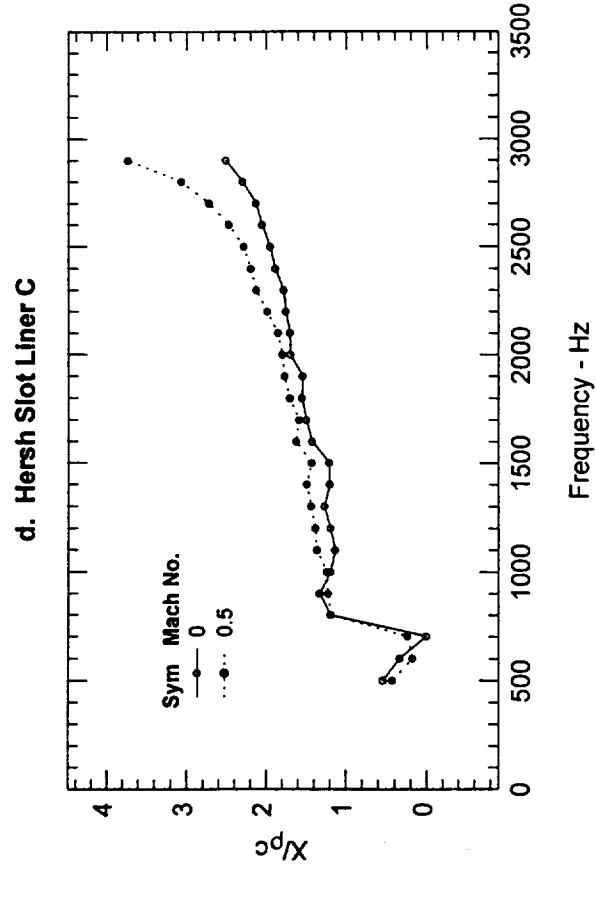
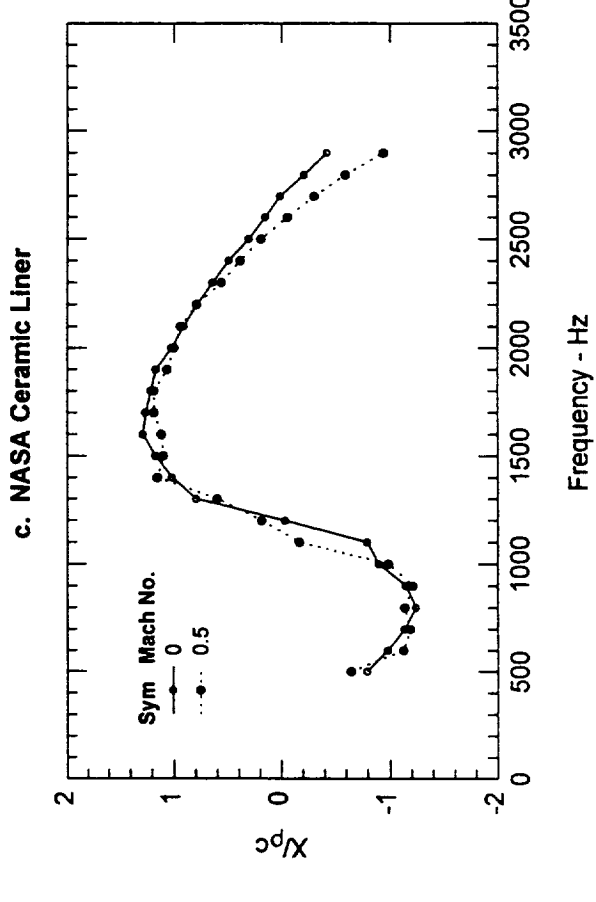
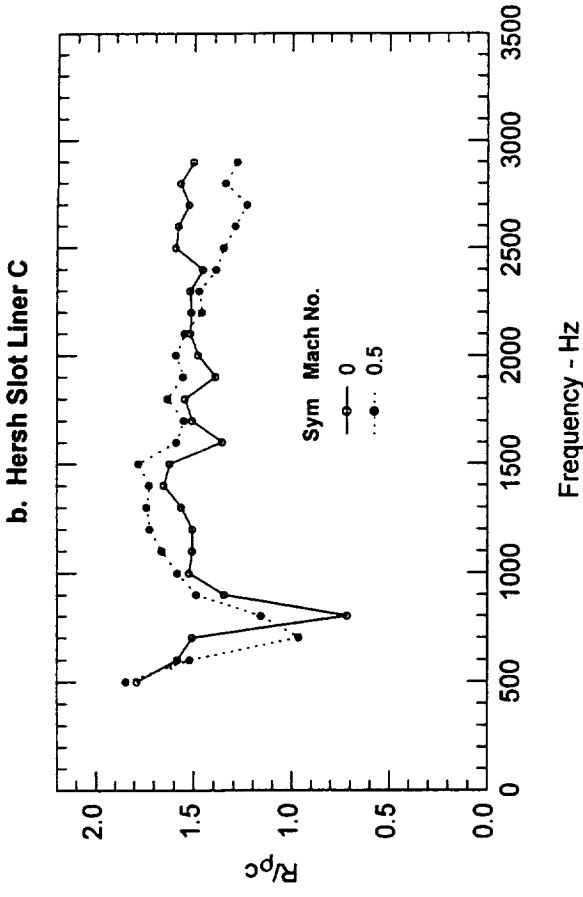
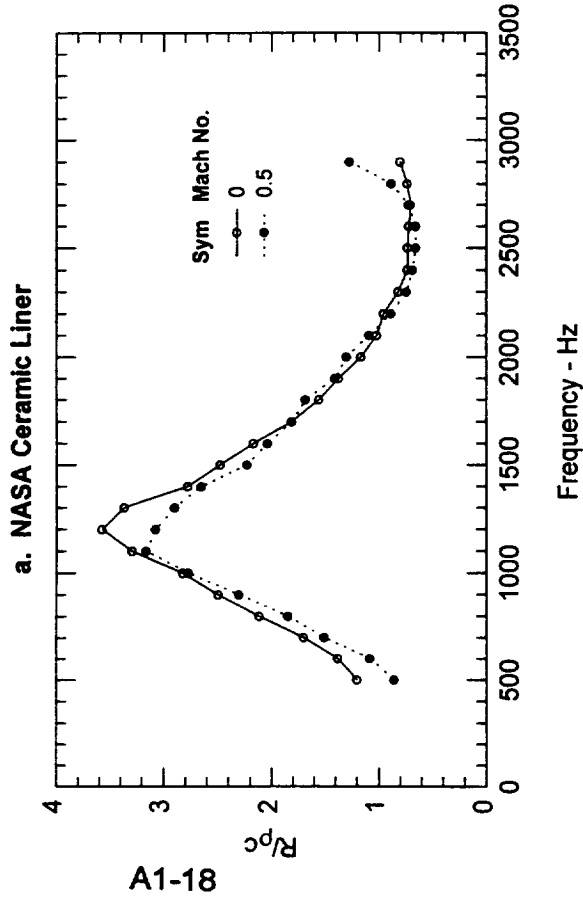


Figure 7a. Effect of Grazing Flow on NASA Langley Linear Ceramic Liner and Slot Liner C @ SPL = 145 dB

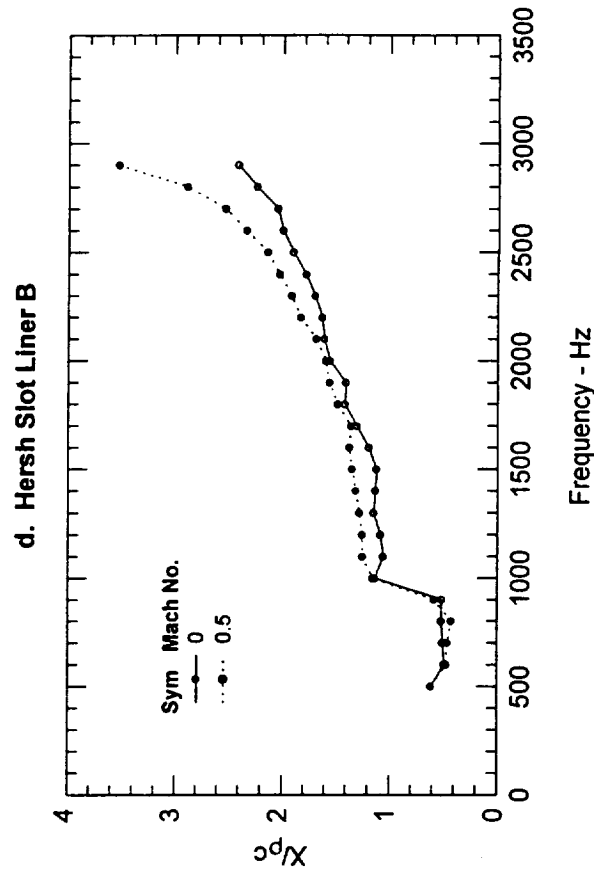
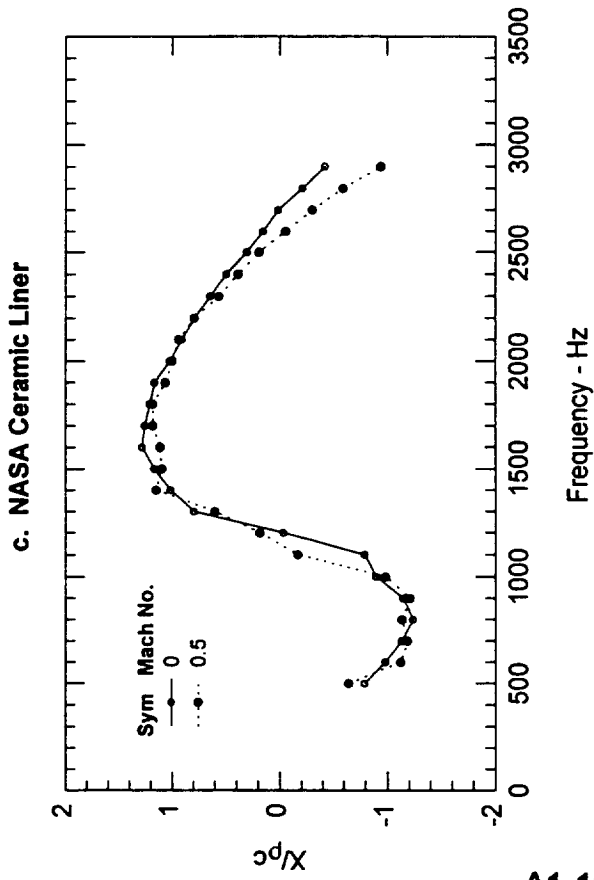
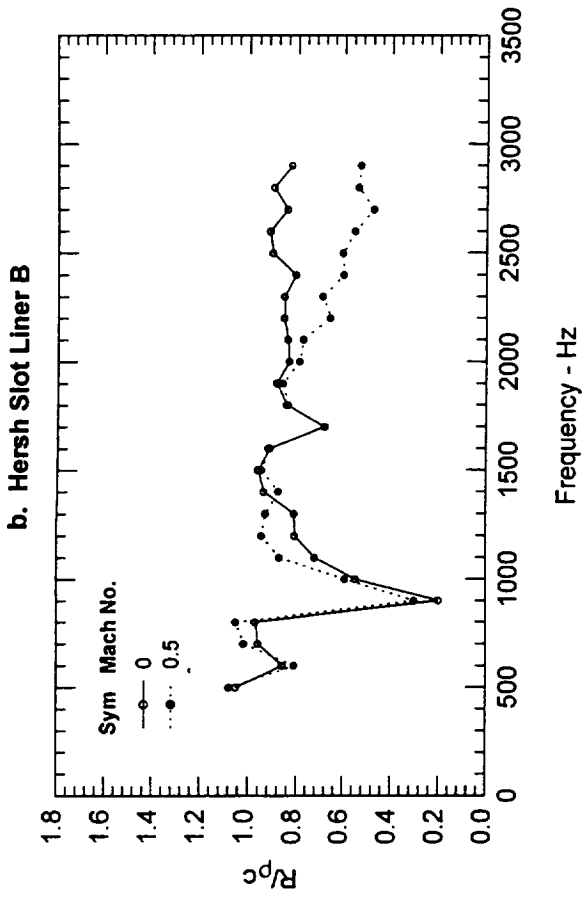
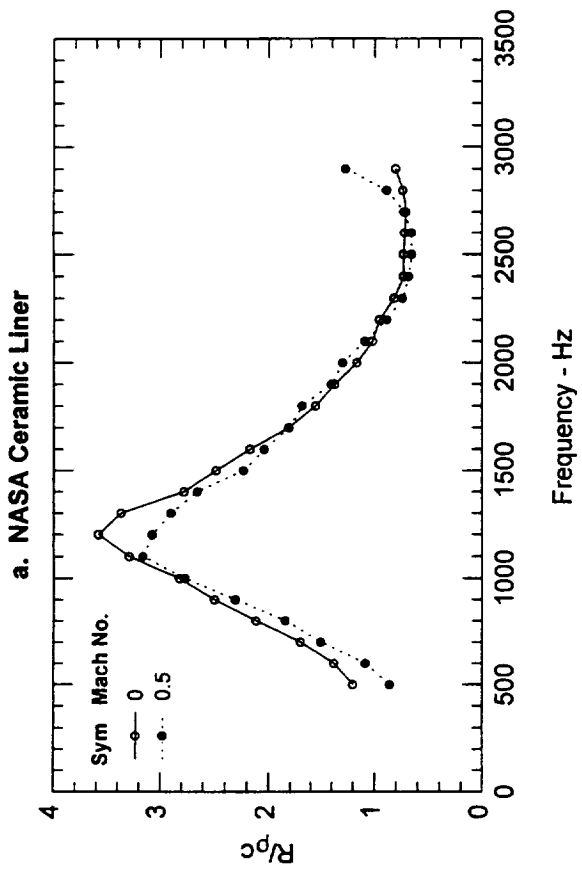


Figure 7b. Effect of Grazing Flow on NASA Langley Linear Ceramic Liner and Slot Liner B @ SPL = 145 dB

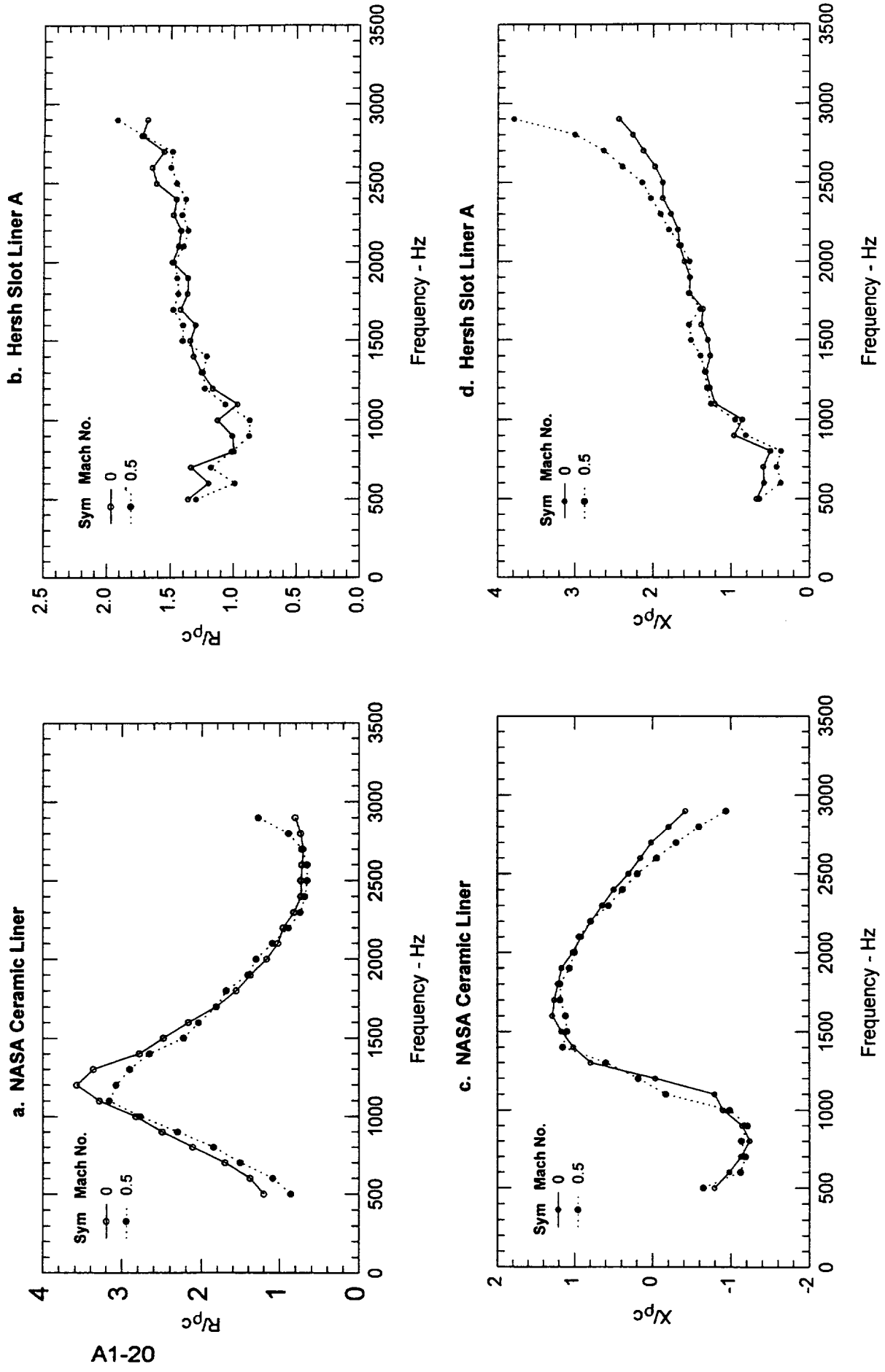


Figure 7c. Effect of Grazing Flow on NASA Langley Linear Ceramic Liner and Slot Liner A @ SPL = 145 dB

Face Plate C - No Blockage

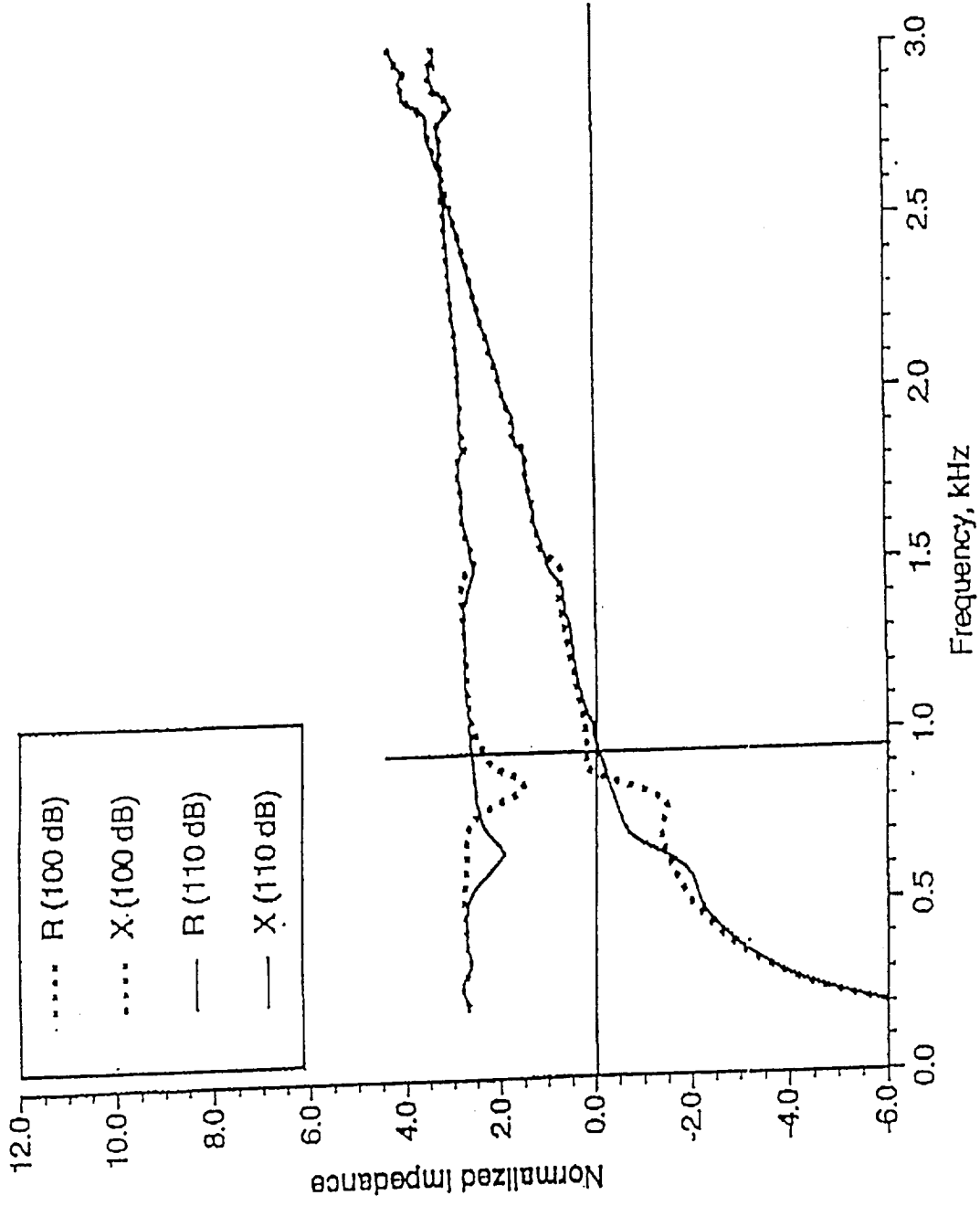


Figure 8a. Effect of SPL on Impedance of C Resonator in Langley Impedance Tube

Face Plate B - No Blockage

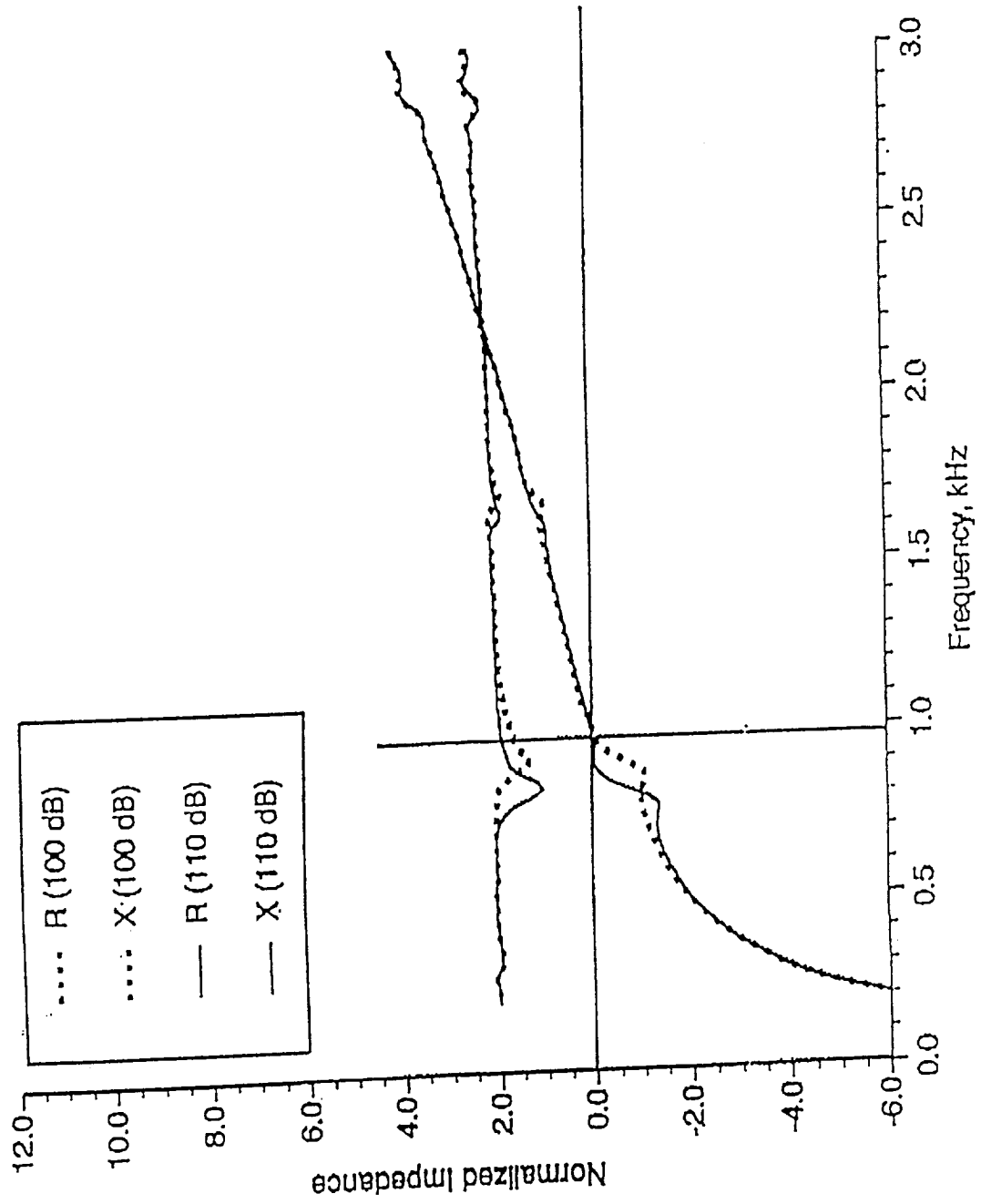


Figure 8b. Effect of SPL on Impedance of R Resonator in Langley Impedance Tube

Face Plate A - No Blockage

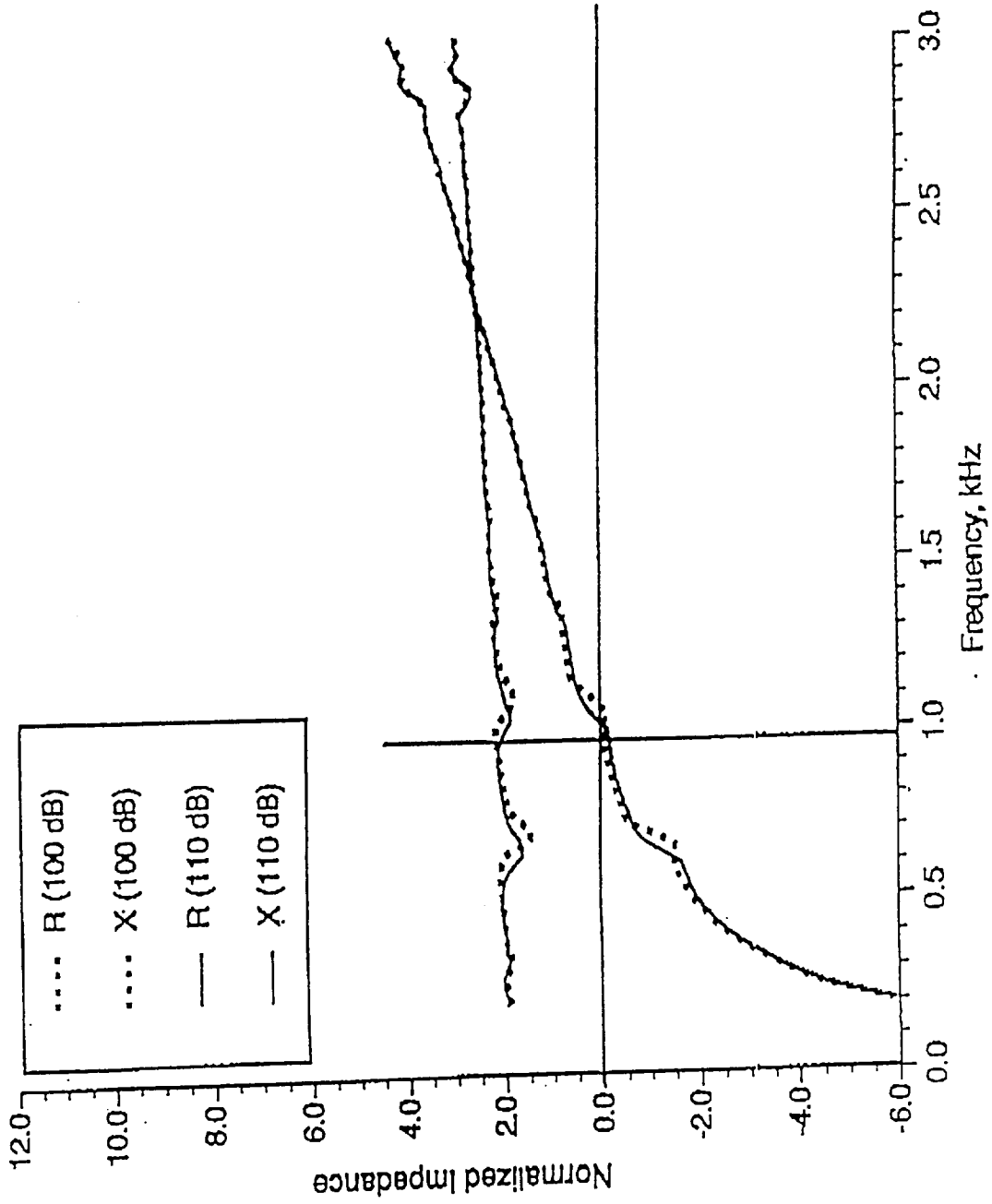


Figure 8c. Effect of SPL on Impedance of A Resonator in Langley Impedance Tube

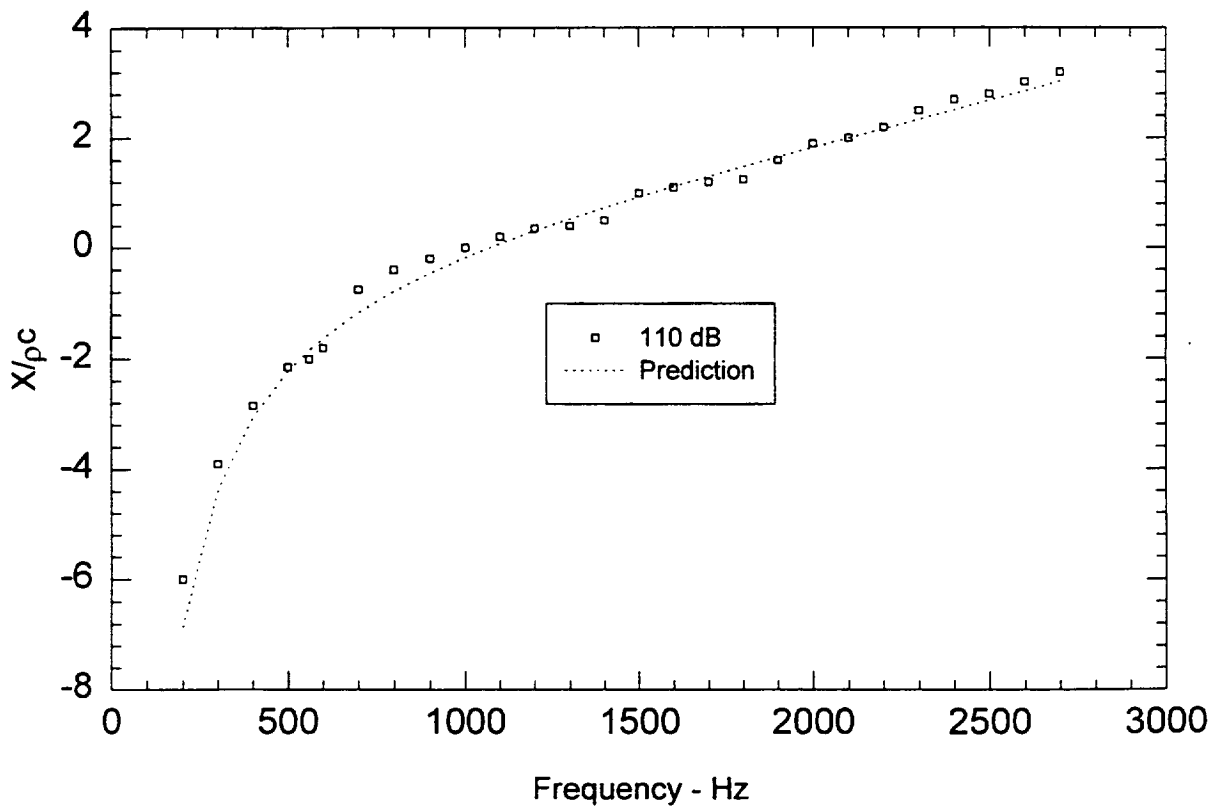
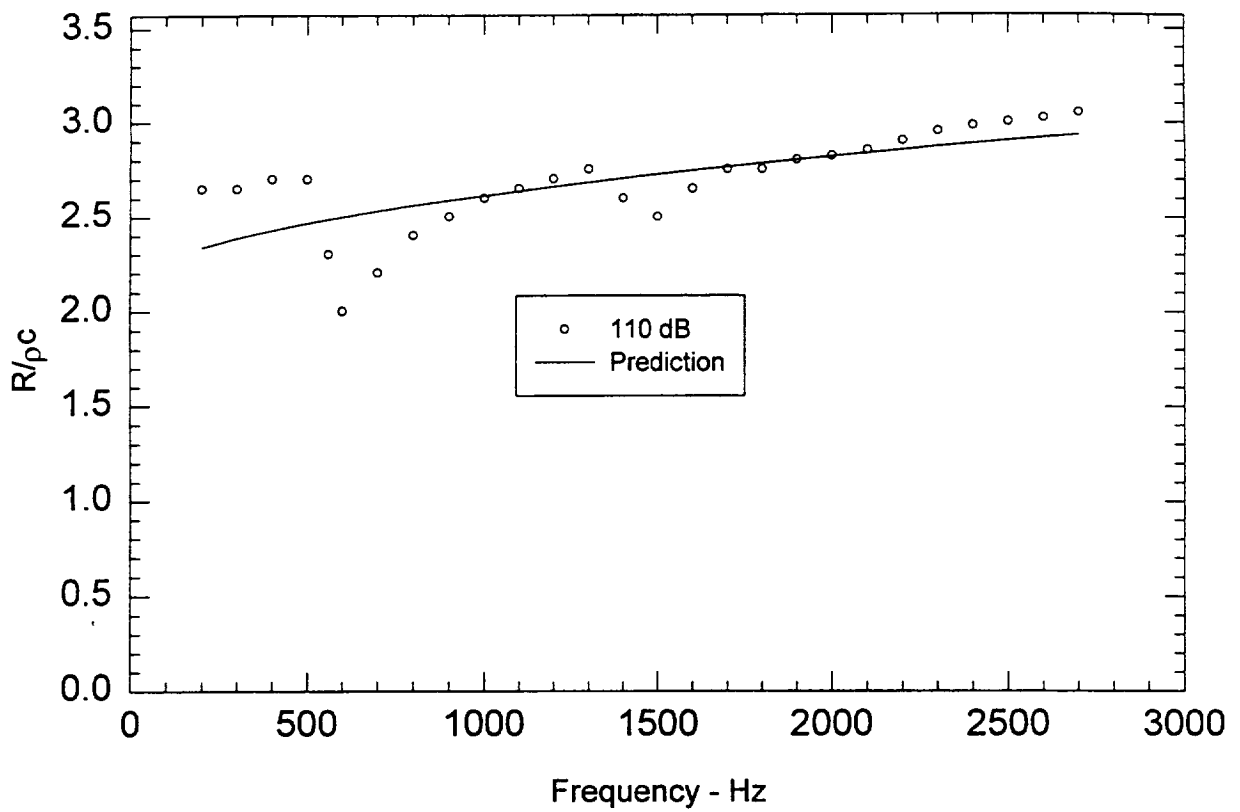


Figure 9a. Measured and Predicted Impedance of Slot C Resonator A1-24

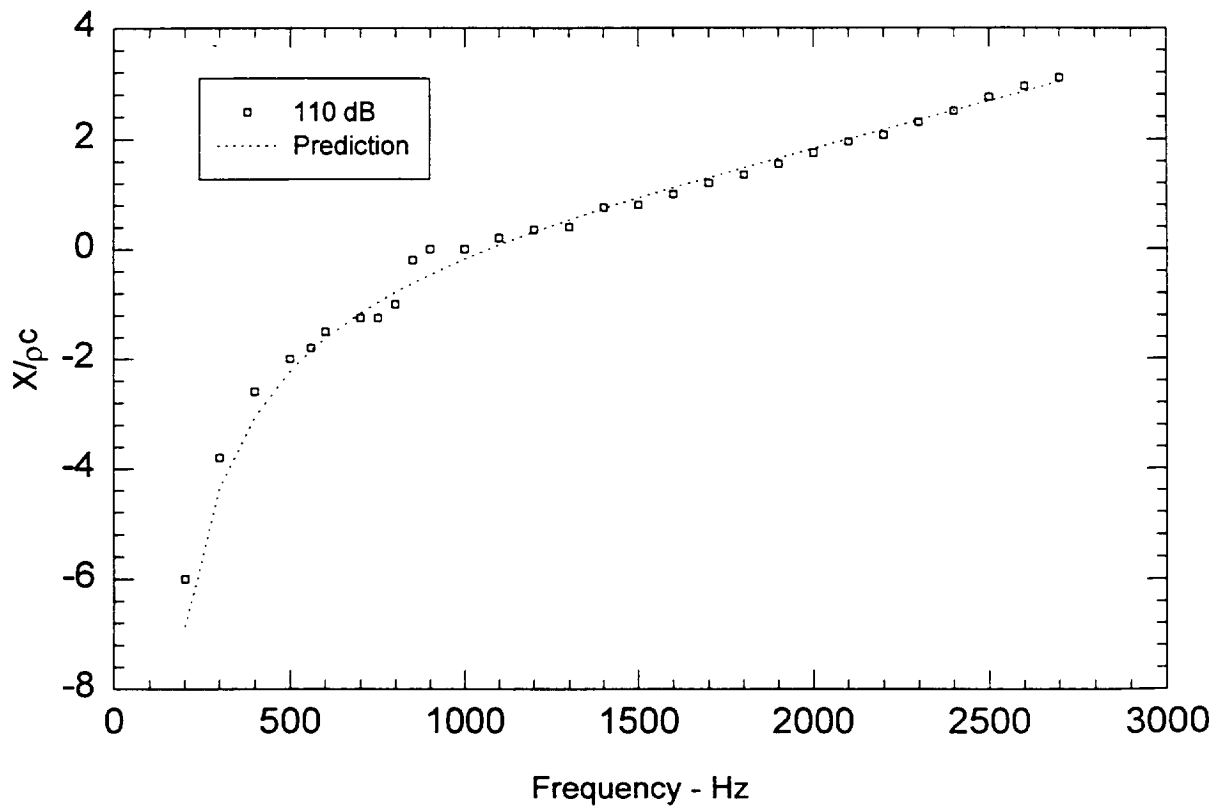
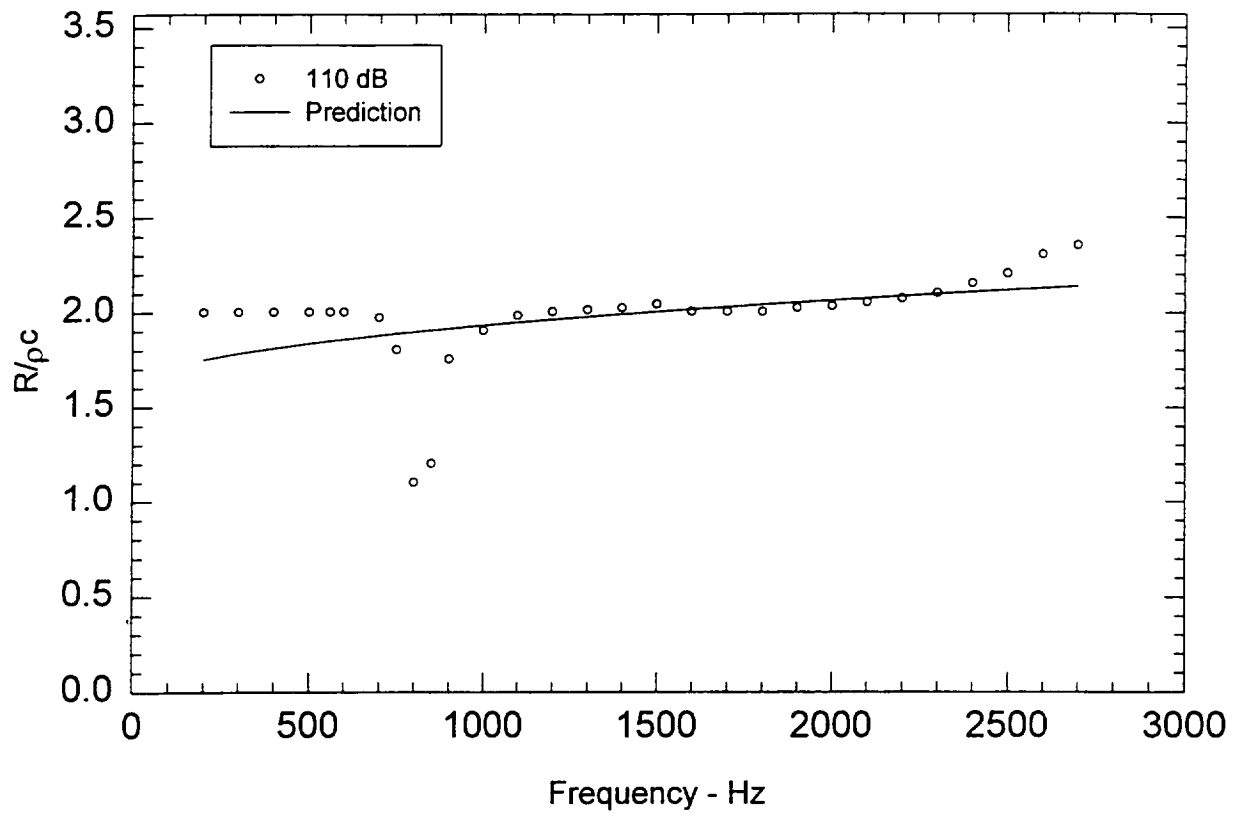


Figure 9b. Measured and Predicted Impedance of Slot B Resonator
A1-25

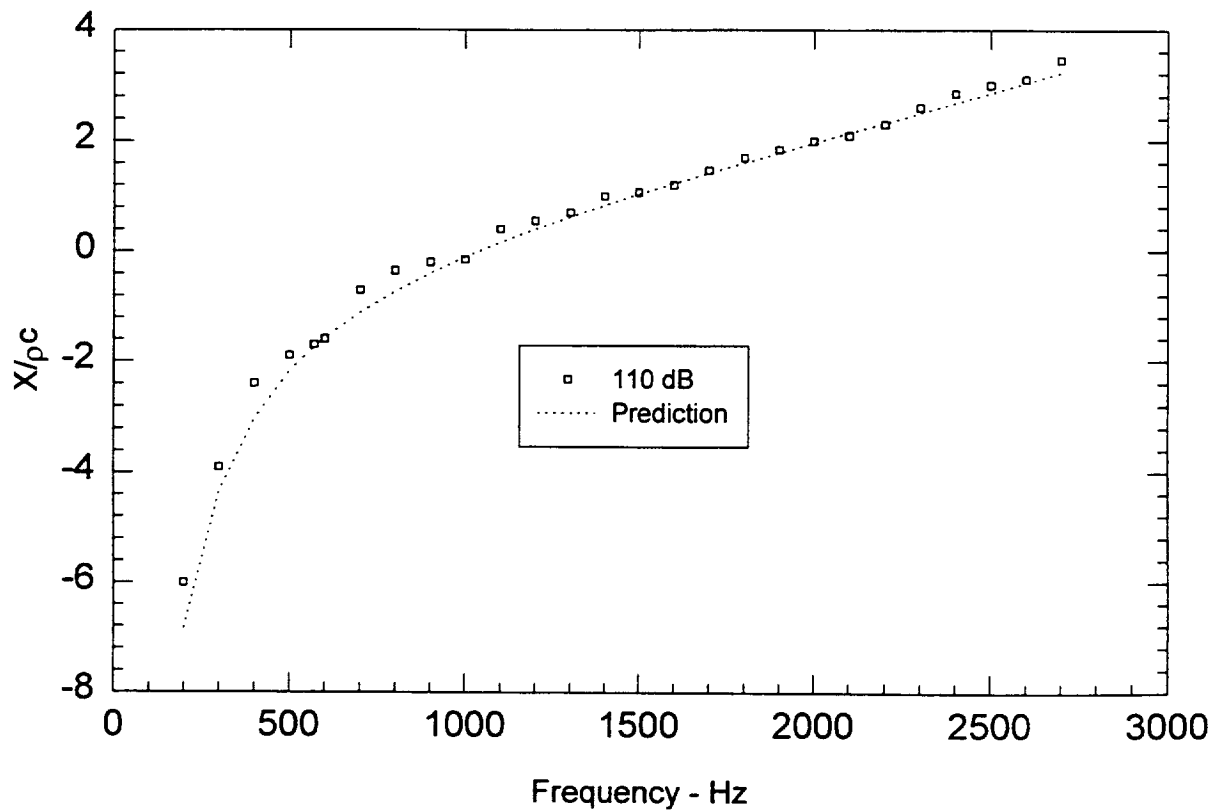
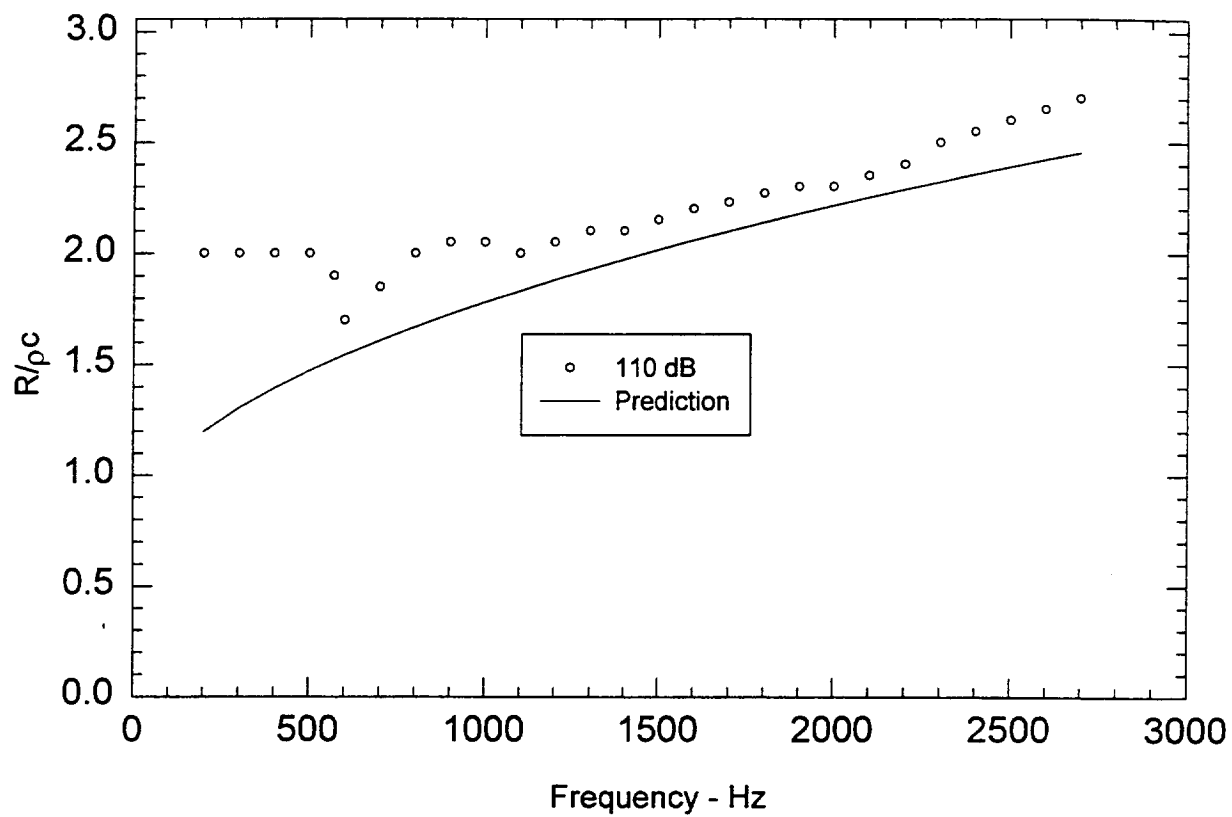


Figure 9c. Measured and Predicted Impedance of Slot A Resonator A1-26

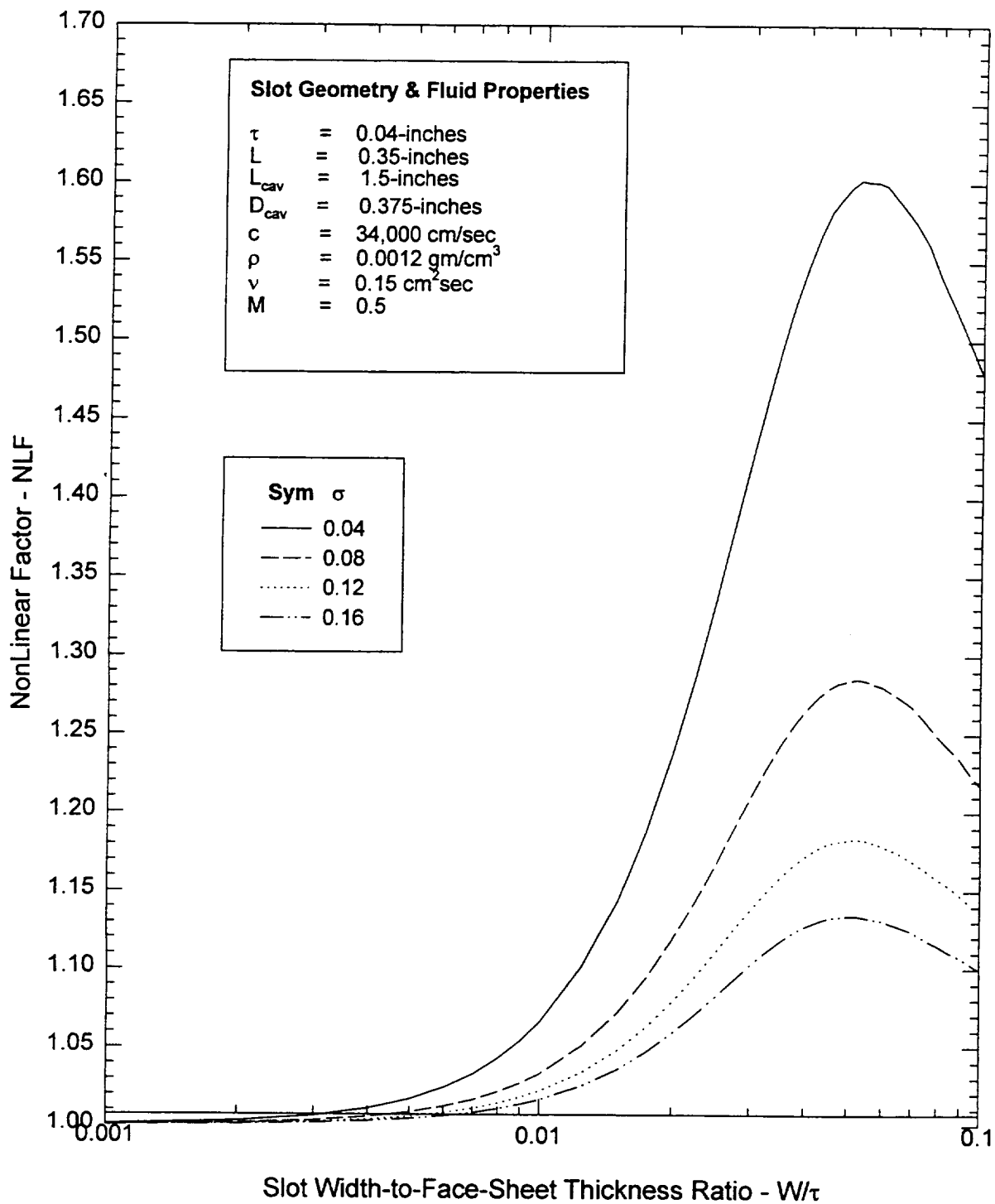


Figure 10. Typical Slot Resonator Predicted NonLinear Factor

Hersh Acoustical Engineering, Inc.

*780 Lakefield Road, Unit G
Westlake Village, CA 91361
(805) 373-8533 Fax (805) 373-0733
e-mail: hae@iswest.com*

FINAL REPORT

BOEING PURCHASE CONTRACT # ZA0075

PRIME CONTRACT NAS1-20090


**THEORY AND DESIGN OF HELMHOLTZ RESONATORS TO SUPPRESS AIRCRAFT
ENGINE NOISE**

by:



Alan S. Hersh

and



Bruce E. Walker

March 7, 1997

Submitted to:

Mr. Jerry Bielak
Noise Research Unit, Noise Engineering
MS 67-ML
P. O. Box 3707
Boeing Commercial Airplane Group
Seattle, WA 98124-2207



1. INTRODUCTION

This report addresses some of the important issues associated with understanding the acoustic behavior of Helmholtz resonators used to suppress aircraft engine noise. A semi-empirical fluid mechanical model has been derived to predict the acoustic behavior of thin-walled, single-orifice Helmholtz resonators in the presence of high speed grazing flow and intense sound.

The report is organized as follows. A review of previous investigations of intense sound and high speed grazing flow on the acoustic behavior of Helmholtz resonators is presented in Section 2. The findings of a flow visualization investigation of the effects of high intensity sound on the acoustic jetting from a resonator orifice is presented in Section 3. The grazing flow resonator impedance model is derived in Section 4 and predicted results are compared to experimental data in Section 5. The report closes with a summary of the important findings of the investigation in Section 6. Appendix A contains a Fortran code of resonator face-sheet impedance as a function of incident particle velocity.

2. REVIEW OF PREVIOUS RESONATOR INVESTIGATIONS

2.1 Non-Grazing Flow Investigations

Rayleigh¹ credits Helmholtz as the originator of the first theoretical analysis describing the acoustic behavior of small cavity-backed resonators. In a recent paper, Junger² reviewed briefly the historical use of the Helmholtz resonator. Apparently, they were used by the Greeks to provide reverberation in open-air theaters. They were also used in Swedish and Danish churches as early as the thirteenth century.

Rayleigh predicted the impedance of cavity-backed orifices by using the concept of lumped elements in a simple slug-mass mechanical oscillator analogy. He assumed that the total mass excited by incident sound pressure waves consisted of the mass within the orifice plus additional masses on both sides of the orifice, called the end correction mass (d_e). The derivation of the lumped (slug-mass) element model is based upon the assumption that harmonic sound waves excite one-dimensional oscillatory motion into and out-of the resonator cavity. The derivation assumes that the fluid displacement - and its derivatives - are *linearly* related to the incident sound pressure. Crandall³ used modern fluid mechanical ideas to solve for the frictional losses in a very thick face-sheet wall containing a small diameter orifice. Later, Ingard⁴ modified Crandall's solution by including additional terms due to frictional losses over the wall containing the orifice.

In 1935, Sivian⁵ observed that at high sound pressure amplitudes, the impedance of Helmholtz resonators were not constant, but were instead strongly affected by the amplitude of the incident sound pressure. He observed experimentally that the acoustic

resistances of Helmholtz resonators are proportional to the acoustic particle velocity within the orifice. Sivian's findings prompted a variety of theoretical and experimental studies to understand and predict the behavior of Helmholtz resonators at high sound pressure levels (SPLs). Mellin⁶ reviewed the historical development of many of these studies through 1973. In terms of predicting the nonlinear behavior of Helmholtz resonators, the works of Ingard and Ising⁷, Sirignano⁸, Zinn⁹, Hersh and Rogers¹⁰, Hersh and Walker^{11,12} and Cummings¹³⁻¹⁵ are particularly important.

Ingard and Ising conducted a detailed experimental investigation of the nonlinear acoustic behavior of an isolated orifice. By measuring simultaneously the amplitude and phase of the sound pressure within the cavity and the particle velocity within the orifice (using a hot wire apparatus), they concluded that for low cavity SPLs, the orifice resistance and reactance were in essential agreement with that predicted by Rayleigh's slug-mass model. At high cavity SPLs, however, their measurements showed that the orifice resistance varied *linearly* with orifice (centerline) particle velocity and the corresponding orifice reactance *decreased* to almost one-half its linear value. Ingard and Ising interpreted the orifice resistance data in terms of Bernoulli's Law suggesting that the flow behavior through the orifice is quasi-steady. The hot-wire measurements indicated that at high SPLs, the flow separates at the orifice forming a high velocity jet. Thus during the in-flow half-cycle, the flow incident to the orifice is irrotational, but is highly rotational (in the form of jetting) after exiting from the orifice. During the other half of the cycle, the flow pattern is reversed. The loss of one-half of the reactance at these high pressure levels was accounted for by assuming that one-half of the end correction is "blown" away by the exiting jet (in their experiments $\tau/d \ll 1$, hence most of the orifice inertia reactance is due to the end correction). Ingard and Ising also measured the particle velocity as a function of axial distance from the orifice. They found that the inflow velocity rapidly decayed to very small values at distances of about two to three diameters from the orifice. This suggested that the near field effects of an orifice extends only to these distances.

Initially Sirignano and later Zinn, recognizing that Rayleigh's slug-mass model was incapable of accounting for the jetting of fluid from the orifice, used fluid mechanical concepts to predict the behavior of the Helmholtz resonator. To simplify their models, they assumed that the characteristic dimensions of both the orifice and cavity were very much smaller than the incident acoustic wavelength and, further, that the acoustic flow through the orifice was one-dimensional, incompressible, quasi-steady and calorically perfect. Both authors based their models on an integral formulation of the conservation of mass and momentum applied to two control volumes, one being the volume bounded by the orifice inlet and outlet surfaces and the other the cavity. To solve these integrals, they used the method of successive approximations with the first-order solution corresponding to the linear case of very small sound pressures incident to an orifice. The orifice nonlinear behavior was introduced through the higher order terms and represents only a second order approximation to the (linear) first order solution.

Hersh and Rogers assumed that the acoustic inflow in the immediate vicinity of an orifice can be modeled as locally spherical. By appropriately normalizing or scaling the acoustic pressure and velocity changes near the orifice, they demonstrated that the acoustic particle velocity behaved to first approximation as an unsteady, incompressible flow. From a physical point-of-view, this appears reasonable because Ingard and Ising's test results showed that large changes in acoustic pressure and velocity occurred over distances on the order of several orifice diameters. Since the orifice diameter is very much smaller than the wavelength of the incident sound wave, the changes must be hydrodynamic rather than acoustic. One of the important findings of their analysis is that their model established explicitly the quasi-steady behavior of orifices exposed to intense sound pressures. Hersh and Rogers were able to correlate the acoustic measurements of Ingard and Ising of the impedance of an orifice exposed to nonlinear incident sound in air with the measurements of Thurston¹⁶ who measured the impedance of an orifice in water.

Hersh and Walker extended the approach adopted by Hersh and Rogers to derive a semi-empirical fluid mechanical model of the acoustic behavior of Helmholtz resonators consisting of single (circular) orifices. Their model assumes (1) that the sound particle velocity approaches the orifice in a spherical manner and (2) that the acoustic pressure and density are adiabatically related. The sound pressures outside and inside the resonator were connected by solving the governing oscillating mass and momentum conservation equations. They derived approximate expressions for the acoustic resistance and reactance of single orifice Helmholtz resonators that agreed well with data. One of the limitations of their model was that it was restricted to values of frequency very near resonance.

Cummings et. al. investigated the acoustic behavior of orifices exposed to intense sound pressure amplitudes. He showed that the loss of acoustic power at the orifice was consistent with the kinetic energy loss of two trains of ring vortices shed alternately from both sides of the orifice.

2.2 Grazing Flow Investigations

Studies of the effects of grazing flow on the acoustic impedance of Helmholtz resonators began in earnest with the early work of Mechel, Mertens and Schliiz¹⁷. Later, Phillips¹⁸, Ronneberger¹⁹ and Dean²⁰ showed that relative to their zero grazing flow values, the effects of grazing flow were to increase resistance and decrease reactance. Dean noted that some of the resonators exhibited an increase in reactance with grazing flow while others exhibited a decrease. He offered no explanation for this.

Starting in the mid-1970s, a large number of research papers on the impedance of Helmholtz resonators exposed to grazing flow were published in the open literature²¹⁻²⁸. All of them investigated the effects of flow on the impedance of Helmholtz resonators

consisting of cavity-backed circular orifices and have added greatly to our understanding of their acoustic behavior.

Rogers and Hersh²¹ correlated measurements of the *steady-state* resistance of isolated square-edged orifices in a grazing flow environment in terms of an effective orifice discharge coefficient. By introducing a simple inviscid model based on thin airfoil theory to account for the interaction between the grazing flow and the orifice inflow and outflow, they showed that the discharge coefficient decreased to very small values relative to its zero grazing flow speed values. They also showed by means of simple flow visualization techniques that the reduction in discharge coefficient resulted from a blockage of the orifice area by interaction between the grazing flow and the orifice inflow and outflow in the form of complicated eddies.

Based on the initial success of the work by Rogers and Hersh, Baumeister and Rice²¹ conducted a very detailed visual study of interaction between a steady-state grazing flow and a harmonically excited cavity sound field. Flow visualization was achieved by constructing a flow channel and a single orifice side branch Helmholtz resonator out of plexiglass and using water as the fluid medium. An oscillatory flow was applied to the resonator cavity and color dyes were injected in both the orifice and the grazing flow. High speed cameras were used to record the motion of the fluid. Figure 1 is a photograph of the interaction between grazing flow and nonlinear sound near a resonator orifice. An important finding of their study is that interaction between the steady-state grazing flow and the oscillating orifice inflow and outflows occurred at the downstream lip of the orifice. This interaction acted to reduce the orifice effective open area. The flow visualization study illustrated the complexity of the interaction between the grazing flow and the incident sound field. During the inflow half-cycles, the grazing flow is deflected laterally into the cavity forming the vena-contracta shown. During outflow, an equal amount of sound particle volume flow is pumped out of the cavity. In both cases, the effective area through which the sound particle volume flow enters and exits the cavity appears to be less than the orifice area. The photographs suggest that the sound particle velocity field separates at the orifice upstream lip - it enters and exits the cavity near the orifice downstream lip.

Hersh and Walker²³ undertook an extensive investigation of the effects of grazing flow on the acoustic impedance of Helmholtz resonators. They developed a semi-empirical model of the acoustic behavior of single-orifice, thin-walled resonators. Their model was motivated by the flow visualization study by Baumeister and Rice and upon the earlier models of Rogers and Hersh²⁴. Recognizing that a detailed solution of the interaction was not practical, a semi-empirical solution was sought which assumed that during the inflow half-cycle, the sound particle enters the resonator cavity in a spherically symmetric manner. Hersh and Walker derived a semi-empirical model of the acoustic discharge coefficient which is a measure of the rate at which acoustic velocity is pumped into and out-of the cavity. At sufficiently high grazing flow speeds, the

discharge coefficient becomes very small. This suggests high acoustic resistance in the sense that the rate at which the acoustic flow is pumped into and out of the cavity is low. Conversely, at very low grazing flow speeds, the effects of grazing flow are negligible. The discharge coefficient model derived by the authors was restricted, however, to frequencies near resonance.

In a recent study, Hersh and Walker used the two-microphone method to measure the effects of grazing flow on the resistance and reactance of typical Helmholtz resonators²⁵. The measurements indicate that the effects of grazing flow become important only above a minimum threshold value. Above this threshold speed, the acoustic resistance becomes almost linearly proportional to the grazing flow and independent of sound pressure amplitude. The corresponding reactance measurements show a decrease with grazing flow speed. Thus at very high grazing flow speeds, the impedance of Helmholtz resonators become linear, independent of sound pressure amplitude. Measurements of the resonator tuned or resonant frequency also showed it to increase with grazing flow above a threshold grazing flow speed. These findings were in qualitative agreement with the earlier findings of Ronneberger¹⁹.

The findings of Hersh and Walker, Baumeister and Rice and Rice were extended in later studies by Charwat and Walker^{26,27} and Kooi and Sarin²⁸. Charwat and Walker conducted detailed measurements of the time-dependent velocities inside and outside the opening of an acoustically excited, two-dimensional Helmholtz resonator imbedded in a grazing flow. Using hot-wire anemometry techniques, the unsteady local perturbation velocity field measurements suggested the existence of a pulsating source and a coherently pulsating vortex pair downstream of the orifice, with the wall as a plane of symmetry.

Kooi and Sarin used the two-microphone method to measure the effects of flow on the acoustic resistance and reactance of locally reacting perforate plate liners. Different boundary-layer velocity distributions were obtained by injecting air upstream of the perforates. They were unable to correlate the impedance solely in terms of mean flow. Instead, they proposed an empirical correlation in terms of a Strouhal number based on the skin friction velocity of the turbulent boundary layer. In contrast to the findings of Hersh and Walker, Kooi and Sarin found the acoustic resistance to decrease somewhat with increasing frequency.

2.3 Resonator Self-Noise Investigations

The self-noise generated from cavities and Helmholtz resonators exposed to grazing flow has been of considerable interest over the past approximate thirty years. Most of the early researchers concentrated on understanding the physical mechanisms responsible for aerodynamically induced pressure oscillations in shallow and deep cavities exposed to turbulent grazing flows²⁹⁻³⁵. These studies were then used to model

and explain the mechanisms responsible for the self-noise generated from Helmholtz resonators exposed to grazing flows.

Applying the ideas put forth by Rossiter²⁹, Heller and Bliss³⁰, Bolton³¹, and DeMetz and Farabee³², the shear layer formed at the orifice upstream separation point is believed to generate wave-like motion due to its inherent instability. These wave-like motions generate fluctuating mass addition and removal to the cavity of a Helmholtz resonator. Assuming that the frequency at which this occurs is proportional to V/d_{on} , then self-noise is generated when this frequency coincides with the natural resonant frequency of the resonator. The Strouhal number, defined as $S_t = f_t d_{on}/V$, connects the grazing flow speed at which the intensity of the self-noise is maximum to the cavity dimensions. Experimental studies by Hersh and Walker²³ and Bolton³¹ for grazing flow over circular orifices and two-dimensional slots respectively, show that $S_t = 0.25 - 0.26$ is valid for both geometries.

In a series of two unique and outstanding companion papers, Nelson, Haliwell and Doak^{33,34}, conducted detailed measurements of the vortical and acoustic flow fields in the neck of a Helmholtz resonator exposed to grazing flow and introduced theoretical concepts different from the usual instability wave-like models used by other investigators to interpret their data. Oil was injected on the topside surface upstream of the resonator neck allowing photographs to be taken of the instantaneous flow field. When the resonator was "singing", a stroboscope light was used to illuminate the neck region. The photographs show that the periodic formation of discrete vortices near the upstream lip grow in size as they are convected towards the downstream lip. The photographs also show that the shear layer at the upstream lip always leaves tangentially implying that the Kutta condition is satisfied at this location. The authors also conducted LDV measurements to obtain power spectra of the horizontal and vertical velocity fluctuations in the resonator slot. The maximum values of the vertical velocity fluctuations were found to occur near the downstream region of the slot. These findings are consistent with the findings of Baumeister and Rice.

To interpret their measurements, Nelson, et al. explained their measurements in terms of two velocity fields: a rotational velocity field induced by the vorticity in the mean flow and an irrotational (potential) velocity field associated with the acoustic field. By assuming a distribution or train of tightly packed vortices across the resonator neck, the strength of which was determined by the grazing flow, the authors were able to predict the measured mean and fluctuating vortical velocity fields with reasonable accuracy. The Coriolis force due to the unsteady potential flow was found to be the principal term in the linearized conservation of momentum which was not directly balanced by a fluctuating pressure gradient. The predicted acceleration of the vortices using the Coriolis force at the downstream lip was in excellent agreement with measurements. One of the more interesting conclusions of their analysis was the conversion of mean energy into acoustic energy near the downstream lip of the orifice. This conversion of

energy is believed to be related to the fluctuating Coriolis forces caused by the interaction of streamwise convected vorticity with uniform transverse fluctuating potential flow. A final conclusion is that the Kutta condition determines the relationship between the amplitude of the reciprocating potential flow and the degree of concentration of vorticity in the unstable vortex sheet.

Worraker and Halliwell³⁵ employed a combination of probe microphone, hot-wire and LDV measurements to map out the instantaneous pressure and velocities near and in a cavity-backed rectangular slot located in the wall of a wind tunnel. Measurements were recorded for sound pressure levels as high as 130 dB, grazing flow Mach numbers up to 0.5 and turbulence intensities levels up to 12%. The authors were interested in interpreting their measurements in terms of the existing theoretical models of the effects of grazing flow on the impedance of cavity backed orifices. They concluded that the existing theories were inadequate in explaining or predicting the measurements and that the theoretical concepts introduced by Nelson et al. warrant further study.

3. FLOW VISUALIZATION EXPERIMENTS

The hot-wire tests conducted by Ingard and Ising⁷ suggested that at high SPLs, intense jets of fluid are ejected from the orifice of a Helmholtz resonator during the outflow half-cycle. Since Helmholtz resonators are often used to suppress sound in aircraft engine nacelles, it is possible that acoustic jetting may significantly increase local boundary-layer thickness and hence static pressure losses. To explore this possibility, an experimental program was undertaken to visualize the acoustic flow field near the orifice.

The experimental program consisted of mounting a resonator face-sheet flush to the bottom of a Plexiglas constructed 12.7 cm wide by 25.4 cm high wind tunnel test section as shown schematically in Figure 2. Acoustic excitation of the resonator was generated from a high intensity loudspeaker, flush mounted in the top of the test section. The loudspeaker was powered by a 100 watt amplifier. The resonator cavity was partially immersed in a bath of liquid nitrogen. This reduced the temperature of the resonator face-plate so that the moisture in the air near the orifice condensed into small particles of ice. Flow visualization was achieved by shining a flashlight into the region surrounding the orifice.

Figures 3(a-d) demonstrate that the penetration distance of the ice particles into the wind tunnel test section was strongly dependent upon the amplitude of the sound incident to the resonator. Although it is not possible to observe from Figure 3d, the ice particles violently impacted against the top of the wind tunnel test section wall which was located a distance of 25.4 cm from the orifice. The orifice diameter was 0.9525 cm which represents a non-dimensional penetration distance of approximately 27:1. Since the ice particles are quite large and heavy, it is reasonable to surmise that the

penetration distance of the ejected sound particle flow was on the order of 100:1. Since SPLs in aircraft nacelles are often on the order 140-160 dB, it is reasonable to conclude that the sound particle flows ejected from a resonator orifice will penetrate well into the nacelle interior. Although the actual penetration will undoubtedly be substantially reduced by mean flow within the nacelle, the influence of the local wall sound pressure field upon static pressure losses within the nacelle is not known.

4. SEMI-EMPIRICAL MODEL

Motivated by the above findings, a semi-empirical fluid mechanical model has been derived which assumes that during the inflow half-cycle, the sound particle enters the resonator cavity in the spherical radial symmetric manner shown in Figure 4. To avoid the singularity at $r^* = 0$, the inflow is truncated at the radius $r^* = L^*$ [the $()^*$ notation denotes dimensional quantities]. The functional dependency of L^* will be determined experimentally.

The spherical inflow model is valid only during the half-cycle when the incident sound particle velocity is approaching the orifice - it is not valid during the other half-cycle when the sound is ejected from the orifice. Both the hot wire measurements by Ingard and Ising and the flow visualization tests described in Section 3 show that the sound particle velocity is ejected from the orifice in a jet-like manner. The restriction of the model to inflow only is not unduly limiting, however, because the quantity of particle flow pumped into and out-of the resonator cavity should be equal over a sound period. Thus an approximate solution over a half-cycle should result in an approximate solution over the entire cycle. Although the spherical inflow model could be applied on the cavity side of the orifice during the out-flow half-cycle, this approach was not pursued.

The fluctuating continuity and momentum conservation equations describing the motion of a *harmonically* driven sound particle velocity field are derived. Following this, the equations of motion are normalized by appropriately scaling the dependent and independent variables. The resulting equations are then simplified by retaining only the important terms. The simplified equations of motion are solved subject to satisfying two boundary conditions. One is that the fluctuating pressure must merge smoothly (asymptotically) into the incident driving pressure. The other is that at the hemispherical surface $r^* = L^*$ (see Figure 4b), the instantaneous area-averaged sound pressure must be equal to the instantaneous cavity pressure.

4.1 Derivation of Governing Equations.

The derivation of the governing equations is based upon the following assumptions. The flow field is decomposed into uniform and fluctuating components. The incident sound particle velocity field approaches the resonator orifice in a spherically symmetric manner. The incident sound is harmonically excited with a wavelength very much larger

than the cavity dimensions. The acoustic pressure and density are adiabatically related. The fluid obeys the perfect gas law. Finally, the resonator cavity response is governed by one-dimensional acoustic wave motion.

The governing acoustic, continuity and momentum conservation equations (the energy equation is replaced by the adiabatic connection between acoustic pressure and density) are non-dimensional by introducing the reference quantities ω^* , L^* , $|P_{inc}^*|$, and $|u_L^*|$. The undefined radius L^* was used to normalize r^* rather than the orifice diameter because of the freedom to use experimental data to define it. It will be shown later that this parameter is related to the resonator orifice inertia length. The acoustic particle velocity amplitude is unknown and assumed to be equal to the amplitude of the sound particle velocity in the orifice vena contracta region shown schematically in Figure 3b. These two undefined parameters will be shown later to be essential elements in the development of the empirical model.

The solution to the following spherical mass and momentum conservation equations are sought,

$$\begin{aligned} \frac{\partial \rho^*}{\partial t^*} + \rho^* \left\{ \frac{1}{r^{*2}} \frac{\partial}{\partial r^*} (r^{*2} V_r^*) + \frac{1}{r^* \sin(\theta)} \frac{\partial}{\partial \theta} [\sin(\theta) V_\theta^*] + \frac{1}{r^* \sin(\theta)} \frac{\partial V_\phi^*}{\partial \phi} \right\} \\ + \left\{ V_r^* \frac{\partial \rho^*}{\partial r^*} + \frac{V_\theta^*}{r^*} \frac{\partial \rho^*}{\partial \theta} + \frac{V_\phi^*}{r^* \sin(\theta)} \frac{\partial \rho^*}{\partial \phi} \right\} = 0 \end{aligned} \quad (1)$$

and

$$\begin{aligned} \rho^* \frac{\partial V_r^*}{\partial t^*} + V_r^* \frac{\partial V_r^*}{\partial r^*} + \frac{V_\theta^*}{r^*} \frac{\partial V_r^*}{\partial \theta} + \frac{V_\phi^*}{r^* \sin(\theta)} \frac{\partial V_r^*}{\partial \phi} - \frac{(V_\theta^{*2} + V_\phi^{*2})}{r^*} = -\frac{1}{\rho^*} \frac{\partial P^*}{\partial r^*} \\ + v^* \left[\frac{1}{r^{*2}} \frac{\partial}{\partial r^*} (r^{*2} \frac{\partial V_r^*}{\partial r^*}) + \frac{1}{r^{*2} \sin(\theta)} \frac{\partial}{\partial \theta} (\sin(\theta) \frac{\partial V_r^*}{\partial \theta}) + \frac{1}{r^{*2} \sin(\theta)} \frac{\partial^2 V_r^*}{\partial \phi^2} \right] \end{aligned} \quad (2)$$

The fluid, mean flow and acoustic quantities are divided into the following mean and acoustic components,

$$\vec{V}^* = (V_r^*, V_\theta^*, V_\phi^*) = (U_r^* + u^*, U_\theta^*, U_\phi^*) \quad (3a)$$

$$P^* = P_0^* + P^{\wedge}; \quad \rho^* = \rho_0^* + \frac{P^{\wedge}}{c_0^{*2}} \quad (3b,c)$$

To simplify the notation, the (\wedge) notation denoting acoustic quantities will be omitted. The mean flow components $(U_r^*, U_\theta^*, U_\phi^*)$ are defined in Figure 3a as

$$(U_r^*, U_\theta^*, U_\phi^*) = [-V_-^* \sin(\theta) \cos(\phi), -V_-^* \cos(\theta) \cos(\phi), V_-^* \sin(\phi)] \quad (4)$$

and the spherical acoustic particle velocity components are

$$\vec{u}^* = (u^*, 0, 0) \quad (5)$$

4.1.1 Conservation of Fluctuating Mass Flux.

Introducing the following non-dimensional quantities,

$$t \equiv \omega^* t^*; \quad r \equiv \frac{r^*}{L^*}; \quad u \equiv \frac{u^*}{|u_L^*|} \quad P \equiv \frac{P^*}{|P_{inc}^*|} \quad (6)$$

into the fluctuating conservation of continuity equation yields respectively after some simplification,

$$\left[\left(\frac{\omega^* L^*}{|u_L^*|} \right) \left(\frac{|P_{inc}^*|}{\rho_0^* c_0^{*2}} \right) \right] \frac{\partial P}{\partial t} + \frac{1}{r^2} \frac{\partial}{\partial r} (r^2 u) + \left(\frac{|P_{inc}^*|}{\rho_0^* c_0^{*2}} \right) \left\{ [-V_{\infty} \sin(\theta) \cos(\phi) + u] \frac{\partial P}{\partial t} - \frac{V_{\infty} \cos(\theta) \cos(\phi)}{r} \frac{\partial P}{\partial t} + \frac{V_{\infty} \sin(\theta)}{r \sin(\theta)} \frac{\partial P}{\partial t} \right\} = 0 \quad (7)$$

For many aircraft engine applications, the amplitudes of the acoustic pressures are usually less than about 1% of the mean pressure (roughly 154 dB at ambient atmospheric conditions). The corresponding frequencies are usually less than 6,000 Hz and typical orifice dimensions are also often less than one cm. It will be shown later that at high sound pressures, $L^*/d_e^* < 0(1)$. With these constraints, the following inequalities are valid,

$$\frac{|P_{inc}^*|}{\rho_0^* c_0^{*2}} \ll 1; \quad \left(\frac{\omega^* L^*}{|u_L^*|} \right) \left[\frac{|P_{inc}^*|}{\rho_0^* c_0^{*2}} \right] \ll 1 \quad (8a,b)$$

The inequalities of Eq. (8) simplify the continuity equation to

$$\frac{\partial}{\partial t} (r^2 u) = 0 \quad \rightarrow \quad u(r, \theta, t) = -\frac{F(\theta, t)}{r^2} \quad (9)$$

where the negative sign denotes inflow in a spherical coordinate system. The simplified continuity equation shows that to lowest order, fluid is pumped into and out-of the cavity in an unsteady, incompressible manner. This is consistent with both the interpretation that significant flow field changes occur over distances small relative to the incident sound wavelength and the experimental findings of Ingard and Ising. Under these conditions, flow field changes occur hydrodynamically rather than acoustically.

4.1.2 Conservation of Fluctuating Radial Momentum Flux.

Substituting Eqs. (3-6) into Eq. (2) yields, after some simplification,

$$\begin{aligned} & \varepsilon\beta \frac{\partial u}{\partial t} + \varepsilon \left[-V_{\infty} \sin(\theta) \cos(\phi) + u \right] \frac{\partial u}{\partial r} + \frac{1}{\rho_0} \frac{\partial P}{\partial r} \\ & = \frac{\varepsilon}{R_c} \left\{ \frac{1}{r^2} \frac{\partial}{\partial r} \left(r^2 \frac{\partial u}{\partial r} \right) + \frac{1}{r^2 \sin(\theta)} \frac{\partial}{\partial \theta} \left[\sin(\theta) \frac{\partial u}{\partial r} \right] \right\} \end{aligned} \quad (10)$$

where only acoustic terms are retained and the parameters ε and β are defined as

$$\varepsilon \equiv \frac{\rho_0^* |u_L^*|^2}{|P_{inc}^*|}; \quad \beta \equiv \frac{\omega^* L^*}{|u_L^*|} \quad (11a,b)$$

Equation (10) is further simplified by substituting Eq. (9) for u to yield

$$\begin{aligned} & -\frac{\varepsilon\beta}{r^2} \frac{\partial F(\theta, t)}{\partial t} + \varepsilon \left[V_{\infty} \sin(\theta) \cos(\phi) + \frac{F(\theta, t)}{r^2} \right] \frac{\partial}{r\theta} \left[\frac{F(\theta, t)}{r^2} \right] + \frac{\partial P}{\partial r} = \\ & -\frac{\varepsilon}{r^4 R_c \sin(\theta)} \frac{\partial}{\partial \theta} \left[\sin(\theta) \frac{\partial F(\theta, t)}{\partial \theta} \right] \end{aligned} \quad (12)$$

Observe that Eq. (12) is nonlinear with respect to both time and amplitude. Its solution is divided into three regimes. The first consists of the low amplitude behavior of resonators in the absence of grazing flow. The second addresses resonator high amplitude behavior and the third solves for the effect of grazing flow.

4.2 Non-Grazing Flow, Low Amplitude Solution

Assuming that both $V_{\infty} = 0$ and the amplitude of the incident sound field is sufficiently low that quadratic velocity terms are negligible, Eq. (12) simplifies to

$$-\frac{\varepsilon\beta}{r^2} \frac{\partial F(\theta, t)}{\partial t} + \frac{\partial P}{\partial r} = -\frac{\varepsilon}{r^4 R_c \sin(\theta)} \frac{\partial}{\partial \theta} \left[\sin(\theta) \frac{\partial F(\theta, t)}{\partial \theta} \right] \quad (13)$$

The right-hand-side (RHS) of Eq. (13) represents the contribution of viscous scrubbing losses on the resonator face-plate. A boundary-layer type solution is sought by solving the inviscid solution for the driving pressure gradient $\partial P_{inv}/\partial r$ and then solving the viscous equations within the boundary layer. The inviscid solution is based upon the following simplifications. First, the RHS of Eq. (13) vanishes in accord with the assumption that the fluid is inviscid (i.e., $\mu^* = 0$). Second, the driving sound pressure field is assumed to be harmonic. These assumptions lead to $F(\theta, t) = Ae^{it}$ where A is the

(complex) amplitude of the oscillating sound particle velocity (independent of θ) in the resonator orifice. Solving the resulting equation for $\partial P_{inv}/\partial r$ yields

$$\frac{\partial P_{inv}}{\partial r} = i \frac{\epsilon \beta A e^{it}}{r^2} \quad (14)$$

The viscous solution is found by setting $F(\theta, t) = A e^{it} f(\theta)$ and substituting Eq. (14) into Eq. (13) to yield

$$i \frac{\epsilon \beta A e^{it}}{r^2} [1 - f(\theta)] = - \frac{\epsilon A e^{it}}{r^4 R_e \sin(\theta)} \frac{\partial}{\partial \theta} [\sin(\theta) f(\theta)] \quad (15)$$

A boundary-layer solution to Eq. (15) is sought by assuming that the viscous effects are localized near the face-plate wall where θ is almost equal to $\pi/2$ (see Figure 4a). Introducing the boundary-layer coordinate $\eta = R_e^{1/2} r(\pi/2 - \theta)$ into Eq. (15), assuming $f(\theta) = f(\eta)$ yields

$$f''(\eta) - i\beta f(\eta) + i\beta = 0 \quad (16)$$

The solution to Eq. (16) subject to the boundary conditions $f(0) = 0$ (the usual no-slip boundary condition) and $f(\theta) = 1$ is

$$f(\eta) = B [1 - e^{-\sqrt{i\beta}\eta}] \quad (17)$$

where B is an unknown parameter to be defined experimentally.

One of the important effects of viscosity is to reduce the sound particle velocity mass flux into the resonator orifice. This can be estimated in terms of the acoustic boundary-layer displacement parameter δ_{DSP} defined as

$$u_{inv}^* \delta_{DSP}^* \equiv \lim_{R_e \rightarrow \infty} \frac{1}{\sqrt{R_e}} \int_0^{\zeta \sqrt{R_e}} [u_{inv}^* - u_{vis}^*] d(r^* \zeta \sqrt{R_e}) \quad (18)$$

where $\zeta \equiv \pi/2 - \theta$. Using Eq. (6) to non-dimensionalize Eq. (18) and solving for δ_{DSP} yields

$$\delta_{DSP} \equiv \frac{1}{\sqrt{R_e}} \int_0^{\infty} \exp[-\sqrt{i\beta}\eta] d\eta = \frac{1}{\sqrt{iR_e\beta}} \quad (19)$$

The parameter δ_{DSP} is a measure of the loss of sound particle velocity due to the fluid viscosity near the face-plate surface.

The final equation governing the motion of the sound particle velocity field within the orifice follows by introducing the above boundary-layer concepts into Eq. (13). This was accomplished by first replacing the viscous velocity term $F(\theta, t)$ of Equation (13) by its inviscid equivalent $F(\theta, t) = Ae^{it}$. The viscous term on the RHS of Eq. (13) was replaced by the approximate expression $(\delta_{DSP}A)e^{it}f''(0)$ where $\delta_{DSP}A$ represents the mass flux loss caused by boundary layer effects and $f''(0)$ was estimated from Eq. (17). Incorporating these assumptions into Eq. (13) results in the simplified expression

$$-\frac{i\varepsilon\beta Ae^{it}}{r^2} + \frac{\partial P}{\partial r} = \frac{\varepsilon(A\delta_{DSP})Be^{it}}{r^2} \left[\frac{\beta(1+i)}{2} \right] \equiv \frac{\varepsilon A B e^{it}}{r^2} \sqrt{\frac{\beta(1+i)}{2R_e}} = \frac{\varepsilon A B e^{it}}{r^2} (1.1 + 0.455i) \sqrt{\frac{\beta}{2R_e}} \quad (20)$$

Equation (20) can be integrated with respect to r to yield

$$\frac{i\varepsilon\beta Ae^{it}}{r} + P(r, t) + \frac{\varepsilon A B e^{it} (1.1 + 0.455i)}{r} \sqrt{\frac{\beta}{2R_e}} = G(t) \quad (21)$$

where $G(t)$ is an arbitrary function of time.

4.2.1 Boundary Conditions

The solution to Eq. (21) requires that the function $G(t)$ and the acoustic pressure $P(r, t)$ be known. They are determined from two boundary conditions. The *first* requires the local pressure $P(r, t)$ to merge smoothly (asymptotically) into the (non-dimensional) incident driving sound pressure,

$$\lim_{r \rightarrow \infty} P(r, t) = e^{it} \quad (22a)$$

From Eq. (21), this yields

$$G(t) = e^{it} \quad (22b)$$

Substituting Eq. (22b) into Eq. (21), the radial momentum equation governing the motion of the sound particle velocity in the resonator orifice becomes

$$\frac{i\varepsilon\beta Ae^{it}}{r} + P(r, t) + \frac{\varepsilon A B e^{it} (1.1 + 0.455i)}{r} \sqrt{\frac{\beta}{2R_e}} = e^{it} \quad (23)$$

The *second* boundary condition is imposed by the requirement that the incident sound pressure *averaged* over the hemisphere $r = L$ must equal the resonator cavity sound pressure. The resonator cavity sound pressure is predicted from the one-dimensional wave equation. With this understanding, the second boundary condition may be written in the following *dimensional* form as

$$P^*(L, t^*) = P_{cav}^* = -i\rho_0^* c_0^* \sigma |u_L^*| \cot(k^* L_{cav}^*) \quad (24a)$$

The non-dimensional form of Eq. (24a) follows by substituting Eq. (6) to yield

$$P(1, t) = -i\varepsilon\beta\kappa A e^{it}; \quad \kappa \equiv \frac{C_{D0} c_0^* \sigma \cot(k^* L_{cav}^*)}{\omega^* L^*} \quad (24b,c)$$

At very low sound pressure amplitudes, the orifice discharge coefficient $C_{D0} = 1$. Substituting Eq. (24b,c) into Eq. (23) yields the following expression for the non-dimensional sound particle velocity in the resonator orifice,

$$u_L(1, t) = -A e^{it} = -\frac{e^{it}}{\varepsilon \left\{ \left[1.1B \sqrt{\frac{\beta}{2R_c}} + i \left[\beta(1-\kappa) + 0.455B \sqrt{\frac{\beta}{2R_c}} \right] \right] \right\}} \quad (25)$$

The impedance Z^* of a Helmholtz resonator excited by the incident harmonic sound wave $|P_{inc}^*| e^{i\omega^* t}$ is defined as

$$Z^* \equiv \frac{P_{inc}^*}{(-u_{cav}^*)} = \frac{|P_{inc}^*|}{|-u_{cav}^*|} = \frac{|P_{inc}^*|}{\sigma |u_L^*|}; \quad |u_{cav}^*| = \sigma |u_L^*| \quad (26)$$

The normalized impedance follows by substituting Eqs. (11) & (25) into Eq. (26) to yield, after some algebra,

$$\frac{Z^*}{\rho_0^* c_0^*} = \frac{1}{\sigma} \left\{ \frac{1.1B}{c_0^*} \sqrt{\frac{v^* \omega^*}{2}} + i \left[\frac{\omega^* d_c^*}{c_0^*} (1-\kappa) + \frac{0.455B}{c_0^*} \sqrt{\frac{v^* \omega^*}{2}} \right] \right\} \quad (27)$$

Observe that the resistance displays the classical $\sqrt{v^* \omega^*}$ behavior characteristic of low amplitude frictional scrubbing losses over thin-walled resonator configurations.

4.3 Non-Grazing Flow, High Amplitude Solution

The high amplitude (nonlinear) behavior of Helmholtz resonators is predicted from Eq. (12). Setting $V_- = 0$ and assuming that the RHS of Eq. (20) models the effects of viscosity, Eq. (12) may be written

$$-\frac{i\varepsilon\beta A e^{it}}{r^2} + \varepsilon \left[\frac{A e^{it}}{r^2} \right] \frac{\partial}{\partial r} \left[\frac{A e^{it}}{r^2} \right] + \frac{\partial P}{\partial t} \equiv \frac{\varepsilon A B e^{it}}{r^2} \sqrt{\frac{\beta}{2R_c}} (1.1 + 0.455i) \quad (28)$$

In deriving Eq. (28), it was assumed that $F(r, \theta, t) = F(r, t) = A e^{it}$ which is consistent with a boundary-layer type solution. Observe that the second term on the LHS of Eq. (28) is nonlinear with respect to time. A rather straight-forward scheme is proposed to simplify

Eq. (28). It consists of assuming that the coefficient of the second term on the LHS of Eq. (28) can be replaced by a term equal to the root-mean-square of the orifice particle velocity, time-averaged over a typical steady-state acoustic period or cycle. This assumption leads to the following simplified model equation of the orifice particle velocity,

$$-\frac{i\varepsilon\beta Ae^{it}}{r^2} + \varepsilon \left[\frac{A}{r^2} \right] \frac{\partial}{\partial t} \left[\frac{Ae^{it}}{r^2} \right] + \frac{\partial P}{\partial t} \equiv \frac{\varepsilon AB e^{it}}{r^2} \sqrt{\frac{\beta}{2R_e}} (1.1 + 0.455i) \quad (28a)$$

Observe that Eq. (28a) is now linear with respect to time, proportional to e^{it} . It is, however, still quadratic with respect to the parameter A.

Integrating Eq. (28a) with respect to r yields

$$\frac{i\varepsilon\beta Ae^{it}}{r} + \varepsilon \left[\frac{A^2 e^{it}}{2r^4} \right] + P(r,t) + \frac{\varepsilon AB e^{it}}{r} (1.1 + 0.455i) \sqrt{\frac{\beta}{2R_e}} = G(t) \quad (29)$$

Applying the two boundary conditions described by Eqs. (22b) and (24b) at $r = 1$ results in the following nonlinear conservation of radial momentum equation governing the motion of the sound particle velocity field jetting into and out-of the resonator orifice,

$$A^2 + 2(F_0 + iH_0)A - \frac{2}{\varepsilon} = 0 \quad (30)$$

where the parameters F_0 and H_0 are defined as,

$$F_0 \equiv 1.1B \sqrt{\frac{\beta}{2R_e}}; \quad H_0 \equiv \beta(1 - \kappa) + 0.455B \sqrt{\frac{\beta}{2R_e}} \quad (31a,b)$$

The solution to Eq. (30) produces the following estimate of the sound particle velocity in the resonator orifice,

$$u_L(1,t) = -Ae^{it} = - \left[\sqrt{\frac{2}{\varepsilon} + (F_0 + iH_0)^2} - (F_0 + iH_0) \right] e^{it} \quad (32)$$

Although the detail structure of the pumping of sound particle volume flow into and out-of the orifice is not symmetrical, Eq. (32) is assumed to be valid over an entire cycle. As discussed earlier, this is based upon the assumption that over long time periods relative to the incident sound period, the time-averaged volume inflow and out-flow must be symmetrical over a cycle to insure that the mean cavity pressure is constant, independent of time.

The resonator impedance is normalized by $\rho_0 \omega_L d_e$ instead of the traditional $\rho_0 c_0$. Although normalizing the impedance by $\rho_0 c_0$ is a well established procedure, it provides

little insight into the basic acoustic behavior of Helmholtz resonators. The motivation here is that normalizing the resonator impedance by $\rho_o \omega_L d_e$ may result in a universal normalization for different sized resonators.

Following the procedure described in Section 3.2 above, the following expression for the normalized resonator impedance $Z/\rho_o \omega_L d_e$ is derived ,

$$\frac{Z^*}{\rho_o \omega_L d_e} = \frac{1}{\sigma} \left\{ \sqrt{\frac{1}{2C_{D0}^2} \left[\frac{|P_{inc}^*|}{\rho_o (\omega_L d_e)^2} \right]^2 + \left(\frac{f_0 + ih_0}{2C_{D0}} \right)^2} + \left(\frac{f_0 + ih_0}{2C_{D0}} \right) \right\} \quad (33)$$

where f_0 and g_0 are defined as

$$f_0 \equiv 11 \frac{B}{\omega_L d_e} \sqrt{\frac{\omega^* v^*}{2}} \quad (34a)$$

and

$$h_0 \equiv \left(\frac{\omega^*}{\omega_L} \right) \left(\frac{L_0}{d_e} \right) (1 - \kappa) + 0.455 \frac{B}{\omega_L d_e} \sqrt{\frac{\omega^* v^*}{2}} \quad (34b)$$

Here L_0 represents the orifice inertial length at high sound pressure amplitudes and C_{D0} represents the orifice discharge coefficient defined as

$$|u_L^*| \equiv C_{D0} |u_o^*| = \sigma C_{D0} |u_{cav}^*| \quad (34c)$$

Equation (34c) allows the interpretation of $|u_L^*|$ as the sound particle velocity in the orifice vena-contracta. The nonlinear character of Eq. (33) can best be illustrated by considering the special case of resonance where the reactance vanishes (i.e., $h_0 = 0$) yielding

$$\frac{R_{res}^*}{\rho_o \omega_L d_e} = \frac{1}{\sigma} \left\{ \sqrt{\frac{1}{2C_{D0}^2} \left[\frac{|P_{inc}^*|}{\rho_o (\omega_L d_e)^2} \right]^2 + \left(\frac{11B}{2C_{D0}} \sqrt{\frac{\omega^* v^*}{2(\omega_L d_e)^2}} \right)^2} + \left(\frac{11B}{2C_{D0}} \sqrt{\frac{\omega^* v^*}{2(\omega_L d_e)^2}} \right) \right\} \quad (35)$$

At very high sound pressure amplitudes, the viscous scrubbing losses are negligible and the tuned resistance further simplifies to

$$\frac{R_{res}^*}{\rho_o \omega_L d_e} \equiv \frac{1}{\sigma C_{D0}} \sqrt{\frac{1}{2} \left[\frac{|P_{inc}^*|}{\rho_o (\omega_L d_e)^2} \right]^2} \quad (35a)$$

Equation (35a) shows that the tuned resistance is highly nonlinear, proportional to the square-root of the amplitude of the incident sound pressure and inversely proportional to the product of the acoustic discharge coefficient and the orifice open area ratio.

4.4 Grazing Flow Solution

The solution to Eq. (12) predicts the effects of grazing flow on the behavior of the sound particle velocity flow pumping into and out-of the resonator orifice. Equation (12) is simplified by first replacing the viscous term of the RHS of Eq. (12) with the RHS of Eq. (20) and then assuming that $F(t) = Ae^{it}$. This yields

$$\begin{aligned}
 & -\frac{i\varepsilon\beta Ae^{it}}{r^2} + \varepsilon \left[V_{\infty} \sin(\theta) \cos(\phi) + \frac{A}{r^2} \right] \frac{\partial}{\partial r} \left[\frac{Ae^{it}}{r^2} \right] + \frac{\partial P}{\partial r} \\
 & \equiv \frac{\varepsilon\beta Ae^{it} (1.1 + 0.455i)}{r^2} \sqrt{\frac{\beta}{2R_c}}
 \end{aligned} \tag{36}$$

where the coefficient of the second term on the LHS of Eq. (36) has been linearized with respect to time in the same manner as Eq. (28a). Integrating Eq. (36) with respect to r yields

$$\begin{aligned}
 & \frac{i\varepsilon\beta Ae^{it}}{r} + \frac{\varepsilon Ae^{it}}{r^2} \left[V_{\infty} \sin(\theta) \cos(\phi) + \frac{A}{2r^2} \right] + P(r,t) \\
 & + \frac{\varepsilon\beta Ae^{it} (1.1 + 0.455i)}{r} \sqrt{\frac{\beta}{2R_c}} = G(t)
 \end{aligned} \tag{37}$$

Equation (37) shows that one of the effects of grazing flow is to introduce the spherical angles (θ, ϕ) which destroys radial symmetry and complicates its solution. Recall that the second boundary condition defined by Eq. (24b) required the incident sound pressure to be first *area-averaged* over the hemisphere $r = 1$ and then set equal to the resonator cavity sound pressure. The flow visualization experiments of Rice and Baumeister, shown in Figure 1, were used to formulate the following strategy to model the effects of the asymmetry introduced by the mean flow. Figure 4 suggests that over a typical dynamically steady-state acoustic period, grazing flow is deflected into the resonator cavity through the orifice trailing edge region during both the inflow and out-flow half-cycles. This behavior is modeled by the sketch of Figure 5, which shows that inflow/out-flow pumping takes place in a pie-shaped region bounded by the angles $-2\pi + \phi_{\infty} < \phi < 2\pi - \phi_{\infty}$ where ϕ_{∞} is an unknown parameter to be defined experimentally.

Introducing the hemispherical area-averaged quantity,

$$\langle () \rangle \equiv \frac{1}{2(\pi - \phi_-)} \int_{-\pi + \phi_-}^{\pi - \phi_-} d\phi \int_0^{\frac{\pi}{2}} () \sin(\theta) d\theta \quad (38)$$

where the angle ϕ over the hemispherical surface at $r = 1$ varies from $\phi = (\pi - \phi_-)$ to $\phi = -(\pi - \phi_-)$. It is straight forward to show that

$$\langle (A) \rangle \equiv \frac{1}{2(\pi - \phi_-)} \int_{-\pi + \phi_-}^{\pi - \phi_-} d\phi \int_0^{\frac{\pi}{2}} (A) \sin(\theta) d\theta = A \quad (38a)$$

where A is a parameter that is *independent* of the angles (θ, ϕ) . With this understanding, applying Eq. (38) to Eq. (37) at $r = 1$ yields,

$$i\varepsilon\beta Ae^u + \varepsilon Ae^u \left\{ \left[\frac{\pi \sin(\pi - \phi_-)}{4(\pi - \phi_-)} \right] V_- + \frac{A}{2} \right\} + P(r, t) + \varepsilon\beta Ae^u \sqrt{\frac{\beta(1+i)}{2R_c}} = G(t) \quad (39)$$

It is of interest to note that by setting $\phi_- = 0$, the coefficient of the grazing flow term on the LHS of Eq. (39) *vanishes*. This was the principal motivation for the introduction of the orifice area-averaging scheme. For convenience, the grazing flow velocity coefficient Θ_- is introduced defined as

$$\Theta_- \equiv \frac{\pi \sin(\pi - \phi_-)}{4(\pi - \phi_-)} \quad (40)$$

Combining Eq. (40) with the boundary conditions defined by Eqs. (22b) and (24b) results in the following equation governing the motion of the sound particle velocity in the resonator orifice in the presence of grazing flow,

$$A^2 + 2(F_v + iH_v)A - \frac{2}{\varepsilon} = 0 \quad (41)$$

where the parameters F_v and G_v are defined as

$$F_v \equiv \Theta_- V_- + 1.1B \sqrt{\frac{\beta}{2R_c}}; \quad H_v \equiv \beta(1 - \kappa) + 0.455B \sqrt{\frac{\beta}{2R_c}} \quad (42a,b)$$

The solution to Eq. (41) yields the following estimate of the (non-dimensional) sound particle velocity in the resonator orifice,

$$u_L(1,t) = -Ae^{it} = -\left[\sqrt{\frac{2}{\varepsilon} + (F_V + iH_V)^2} - (F_V + iH_V) \right] e^{it} \quad (43)$$

Using Eq. (43), the following expression for the normalized resonator impedance is derived,

$$\frac{Z^*}{\rho_o^* \omega_L^* d_c^*} = \frac{1}{\sigma} \left\{ \sqrt{\frac{1}{2C_{D0}^2} \left[\frac{|P_{inc}^*|}{\rho_o^* (\omega_L^* d_c^*)^2} \right] + \left(\frac{f_V + ih_V}{2C_{D0}} \right)^2} + \left(\frac{f_V + ih_V}{2C_{D0}} \right) \right\} \quad (44)$$

where f_V and h_V are defined as

$$f_V \equiv \Theta_- \frac{V_o^*}{\omega_L^* d_c^*} + 1.1 \frac{B}{\omega_L^* d_c^*} \sqrt{\frac{\omega^* v^*}{2}} \quad (45a)$$

and

$$h_V = \frac{\omega^* L_v}{\omega_L^* d_c^*} (1 - \kappa) + 0.455 \frac{B}{\omega_L^* d_c^*} \sqrt{\frac{\omega^* v^*}{2}} \quad (45b)$$

Here L_v represents the orifice inertia length parameter in the presence of grazing flow. Observe that the impedance is divided by the zero grazing flow discharge coefficient C_{D0} . This is consistent with the model used to derive the grazing flow parameter Θ_- . The sound pressure field is assumed to interact with the grazing flow to pump the grazing flow into and out-of the resonator orifice. The model assumes that the sound particle velocity field is independent of the grazing flow and thus is independent of the angles ϕ and θ .

The behaviors of the five unknown parameters, B , C_{D0} , Θ_- , L_o^* and L_v^* are determined experimentally in Section 5 below.

5. EXPERIMENTAL PROGRAM

An experimental program was undertaken to determine the unknown parameters, B , C_{D0} , Θ_- , L_o^* and L_v^* . Extensive measurements of the impedance of the three resonators identified in Table I were undertaken as a function of frequency, SPL and grazing flow speed in the HAE Subsonic Wind Tunnel facility. Figure 6 is a schematic of the test setup and data acquisition system. The resonator face-sheet was mounted flush on the side of a 12.7 cm wide by 25.4 cm high wind tunnel test section. Acoustic excitation of the resonator was generated from a loudspeaker mounted flush on the opposite wall of the test section.

The impedance of the resonators was measured using Dean's two-microphone method²⁰. This method requires the simultaneous measurement of the incident and cavity sound pressure amplitudes and their relative phases. These measurements were obtained by mounting one microphone at the cavity base and the other flush with the wall containing the orifice as shown in Figure 6. It is important to locate the incident microphone sufficiently far from the orifice to avoid near field effects. The hot wire measurements of Ingard and Ising indicated that distances on the order of about three diameters were sufficient. On the other hand, the microphone should be located sufficiently close so that the separation distance is small relative to the wavelength of the incident sound field. This is necessary to insure accurate measurement of the incident sound wave amplitude and phase.

Table I. Geometry of Test Resonators

Description	d_{ori} (inches)	τ (inches)	L_{cav} (inches)	D_{cav} (inches)	σ	f_L (Hz)	d_e (inches)
Small	0.120	0.064	0.50	2.00	0.0036	600	0.187
Middle	0.300	0.064	0.95	2.00	0.0225	600	0.298
Large	0.375	0.064	1.20	2.00	0.0352	423	0.378

Following Dean, the resonator normalized resistance and reactance are written

$$\frac{R^*}{\rho_0^* c_0^*} = \frac{|P_{inc}^*| \sin(\phi_{inc} - \phi_{cav})}{|P_{cav}^*| \sin(k^* L_{cav}^*)}, \quad \frac{X^*}{\rho_0^* c_0^*} = - \frac{|P_{inc}^*| \cos(\phi_{inc} - \phi_{cav})}{|P_{cav}^*| \sin(k^* L_{cav}^*)} \quad (46)$$

where $\phi_{inc} - \phi_{cav}$ represents the phase difference across the resonator orifice. Sound pressures were measured inside and outside the resonators for frequencies from 400 - 900 Hz, incident SPLs from 70 - 140 dB and grazing flow speeds to 77meters/second.

Figure 6 also displays a block diagram of the data acquisition system used in the measurement program. System components include a low distortion oscillator, power amplifier, high-intensity loudspeaker, microphones, precision microphone amplifiers, band-limiting filters and a HP DT-VEE Signal Analysis software. coupled to a high speed 16 channel, 12 bit high speed analog-to-digital converter. The data acquisition program used three input channels representing signals from the two microphones and the test oscillator reference signal.

The oscillator reference signal and two microphone signals are digitized at a 20 kHz sampling rate and read into data arrays of 131,072 samples each. The stored signals are Hanning weighted and Fourier transformed into three, 65,537 line complex spectra with 0.23 Hz resolution (0.153 Hz line spacing). The analysis line corresponding to the spectral peak of the reference signal is used as a pointer to the desired frequency component of the microphone signals. The amplitudes and phases of the two microphone signals are determined from the complex spectra and corrected for a 12.5 μ s sampling delay between channels. Resistance and reactance are computed in accordance with Eq. (46).

5.1 Parameter B.

The parameter B was determined by setting the imaginary component of Eq. (27) to zero (resonance) resulting in the following simplified expression for the resonator tuned resistance,

$$\frac{R_{res}^*}{\rho_o^* c_o^*} = \frac{11B}{\sigma c_o^*} \sqrt{\frac{v^* \omega^*}{2}} \quad (47)$$

Equation (47) was applied to the tuned resistance data of the small and large resonator configurations summarized in Table I and to the resonator configurations summarized in Table II below.

Figure 7 displays measured values of B calculated using Eq. (47). The following simple empirical curve-fit of the data was derived in terms of the ratio of plate thickness-to-orifice diameter ratio (τ^*/d_{ori}^*),

$$B \equiv \frac{2.19 + 17 \left(\frac{\tau^*}{d_{ori}^*} \right)^2 + 473 \left(\frac{\tau^*}{d_{ori}^*} \right)^4}{1 + 64 \left(\frac{\tau^*}{d_{ori}^*} \right)^4} \quad (48)$$

The low amplitude impedance measurements of Ingard and Ising⁷ were used to determine the behavior of B for small values of τ^*/d_{ori}^* . Because of viscous scubbing losses along the face-sheet, it is reasonable to assume that B reaches some limiting constant as $\tau^*/d_{ori}^* \rightarrow 0$. Further measurements will be required to substantiate the behavior of B when the face-plate thickness becomes very small.

Table II. Geometry of Resonators Used to Determine the Parameter B (Ref. 23)

Model No.	d_{ori} (Inches)	τ (Inches)	L_{cav} (Inches)	D_{cav} (Inches)	f_L (Hz)	d_e (Inches)
2	0.036	0.01	1.0	0.75	495	0.043
4	0.036	0.02	1.0	0.75	416	0.061
5	0.052	0.032	0.5	1.25	428	0.087
10	0.052	0.032	1.0	0.75	493	0.089
12	0.063	0.032	0.5	1.25	485	0.100

5.2 Parameter C_{D0} .

The parameter C_{D0} was determined by applying Eq. (35) to the tuned resistance data of the resonators summarized in Table I and the impedance measurements of Ingard and Ising. Substituting Eq. (48) for the parameter B into Eq. (35) and solving for C_{D0} yields,

$$C_{D0} = \sqrt{\frac{P_{non}}{2R_m^2} + \left(\frac{R_{Lin}}{2R_m}\right)^2} + \left(\frac{R_{Lin}}{2R_m}\right) \quad (49)$$

where

$$R_m \equiv \frac{R_{ret}^*}{\rho_o^* \omega_L^* d_e^*}; \quad P_{non} \equiv \frac{|P_{inc}^*|}{\rho_o^* (\omega_L^* d_e^*)^2}; \quad R_{Lin} \equiv 1.1B \sqrt{\frac{\omega^* v^*}{2(\omega_L^* d_e^*)^2}} \quad (50a,b,c)$$

Figure 8 displays measured values of C_{D0} calculated using Eq. (49). The following simple empirical curve-fit of the data was derived,

$$C_{D0} = \frac{(1 + \sqrt{P_{non}})^3 \sqrt{1 + \frac{\tau^*}{d_{ori}^*}}}{1 + 4.2x + 2.3x^{1.5} + 0.02x^2 + 5.5x^{2.5}}; \quad x \equiv \sqrt{P_{non}} \left(1 + 0.5 \frac{\tau^*}{d_e^*}\right)^{0.1} \quad (51a,b)$$

where P_{non} is defined by Eq. (50b). Figure 8 shows that when $P_{non} \rightarrow 0$, $C_{D0} \rightarrow 1$ which is consistent with the interpretation that orifice nonlinear jetting vanishes and the resonator resistance is linear, independent of sound pressure amplitude. The successful correlation of the data, including the resistance values of Ingard and Ising, with the parameter $P_{non}^{1/2}$ demonstrates the value of non-dimensionalizing impedance using $\rho_o^* \omega_L^* d_e^*$ instead of $\rho_o^* c_o^*$. The parameter $P_{non}^{1/2}$ can be interpreted as the ratio of two characteristic velocities, $\omega_L^* d_e^*$ and $(|P_{inc}^*|/\rho_o^*)^{1/2}$. Here $\omega_L^* d_e^*$ represents a very low amplitude inertia characteristic velocity in contrast to $(|P_{inc}^*|/\rho_o^*)^{1/2}$, a nonlinear characteristic velocity.

Figure 9 shows that at high values of P_{non} , the discharge coefficient of the small orifice

resonator approaches, at very high sound pressure amplitudes, the classical, high Reynolds number, steady-state value of 0.6. The reasonable behavior of the discharge coefficient validates the simplifying assumptions used in deriving the model.

5.3 Parameter L_0^*/d_e^*

The derivation of the normalized nonlinear inertial length parameter L_0^*/d_e^* was calculated by setting $h_0 = 0$ in Eq. (34b) and solving L_0^*/d_e^* to yield

$$\frac{L_0^*}{d_e^*} = \left(\frac{C_{D0} \sigma c^*}{\omega^* d_e^*} \right) \cot \left(\frac{\omega^* L_{cav}^*}{c^*} \right) - 0.455 \frac{B}{\omega^* d_e^*} \sqrt{\frac{\omega^* v^*}{2}} \quad (52)$$

Equation (52) shows explicitly through the discharge coefficient C_{D0} , the nonlinear coupling between the resistance and reactance. Figure 10 displays measured values of L_0^*/d_e^* calculated using Eq. (52). Observe the excellent collapse of the data for the small, middle and large diameter orifice resonator configurations. This validates correlation of the data by the non-dimensional parameter P_{non} . The data shows that as $P_{non} \rightarrow 0$ (i.e., the so-called linear regime), $L_0^*/d_e^* \rightarrow 1$

Figure 11 shows that at high values of P_{non} , the reactance measurements for the small diameter orifice configuration suggest that $L_0^*/d_e^* < 0.5$ which can be interpreted as the “blowing away” of more than 50% of the end correction due to orifice nonlinear jetting. This is in contrast to the claim of Ingard and Ising¹¹ that only one-half of the end correction is “blown away” by orifice jetting. This interpretation is tentative, however, because of the sparseness of the data.

A simple empirical curve-fit of the data was derived, expressed below in terms of P_{non} and τ^*/d_{ori}^* ,

$$\frac{L_0^*}{d_e^*} \equiv \frac{(1 + \sqrt{P_{non}})^3}{(1 + 10x^{1.5} + 9x^3 + 20x^4)}; \quad x \equiv \frac{\sqrt{P_{non}}}{\left[1 + \frac{\tau^*}{d_{ori}^*}\right]^{0.4}} \quad (53)$$

Figure 12 shows that the effect of incident sound pressure amplitude on resonator high amplitude tuned frequency f_{NL} can be empirically correlated in terms of resonator geometry and non-dimensional acoustic pressure P_{non} by the expression

$$\frac{f_{NL}^*}{f_L^*} \equiv \frac{(1 + \sqrt{P_{non}})^3}{(1 + 2.7\sqrt{P_{non}} + 2.3P_{non})} \quad (54)$$

Both Eq. (54) and the data show that $f_{NL}^*/f_L^* \rightarrow 1$ as $P_{non} \rightarrow 0$.

5.4 Parameter Θ_-

The effects of grazing flow on the parameter Θ_- were determined by setting $h_v = 0$ (resonance) in Eq. (44) to yield

$$\Theta_- = C_{D0} \frac{R_m}{V_{non}} - \frac{P_m}{2C_{D0} R_m V_{non}} - \frac{R_{lin}}{V_{non}} \quad (55)$$

where R_m , P_{non} and R_{lin} are defined by Eq. (50). Based on impedance measurements, the following correlation of the parameter Θ_- was achieved,

$$\Theta_- \equiv \frac{\left(\frac{\delta_{BL}^*}{d_{ori}^*} \right)^{-0.2} [1+x]^5}{1+1000x^{1.5} + 25x^{4.5}}; \quad x \equiv \sqrt{\frac{\rho_0^* V^*{}^2}{|P_{inc}^*|}} \quad (56)$$

As shown in Figure 13, the data was collapsed over a very wide range of sound pressure amplitudes, frequencies, grazing flow speeds and boundary-layer thicknesses.

Figure 14 was constructed from Eqs. (40) and (56) to connect the parameter Θ_- to the angle ϕ_- . Observe that at high grazing flow speeds, $\phi_- = 45^\circ$ which is consistent with the orifice downstream pumping of inflow/outflow suggested by the flow visualization photographs of Baumeister and Rice.

Boundary-Layer Measurements. The simple curve-fits of normalized boundary-layer thickness parameter δ_{BL}^*/d_{ori}^* vs grazing flow speed shown in Figure 15e were used to correlate the parameter Θ_- . The curve-fits were derived from the boundary-layer surveys shown in Figures 15(a-d).

5.5 Parameter L_V^*/d_e^*

The effect of grazing flow on the orifice inertial length parameter L_V^*/d_e^* was calculated by setting $h_v = 0$ in Eq. (45b) to yield

$$\frac{L_V^*}{d_e^*} = \frac{\sigma C_{D0} c_0^*}{\omega_L^* d_e^*} - 0.455 \frac{B}{\omega_L^* d_e^*} \sqrt{\frac{\omega_{res}^* V^*}{2}} \quad (57)$$

where $\omega_{res}^* = 2\pi f_{res}^*$ represents measured values of resonator tuned or resonant frequency as a function of grazing flow. Figure 16 displays measured values of L_V^*/d_e^* calculated using Eq. (57). The non-dimensional parameter $[\rho_0^* V^*{}^2 / |P_{inc}^*|]^{1/2}$ was used to collapse the data over a wide range of sound pressure amplitudes, frequencies and grazing flow speeds.

The following rather complicated curve-fit of the data was derived in terms of the ratio L_V^*/L_0^* ,

$$\left[\frac{L_V^*}{L_0^*} \right] \equiv \frac{[1+x]^4 [1+\sqrt{P_{non}}]^{-0.2}}{(1+7.4x^3+0.55x^{4.5})}; \quad x \equiv \sqrt{\frac{\rho_0^* V_\infty^{*2}}{|P_{inc}^*|}} \quad (58a,b)$$

where V_{non} is defined by Eq. (50c). Observe that the correlation of the inertial length parameter L_V^* is independent of the boundary-layer thickness parameter δ_{DSP} .

Figure 17 displays measured values of the grazing flow on the inertial length parameter L_V^*/d_e^* for the small, middle and large orifice resonator configurations tested. Note that $L_V^*/d_e^* < 0.5$ for all three resonators which suggests that at high grazing flow speeds, the interaction between the grazing flow and sound field produces intense jetting from the orifice affecting the inertial length parameter L_V^*/d_e^* on *both* sides of the orifice.

Figure 18 shows that the increase of resonator tuned frequency with sound pressure amplitude and grazing flow speed can be correlated in terms of the following empirical expression,

$$\frac{f_{NL}^*(V_\infty)}{f_L^*(0)} \equiv \frac{1 + \sqrt{\frac{\rho_0^* V_\infty^{*2}}{|P_{inc}^*|}}}{1 + 2.5 \sqrt{\frac{\rho_0^* V_\infty^{*2}}{|P_{inc}^*|}} + 0.65 \frac{\rho_0^* V_\infty^{*2}}{|P_{inc}^*|}} \quad (59)$$

5.6 Comparison Between Predicted & Measured Impedance

The empirical correlation of the parameters B , C_{D0} , Θ_- , L_0^*/d_e^* and L_V^*/d_e^* will now be used to predict the impedance of the Table I resonators and the resonator tested by Ingard and Ising. The predictions will start with non-grazing flow impedance and then include grazing flow.

Figure 19 illustrates a fundamental problem that arose when trying to use the above correlation's of the parameters B , C_{D0} , Θ_- , L_0^*/d_e^* and L_V^*/d_e^* in conjunction with the imaginary part of Eq. (33) to solve for the reactance of the small orifice resonator. Although the predicted resistance compares well with measurements for frequencies below resonance and moderately well above resonance, the agreement between predicted and measured reactance is poor.

For reasons not well understood, reasonable agreement between predicted and measured reactance was achieved for frequencies below resonance by replacing the imaginary part of Eq. (33) with the expression,

$$IM \left[\frac{Z^*}{\rho_0^* \omega_l^* d_e^*} \right] = \frac{X^*}{\rho_0^* \omega_l^* d_e^*} = \frac{h_0}{\sigma C_{D0}} \quad (60)$$

Equation (60) is an approximate solution to the imaginary component of Eq. (33) when resistance is very small relative to the absolute value of reactance. To show this, the notation of Eq. (33) is simplified by introducing the notation,

$$R_{NL}^2 \equiv \frac{1}{2C_{D0}^2} \left[\frac{P_{inc}^*}{\rho_0^* (\omega_L^* d_e^*)^2} \right] \quad (61)$$

which yields upon substitution into Eq. (33), the expression

$$\frac{Z^*}{\rho_0^* \omega_L^* d_e^*} = \frac{1}{\sigma} \sqrt{R_{NL}^2 + \left(\frac{f_0 + ih_0}{2C_{D0}} \right)^2} + \frac{f_0 + ih_0}{2\sigma C_{D0}} \quad (62)$$

At very low or high frequencies where $|h_0/C_{D0}| \gg R_{NL}^2$ or when R_{NL}^2 is very small, Eq. (62) simplifies to

$$\frac{Z^*}{\rho_0^* \omega_L^* d_e^*} \equiv \frac{f_0}{\sigma C_{D0}} + i \frac{h_0}{\sigma C_{D0}} \quad (63)$$

Under these conditions, the normalized reactance $X^*/\rho_0^* \omega_L^* d_e^*$ of a resonator may be written,

$$\frac{X^*}{\rho_0^* \omega_L^* d_e^*} \equiv \frac{h_0}{\sigma C_{D0}} \quad (64)$$

Referring to Figure 19, the quantity $h_0/\sigma C_{D0}$ fits the measured reactance data very accurately below resonance and somewhat accurately above resonance. For this reason, Eq. (64) will be used to predict resonator reactance for both the non-grazing flow and grazing flow models. The real component of Eqs. (33) and (44) will be used to predict the corresponding resonator resistance.

5.6.1. Non-Grazing Flow

Figures 20(a-c) compare predicted with measured resistance and reactance, respectively, of the small, middle and large diameter orifice resonator configurations of Table I. Equation (33) in conjunction with the parameters B , C_{D0} and L_0/d_e predict quite accurately the nonlinear resistive losses of all three diameter resonators over a reasonably wide frequency and SPL range. Equation (64) also accurately predicts the corresponding nonlinear reactance.

The impedance measurements show that resonator resistance is very sensitive to incident sound pressure amplitude in a frequency range centered at its tuned frequency. At frequencies very much below or above resonance, the resistance becomes increasingly independent of SPL. This occurs because the resonator impedance is

controlled by cavity stiffness at very low frequencies and by orifice inertia at very high frequencies and the acoustic nonlinear jetting from the orifice is reduced accordingly.

Despite the intense nonlinear orifice jetting at high sound pressure amplitudes, both data and the model show that resonator reactance has a profound effect upon the resonator resistance but the resistance only negligibly affects resonator reactance. The negligible coupling between nonlinear resistance and resonator reactance permits the partition of reactance into the familiar inertial and stiffness components.

Using Eq. (48) to predict the parameter B and Eq. (49) to predict the parameter C_{D0} , Figure 21 correlates the tuned resistances of the small, middle and large orifice resonator configurations and the resonator configuration tested by Ingard and Ising. Observe that all the data collapsed quite accurately by normalizing the resistance by $\rho_0 \omega_L d_e^2$ and plotting it against the parameter $P_{non}^{1/2}$. The agreement between prediction and measurement is excellent over a wide range of resonator geometry's and sound pressure amplitudes.

5.6.2 Effect of Grazing Flow

Figures 22(a,b) compare the predicted resistances and reactances of the small and large diameter orifices defined in Table I respectively with experimental values. The model predicted resonator impedance reasonably well over the entire range of sound pressure amplitudes, frequencies and grazing flow speeds tested. However, the model does not predict the measured decrease in resistance with frequency.

Figures 23(a,b,c) shows that the model accurately predicts the effect of grazing flow on the tuned resistance of the three resonators defined in Table I. Observe that the effects of grazing flow are small when $V_{\infty} / \omega_L d_e < 1$ and become large when $V_{\infty} / \omega_L d_e > 1$. Thus $V_{\infty} / \omega_L d_e$ represents a useful parameter to gauge when grazing flow effects significantly affect resonator resistance.

6. CONCLUDING REMARKS

- Despite its highly simplified formulation, the impedance model is sufficiently accurate to connect aircraft engine nacelle liner optimum impedance to single orifice resonator geometry. The simplicity of the model permits rapid preliminary design analyses.
- The nonlinear behavior of Helmholtz resonators can be correlated in terms of acoustic discharge coefficient and orifice inertial length parameters. Both parameters can be described in terms of the characteristic velocities $\omega_L d_e$ and $\sqrt{|P_{inc}|} / \rho_0$.
- Nonlinear orifice jetting is most pronounced for frequencies sufficiently close to

resonance that resonator reactance is small compared to resistance. Near resonance, the orifice resistance is proportional to the square root of the amplitude of the incident sound and inversely proportional to orifice discharge coefficient. At frequencies very much below or above resonance, the resistance becomes independent of SPL, the so-called linear regime. This occurs because the resonator impedance is controlled by cavity stiffness at very low frequencies and by orifice inertia at very high frequencies. Thus the strength of acoustic nonlinear jetting from the orifice is reduced and more nearly linear resistance behavior is displayed.

- Due to the weak coupling between orifice nonlinear resistance and reactance, the nonlinear behavior of the resonator does not prevent the familiar partition of reactance into separate orifice inertia and cavity stiffness components.
- The reduction of reactance with sound pressure amplitude was correlated in terms of the reduction of the orifice inertia length parameter. The data supports the interpretation initially proposed by Ingard and Ising that the “blowing away” of the orifice inertia length by nonlinear jetting is the principal cause of the reduction of reactance. Although not discussed by Ingard and Ising, this interpretation is also consistent with the “blowing away” of orifice inertia length and hence reduction of reactance by grazing flow .
- The model predicted resonator impedance reasonably well over the entire range of sound pressure amplitudes, frequencies and grazing flow speeds tested. The effect of grazing flow was shown to be small when the parameter $V_0/\omega_L d_e < 1$ and large when $V_0/\omega_L d_e > 1$.
- Flow visualization photographs show that the nonlinear behavior of Helmholtz resonators are characterized by intense jetting of fluid from the orifice. Penetration distances on the order of 100 orifice diameters are believed to be generated at very high SPLs. Since SPLs in aircraft engine motors are often on the order of 1% of the mean pressure, it is reasonable to conclude that the jets penetrate and disturb the engine boundary layer causing an increase in static pressure losses. The actual penetration depth will undoubtedly be reduced by mean flow within the motor interior. This behavior is not well understood and warrants further study.
- Helmholtz resonators *generate* higher harmonic sound due to nonlinear orifice jetting when exposed to intense high amplitude incident sound. The possibility exists that Helmholtz resonators may generate higher harmonic sound pressures that may couple with the engine interior sound fields to excite difficult to attenuate higher-order modes. This behavior is not well understood and warrants further study.

REFERENCES

1. Rayleigh, Lord, *Theory of Sound*, Dover Publications, New York, 1945.
2. Junger, M. C., “Helmholtz Resonators in Load-Bearing Walls”, *Noise Control Engineering*, Vol. 4, No. 1, pp. 17-25, Jan-Feb., 1975.

3. Crandall, I. B., *Theory of Vibration Systems and Sound*, D. Van Nostrand & Co., New York, 1927.
4. Ingard, U., "On the Theory and Design of Acoustical Resonators", *JASA*, V. 25, pp. 1037-1062, 1953.
5. Sivian, L. J., "Acoustic Impedance of Small Orifices", *JASA.*, V. 7, 94-101, 1935.
6. Melling, T. H., "The Acoustic Impedance of Perforates at Medium and High Sound Pressure Levels," *JSV.*, V. 29, No. 1, 1-65, 1973.
7. Ingard, U. and Ising, H., "Acoustic Nonlinearity of an Orifice", *JASA*, Vol. 42, No. 1. 6-17. 1967.
8. Sirignano, W. A., "Non Linearity dei Risonatori di Helmholtz", *Aerotecnica Missili E. Spazio N.*, 4-1972.
9. Zinn, B. T., "A Theoretical Study of Nonlinear Damping by Helmholtz Resonators", *JSV*. 13(3), 347-356, 1970.
10. Hersh, A. S. and Rogers, T., "Fluid Mechanical Model of the Acoustic Impedance of Small Orifices", *NASA CR-2682*, May 1976.
11. Hersh, A. S. and Walker, B., "Effect of Grazing Flow on the Impedance of Helmholtz Resonators Consisting of Single and Clustered Orifices", *NASA CR-3177*, August, 1979.
12. Hersh, A. S. And Walker, B. E. ,"Nonlinear Acoustic Behavior of Helmholtz Resonators", *U. S. Air Force Phillips Laboratory Report, PL-TR-91-3077*, Dec., 1991.
13. Cummings, A., "Acoustic Nonlinearities and Power Losses at Orifices", *Paper AIAA-83-0739*, April, 1983.
14. Cummings, A. and Eversman, W., "High Amplitude Acoustic Transmission Through Duct Terminations: Theory", *JSV*, 91, 503-518, 1983.
15. Yang, I. J. and Cummings, A. , A Time Domain Solution for the Attenuation, At High Amplitudes, of Perforated Tube Silencers and Comparison with Experiment, *JSV*,122, 243-259, 1988.
16. Thurston, G. B., Hargrove, Jr., L. E., and Cook, W. D., "Non-linear Properties of Circular Orifices", *JASA.*, Vol 29, No. 9, 1957, 992-1001.
17. Mechel, F., Mertens, P., and Schilz, W., "Research on Sound Propagation in Sound Absorbent Ducts with Superimposed Air Streams", *AMRL-TDR-62-140*, Vol. III, Physik, Inst., Univ. Gottingen, West Germany (1962).
18. Phillips, B., "Effects of High Wave Amplitude and Mean Flow on a Helmholtz

- Resonator", NASA TM X-1582 (1968).
19. Ronneberger, D., "The Acoustic Impedance of Holes in the Wall of Flow Ducts", JSV, Vol. 32, No 1, pp. 133-150, (1972).
 20. Dean, P. D., "An InSitu Method of Wall Acoustic Impedance Measurement in Flow Ducts", JSV, Vol. 34, No 1, p 97, 1974.
 21. Rogers, T. and Hersh, A. S., "The Effect of Grazing Flow on the Steady-State Resistance of Isolated Square-Edged Orifices", NASA CR-2681, (1976).
 22. Baumeister, K. J. and Rice, E. J., "Visual Study of the Effect of Grazing Flow on the Oscillatory Flow in a Resonator Orifice", NASA TM X-3288 (1975).
 23. Hersh, A. S. and Walker, B., "Effect of Grazing Flow on the Impedance of Helmholtz Resonators Consisting of Single and Clustered Orifices", NASA CR-3177, August, 1979.
 24. Rice, E. J., "A Theoretical Study of the Acoustic-Impedance of Orifices in the Presence of a Steady Grazing Flow", NASA TM X-71903, April (1976).
 25. Hersh, A. S. And Walker, B. E. , "Nonlinear Acoustic Behavior of Helmholtz Resonators", U. S. Air Force Phillips Laboratory Report, PL-TR-91-3077, Dec., 1991.
 26. Charwat, A. F. and Walker, B.E., "The Velocity Field Near the Orifice of a Helmholtz Resonator in Grazing Flow", UCLA-ENG-81-101, March, 1981.
 27. Charwat, A. F. and Walker, B.E., "The Velocity Perturbations Above the Orifice of an Acoustically Excited Cavity in Grazing Flow", J. Fluid Mech., V. 128, pp. 413-426, (1983).
 28. Kooi, J. W. and Sarin, S. L., "An Experimental Study of the Acoustic Impedance of Helmholtz Resonator Arrays Under a Turbulent Boundary", AIAA-81-1998, Oct. 1981.
 29. Rossiter, J. E., "Wind Tunnel Experiments on the Flow Over Rectangular Cavities at Subsonic and Transonic Speeds", Royal ARC R&M 3438, 1966.
 30. Heller, H. H. and Bliss, D. B., "The Physical Mechanism of Flow-Induced Pressure Fluctuations in Cavities and Concepts for their Suppression", AIAA Paper No. 75-491, March, 1975.
 31. Bolton, J.S., "The Excitation of an Acoustic Resonator by Pipe Flow", M. Sc. Dissertation, Institute of Sound And Vibration Research, Univ. of South Hampton, 1972.
 32. DeMetz, F. M. and Farabee, T. M., "Laminar and Turbulent Shear Flow Induced Cavity Resonances", AIAA Paper No. 77-1293, October, 1977.

33. Nelson, P.A., Halliwell, N. A. and Doak, P.W., "Fluid Dynamics of a Flow Excited Resonance, Part I: Experiment", JSV, Vol. 78, No 1, pp. 15-38, (1981).
34. Nelson, P.A., Halliwell, N. A. and Doak, P.W., "Fluid Dynamics of a Flow Excited Resonance, Part II: Flow Acoustic Interaction", JSV, Vol. 78, No 1, pp. 15-38, (1981).
35. Worraker, W. J. and Halliwell, N. A., "Jet Engine Liner Impedance: An Experimental Investigation of Cavity Neck Flow/Acoustics in the Presence of a Mach 0.5 Tangential Shear Flow", JSV, Vol. 103, No 4, pp. 573-592, (1985).

```

C C *****
C
C           APPENDIX A.  PROGRAM FACE-SHEET VELOCITY.FOR
C
C   Program to Compute the Face-Sheet Impedance of a SDOF, Cavity-Backed,
C   Single Circular Perforate in Orifice a Grazing Flow Environment.
C
C   Based on Hersh Impedance Model
C
C   ASH - 2/3/97
C
C *****
C
C   PROGRAM FACESHEET
C   REAL FREQ, RESIS, REACT, TAU, SPL, FREQINIT,
+   SIGMA, EPSILON, UREF, DELTABL, DCAV, DORI,
+   NU, PI, RHO, PINC, VINP, CM, CO, LCAV, MACH, DELFREQ
C
C   INTEGER*2 ITERATIONS, NFREQ
C
C   CHARACTER*80 FILENAME
C
C   WRITE (*,*) 'SPECIFY NAME OF OUTPUT FILE'
C   READ(*,11,END=1000) FILENAME
C   WRITE(*,*) FILENAME
11  FORMAT(A8)
C   OPEN(UNIT=3, FILE=FILENAME, FORM='FORMATTED', STATUS='UNKNOWN')
C
C   DATA CM,NU, PI, RHO, CO / 2.54,0.15,3.14159,0.0012,34400. /
C   EPSILON = 0.01
C   ITERATIONS = 0
C
C   THE RESONATOR PARAMETERS,LCAV,DCAV,DORI,TAU ARE ASSUMED KNOWN AND
C   ARE INPUT IN INCHES.  HERE LCAV = CAVITY DEPTH, DCAV = CAVITY DIAMETER,
C   DORI = ORIFICE DIAMETER, TAU = FACE-PLATE THICKNESS AND OPEN AREA RATIO
C   PARAMETER SIGMA = (DORI/DCAV)**2.
C
C   WRITE (*,*) 'INPUT CAVITY DEPTH (INCHES) '
C   READ(*,*) LCAV
C   LCAV = LCAV*CM
C   WRITE (*,*)
C
C   WRITE (*,*) 'INPUT CAVITY DIAMETER (INCHES) '
C   READ(*,*) DCAV
C   DCAV = DCAV*CM
C   WRITE (*,*)
C
C   WRITE (*,*) 'INPUT ORIFICE DIAMETER (INCHES) '
C   READ(*,*) DORI
C   DORI = DORI*CM
C   WRITE (*,*)
C
C   WRITE (*,*) 'INPUT FACE-PLATE THICKNESS (INCHES) '
C   READ(*,*) TAU
C   TAU = TAU*CM
C   WRITE (*,*)
C   SIGMA = (DORI/DCAV)**2
C
C *****
C
C   INPUT (REAL) FACE-SHEET VELOCITY (UREF), SOUND FREQUENCY (FREQ), GRAZING
C   FLOW MACH NO. (MACH) AND BOUNDARY-LAYER DISPLACEMENT THICKNESS (DELTABL).
C
C   WRITE (*,*) 'INPUT FACE-SHEET VELOCITY UREF (CM/SEC) '
C   READ(*,*) UREF
C   WRITE (*,*)
C
C   WRITE (*,*) 'INPUT INITIAL SOUND FREQUENCY (Hz) '
C   READ(*,*) FREQINIT
C   WRITE (*,*)

```

```

WRITE (*,*) 'INPUT FREQUENCY INCREMENT (Hz)'
READ(*,*) DELFREQ
WRITE (*,*)

WRITE (*,*) 'INPUT NO FREQUENCY INTERVALS'
READ(*,*) NFREQ
WRITE (*,*)

C
WRITE (*,*) 'INPUT GRAZING FLOW MACH NO. '
READ(*,*) MACH
VINP = MACH*CO
WRITE (*,*)

C
WRITE (*,*) 'INPUT BOUNDARY-LAYER DISPLACEMENT THICKNESS (INCHES)'
READ(*,*) DELTABL
DELTABL = DELTABL*CM
IF(DELTABL.EQ.0.) DELTABL = DELTABL + 0.0001
WRITE (*,*)

C
C
WRITE(3,*)' LCAV      DCAV      TAU      DORI      MACH      BL-THICK'
WRITE(3,*)' (in)      (in)      (in)      (in)      No.      (in)'
WRITE(3,*)' '
WRITE(3,78) LCAV/CM, DCAV/CM, TAU/CM, DORI/CM, MACH, DELTABL/CM
WRITE(3,*)' '
WRITE(3,*)' '
WRITE(3,*)' '
WRITE(3,*)' '
WRITE(3,*)' '
WRITE(3,*)' UFS      FREQ      SPL      RESIS      X_FACE
+ REACT      N_ITERS'
WRITE(3,*)' (cm/s)      (Hz)      (dB)      '
WRITE(3,*)

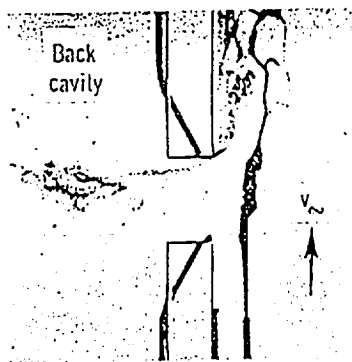
C
C
*****
C
START WITH CREATING DO-LOOP ON FREQUENCY FROM FREQINIT TO FINAL DESIRED FREQUENCY
C
C
THEN START WITH INITIAL GUESS OF SPL = 120 dB, CALCULATE IMPEDANCE Z AND COMPARE
C
IMPEDANCE MODEL PREDICTED FACE-SHEET VELOCITY (UFS) WITH INPUT FACE-SHEET
C
VELOCITY UREF CALCULATED FROM EXPRESSION UFS = PINC/Z.
C
C
THEN PREDICT NEW PINC USING PREDICTED Z AND INPUT FACE-SHEET VELOCITY UREF
C
USING EXPRESSION PINC = UREF*SQRT(R**2 + X**2). REPEAT THIS PROCEDURE UNTIL
C
THE QUANTITY ABS[1 - UREF/UFS] < EPSILON = 0.01.
C
C
C
DO 2 I = 1, NFREQ
FREQ = FREQINIT + (I-1)*DELFREQ
C
C
PINC = 200
3 CALL IMPEDANCE (PINC, RESIS, FACERACT, NU, PI, RHO, FREQ, CO, VINP,
+ DORI, TAU, SIGMA, LCAV, REACT, DELTABL)
UFS = PINC/(RHO*CO*SQRT(RESIS*RESIS+REACT*REACT))
ITERATIONS = ITERATIONS + 1
IF (ITERATIONS.LT.10000) GOTO 22
WRITE(3,*)' '
WRITE(3,*)'PROGRAM STOP: NO. OF ITERATIONS > 10000'
STOP
22 CONTINUE
IF (ABS(1-UFS/UREF).GT.EPSILON) THEN
PINC = RHO*CO*UREF*SQRT(RESIS*RESIS+REACT*REACT)
GOTO 3
ELSE
C
C
*****
C
PRINT FOLLOWING OUTPUT: UFS, FREQ, SPL, RESISTANCE, FACE_SHEET REACTANCE,
C
RESONATOR REACTANCE AND NUMBER OF ITERATIONS
C
REQUIRED FOR CONVERGENCE.
C
C
SPL = 20.*ALOG10(PINC/0.0002)
WRITE(3,66) UFS, FREQ, SPL, RESIS, FACERACT, REACT, ITERATIONS
WRITE(3,*)

```

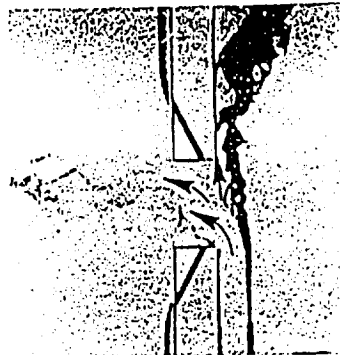
```

C
66 FORMAT(1X,3(F7.1,5X),F6.3,3X,2(F8.4,5X),2X,I4)
78 FORMAT(1X,5(F7.4,2X),F7.4)
  ENDIF
  2 CONTINUE
1000 stop
  END
C
C ***** SUBROUTINE IMPEDANCE *****
C
C THIS SUBROUTINE CALCULATES THE RESONATOR RESISTANCE, REACTANCE
C SUBROUTINE IMPEDANCE (PINC,RESIS,FACERACT,NU,PI,RHO,FREQ,C0,
+   VINF,DORI,TAU,SIGMA,LCAV,REACT,DELTABL)
C
C COMPLEX ALPHABETA,Z
C
C REAL FREQ, RESIS, REACT, DORI,TAU,FL,VREF,PNON,XLIN,
+   SIGMA, DELTABL,OMEGA,OMEGAL,X,Y,B,XV,NU,
+   VINF,C0,LCAV,L0DE,LVDE,UUU,PSIV,VVV,
+   ALPHA,ALPHA1,ALPHA2,BETA,BETA1,BETA2,BETA3
C
C OMEGA = 2*PI*FREQ
C DE = TAU + .85*DORI/(1 + 0.625*SQRT(SIGMA))
C OMEGAL = C0*SQRT(SIGMA)/(DE*LCAV)
C FL = OMEGAL/(2*PI)
C VREF = OMEGAL*DE
C PNON = PINC/(RHO*VREF**2)
C DISPL = DELTABL/DORI
C
C ** RESONATOR PARAMETERS *****
C
C X = SQRT(PNON)*(1+TAU/DORI)**0.1
C CD0 = SQRT(1+TAU/DORI)*(1+SQRT(PNON))**3/
+   (1+4.2*X + 2.3*X**1.5 + 0.02*X*X + 5.5*X**2.5)
C Y = SQRT(PNON)/(1+TAU/DORI)**0.4
C L0DE = (1+SQRT(PNON))**3/(1+10*Y**1.25+9*Y**3+20*Y**4)
C XLIN = (TAU/DORI)**2
C B = (2.19 + 17*XLIN+473.*XLIN**2)/(1 + 64.*XLIN**2)
C XV = SQRT(RHO*VINF*VINF/PINC)
C UUU = ((1+XV)**5)/DISPL**0.2
C PSIV = UUU/(1 + 1000*XV**1.5 + 25*XV**4.5)
C VVV = ((1 + XV)**4)/(1+SQRT(PNON))**0.2
C LVDE = L0DE*VVV/(1 + 7.4*XV**3 + 0.56*XV**4.5)
C
C *** PARAMETERS ALPHA AND BETA *****
C
C PNL = PNON/(2*CD0*CD0)
C ALPHA1 = PSIV*VINF/(2*CD0*VREF)
C ALPHA2 = B*SQRT(OMEGA*NU/2)/(2*CD0*VREF)
C ALPHA = ALPHA1 + 1.1*ALPHA2
C BETA1 = OMEGA*LVDE/(2*CD0*OMEGAL)
C BETA2 = SIGMA*C0/(2*VREF*TAN(OMEGA*LCAV/C0))
C BETA3 = 0.455*ALPHA2
C BETA = BETA1 - BETA2 + BETA3
C ALPHABETA = CMPLX(ALPHA,BETA)
C
C *** PRINT OUTPUT *****
C
C Z = ALPHABETA + CSQRT(PNL + ALPHABETA**2)
C RESIS = REAL(Z)*VREF/(SIGMA*C0)
C REACT = 2*BETA*VREF/(SIGMA*C0)
C FACERACT = 2*(BETA1+BETA3)*VREF/(SIGMA*C0)
C
C END

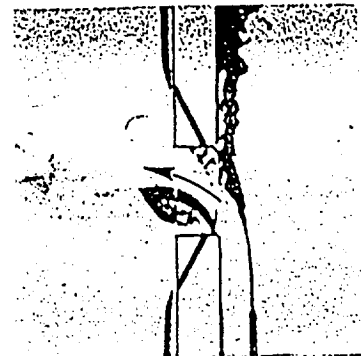
```



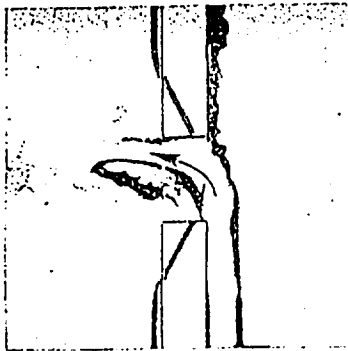
$t = 0.0$ sec
Start of cycle



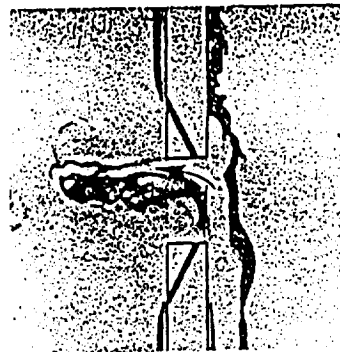
$t = 0.1$ sec
Inflow



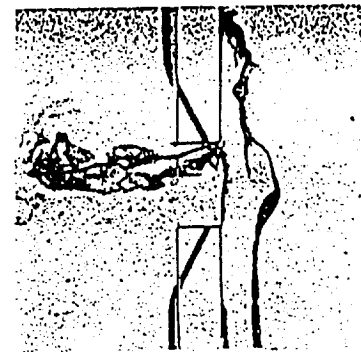
$t = 0.218$ sec
Inflow



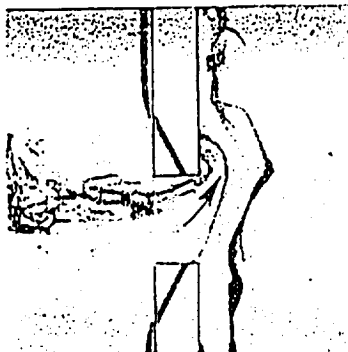
$t = 0.268$ sec
Maximum
inflow



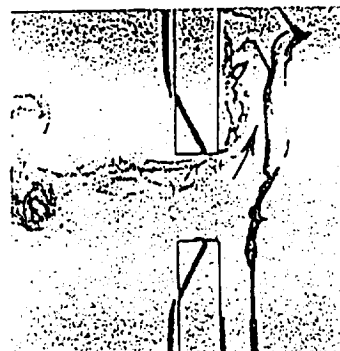
$t = 0.316$ sec
Beginning of flow
reversal



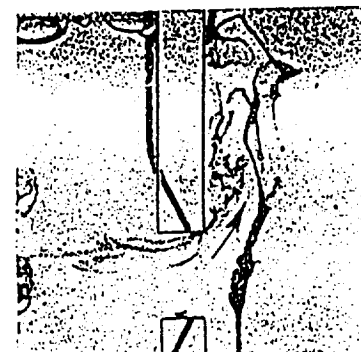
$t = 0.364$ sec
Outflow



$t = 0.404$ sec
Outflow



$t = 0.476$ sec
Outflow



$t = 0.50$ sec
End of cycle

Figure 1. Flow Visualization Photographs of Grazing Flow - Sound Interaction Near Resonator Orifice (Reference 22)

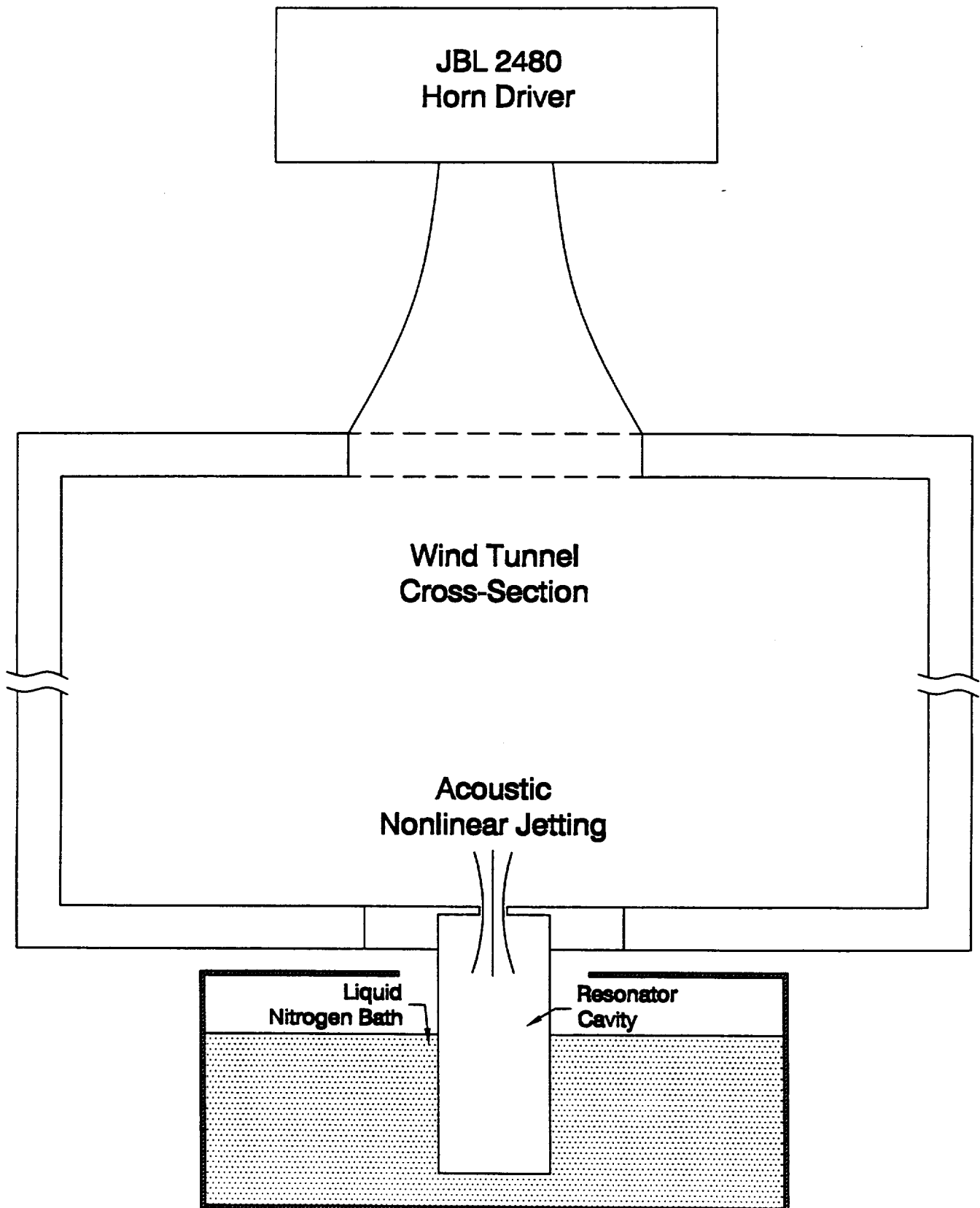


Figure 2
Schematic of Flow
Visualization Test

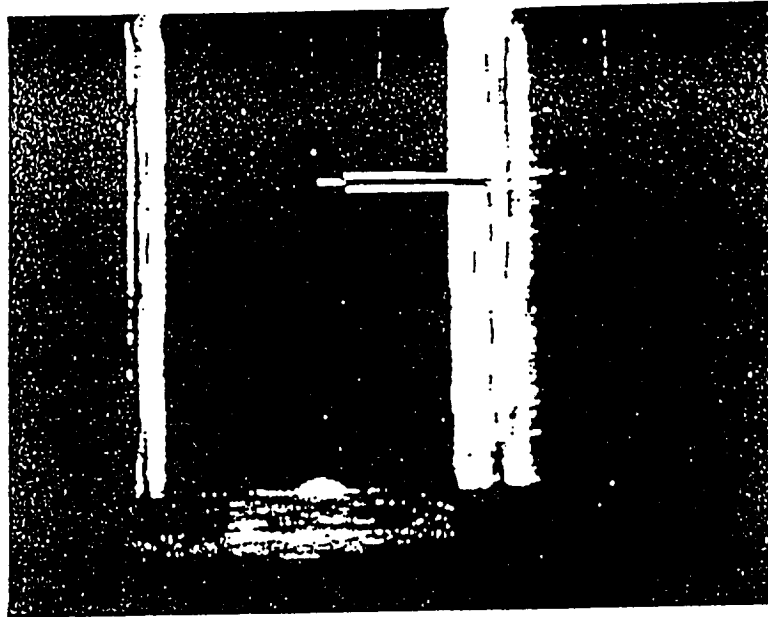


Figure 3a. Flow Visualization of Nonlinear Orifice Jetting: SPL = 100 dB

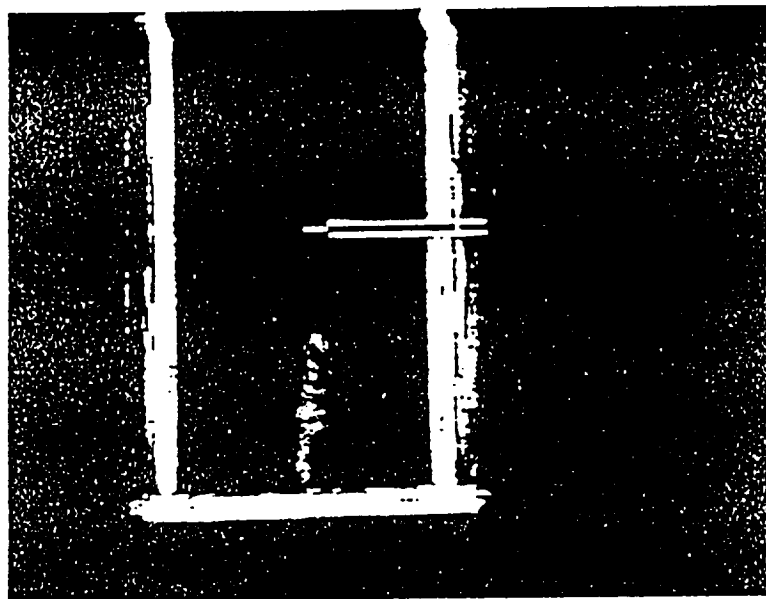


Figure 3b. Flow Visualization of Nonlinear Orifice Jetting: SPL = 110 dB

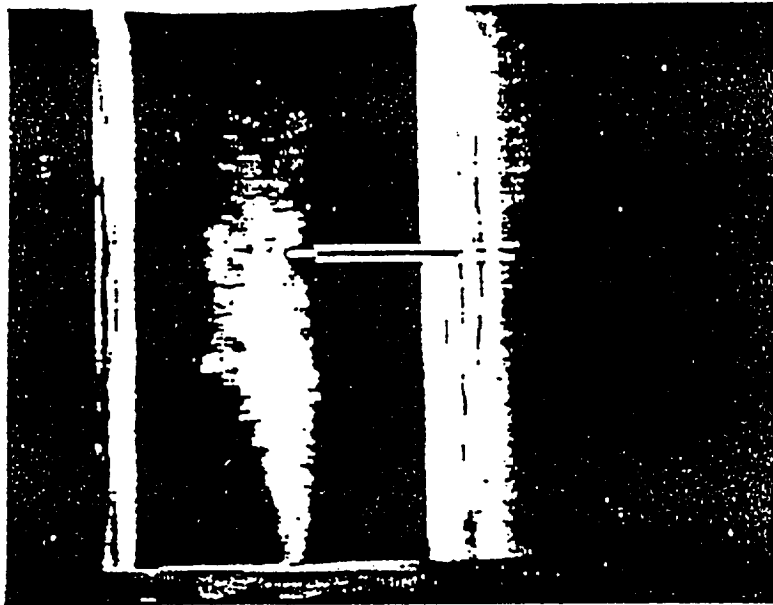


Figure 3c. Flow Visualization of Nonlinear Orifice Jetting: SPL = 120 dB

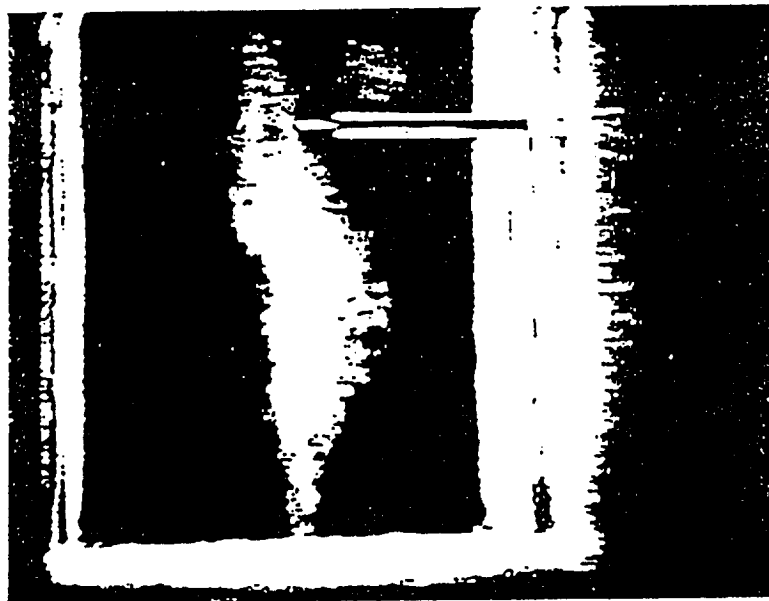


Figure 3d. Flow Visualization of Nonlinear Orifice Jetting: SPL = 130 dB

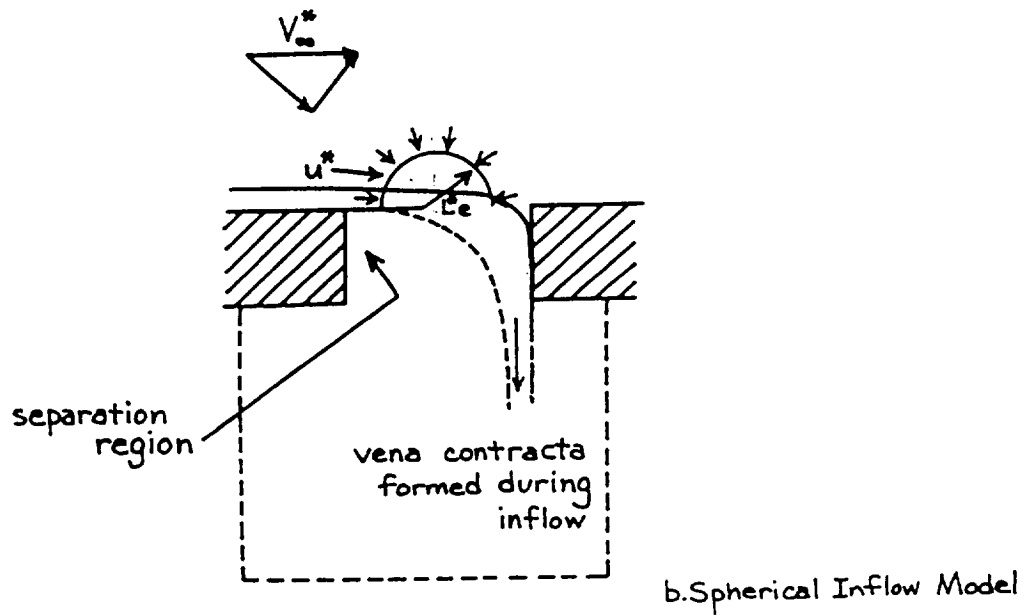
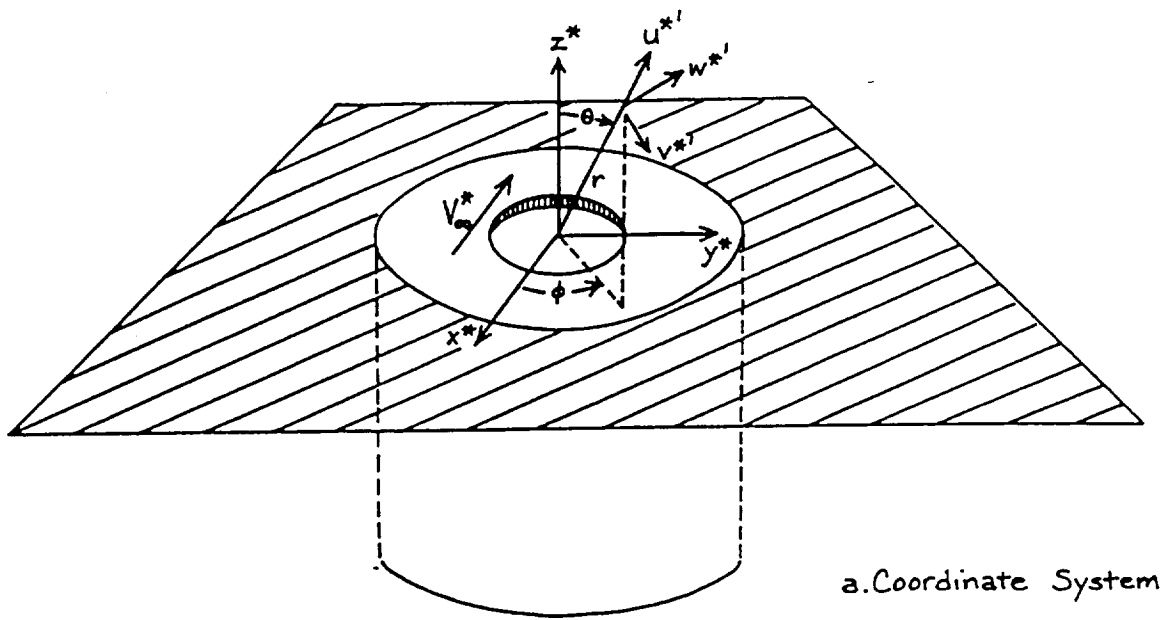


Figure 4. Schematic of Coordinate System and Spherical Inflow Model

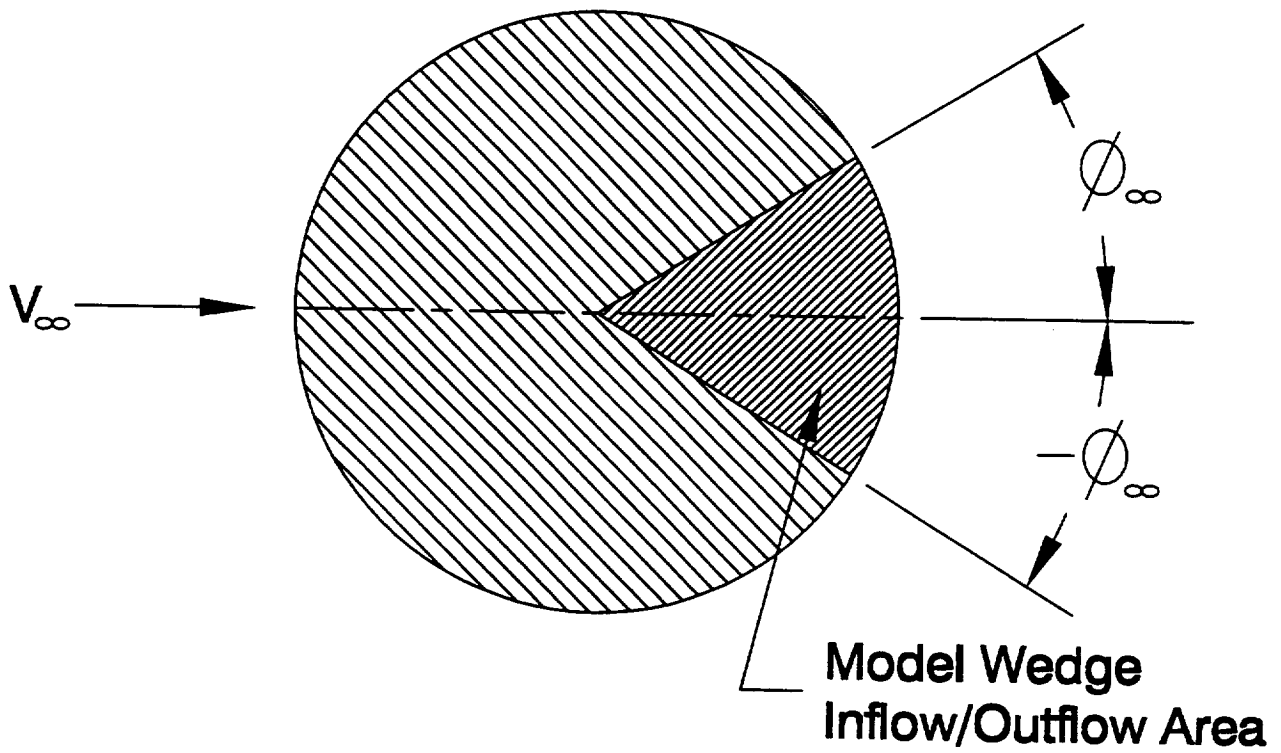


Figure 5
Schematic of Proposed Grazing
Flow - Sound Interaction Model

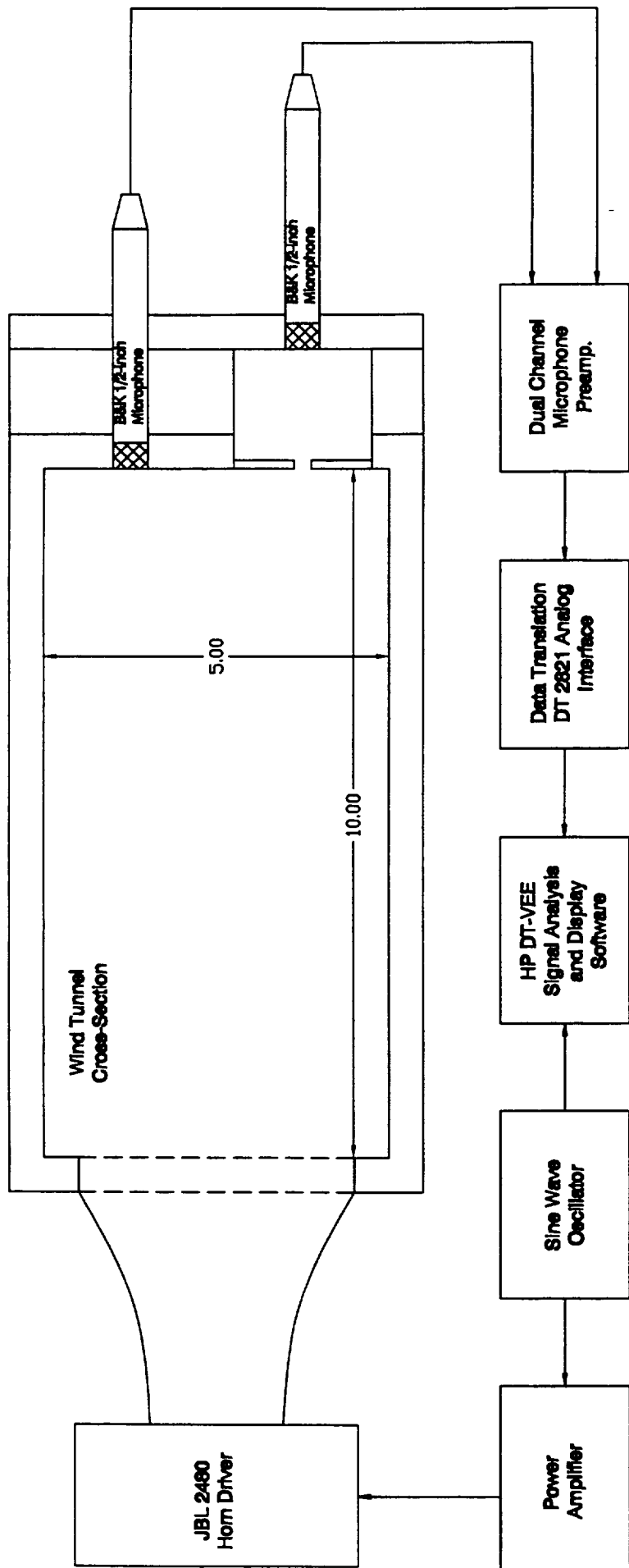


Figure 6. Schematic of Test Setup and Data Collection System

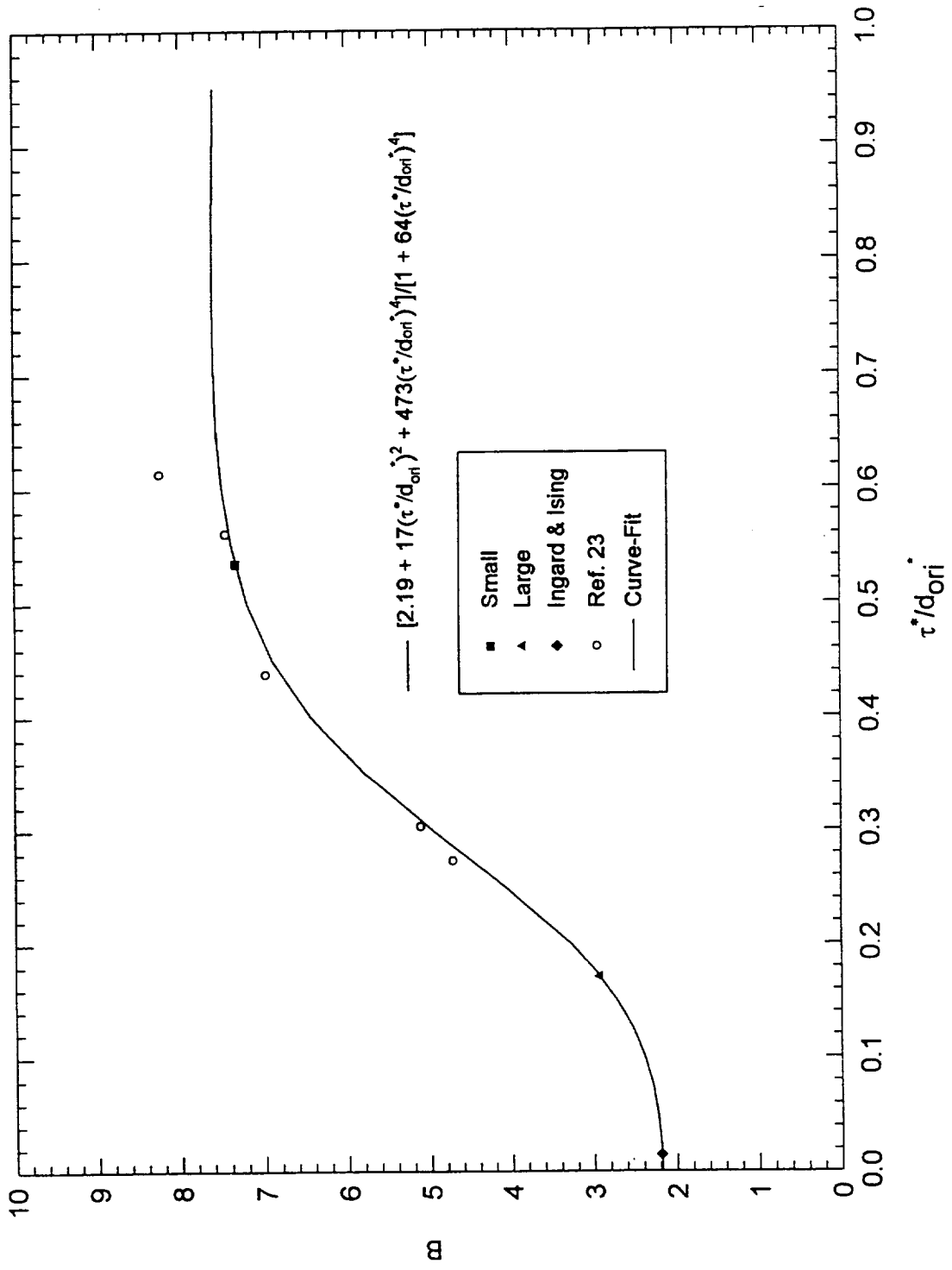


Figure 7. Correlation of Viscous Scrubbing Loss Parameter B

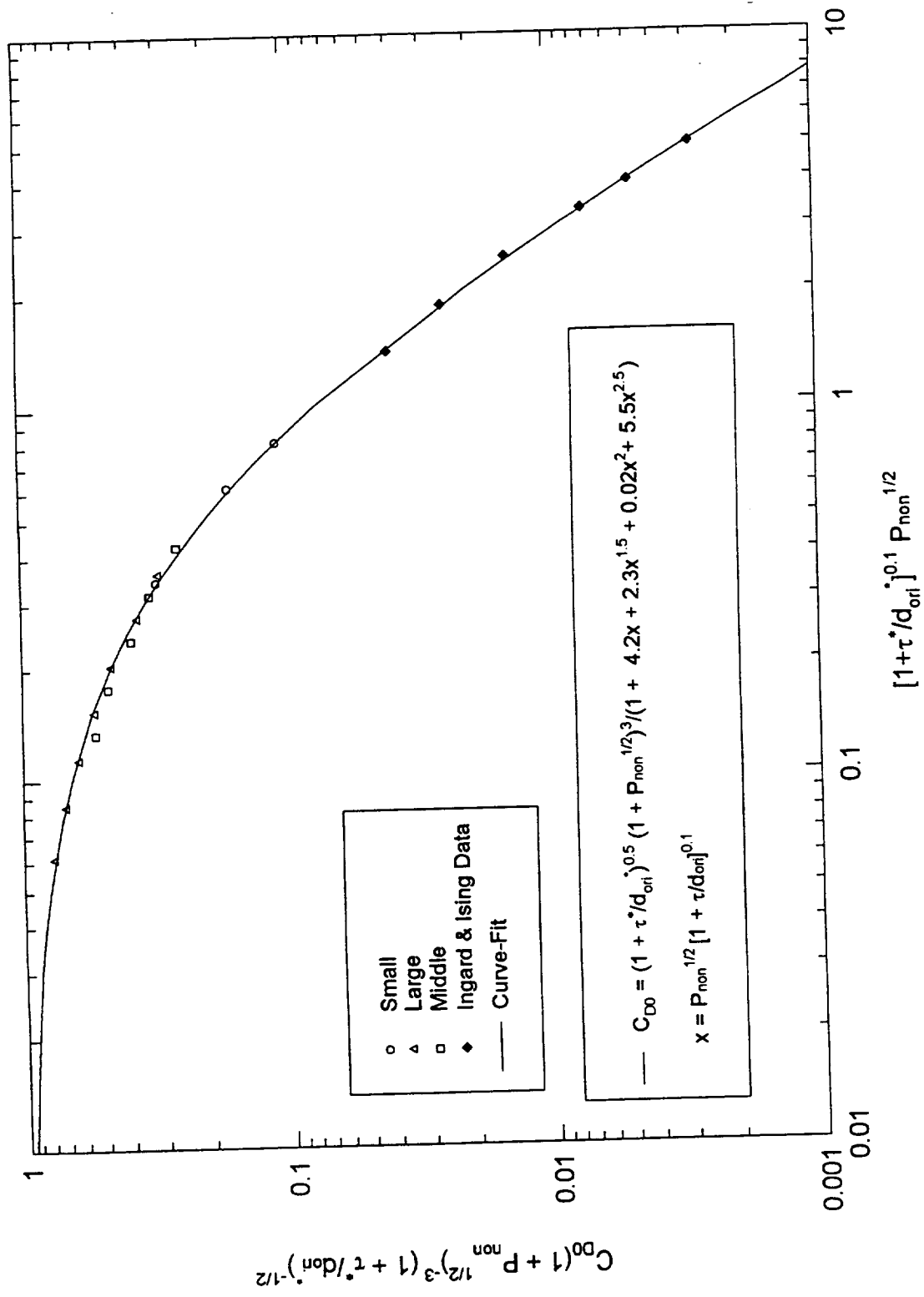


Figure 8. Correlation of Non-Grazing Flow Parameter C_{D0}

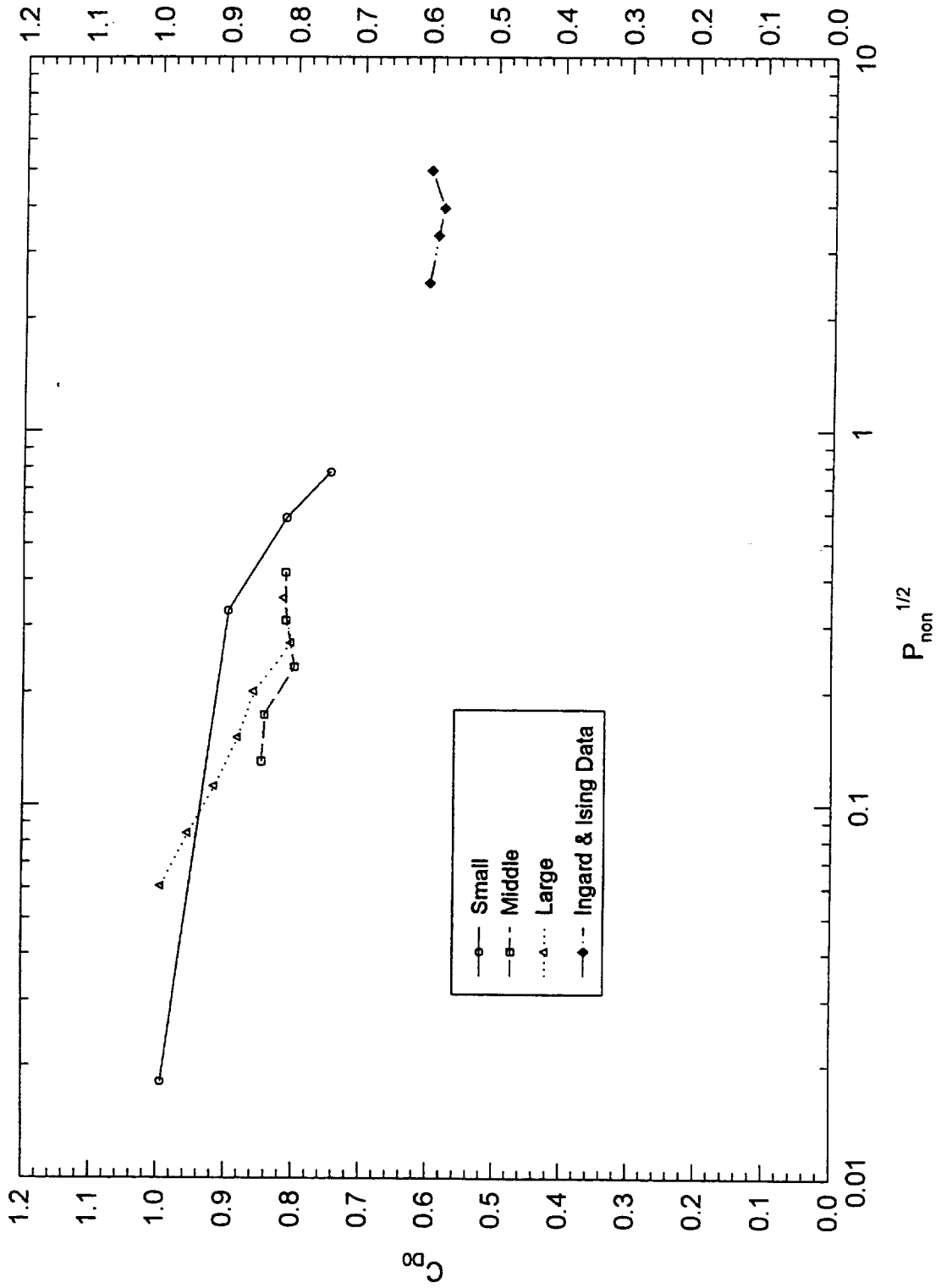


Figure 9. Effect of SPL on Non-Grazing Flow Discharge Coefficient Parameter C_{D0}

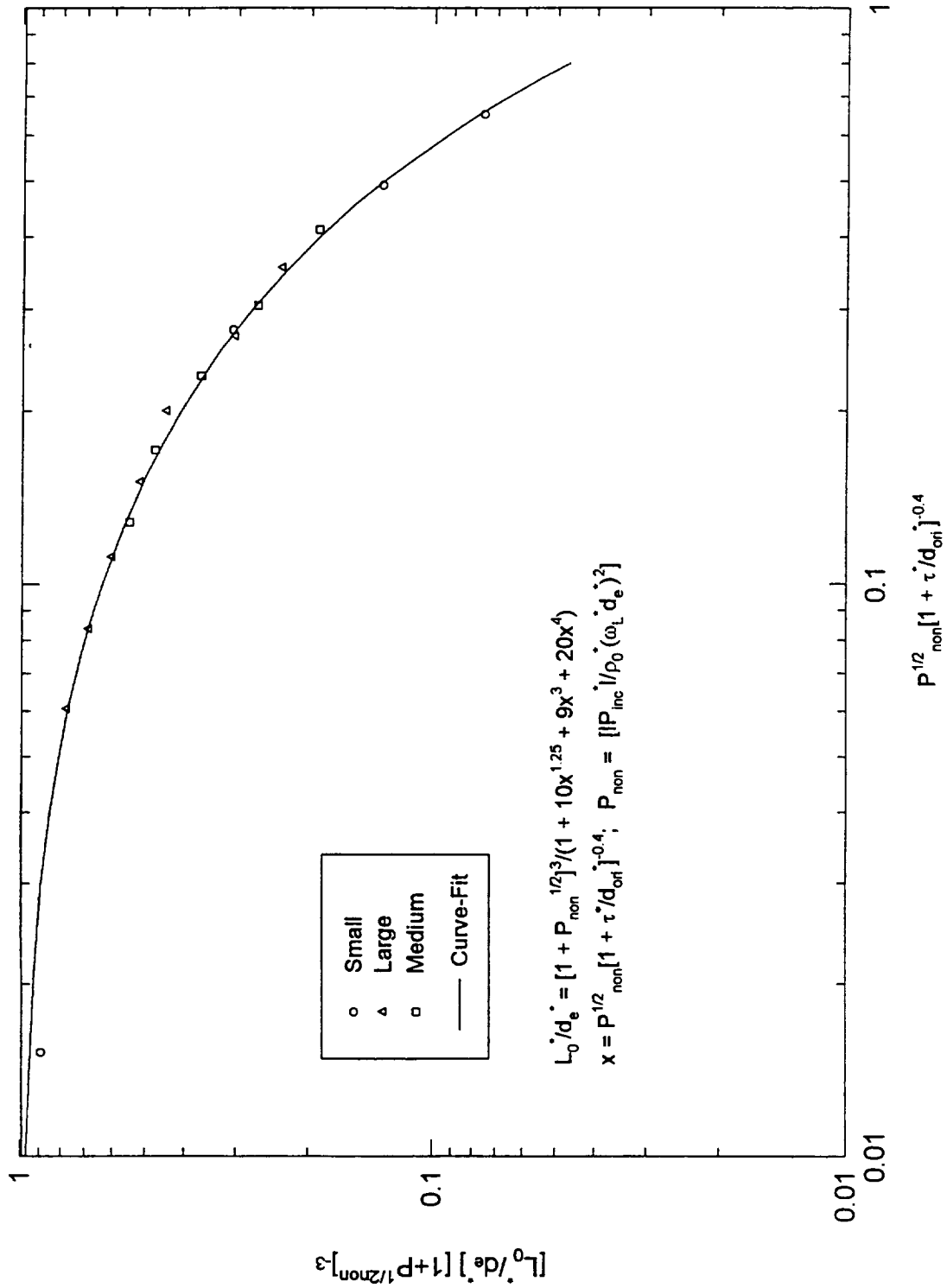


Figure 10. Correlation of Non-Grazing Flow Inertia Length Parameter L_0^*/d_e^*

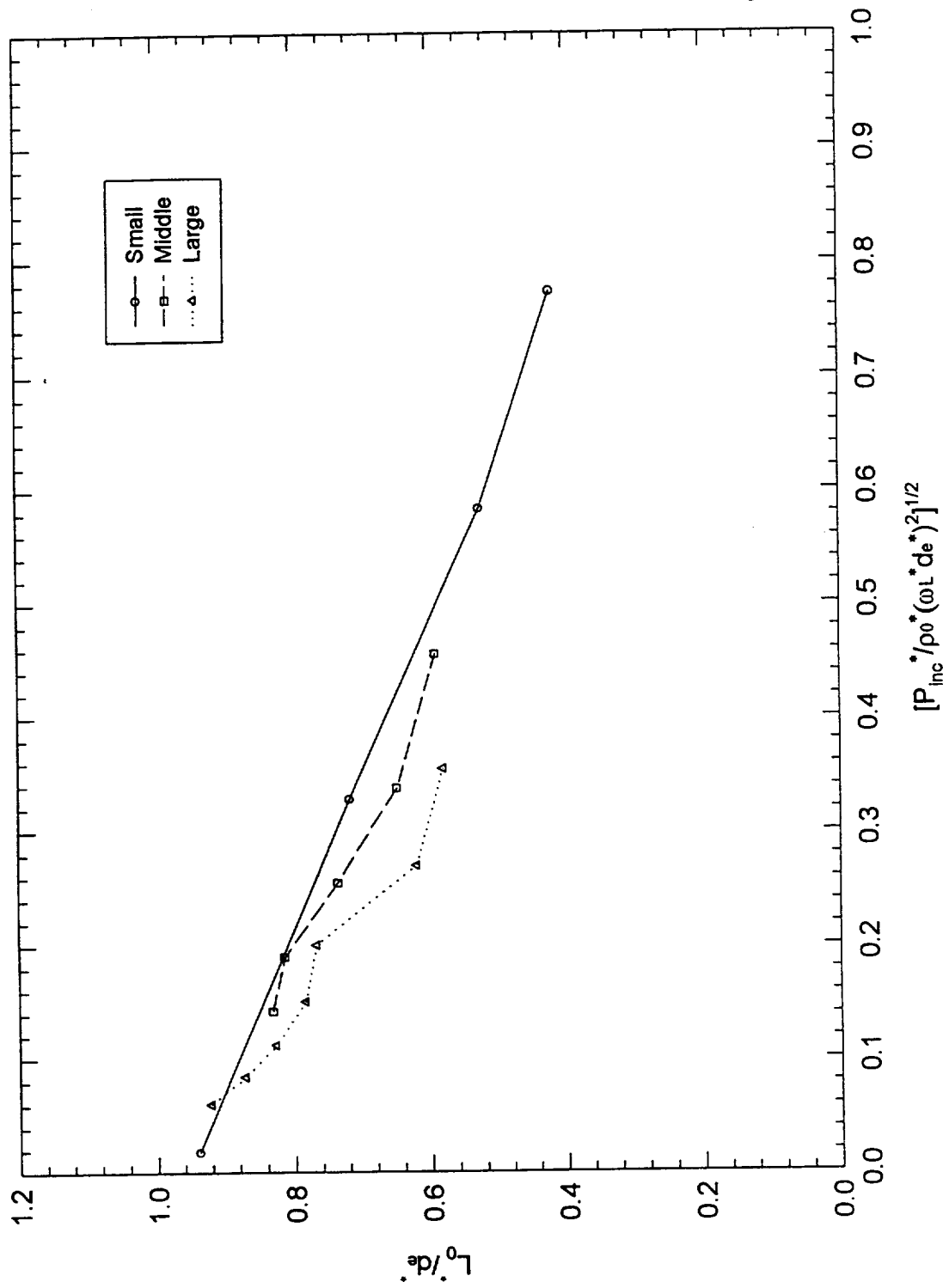


Figure 11. Effect of SPL on Non-Grazing Flow Inertia Length Parameter L_0^*/de^*

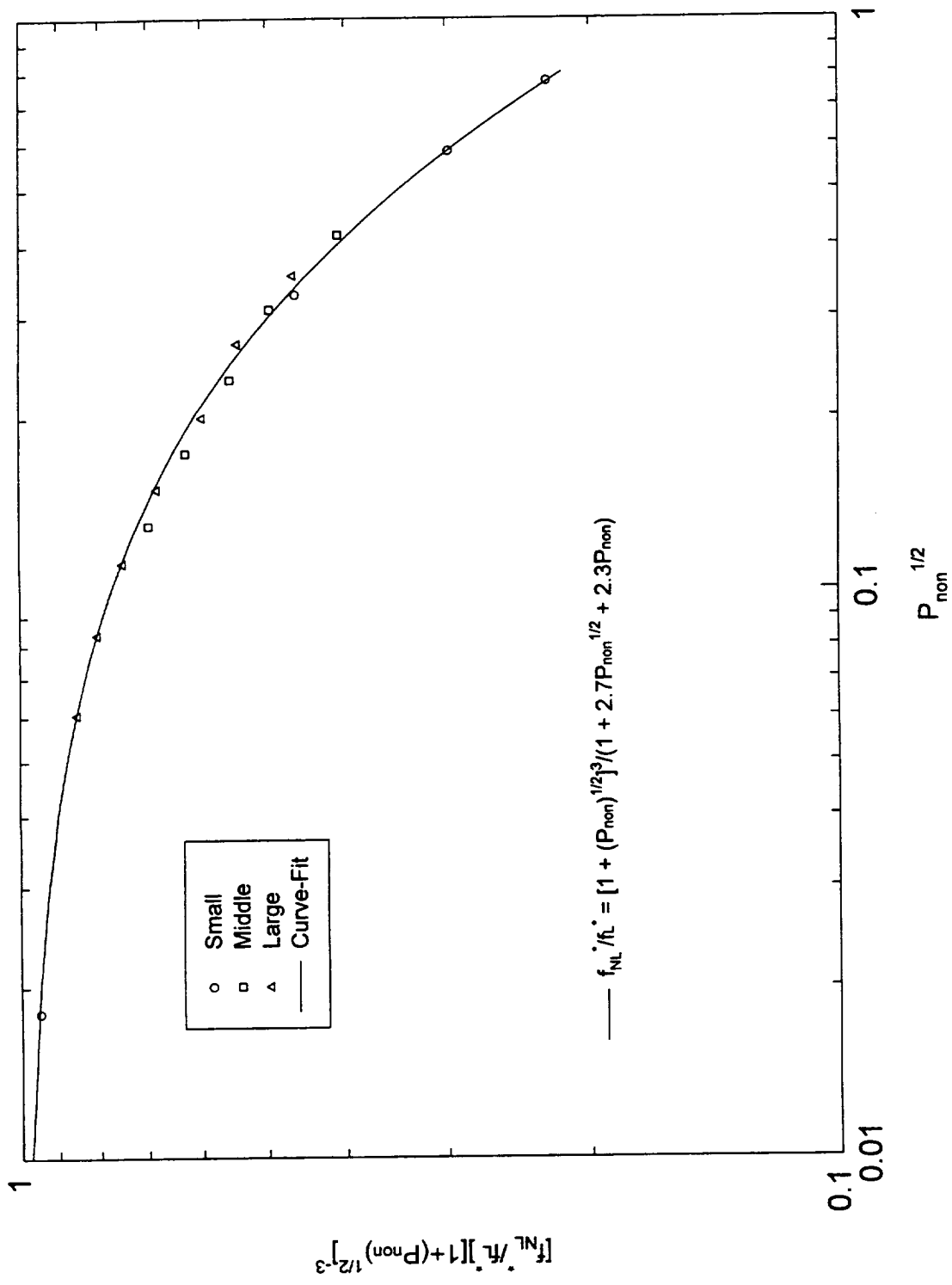


Figure 12. Correlation of Non-Grazing Flow, Nonlinear Resonant Frequencies

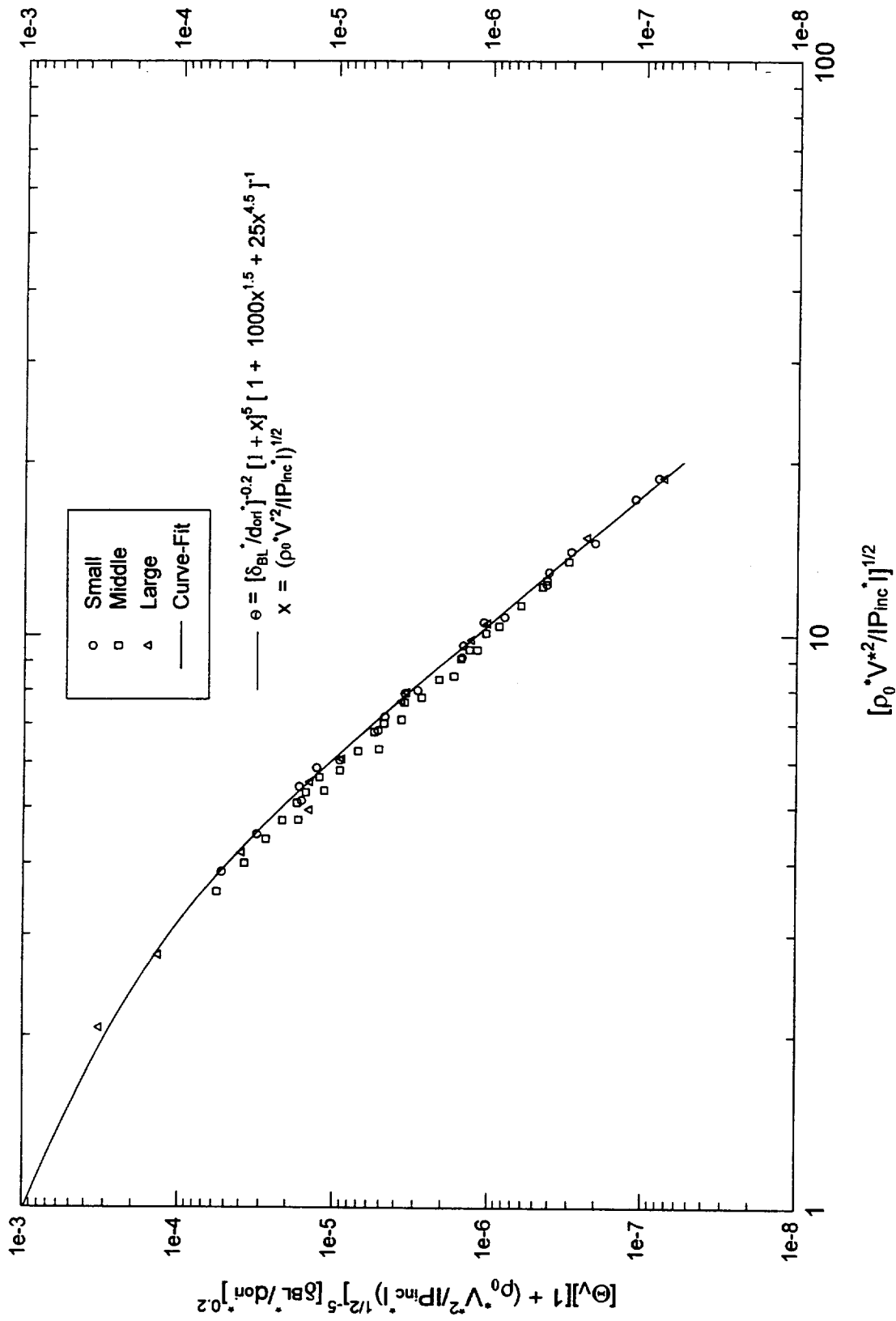


Figure 13. Correlation of Grazing Flow Parameter Θ_V

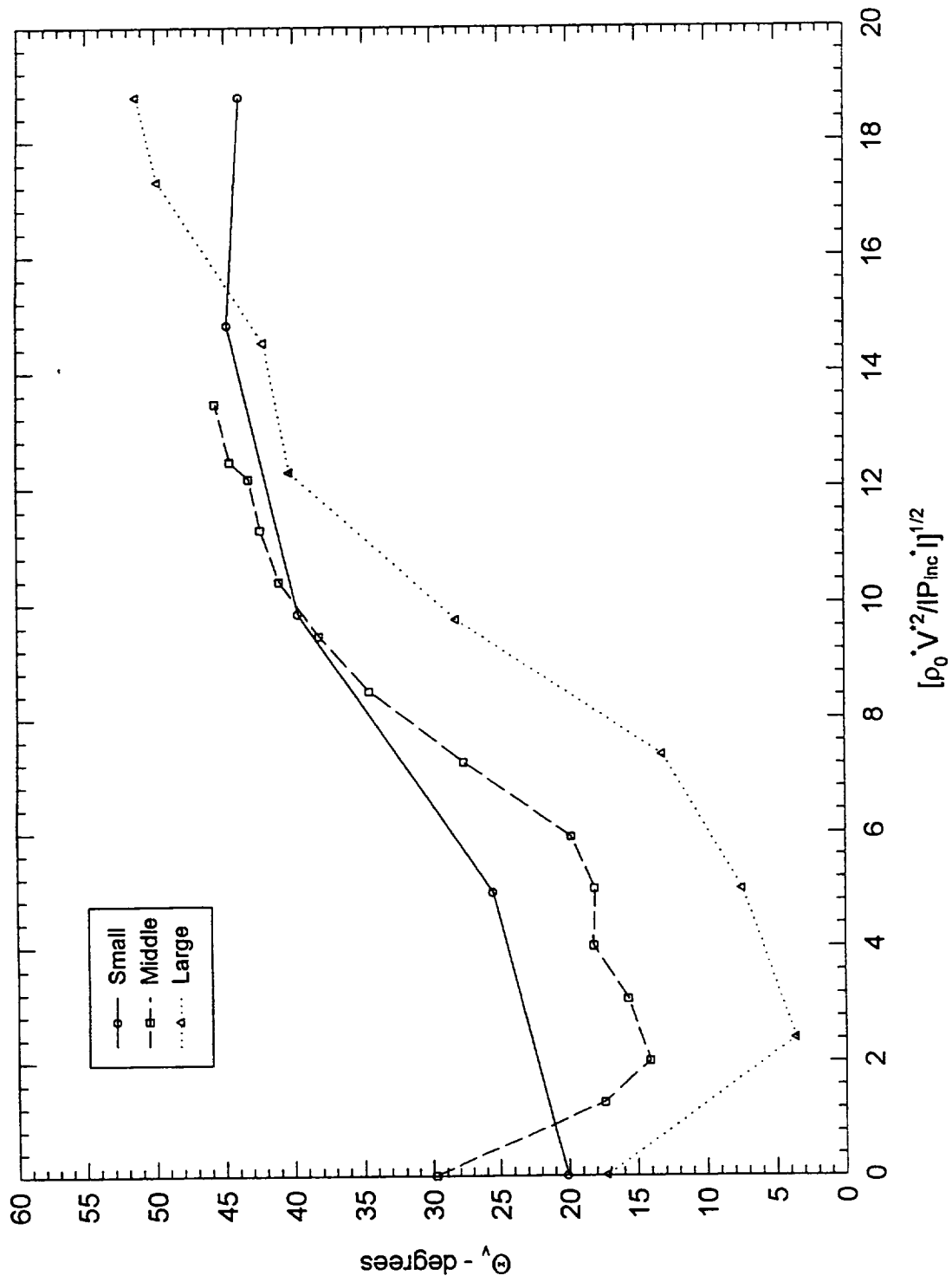


Figure 14. Measured Grazing Flow-Acoustic Interaction Angle ϕ_0

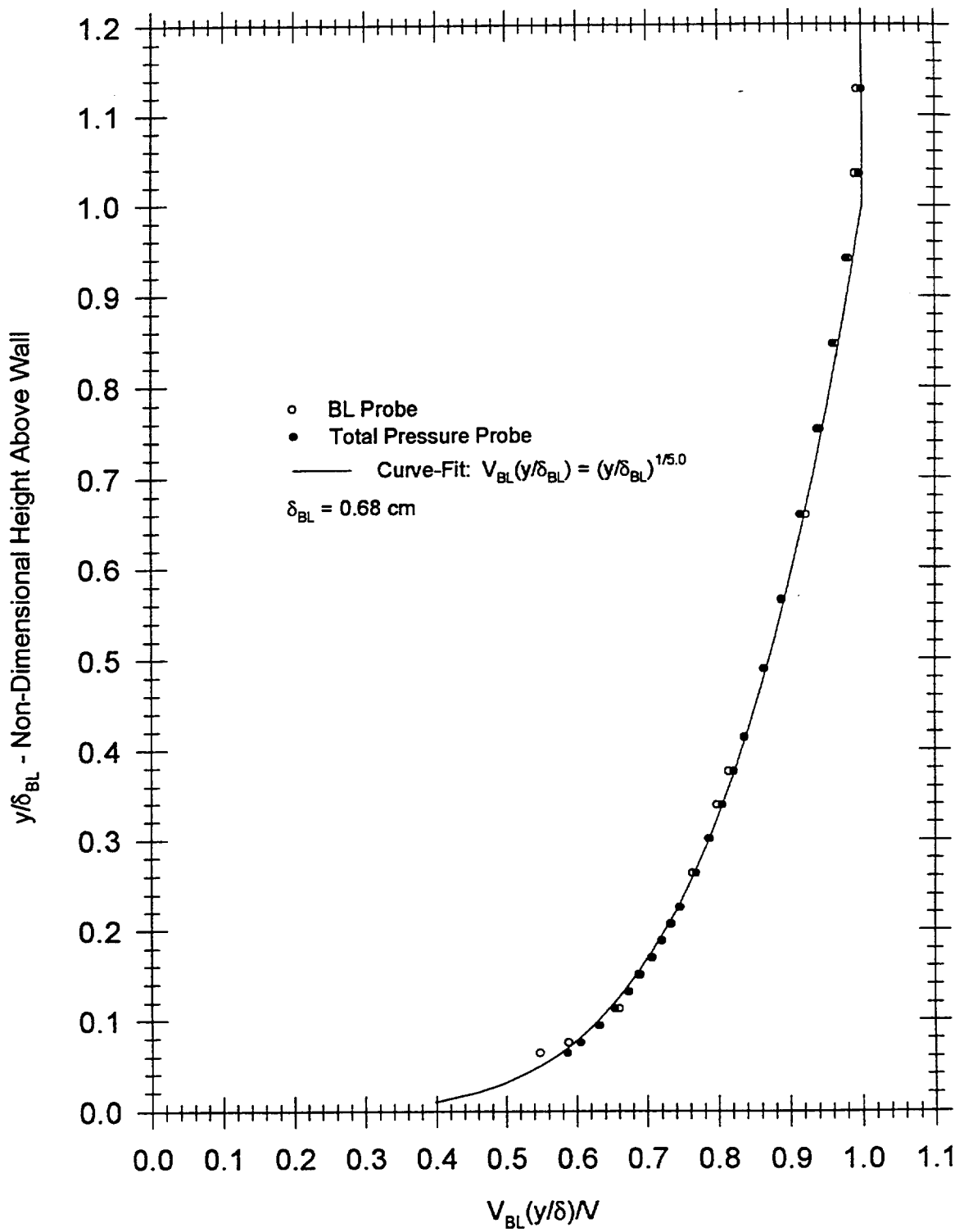


Figure 15a. Boundary-Layer Profile for $V = 22 \text{ m/s}$

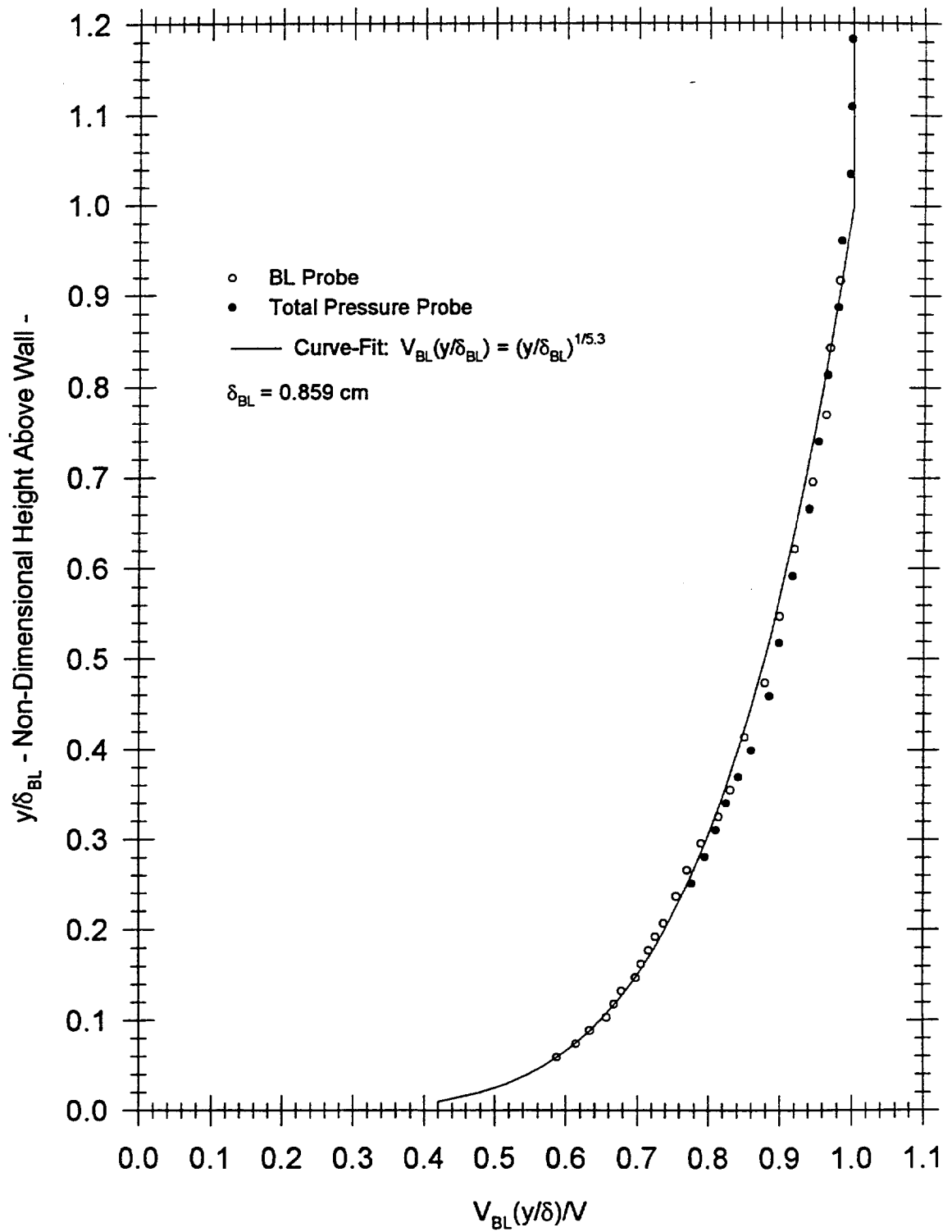


Figure 15c. Boundary-Layer Profile for $V = 67 \text{ m/s}$

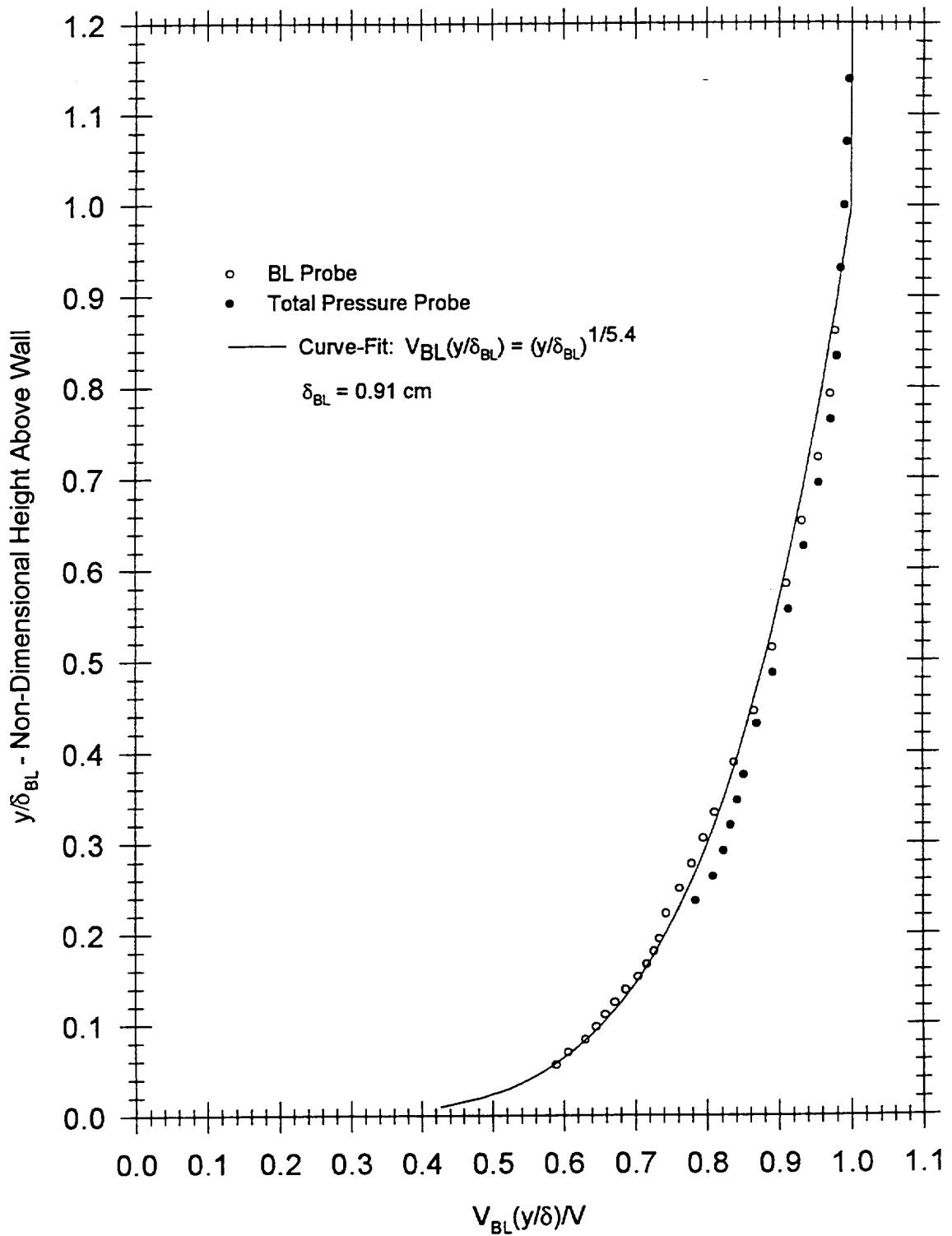


Figure 15d. Boundary-Layer Profile for $V = 72 \text{ m/s}$

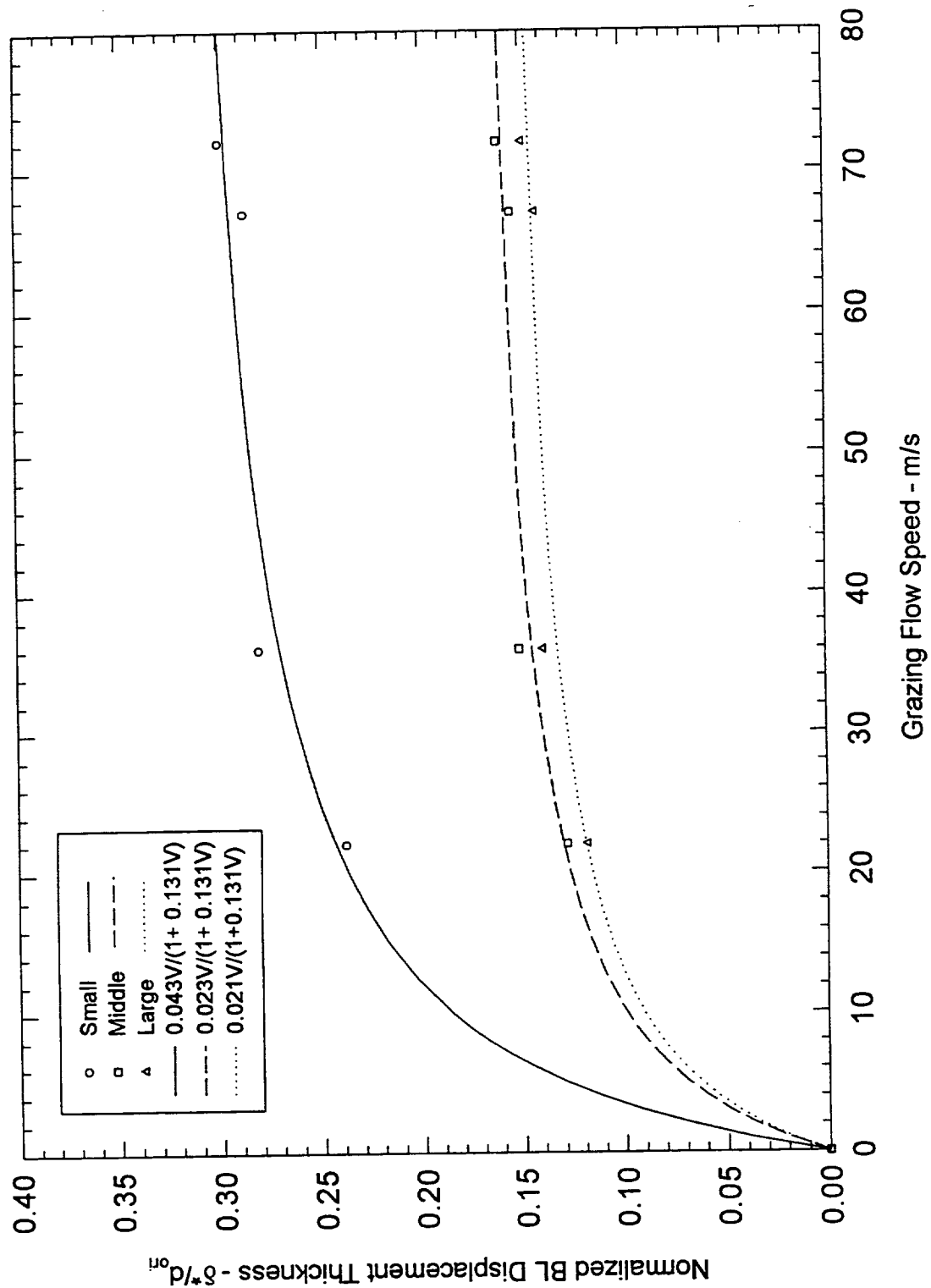


Figure 15e. Normalized Boundary-Layer Displacement Parameter

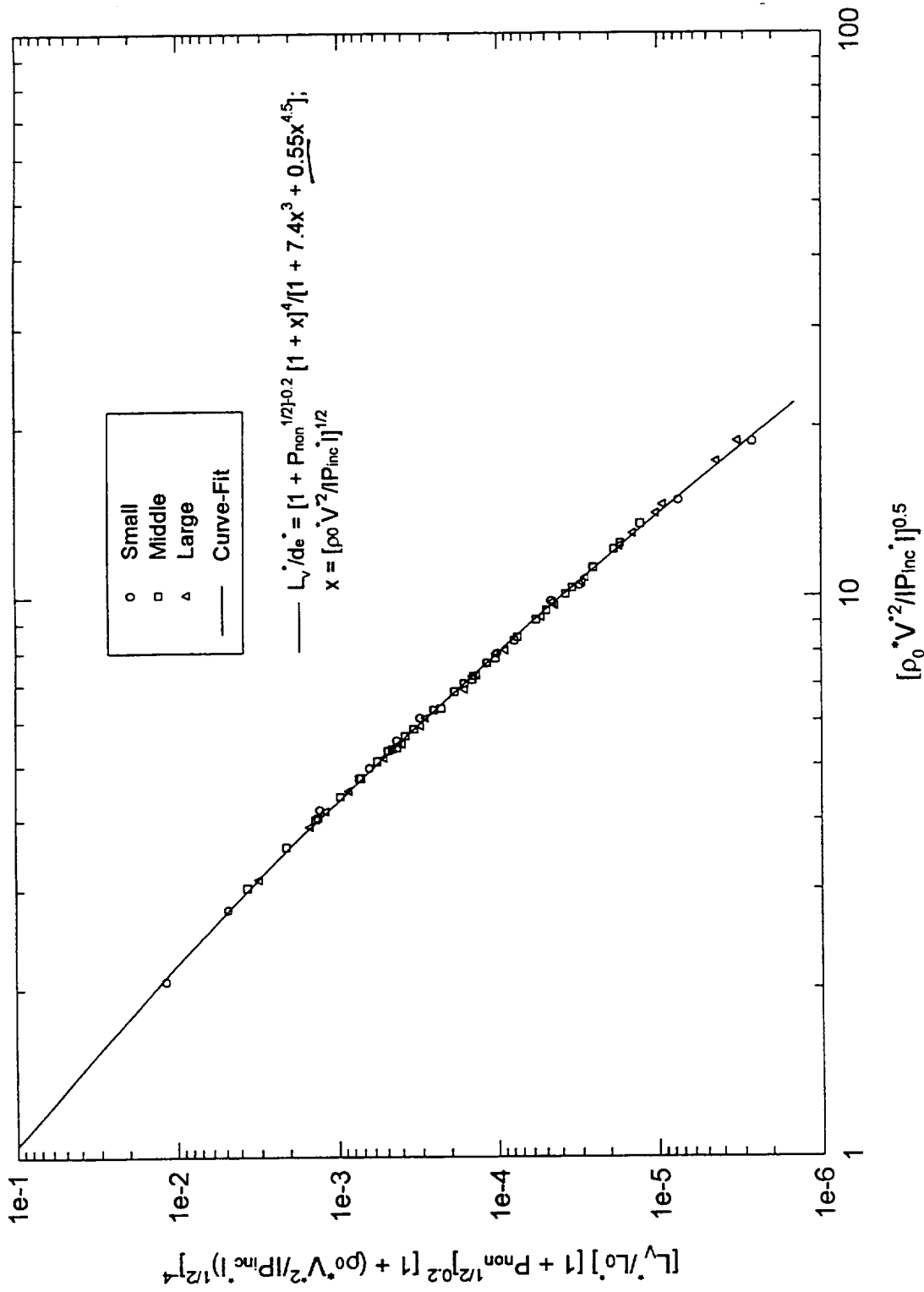


Figure 16. Correlation of Grazing Flow Inertial Length Parameter L_V^*/d_e^*

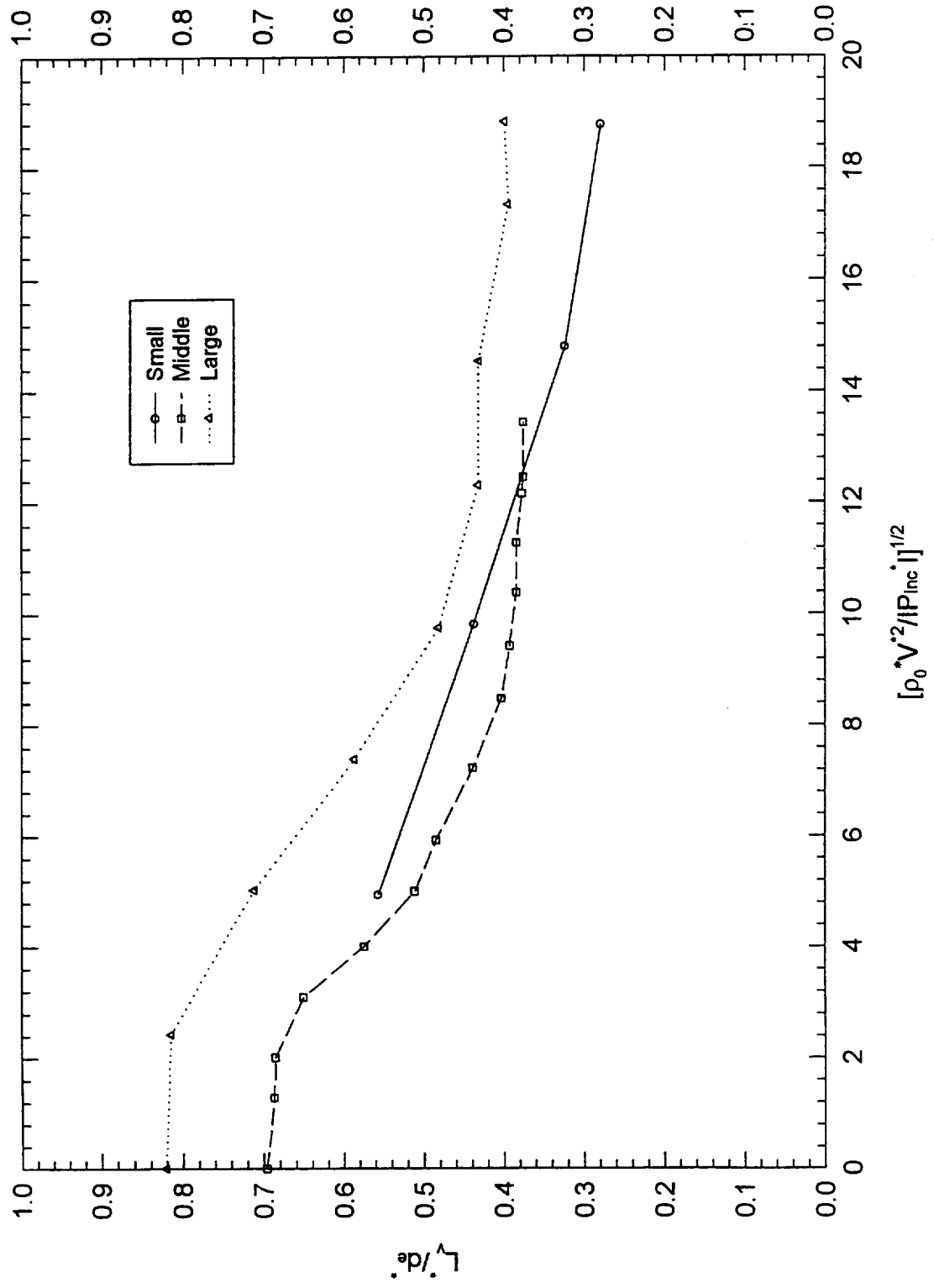


Figure 17. Effect of Grazing Flow on Inertia Length Parameter L_v/d_e

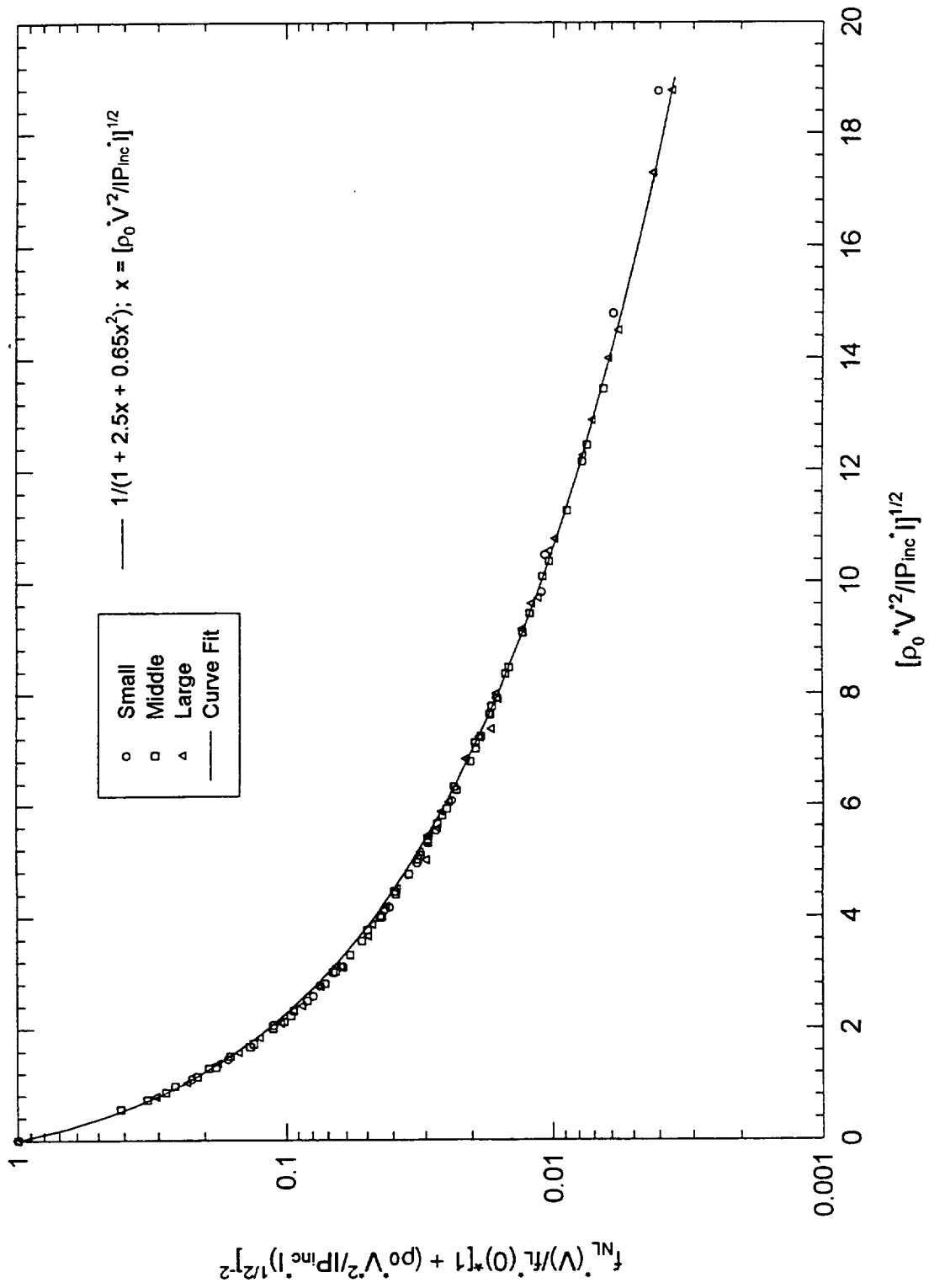
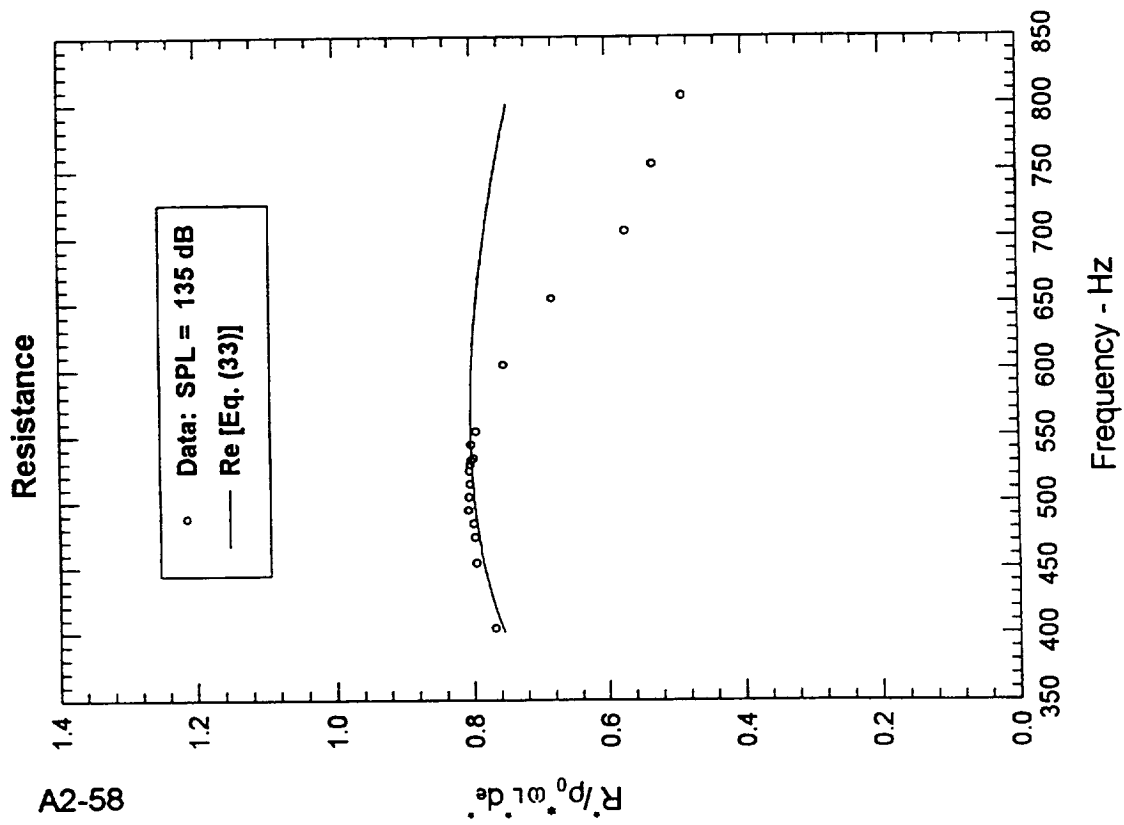
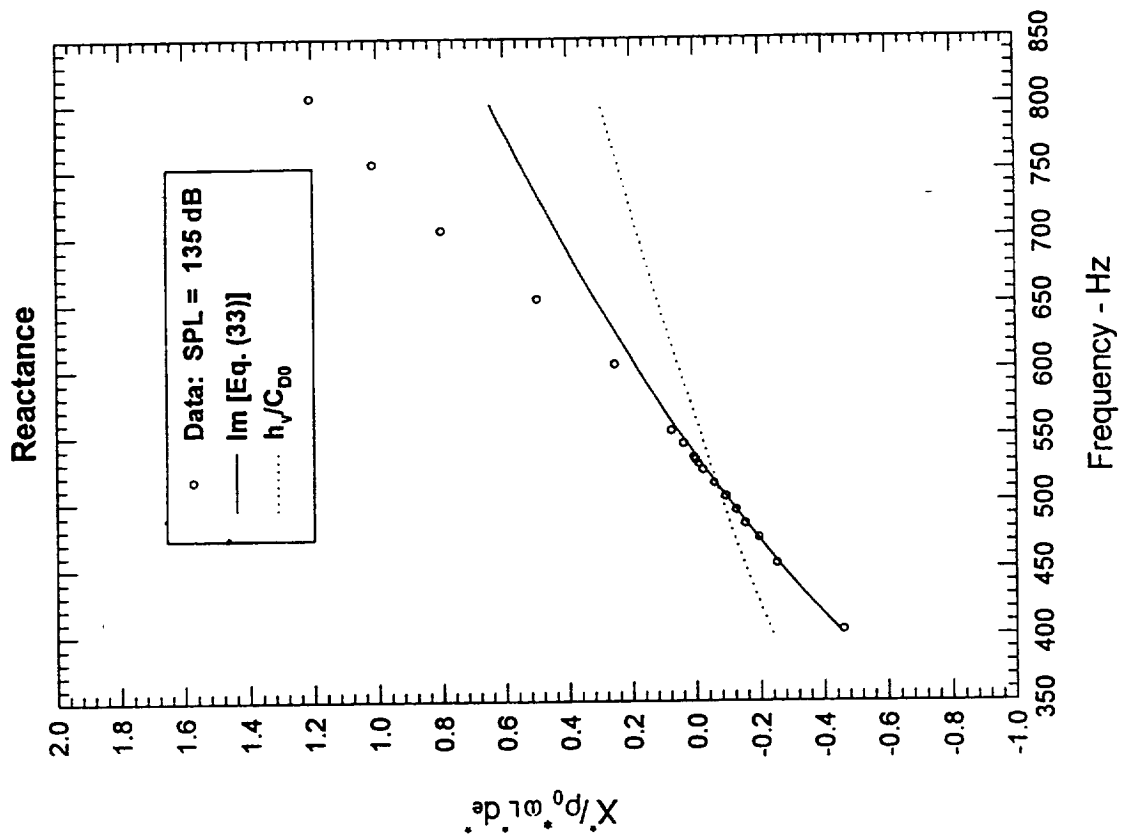


Figure 18. Correlation of Resonator Tuned Frequency with Grazing Flow



A2-58

Figure 19. Measured and Predicted Non-Grazing Flow Impedance of Small Orifice Resonator

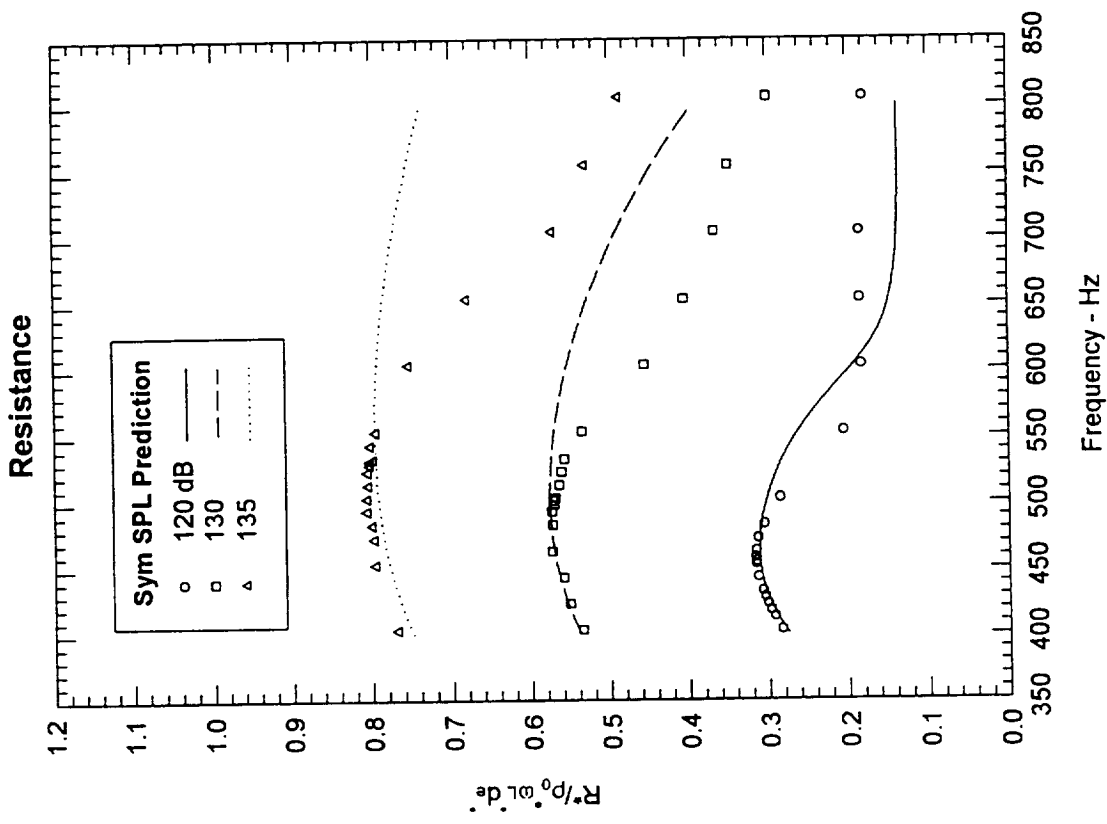
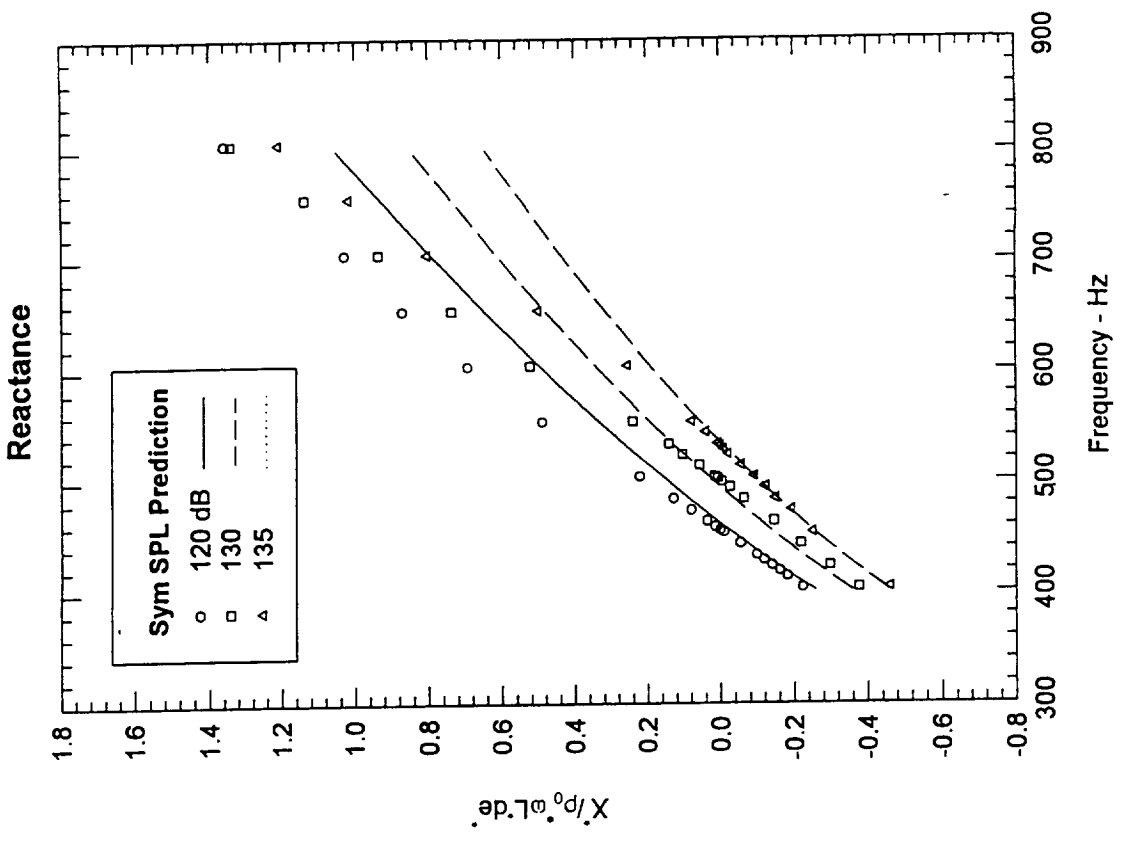


Figure 20a. Measured and Predicted Non-Grazing Flow Impedance of Small Orifice Resonator

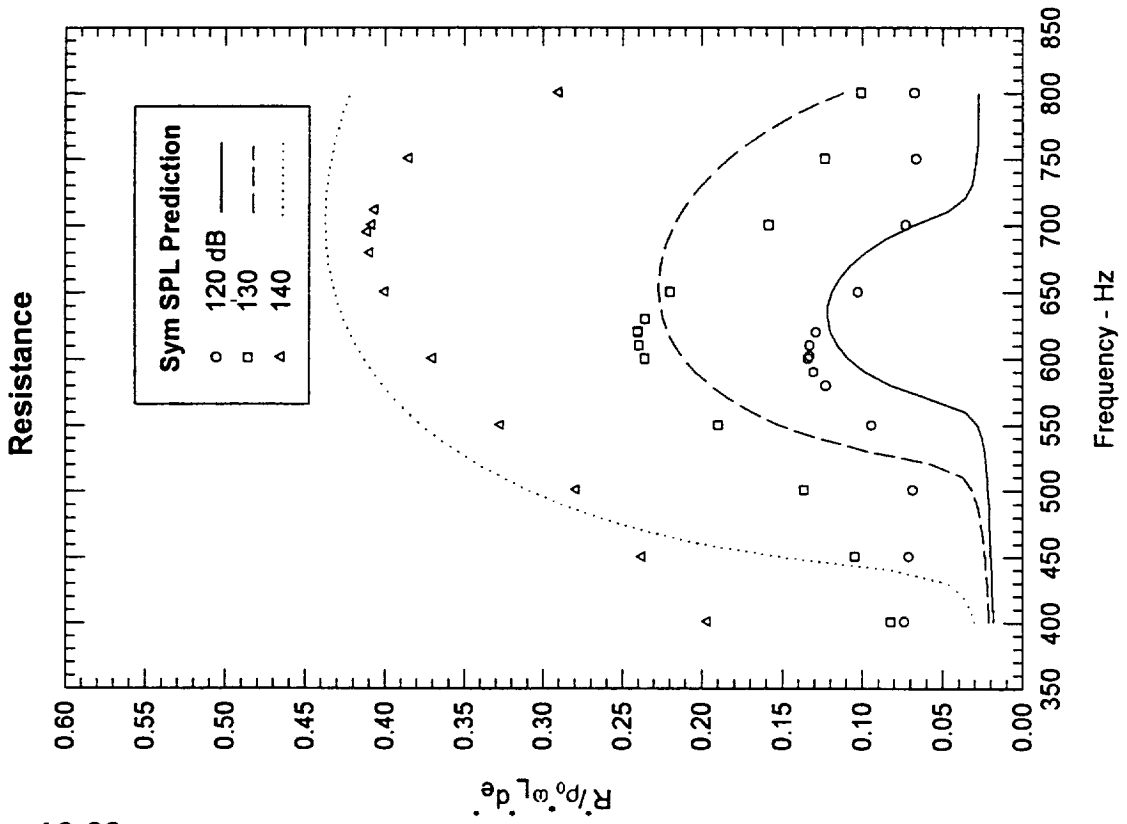
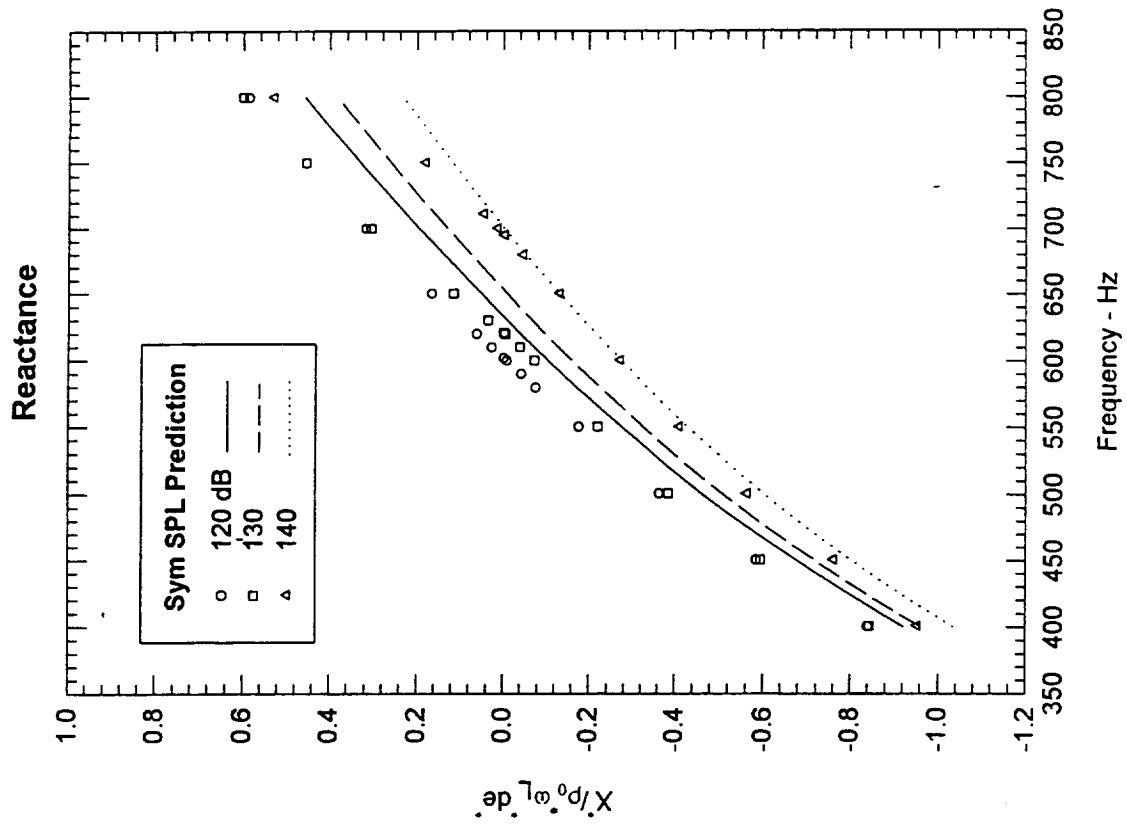


Figure 20b. Measured and Predicted Non-Grazing Flow Impedance of Middle Orifice Resonator

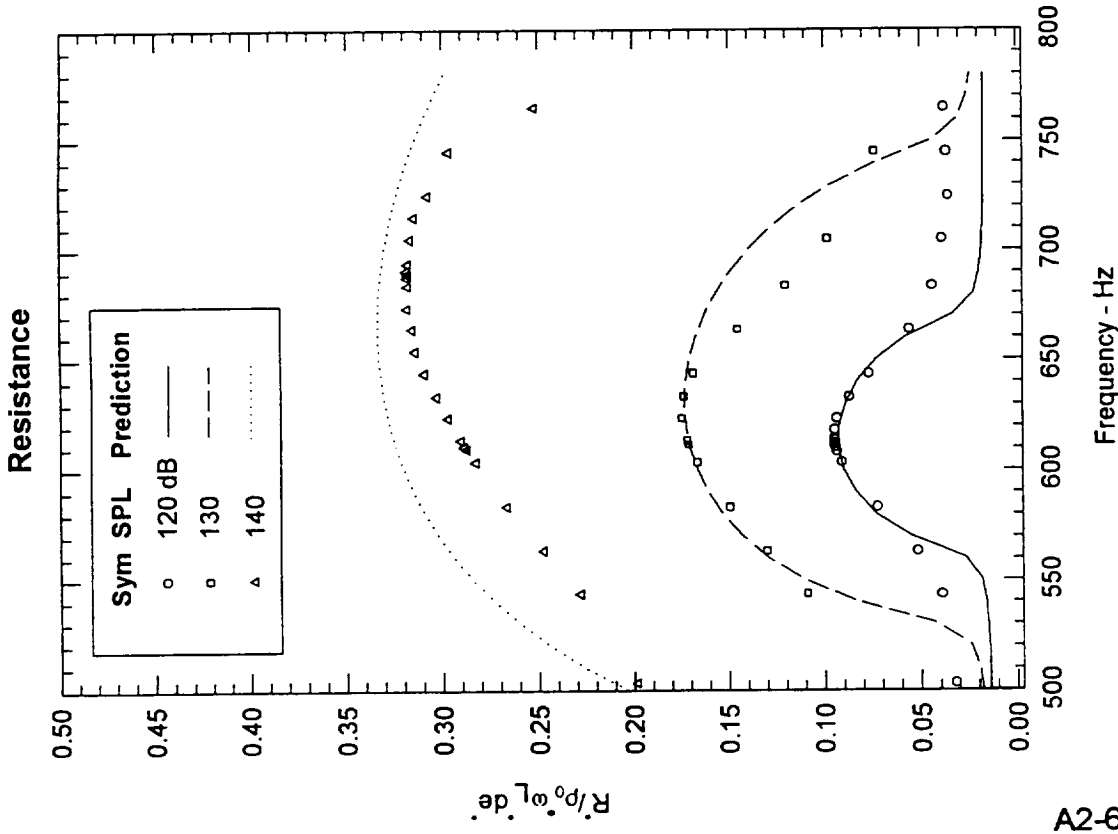
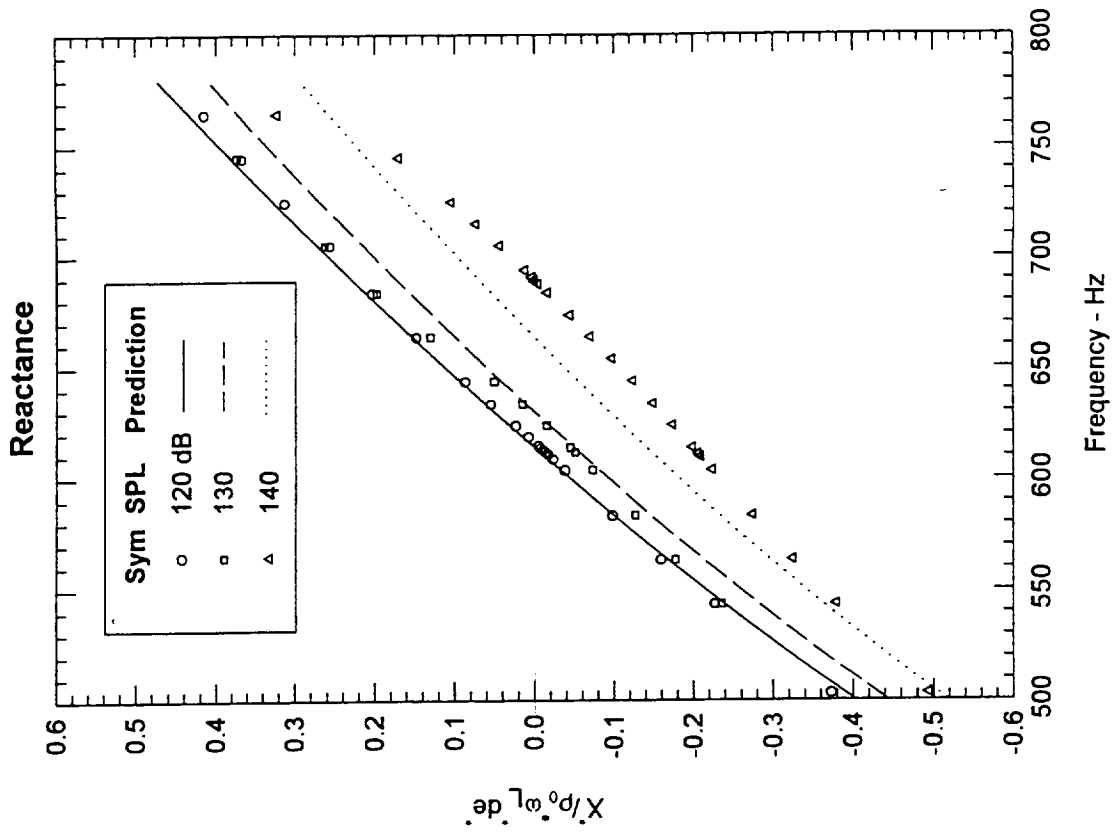


Figure 20c. Measured and Predicted Non-Grazing Flow Impedance of Large Orifice Resonator

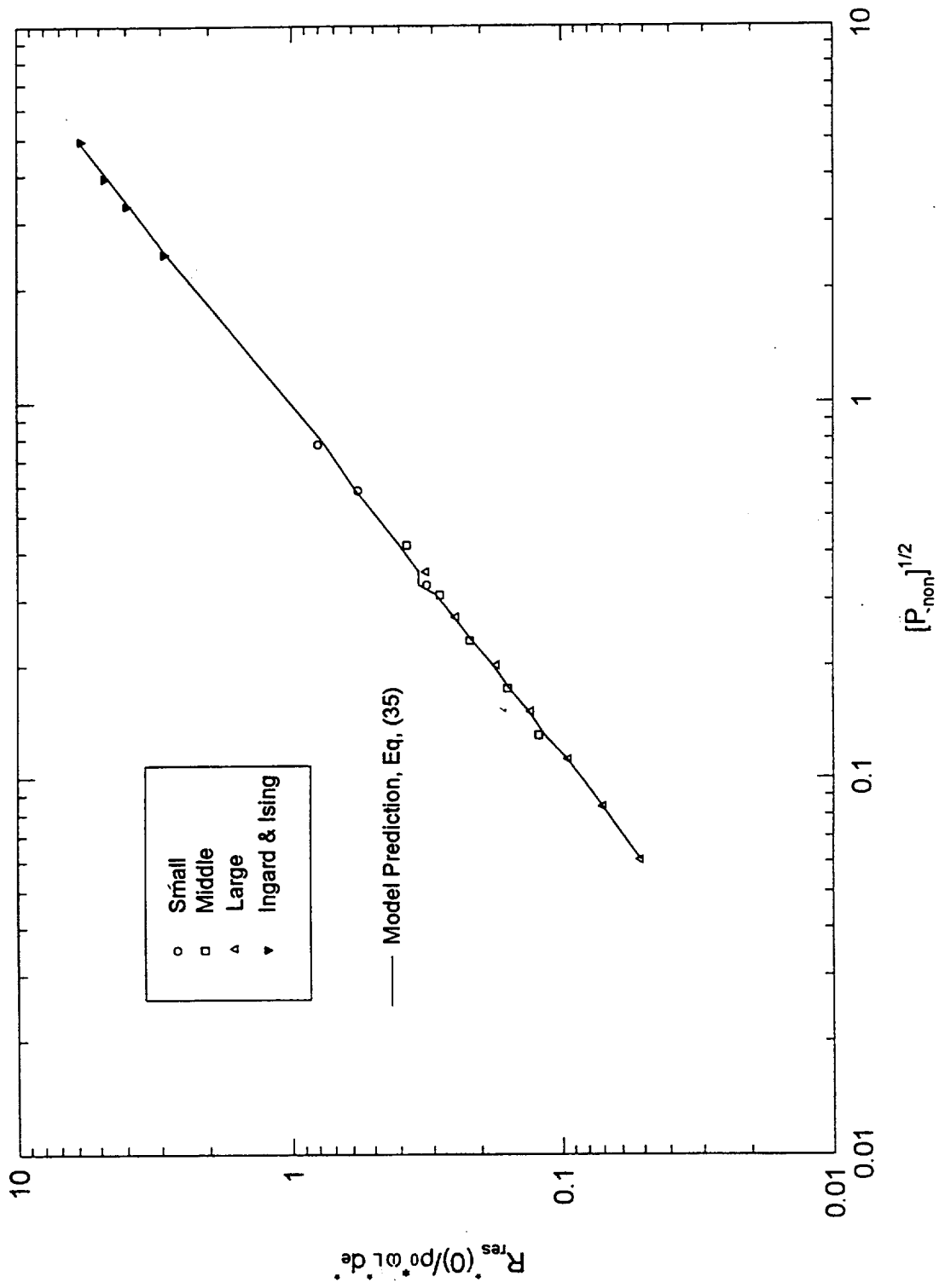


Figure 21. Measured and Predicted Effect of SPL on Non-Grazing Flow Tuned Resistance

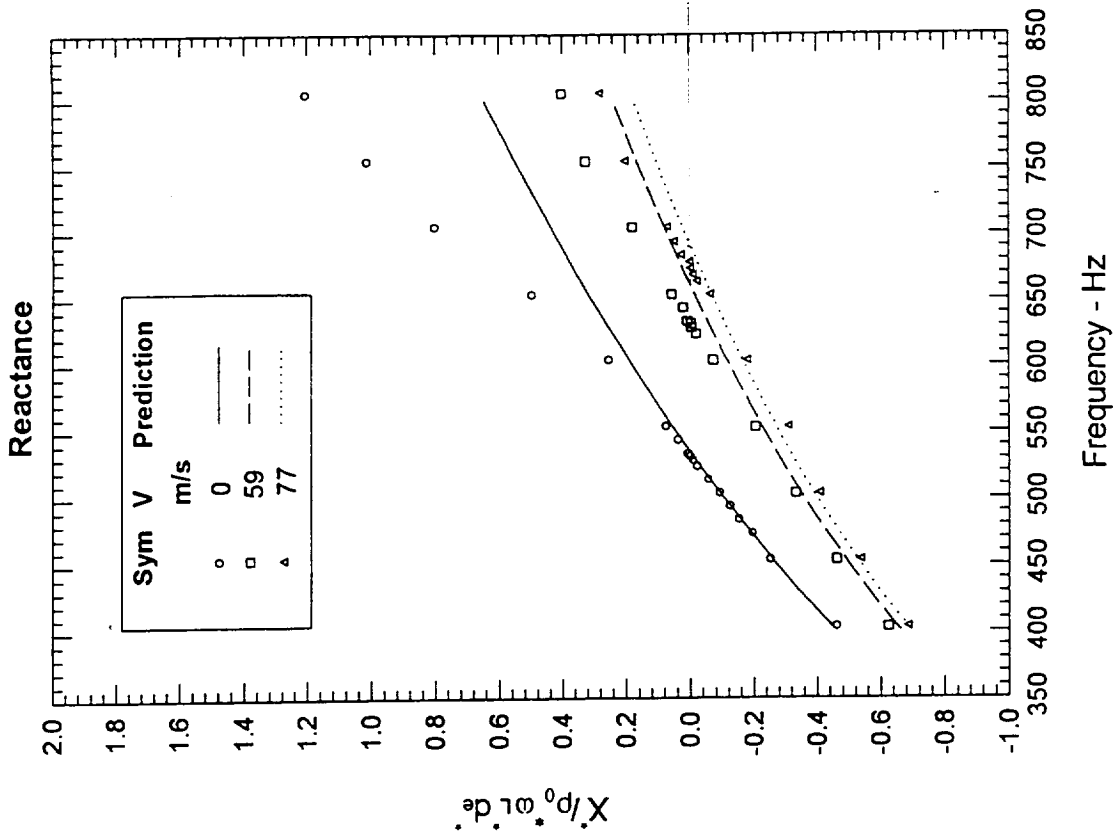
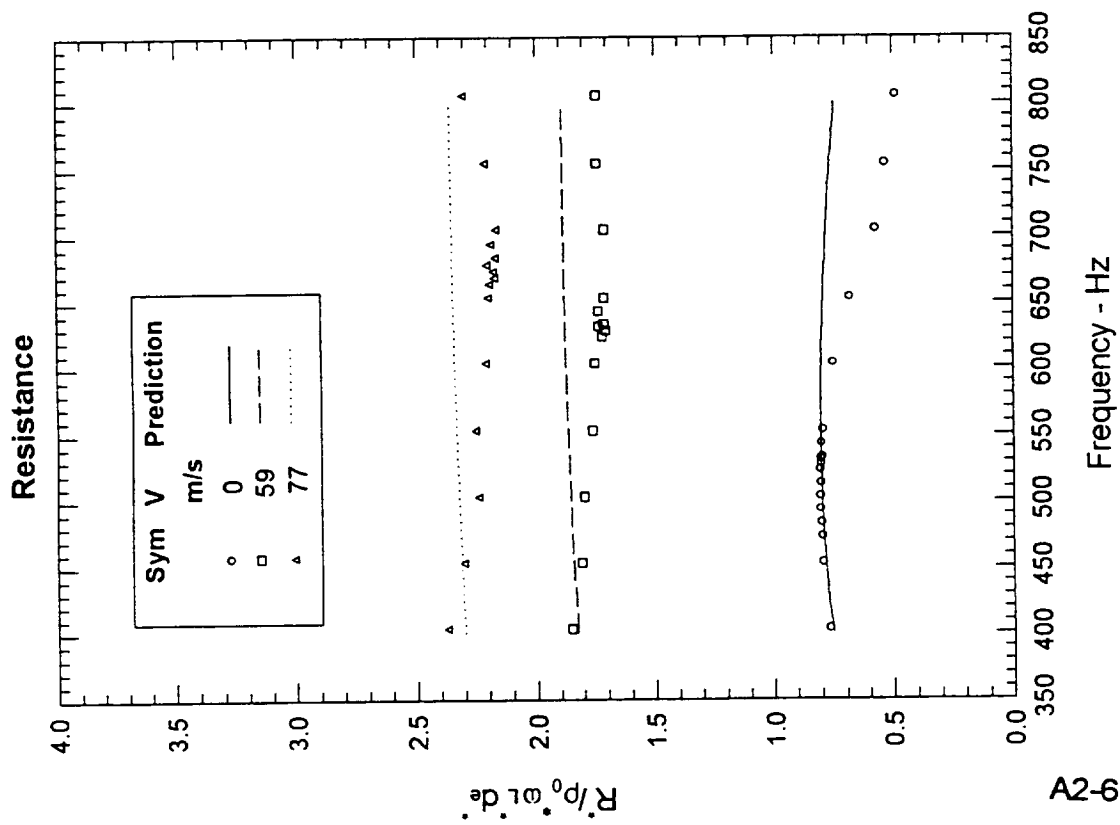
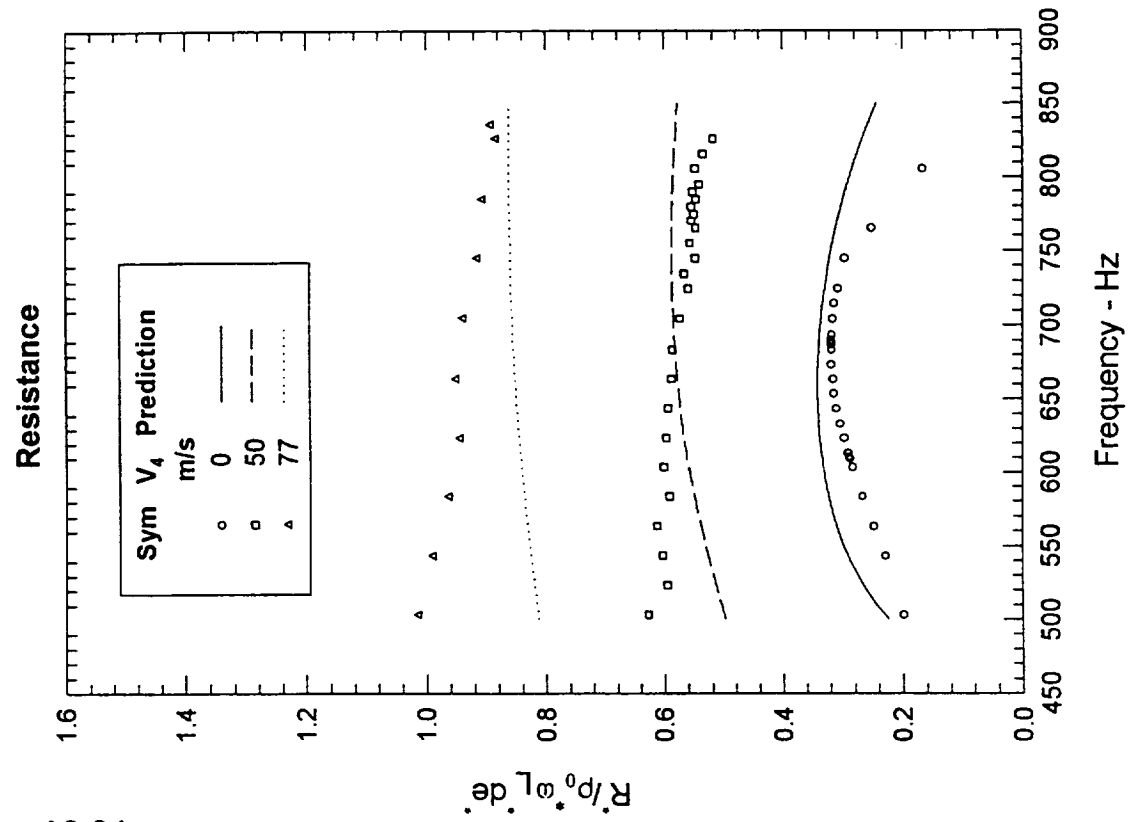
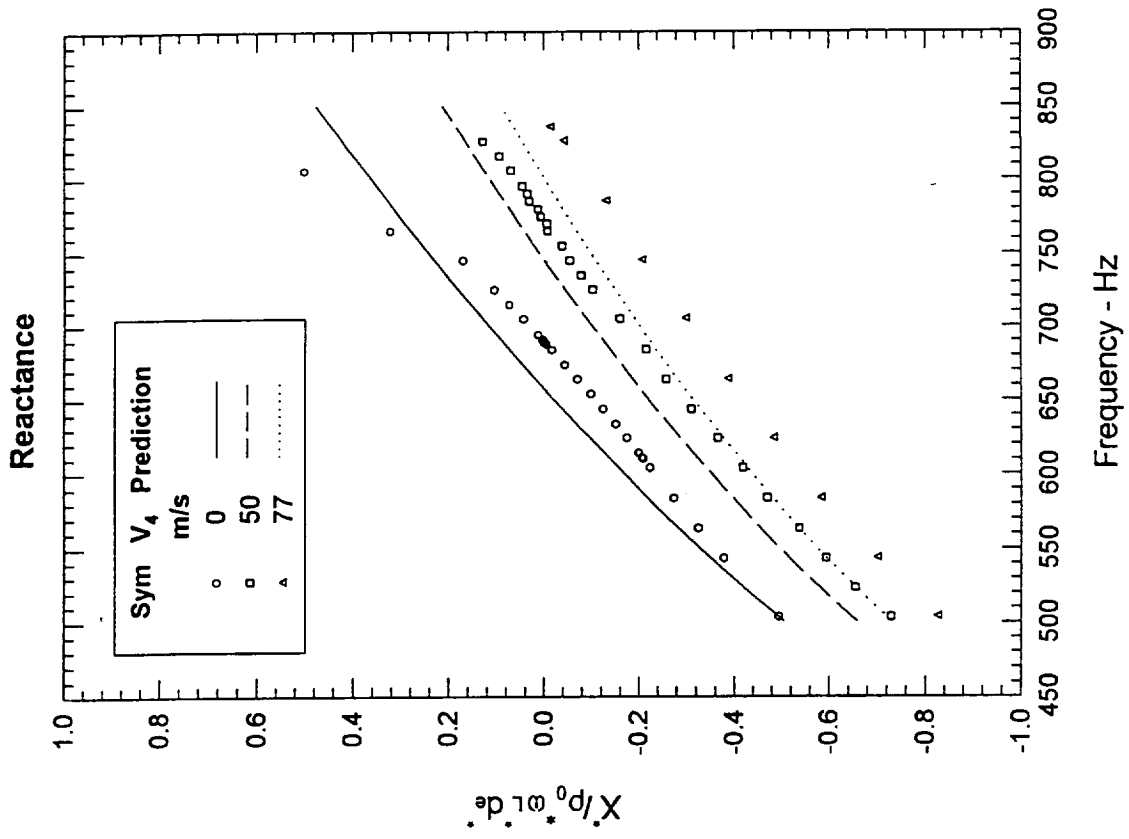


Figure 22a. Effect of Grazing Flow on Impedance of Small Orifice Resonator: SPL = 135 dB



A2-64

Figure 22b. Effect of Grazing Flow on Impedance of Large Orifice Resonator: SPL = 140 dB

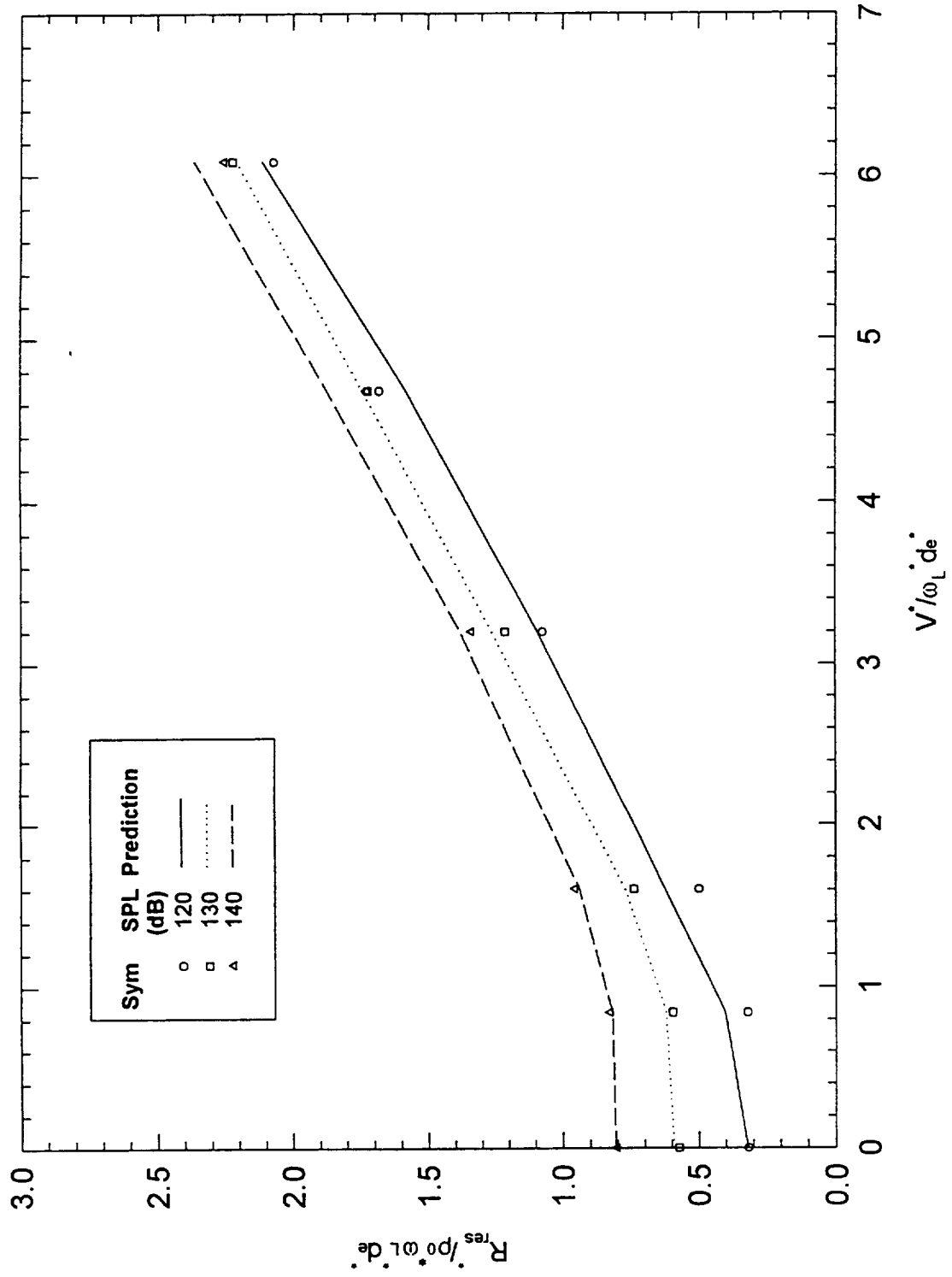


Figure 23a. Measured & Predicted Effect of Grazing Flow on Tuned Resistance of Small Orifice Resonator

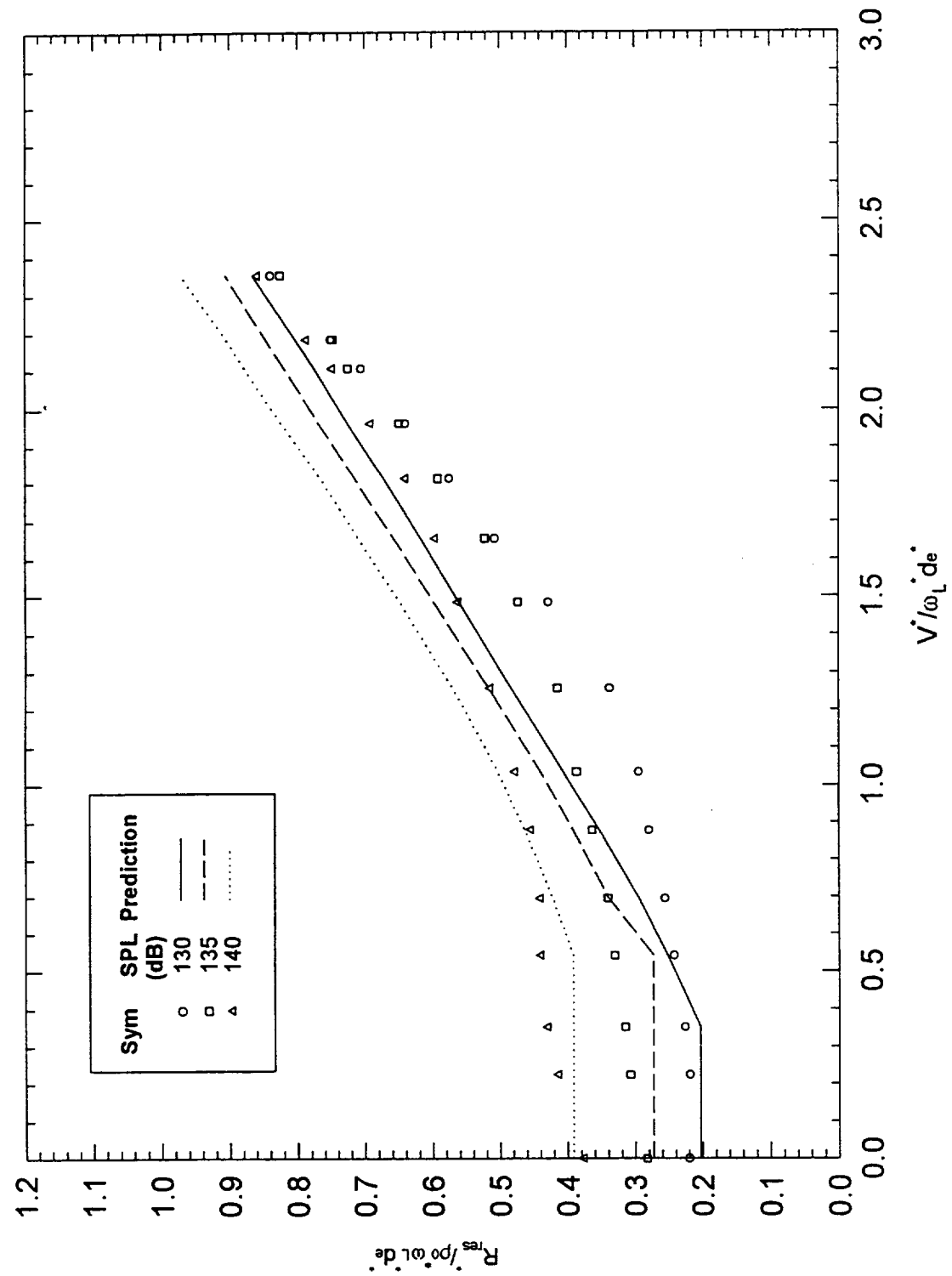
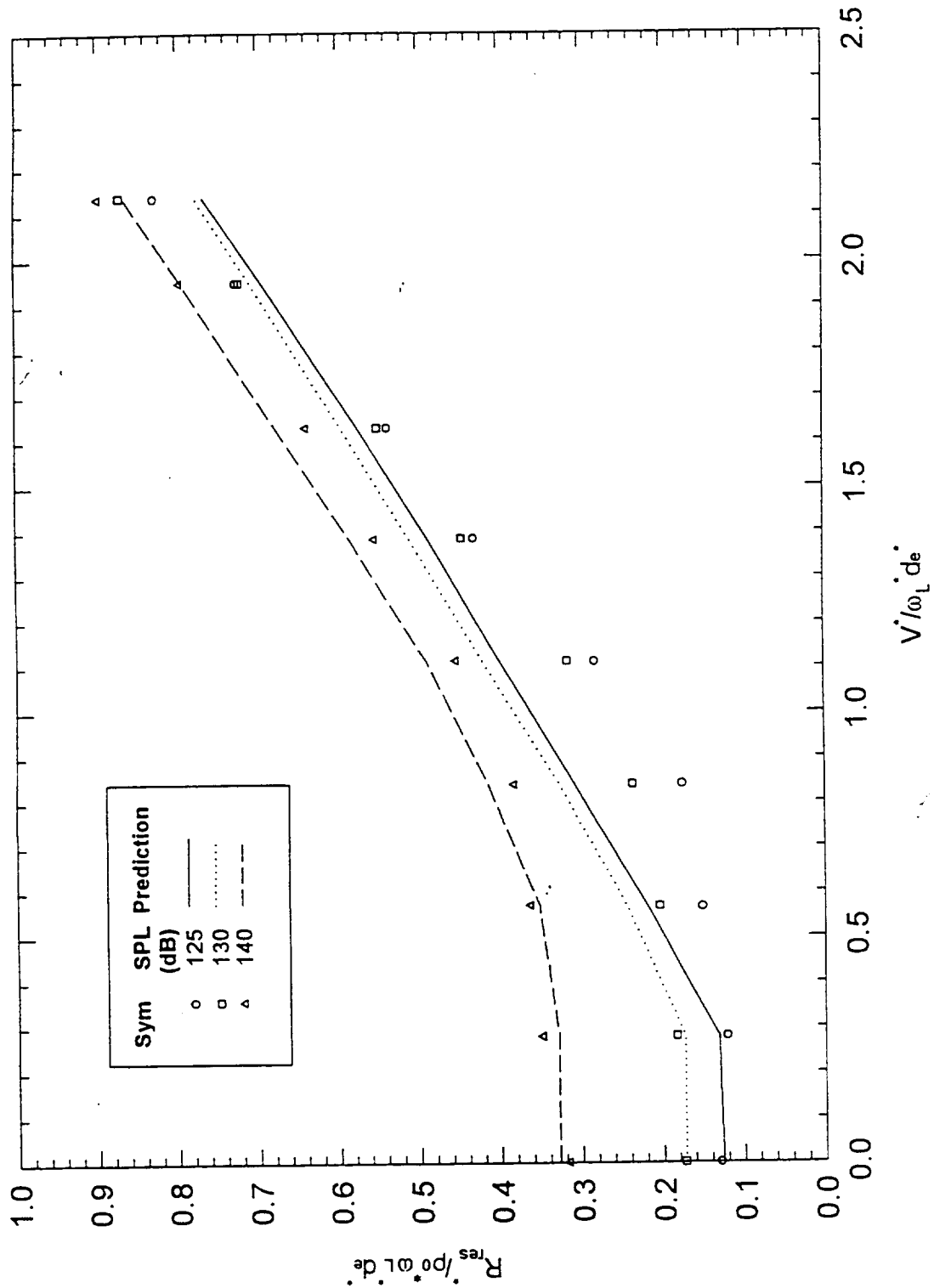


Figure 23b. Measured & Predicted Effect of Grazing Flow on Tuned Resistance of Middle Orifice Resonator



A2-67

Figure 23c. Measured & Predicted Effect of Grazing Flow on Tuned Resistance of Large Orifice Resonator

Appendix A3

Hersh Acoustical Engineering, Inc

780 Lakefield Road, Unit G
Westlake Village, CA 91361
(805) 373-8533 Fax (805) 373-0733
e-mail: hae@iswest.com

INTERIM REPORT

BOEING PURCHASE CONTRACT # ZA0075

PRIME CONTRACT NAS1-20090

THEORY AND DESIGN OF HELMHOLTZ RESONATORS CONSTRUCTED WITH
MICRO-DIAMETER PERFORATES

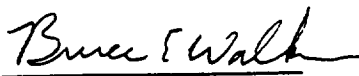
by:



Alan S. Hersh



Joseph W. Celano



Bruce E. Walker

March 12, 1997

Submitted to:

Mr. Jerry Bielak
Noise Research Unit, Noise Engineering
MS 67-ML
P. O. Box 3707
Boeing Commercial Airplane Group
Seattle, WA 98124-2207

I. INTRODUCTION

It is reasonable to assume that future commercial aircraft will have to comply with increasingly stringent environmental noise pollution regulations. This may require engine and engine nacelle manufacturers to improve the efficiency of current acoustic liner designs which often consist of fine wire-mesh screens bonded to honeycomb-backed circular orifices. It has been well documented that the acoustic resistance of these kinds of liners in flow duct applications are insensitive to the effects of grazing flow speed and sound pressure amplitude¹. However, the bonding of screens to honeycomb-backed circular orifices significantly increases production and maintenance costs and imposes additional weight relative to non-screen liners.

A research program was undertaken to assess the practicality of designing liners constructed with multiple micro-diameter perforates to achieve linear or near linear impedance in aircraft engine applications. The objectives of this report are twofold and consist of (1) development of a semi-empirical impedance prediction model and (2) validation of model with test data.

The report is organized as follows. An impedance model is derived in Section II followed by a description of the experimental program and test results in Section III. The report closes in Section IV with a discussion of further work required to assess the practicality of designing liners constructed with multiple micro-diameter perforates.

II. MODEL DERIVATION

A semi-empirical impedance prediction model is derived for the case of N micro-diameter (d_N) perforates backed by a common cavity. The derivation is based on applying conservation of unsteady mass and vertical momentum flux across the control volume of a typical orifice as sketched in Figure 1. It is assumed that the cavity pressure P_{cav} can be accurately modeled using one-dimensional acoustics. Referring to Figure 1, $V_{\infty}S_{\infty}$ represents the grazing volume flow deflected into the resonator cavity by the local sound pressure field P_{inc} incident to the control volume surface $S_N = \pi d_N^2/4$, $u_N S_N$ represents the (vertical) acoustic volume flow entering the control volume upper surface, H_N represents the orifice lumped element inertial length parameter, $u_{vcN} S_{vcN}$ represents the sound particle volume flow at the control volume lower surface, the so-called "vena contracta" where S_{vcN} represents the cross-sectional area of the "vena contracta". The face-plate thickness is denoted by τ , the cavity depth by L_{cav} and the cavity cross-sectional area by S_{cav} .

Conservation of Mass. Assuming $H_N \ll \lambda$, the conservation of mass flux within the control volume of N perforates may be written,

$$Nu_{vcN}S_{vcN} = NV_{\infty}S_{\infty} + Nu_N S_N \quad (1)$$

Thus to first order, the pumping of volume flow into and out-of a resonator orifice is governed by unsteady, incompressible motion. This makes sense because acoustic changes can occur only over scale lengths on the order of an acoustic wavelength.

Conservation of Vertical Momentum. The conservation of momentum in the vertical direction may be written,

$$\rho_0(NS_N)H_N \frac{du_N}{dt} + \rho_0 \left[u_{vcN}^2(NS_{vcN}) - u_N^2(NS_N) \right] = P_{inc}(NS_N) - P_{cav}(NS_N) - T_{wN}(NS_{wN}) \quad (2)$$

The various terms in Eq. (2) are described below:

- The first term on the left-hand-side (LHS) represents the rate of increase of momentum stored in the control volume. Here H_N is a length lumped element inertial length parameter that is unknown and must be modeled experimentally. The quantity NS_N represents the total area of the N orifices.
- The second term on the LHS represents a Bernoulli type of nonlinear increase in momentum flux across the control surfaces S_{oN} and S_{vcN} .
- The first term on the right-hand-side (RHS) represents the incident acoustic driving force acting on the control surface area NS_N .
- The second term on the RHS represents the cavity restoring force acting upon the fluid deflected into the cavity interior volume.
- The third term on the RHS represents the momentum loss from frictional wall shear stresses T_{wN} distributed over the face-plate thickness wetted area $S_{wN} = \pi d_N \tau$ where τ represents the constant face-plate thickness.

The cavity pressure P_{cav} is estimated by solving the one-dimensional wave equation in the cavity resulting in the following expression,

$$P_{cav} = -i\rho_0 c_0 \sigma \cot\left(\frac{\omega L_{cav}}{c}\right) u_N; \quad \sigma \equiv \frac{NS_N}{S_{cav}} \quad (3)$$

The wall shear stress T_{wN} is assumed to be generated from the following acoustic boundary-layer viscous scrubbing losses and steady-state (zero frequency) fully developed pipe flow pressure drop losses,

$$T_{wN} S_{wN} \approx \left[\left(\underbrace{8K_{SS} \frac{\mu_0}{d_N}}_{\text{steady-state}} + \underbrace{K_{AC} \mu_0 \sqrt{\frac{\omega}{\nu_0}}}_{\text{acoustic}} \right) u_N \right] N\pi\tau d_N \quad (4)$$

where K_{SS} and K_{AC} are arbitrary constants.

Substituting Eqs. (1, 3 & 4) into Eq. (2) and introducing an acoustic discharge coefficient C_{DN} and a grazing flow coefficient $C_{\infty N}$, defined as,

$$C_{DN} \equiv \frac{S_{vcN}}{S_N}; \quad C_{\infty N} \equiv \frac{S_{\infty}}{S_N} \quad (5a,b)$$

yields

$$\rho_0 NS_N H_N \frac{du_N}{dt} + N\rho_0 S_N \left[\left(\frac{1-C_{DN}}{C_{DN}} \right) u_N^2 + \left(\frac{2C_\infty}{C_{DN}} V_\infty \right) u_N \right] =$$

$$P_{inc}(NS_N) + iNS_N \rho_0 c_0 \sigma \cot(kL_{cav}) - N\pi\tau d_N \left[\frac{8K_{SS}\mu_0}{d_N} + K_{AC}\mu_0 \sqrt{\frac{\omega}{V_0}} \right] u_N \quad (6)$$

In deriving Eq. (6), steady-state terms proportional to V_∞^2 were ignored and only acoustic terms retained. Observe that the second term on the LHS of Eq. (6) is nonlinear with respect to the sound particle velocity u_N . It should be solved numerically to achieve a dynamically steady-state solution followed by a FFT analysis to calculate the fundamental harmonic time-dependent velocity component. Although this procedure is numerically straight-forward, it greatly complicates the design of efficient sound absorbing liners. The following simplified scheme is proposed. First, assume that the sound field is harmonic so that acoustic quantities are written as,

$$u_N = \hat{u}_N e^{i\omega t} \quad (7)$$

To simplify the notation, the symbol ($\hat{}$) is deleted in the remainder of this report and it is understood that only acoustic amplitudes are considered. Second, the quantity u_N^2 on the LHS of Eq. (6) is written as

$$u_N^2 \cong e^{i\omega t} u_N^2 \quad (8)$$

Equation (8) can be interpreted as retaining only the harmonic acoustic energy or equivalently the simplification results in the loss of higher harmonic acoustic energy. It is important to understand that nonlinear acoustic jetting effects are unaffected by this simplification. Since we are interested in using micro-diameter perforate liners to achieve linear or near linear sound absorbing liners, this simplification is quite reasonable.

Incorporating these ideas into Eq. (8) yields,

$$\rho_0 (NS_N) (i\omega H_N) u_N + N\rho_0 S_N \left[\left(\frac{1-C_{DN}}{C_{DN}} \right) u_N^2 + \left(\frac{2C_\infty}{C_{DN}} V_\infty \right) u_N \right] =$$

$$P_{inc}(NS_N) + iNS_N \rho_0 c_0 \sigma \cot(kL_{cav}) - N\pi\tau d_N \left[\frac{8K_{SS}\mu_0}{d_N} + K_{AC}\mu_0 \sqrt{\frac{\omega}{V_0}} \right] u_N \quad (9)$$

Dividing Eq. (9) by $\rho_0 NS_N$ and rearranging leads to the following equation governing the sound particle velocity field within the perforates,

$$u_N^2 + \left(\frac{1-C_{DN}}{C_{DN}} \right) \left[2 \left(\frac{C_\infty}{C_{DN}} \right) V_\infty + 32K_{SS} \left(\frac{\tau V_0}{d_N^2} \right) + 4K_{AC} \left(\frac{\tau}{d_N} \right) \sqrt{V_0 \omega} + \right] u_N$$

$$+ i\omega H_N (1 - \kappa_N) u_N - \left(\frac{1-C_{DN}}{C_{DN}} \right) \frac{P_{inc}}{\rho_0} = 0 \quad (10)$$

where the parameter κ_N is defined as,

$$\kappa_N \equiv \frac{\rho_0 c_0 \sigma \cot(kL_{cav})}{\omega H_N} \quad (11)$$

In deriving Eq. (10), it was assumed that total perforate area was held constant, independent of perforate number, which leads to the following relationship between a single and multiple diameter perforate face-sheet configurations,

$$NS_N = N \frac{\pi d_N^2}{4} = S_1 = \frac{\pi d_1^2}{4} \rightarrow d_N = \frac{d_1}{\sqrt{N}} \quad (12)$$

Although the detail structure of the pumping of acoustic volume flow into and out of the orifice is not symmetrical, Eq. (10) is assumed to be valid over an entire cycle. This is based upon the assumption that over long time periods relative to the incident sound period, the time-averaged volume inflow and out-flow must be equal over a cycle to insure that the mean cavity pressure is constant, independent of time.

Over the inflow half-cycle, the solution to Eq. (10) is

$$u_N = \sqrt{\frac{C_{DN}}{(1-C_{DN})} \frac{P_{inc}}{\rho_0} + \left[\frac{C_{DN}}{(1-C_{DN})} \frac{(\alpha' + i\beta')}{2} \right]^2} - \frac{1}{2} \left[\frac{C_{DN}}{(1-C_{DN})} (\alpha' + i\beta') \right] \quad (13)$$

where the quantities α' and β' are defined as,

$$\alpha' \equiv 2 \frac{C_\infty}{C_{DN}} V_\infty + 32K_{SS} \left(\frac{\tau v_0}{d_N^2} \right) + 4K_{AC} \left(\frac{\tau}{d_N} \right) \sqrt{v_0 \omega}; \quad \beta' \equiv \omega H_N (1 - \kappa_N) \quad (14a,b)$$

The normalized impedance $Z/\rho_0 c_0$ of a Helmholtz resonator is defined as

$$\frac{Z}{\rho_0 c_0} \equiv \frac{P_{inc}}{\rho_0 c_0 u_{cav}} = \frac{P_{inc}}{\rho_0 c_0 \sigma u_N}; \quad S_{cav} u_{cav} = NS_N u_N \rightarrow u_{cav} = \sigma u_N \quad (15a,b)$$

Replacing u_N by Eq. (13) results in the following expression for the impedance of N micro-diameter circular or almost circular perforates backed by a common cavity,

$$\frac{Z}{\rho_0 c_0} = \frac{(\alpha + i\beta)}{2\sigma} + \frac{1}{\sigma} \sqrt{\left(\frac{1-C_{DN}}{C_{DN}} \right) \left(\frac{P_{inc}}{\rho_0 c_0^2} \right) + \left(\frac{\alpha + i\beta}{2} \right)^2} \quad (16)$$

where α and β are defined as,

$$\alpha \equiv 2 \left(\frac{C_{\infty}}{C_{DN}} \right) \frac{V_{\infty}}{c_0} + 32K_{SS} \left(\frac{\tau v_0}{c_0 d_N^2} \right) + 4K_{AC} \left(\frac{\tau}{d_N} \right) \sqrt{\frac{v_0 \omega}{c_0^2}}; \quad \beta \equiv \left(\frac{\omega H_N}{c_0} \right) (1 - \kappa_N) \quad (17a,b)$$

Equation (16) shows resonance occurs when $\beta = 0$. This leads to the following expression for resonance,

$$\frac{R_{res}}{\rho_0 c_0} = \frac{\alpha}{2\sigma} + \frac{1}{\sigma} \sqrt{\frac{(1 - C_{DN})}{C_{DN}} \left(\frac{P_{inc}}{\rho_0 c_0^2} \right) + \left(\frac{\alpha}{2} \right)^2} \quad (18)$$

When viscous scrubbing losses are large relative to nonlinear and/or grazing flow resistive losses, the resonator impedance simplifies to,

$$\frac{Z}{\rho_0 c_0} \equiv \frac{\alpha + i\beta}{\sigma} \quad (20)$$

Observe from Eq. (17a) that the viscous scrubbing losses exhibit a dependency on both frequency and number of perforates.

The resonator impedance is defined in terms of the following five unknown parameters: K_{SS} , K_{AC} , C_{DN} , C_{∞} and H_N . These parameters are assumed to be independent of time and hence frequency. Since they are unknown, they must be determined from experimental data.

III. EXPERIMENTAL PROGRAM

An experimental program was undertaken to provide a data base in order to generate empirical curve-fits of the five parameters defined above. Table I below defines the important parameters of twelve micro-diameter orifice perforate resonator configurations. Figure 2 displays enlarged photographs of the $N = 1, 4, 16$ and 100 micro-diameter perforate face-sheet specimens. The photographs show that the laser drilling manufacturing process results in non-circular shapes. Thus it was necessary to measure the average diameters of the perforates optically. This resulted in the variable spacings between perforates as shown in column 4 of Table I.

Because of lack of precision associated with the laser drilling process, detailed impedance measurement of only the five resonator configurations identified by a (*) in the third column in Table I were obtained using Dean's two microphone method³. The impedances of the remaining specimens are planned to be measured in 1997.

Table I. Summary of Micro-Diameter Resonator Geometries

N	S (inches)	<d _{ori} > (inches)	S/<d _{ori} >	Lcav (inches)	Dcav (inches)	τ (inches)	τ/<d _{ori} >	σ
1	NA*	0.079	NA	4.0	0.3906	0.040	0.506	0.0343
4	0.06	0.0380	1.58	'	'	'	1.053	0.0379
	0.08*	0.0385	2.08	'	'	'	1.039	0.0389
	0.10	0.0373	2.68	'	'	'	1.072	0.0364
16	0.03	0.0210	1.43	'	'	'	1.905	0.0461
	0.04*	0.0213	1.88	'	'	'	1.878	0.0476
	0.05	0.0213	2.34	'	'	'	1.878	0.0478
100	0.012*	0.0063	1.91	'	'	'	6.349	0.0258
	0.013	0.0061	2.64	'	'	'	6.557	0.0240
	0.020	0.0063	3.18	'	'	'	6.349	0.0259
400	0.008*	0.0035	2.32	'	'	'	11.429	0.0314
	0.010	0.0031	3.21	'	'	'	12.903	0.0255

Test Results

The impedance measurements are summarized in Figures 3-5. Figure 3 displays the effect of SPL on the resistance and reactance of the N = 1 configuration. The work of Hersh and Walker^{4,5} have shown that the increase in resonator resistance with frequency in the neighborhood of the resonator tuned frequency is caused by nonlinear (SPL) jetting effects. This is valid only for resonator configurations with $\tau/d_{ori} < 1$. The effect of orifice number and hence τ/d_{ori} , displayed in Figure 4, show the increase in resistance with frequency near resonance to virtually disappear when N = 100, 400. The data suggests that the increase in wetted area and hence orifice number increases both C_{DN} and frictional resistive losses. Referring to Eq. (16), the increase in C_{DN} as N increases explains the insensitivity of the resistance to frequency at large values of N. The increase in resistance with N can be explained by combining Eqs. (12) and (17a) to yield,

$$\alpha = 2 \left(\frac{C_{\infty N}}{C_{DN}} \right) \frac{V_{\infty}}{C_0} + 32K_{SS} N \left(\frac{\tau V_0}{C_0 d_1^2} \right) + 4K_{AC} \sqrt{N} \left(\frac{\tau}{d_1} \right) \sqrt{\frac{V_0 \omega}{C_0^2}} \quad (21a)$$

At very large values of N, the resistance is dominated by steady-state viscous scrubbing losses that are independent of frequency. This is consistent with the data shown in Figure 4. The corresponding effect on face-sheet reactance shows an increase with N below resonance and a decrease above resonance. This is difficult to understand and may be related to the variation of orifice geometry as suggested in Figure 2. Further research is required before an explanation is offered.

Figures 5a and 5b display the effect of grazing flow on resonator resistance and face-sheet reactance respectively. The effect of grazing flow on resistance diminishes as N increases and becomes negligible for $N = 100, 400$. The corresponding effect of grazing flow on face-sheet reactance again shows an increase with N below resonance and a decrease above resonance. This is also difficult to understand and an explanation is deferred until further research is conducted.

References

1. Rice, E. J., "A Model for the Acoustic Impedance of Linear Suppressor Materials Bonded on Perforated Plate", AIAA Paper 81-1999.
2. Temkin, S. Elements of Acoustics, John Wiley & Sons, pg. 179, 1981.
3. Dean, P. D. , "An In-Situ Method of Wall Acoustic Impedance Measurement in Flow Ducts", JSV, Vol. 34, No. 1, p. 97, 1974.
4. Hersh, A. S. and Walker, B. E., "Acoustic Behavior of Helmholtz Resonators: Part I. Nonlinear Model", AIAA Paper No. 95-079, 1995.
5. Hersh, A. S. and Walker, B. E., "Acoustic Behavior of Helmholtz Resonators: Part II. Grazing Flow Model", AIAA Paper No. 95-080, 1995.

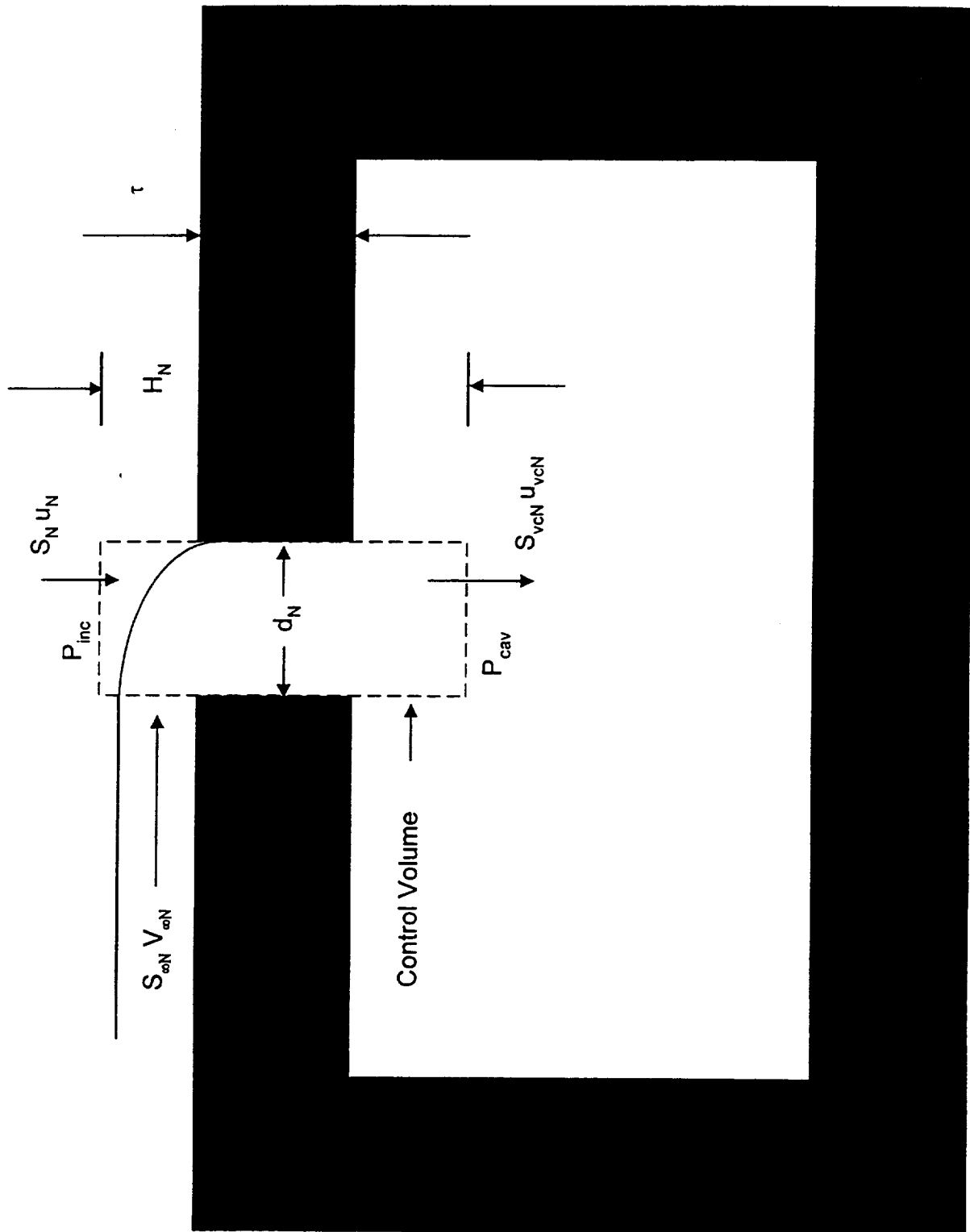


Figure 1. Control Volume Used in Model Derivation

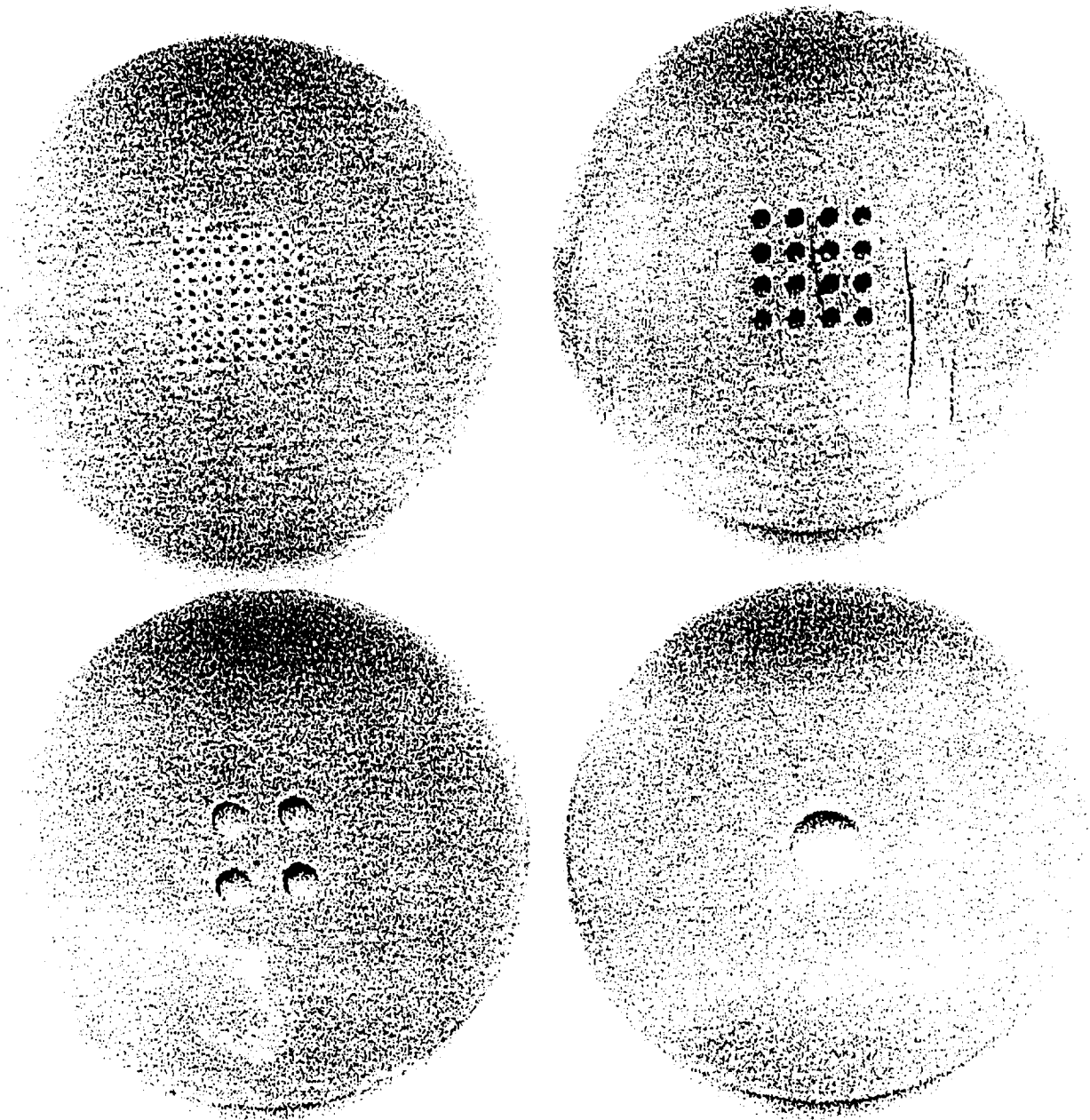


Figure 2. Enlarged Photographs of the N = 1, 4, 16 and 100 Micro-Diameter Face-Sheet Specimens

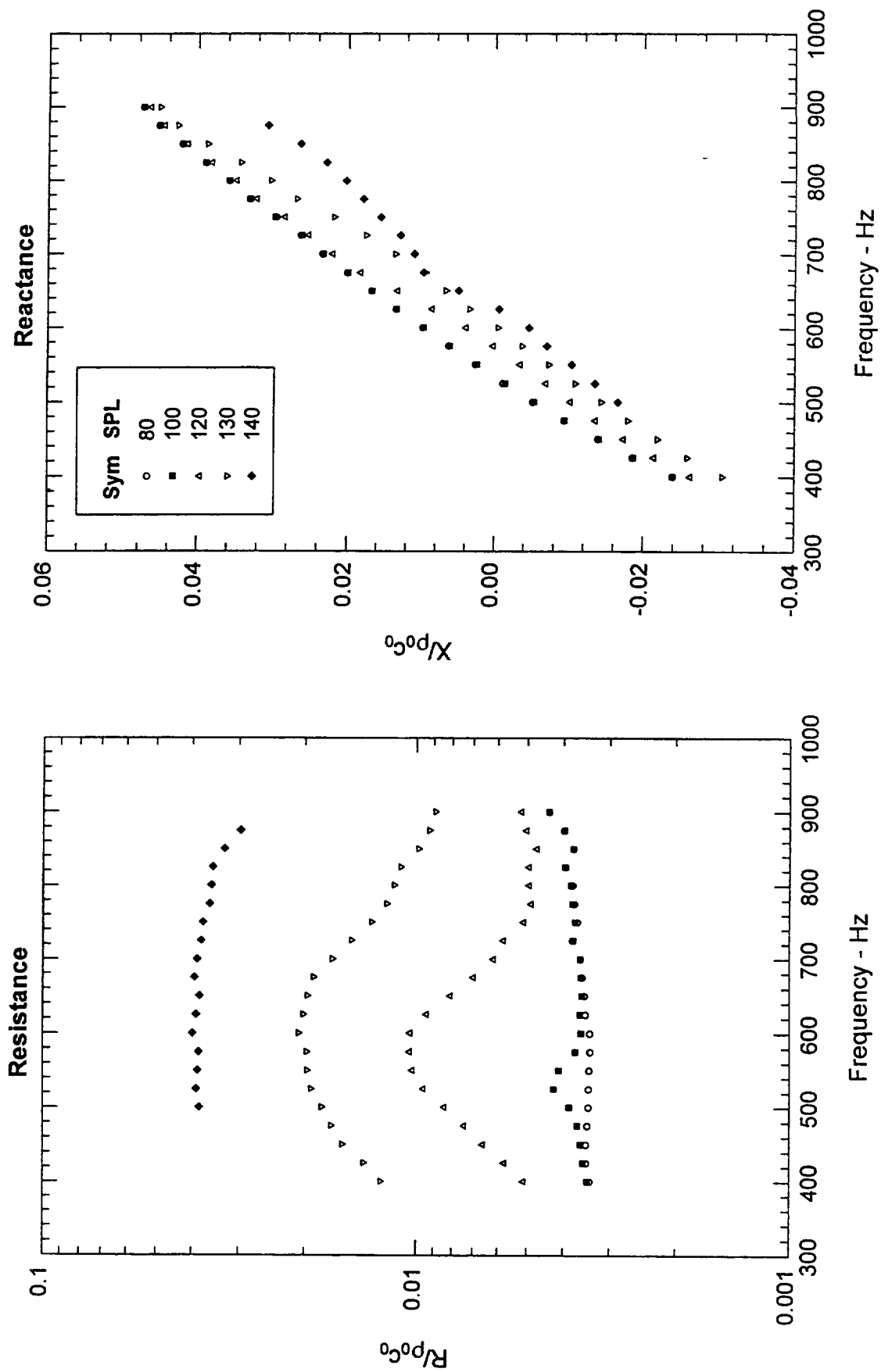


Figure 3. Effect of SPL on Resistance and Reactance of $N = 1$ Orifice Resonator: $V = 0$

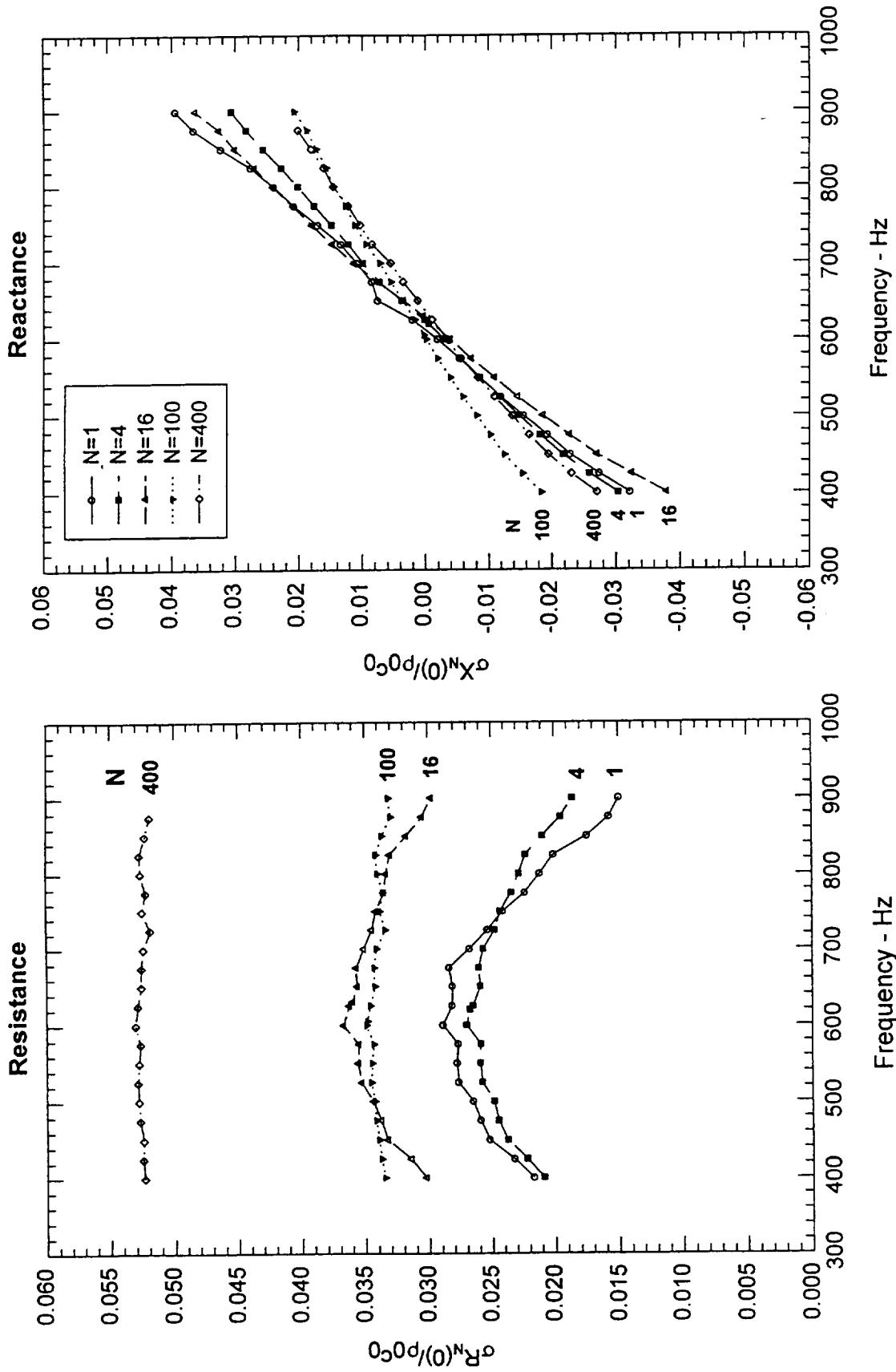


Figure 4. Effect of Orifice Number on Resonator Impedance: SPL = 135 dB and V = 0

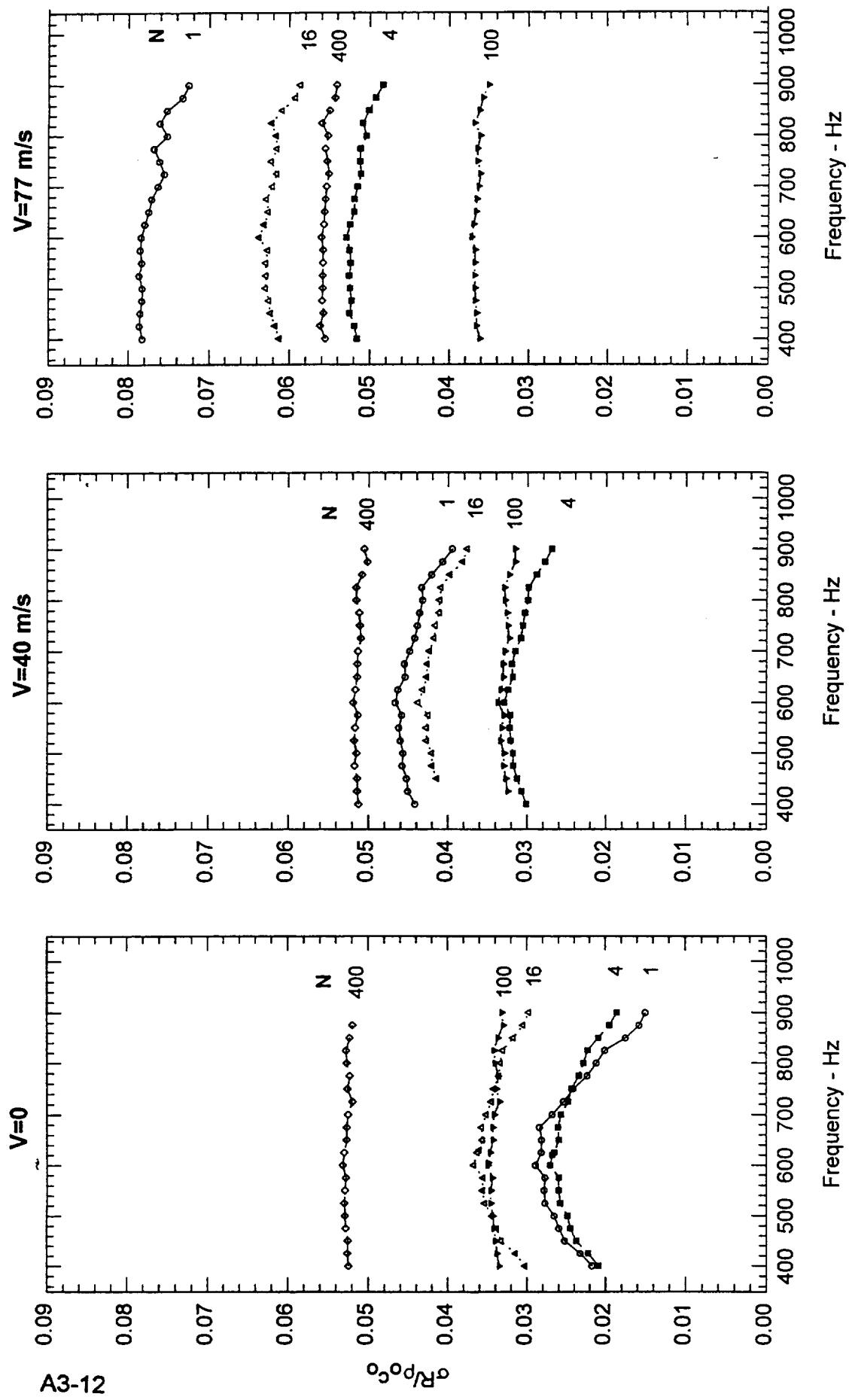


Figure 5a. Effect of Orifice Number and Grazing Flow Speed on Resonator Resistance: SPL = 135 dB

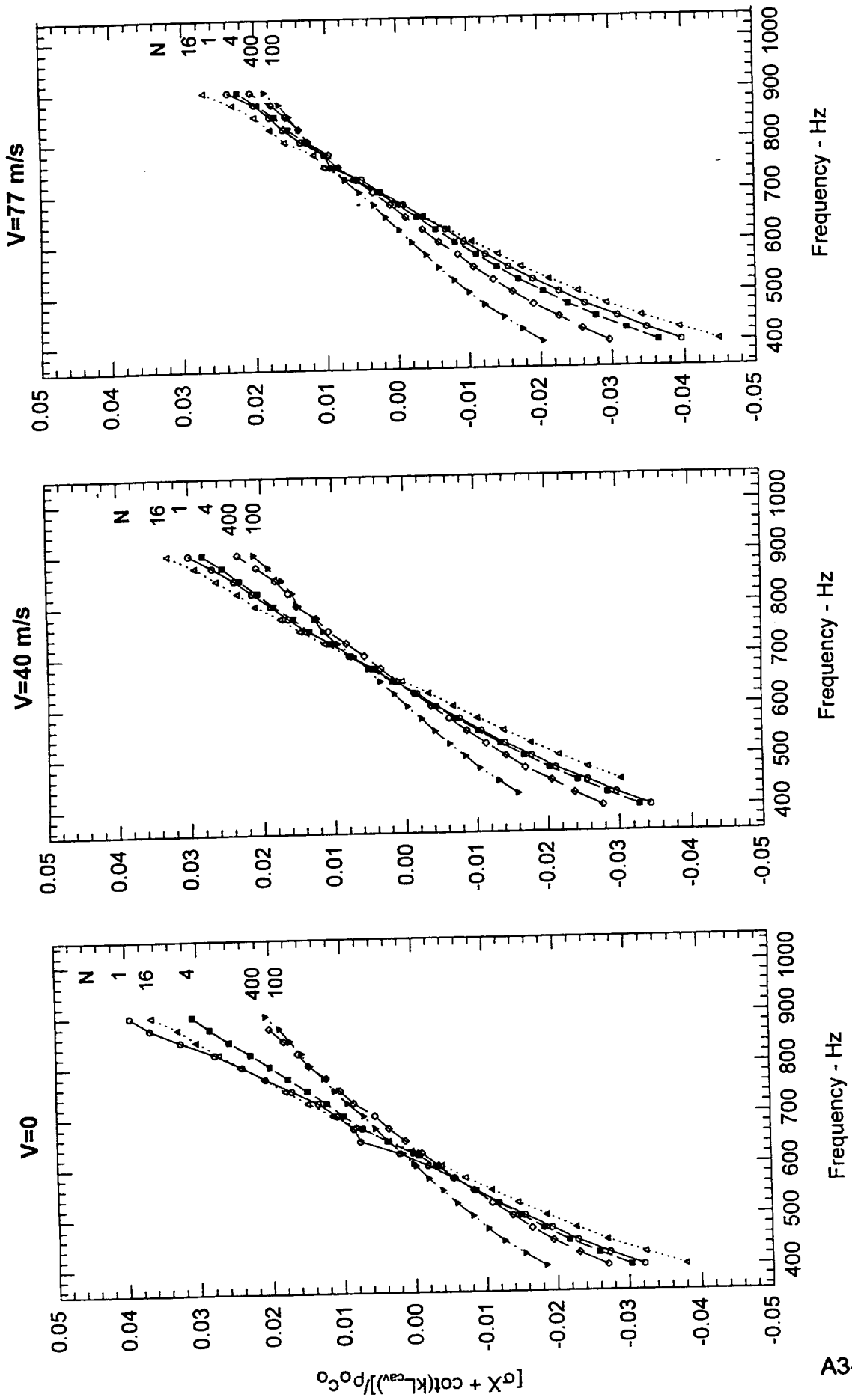


Figure 5b. Effect of Orifice Number and Grazing Flow Speed on Resonator Face-Sheet
 Mass Reactance: SPL = 135 dB

REPORT DOCUMENTATION PAGE			Form Approved OMB No. 0704-0188
Public reporting burden for this collection of information is estimated to average 1 hour per response, including the time for reviewing instructions, searching existing data sources, gathering and maintaining the data needed, and completing and reviewing the collection of information. Send comments regarding this burden estimate or any other aspect of this collection of information, including suggestions for reducing this burden, to Washington Headquarters Services, Directorate for Information Operations and Reports, 1215 Jefferson Davis Highway, Suite 1204, Arlington, VA 22202-4302, and to the Office of Management and Budget, Paperwork Reduction Project (0704-0188), Washington, DC 20503.			
1. AGENCY USE ONLY (Leave blank)	2. REPORT DATE February 1999	3. REPORT TYPE AND DATES COVERED Contractor Report	
4. TITLE AND SUBTITLE Advanced Turbofan Duct Liner Concepts		5. FUNDING NUMBERS C NAS1-20090 WU 538-03-12-02	
6. AUTHOR(S) Gerald W. Bielak, John W. Premo, and Alan S. Hersh			
7. PERFORMING ORGANIZATION NAME(S) AND ADDRESS(ES) Boeing Commercial Airplane Group MS 67-MK; P.O. Box 3707 Seattle, WA 98124-2207		8. PERFORMING ORGANIZATION REPORT NUMBER Hersh Acoustical Engineering, Inc. 780 Lakefield Rd., Unit G Westlake Village, CA 91361	
9. SPONSORING/MONITORING AGENCY NAME(S) AND ADDRESS(ES) National Aeronautics and Space Administration Langley Research Center Hampton, VA 23681-2199		10. SPONSORING/MONITORING AGENCY REPORT NUMBER NASA/CR-1999-209002	
11. SUPPLEMENTARY NOTES Bielak and Premo: Boeing Commercial Airplane Group; Hersh: Hersh Acoustical Engineering, Inc. Langley Technical Monitor: Tony L. Parrott			
12a. DISTRIBUTION/AVAILABILITY STATEMENT Unclassified-Unlimited Subject Category 71 Availability: NASA CASI (301) 621-0390		12b. DISTRIBUTION CODE Distribution: Nonstandard	
13. ABSTRACT (Maximum 200 words) The Advanced Subsonic Technology Noise Reduction Program goal is to reduce aircraft noise by 10 EPNdB by the year 2000, relative to 1992 technology. The improvement goal for nacelle attenuation is 25% relative to 1992 technology by 1997 and 50% by 2000. The Advanced Turbofan Duct Liner Concepts Task work by Boeing presented in this document was in support of these goals. The basis for the technical approach was a Boeing study conducted in 1993-94 under NASA/FAA contract NAS1-19349, Task 6, investigating broadband acoustic liner concepts. As a result of this work, it was recommended that linear double layer, linear and perforate triple layer, parallel element, and bulk absorber liners be further investigated to improve nacelle attenuations. NASA LaRC also suggested that "adaptive" liner concepts that would allow "in-situ" acoustic impedance control also be considered. As a result, bias flow and high-temperature liner concepts were also added to the investigation. The major conclusion from the above studies is that improvements in nacelle liner average acoustic impedance characteristics alone will not result in 25% increased nacelle noise reduction relative to 1992 technology. Nacelle design advancements currently being developed by Boeing are expected to add 20-40% more acoustic lining to hardwall regions in current inlets, which is predicted to result in an additional 40-80% attenuation improvement. Similar advancements are expected to allow 10-30% more acoustic lining in current fan ducts with 10-30% more attenuation expected. In addition, Boeing is currently developing a scarf inlet concept which is expected to give an additional 40-80% attenuation improvement for equivalent lining areas.			
14. SUBJECT TERMS Noise; Duct linings; Turbofan engines		15. NUMBER OF PAGES 235	
		16. PRICE CODE A11	
17. SECURITY CLASSIFICATION OF REPORT Unclassified	18. SECURITY CLASSIFICATION OF THIS PAGE Unclassified	19. SECURITY CLASSIFICATION OF ABSTRACT Unclassified	20. LIMITATION OF ABSTRACT UL